STRUCTURAL INTEGRITY OF POWER TRANSFORMERS

GÖKHAN KALKAN

May 2012

Mechanics of Materials

Department of Mechanical Engineering

Imperial College London

A thesis submitted for the degree of Doctor of Philosophy of Imperial College London and the Diploma of Imperial College

DECLARATION OF ORIGINALITY

I declare that this thesis is my own work and has not been submitted in any form for another degree or diploma at any university or other institute of tertiary education. Information derived from the published and unpublished work of others has been acknowledged in the text and a list of references is given in the bibliography.

ABSTRACT

The subject of this thesis is to study the mechanical integrity and performance of insulation materials used in power transformers under short circuit conditions. There are a number of methods to calculate short circuit forces in the literature. These methods were developed to determine the magnetic properties related to the short circuit condition and cannot be used in the open circuit condition due to the assumption of infinitely permeable core. To this end, a new solution strategy is introduced which is able to calculate magnetic properties of power transformers both in open circuit and in short circuit conditions. A solution was derived utilizing transform techniques and multiple connected permeable regions can now be solved.

Mechanical failure modes of transformer winding are presented and new solution methods are introduced for some failure modes. Dynamic representation of the transformer winding is achieved by treating the winding turn by turn. Particular attention is given to stress calculations of Continuously Transposed Cable (CTC) and resin bonded CTC.

Digital Image Correlation (DIC) technique maps the strain distribution on the test specimen and the strain distribution can be extracted at any cross section of interest. 3-D DIC technique is used to determine the response of transformerboard material under tensional and bending loads and material properties are determined. It is also shown that the DIC method provides much more accurate results compared to strain gauges due to its manufacturing technique. DIC results are used to determine material properties related to both tensional and bending type loading conditions. Resin laminate wood is also compared to transformerboard.

Viscoelastic properties of transformerboard are examined. Because a short circuit event is dynamic in nature, storage and loss modulus of transformerboard are determined as a function of temperature and frequency under cyclic loading conditions. Conventional creep test setups cannot be used for transformerboard. A test setup is designed to measure creep curves of transformerboard. The test setup measures the creep curves both in oil and in air and the displacements are recorded automatically. Tests are performed at a wide range of temperatures encountered in real service conditions of transformerboard material.

The developed method can be introduced in PC codes to determine the magnetic properties related to the magnetic field. Also the method can be used to determine turn to turn or disc to disc mutual inductances of a transformer. Electromagnetic forces calculated with the introduced method are also more accurate than the methods developed earlier. Methods to calculate mechanical stresses acting on transformer components are also reviewed and new solution techniques for some failure modes are developed. Mechanical performance of insulation materials under tension and bending type loadings are measured and monitored using DIC technique. Finally, time dependent material properties of the transformerboard under constant and cyclic loading conditions are determined.

Both analytical and experimental techniques are utilized to determine the material properties of the transformer components and their behaviour under different loading conditions. New solution techniques are developed and the material behaviour of the insulation materials under different loading conditions is determined. With the data obtained and solutions developed, mechanical stress calculations of the power transformer components can be made more accurately.

ACKNOWLEDGMENTS

I would like to acknowledge the help and supervision of Dr. John Dear during my PhD studies, Professor Andy Morris of E.ON for helpful discussions and additionally Balikesir Electromechanical Plants Corporation for their funding. Thanks are due to my colleagues who are too many to list here entirely. I specifically thank Paolo and Hari for their useful discussions and assistance in the laboratories, Tim and Amit for their help with DIC analysis and Yatish, Kunal, Idris, Koucheng, Chris and Catrin for help and support over the last three years. I also would like to thank to my parents for their support throughout without whom I would not have submitted.

CONTENTS

ABSTRACT 3

ACKNOWLEDGMENTS 5

CONTENTS 6

LIST OF FIGURES 9

LIST OF TABLES 16

NOMENCLATURE 17

- Chapter-3: Electromagnetic Force Calculations 17
- Chapter-4: Structural Integrity of Transformer Active Part 19
- Chapter-6: Bending Tests of Transformerboard 22

CHAPTER-1: INTRODUCTION 24

CHAPTER-2: LITERATURE REVIEW 27

- 2.1 Analytical and Numerical Techniques to Calculate Electromagnetic Field and Force 27
- 2.2 Material Properties of the Transformerboard 39
- 2.3 Digital Image Correlation (DIC) Technique 43

CHAPTER-3: ELECTROMAGNETIC FORCE CALCULATIONS 45

- 3.1 Introduction 45
- 3.2 Short Circuit Currents 46
- 3.3 Current Density 49
- 3.4 Review of Maxwell's Equations and Vector Potential 51
- 3.5 Methods Developed to Calculate Magnetic Properties of Transformers 52
- 3.6 Magnetic flux Density and Vector Potential Calculations with Roth's Method 53
- 3.7 Proposed Method Taking Finite Permeability of the Core into Account 56
- 3.8 Comparison of the Proposed Method with FEA and Roth's Solution 76
- 3.9 Electromagnetic Force Calculations 81
- 3.10 Dynamic Electromagnetic Force Calculations 85
- 3.11 Inductance, Reactance and Magnetic Energy Calculations 86

- 3.12 Electromagnetic Finite Elements Solutions 87
- 3.13 Conclusions 89

4- STRUCTURAL INTEGRITY OF TRANSFORMER ACTIVE PART 91

- 4.1 Introduction 91
- 4.2 Radial and Axial Electromagnetic Forces 93
- 4.3 Radial Failure Modes and the Integrity of the Windings 96
    - 4.3.1 Radial Bending 98
- 4.4 Axial Failure Modes and the Integrity of the Windings 103
- 4.5 Conclusions 110

5- BEHAVIOUR OF TRANSFORMERBOARD UNDER TENSIONAL LOADING 112

- 5.1 Introduction 112
- 5.2 Description of Test Setup and Digital Image Correlation Post-processing Procedure 112
- 5.3 Tensile Tests Performed on Transformerboard in Machine Direction and Cross Machine Direction 118
- 5.4 Conclusions 127

6-BENDING TESTS OF TRANSFORMERBOARD 130

- 6.1 Introduction 130
- 6.2 Full Analytical Solution to Three and Four Point Bending Tests 131
- 6.3 Solution to Symmetric- Symmetric (SS) Case 134
- 6.4 Solution to Symmetric – Asymmetric (SA) Case 136
- 6.5 Three Point Bending Tests 140
- 6.6 Delamination Initiation 142
- 6.7 Three Point Bending Test Results of Variant-1 and 2 144
- 6.8 Three Point Bending Test Results of Variant-3 and 4 150
- 6.9 Final Comments on Bending Tests of Transformerboard 160
- 6.10 Laminated Wood 161
- 6.11 Laminated Wood Reinforced with Glass Fibre 162
- 6.12 Comparison of Transformerboard and Laminated Wood 166

7- VISCOELASTIC PROPERTIES OF TRANSFORMERBOARD 167

- 7.1 Introduction 167
- 7.2 Dynamic Mechanical Thermal Analysis (DMTA) Tests 168
- 7.3 Test Setup to Determine Time Dependent Behaviour of the Transformerboard 172
- 7.4 Creep Test Results 180
- 7.5 Conclusions 187

8- CONCLUSIONS & FUTURE WORK RECOMMENDATIONS 189

APPENDIX-A 192

APPENDIX-B 200

REFERENCES 202

LIST OF FIGURES

FIGURE-1.1: Typical Winding Arrangement 25

FIGURE-2.1: Radial Magnetic Flux and Forces in concentric Windings [From-Ref.1] 27

FIGURE-2.2: Determination of Residual Ampere-Turn Diagram for a Winding Tapped at one end [From- Ref.1] 28

FIGURE-2.3: Conductor (Top Figure) and Current Density (Bottom Figure) Distribution for Rogowski Model 30

FIGURE-2.4: Rogowski's Transformer Model 30

FIGURE-2.5: Current Density Distribution for Rabin's Method 33

FIGURE-2.6: Detector Unit used in Short Circuit Test [From-Ref.11] 35

FIGURE-2.7: Mathematical Model for three Phase Transformer, Fault on Middle Phase 37

FIGURE-2.8: Mathematical Model Representing Oil Impregnated Insulation Material 38

FIGURE-2.9: Complete Winding and Clamp Model, Fault on Middle Phase 38

FIGURE-2.10: Decrease in Residual Length after Several and First Pressing 41

FIGURE-2.11: Ratio of Residual Length Change to Total Length Change vs Specific Weight after the First Pre-stress with 200 kg/cm^2 41

FIGURE-2.12: Test Rig to Test Transformerboard 43

FIGURE-2.13: Image Correlation Full-Field Principal Strain Map with Strain Gauge Location Indicated by Black Outline (From [54]) 44

FIGURE-3.1: Symmetrical Current 46

FIGURE-3.2: Equivalent Circuit at Short Circuit 47

FIGURE-3.3: Asymmetrical Fault Current vs Time 49

FIGURE-3.4: Cross Section of Simplified Transformer Window 50

FIGURE-3.5 Images of Transformer Window in x and y Directions 54

FIGURE-3.6: Transformer Window Including Core 57

FIGURE-3.7: Transformer Window Neighbours to Highly Permeable Core 58

FIGURE-3.8: Superposition of Laplace Field based on the Boundary Conditions 61

FIGURE-3.9: Flux Lines – Open Circuit Condition FEA – Proposed Theory 78

FIGURE-3.10: Comparison of Vector Potential Values – Short Circuit Condition at y=1650mm 78

FIGURE-3.11: Comparison of Vector Potential Values – Short Circuit Condition at x=500mm 80

FIGURE-3.12: Comparison of Vector Potential Values – Open Circuit Condition at y=500mm 80

FIGURE-3.13: Some Tapping Arrangements on HV Winding 82

FIGURE-3.14: Force Density Distribution through the Winding Height 83

FIGURE-3.15: Force Density Distribution of an Example Winding 84

FIGURE-3.16: Dynamic Short Circuit Forces Acting on Turn of a Transformer Winding 86

FIGURE-3.17: Typical B-H curve for FEA Analysis from ANSYS Documentation 88

FIGURE-3.18: Cross-section of Stranded Coil, from ANSYS Documentation 89

FIGURE-4.1: Continuously Transposed Cable 92

FIGURE-4.2: Short Circuit Current and Dynamic Short Circuit Force Respectively 92

FIGURE-4.3: Electromagnetic Forces Acting on Outer and Inner Windings 93

FIGURE-4.4: Distribution of Electromagnetic Forces along the Winding a) Radial Forces b) Axial Forces c) Cumulative Axial Forces 94

FIGURE-4.5: Electromagnetic Axial Forces Acting on a Winding Consists of 5 Turns and Their Cumulative Effect 95

FIGURE-4.6: Layer Winding Configuration 96

FIGURE-4.7: CTC Cross-Section 97

FIGURE-4.8: Position of Axial Sticks 98

FIGURE-4.9: Free Body Diagram of Inner Winding 99

FIGURE-4.10: Distances to Consider for Moment Relations 100

FIGURE-4.11: Axial Bending of Conductor between two Radial Spacers 103

FIGURE-4.12: Discrete Representation of Transformer Winding 104

FIGURE-4.13: Displacement of Top Turn 110

FIGURE-4.14: Displacement of Bottom Turn 110

FIGURE-5.1: Planes where Strain Gauges are Attached and Speckle Patterns are Created for DIC Measurement 114

FIGURE-5.2 Position of the Test Specimen and DIC Cameras for 3-D DIC Measurements 115

FIGURE-5.3: Test Specimen Images- Left and Right Camera Respectively 116

FIGURE-5.4: Image Obtained from 3-D ARAMIS DIC Software – Right Camera 116

FIGURE-5.5: Lines Generated by ARAMIS Software to Study Strains/Extensions 117

FIGURE-5.6: Position of the Pixel Points for Coordinate Transformation 117

FIGURE-5.7: DIC Data Contains Information on 1-3 Plane Only 118

FIGURE-5.8: Tensile Test specimen Configuration 119

FIGURE-5.9: Load – Extension Curves for Machine & Cross Machine Direction Specimens 120

FIGURE-5.10: Failure Mechanism of Machine Direction Specimens – Oil Impregnated 120

FIGURE-5.11: % Strain in Direction-3, MD Specimen a) Strain Gauge-2 Data b) DIC Data 122

FIGURE-5.12: Comparison of %Strain in Direction 1 – MD Specimen 122

FIGURE-5.13: Poisson's Ratio v_{13}, MD Specimen a) Strain Gauge-1 Data b) DIC Data 123

FIGURE-5.14: Comparison of Strain in Direction 2 – Strain Gauge and DIC Data 124

FIGURE-5.15: Comparison of Poisson's Ratio v_{12}, MD Specimen – Strain Gauge and DIC Data 124

FIGURE-5.16: % Strain in Direction-3, CMD Specimen a) Strain Gauge-2 Data b) DIC Data 125

FIGURE-5.17: Comparison of %Strain in Direction 2 – CMD Specimen 125

FIGURE-5.18: Poisson's Ratio v_{23}, MD Specimen a) Strain Gauge-1 Data b) DIC Data 126

FIGURE-5.19: Comparison of Strain in Direction 1 for CMD Specimen– Strain Gauge and DIC Data 126

FIGURE-5.20: Comparison of Poisson's Ratio v_{21}, CMD Specimen – Strain Gauge and DIC Data 127

FIGURE-6.1: Position of Clamping Ring and Metal Nuts 130

FIGURE-6.2: Bending Test Arrangement for Complete Clamping Ring [From Ref.2] 131

FIGURE-6.3: Four-Point Bending Test Arrangement 132

FIGURE-6.4: Decomposition of 4PB Test Arrangement 132

FIGURE-6.5: Comparison of Bending and Shear Strain Distribution at -40mm 139

FIGURE-6.6: Comparison of Normal and Shear Strain Distribution at -5mm 139

FIGURE-6.7: Comparison of Shear Strain Distribution at -90mm 133

FIGURE-6.8: Shear Strain Distribution 140

FIGURE-6.9: Bending Strain Distribution 140

FIGURE-6.10: Dimensions of Three-Point Test Specimen for Variants 1 and 2 141

FIGURE-6.11: Dimensions of Three-Point Test Specimen for Variants 3 and 4 141

FIGURE-6.12: Start of Delamination 142

FIGURE-6.13: Strain Concentration before Delamination 143

FIGURE-6.14: Shear Stress Mapping after Delamination 143

FIGURE-6.15: DIC Results for Bending Strain at 3 and 5 mm respectively 144

FIGURE-6.16: Local Separation after Test 144

FIGURE-6.17: Load-Extension Curve for Variant-1 145

FIGURE-6.18: Distribution of the Bending Strain at Mid-Plane- From DIC 146

FIGURE-6.19: Corrected Distribution of the Bending Strain at Mid-Plane- From DIC at 580N Load 146

FIGURE-6.20: Comparison of Bending Strain at Mid-Plane at 580N 147

FIGURE-6.21: Shear Strain Distribution at 3 and 5mm respectively for Variant-1 148

FIGURE-6.22: Shear Strain Distribution at 0.9mm and 1.55mm Crosshead Displacement 148

FIGURE-6.23: Load-Extension Curve for Variant-2 149

FIGURE-6.24: Corrected Distribution of the Bending Strain at Mid-Plane- From DIC at 1300N 149

FIGURE-6.25: Bending Strain Distribution 150

FIGURE-6.26: Shear Strain Distribution 150

FIGURE-6.27: Load-Extension Curve for Variant-3 151

FIGURE-6.28: Cross-Section Geometry and Material Properties 152

FIGURE-6.29: Expected Shear Strain Distribution for Multi-Layer Beam 152

FIGURE-6.30: Bending Strain Distribution for Variant-3 153

FIGURE-6.31: Comparison of Theoretical and Experimental Shear Strain for Variant-3 at 2.38Kn 153

FIGURE-6.32: Shear Strain Map on Variant-4 154

FIGURE-6.33: Comparison of Theoretical and Experimental Shear Strain for Variant-4 at 1kN 155

FIGURE-6.34: Shear Strain Distribution at Different Cross Sections – Full Solution Results 157

FIGURE-6.35: Comparison of Shear Strain Distribution at x=60mm 157

FIGURE-6.36: Comparison of Bending Strain Distribution at x=60mm 158

FIGURE-6.37: Shear Strain Distribution Prior to Final Failure 158

FIGURE-6.38: Comparison of Bending Strain Distribution at 4700N Loading – Theory vs DIC 160

FIGURE-6.39: Comparison of Shear Strain Distribution at 4700N Loading – Proposed Theory vs DIC 160

FIGURE-6.40: Comparison of Load – Extension curves of Laminated Wood Aged at Three Different Temperatures 162

FIGURE-6.41: Laminated Wood Reinforced with Glass Fibre 163

FIGURE-6.42: Shear Strain Map on Laminated Wood Reinforced with Glass Fibre Specimen 163

FIGURE-6.43: Shear Strain Distribution at Mid-Plane between the Support and Loading Pin 164

FIGURE-6.44: Bending Strain Map on Laminated Wood Reinforced with Glass Fibre Specimen 165

FIGURE-6.45: Bending Strain Comparison at Cross Sections 1 and 2 165

FIGURE-7.1: Storage Modulus of Transformerboard between -10^0C and 190^0C at Six Different Frequencies for Dried Specimen – CM Direction 169

FIGURE-7.2: Tan Delta of Transformerboard between -10^0C and 190^0C at Six Different Frequencies for Dried Specimen – CM Direction 170

FIGURE-7.3: Tan Delta and Storage Modulus of Transformerboard between 20^0C and 190^0C at Five Different Frequencies for Oil Impregnated Specimen – CM Direction 171

FIGURE-7.4: Tan Delta and Storage Modulus of Transformerboard between 20^0C and 190^0C at Six Different Frequencies for Dried Specimen after the Ageing Limit is Exceeded– CM Direction 172

FIGURE-7.5: Creep Test Setup Design 173

FIGURE-7.6: Grips and Test Specimen 174

FIGURE-7.7: Creep Rig – View.1 176

FIGURE-7.8: Creep Rig – View.2 177

FIGURE-7.9: Creep Rig – View.3 178

FIGURE-7.10: Creep Test Specimen Dimensions 180

FIGURE-7.11: Failed Specimen 181

FIGURE-7.12: Displacement – Time Curve for Transformerboard Tested in Transformer Oil at 140^0C – Applied Stress 4MPa 182

FIGURE-7.13: %Strain – Time Curve for Transformerboard Tested in Transformer Oil at 140^0C– Applied Stress 4MPa 183

FIGURE-7.14: %Strain – Time Curve for Transformerboard Tested in Transformer Oil at 120^0C– Applied Stress 4MPa 184

FIGURE-7.15: %Strain – Time Curve for Transformerboard Tested in Transformer Oil at Various Temperatures– Applied Stress 4MPa 185

FIGURE-7.16: Test Specimen 186

FIGURE-7.17: Comparison of %Strain – Time Curve for Transformerboard Tested in Transformer Oil at 100^0C for Notched and Normal Specimens 186

FIGURE-B.1: Wiring Diagram for Test Setup – For Tests in Air 200

FIGURE-B.2: Wiring Diagram for Test Setup – For Tests in Oil 201

LIST OF TABLES

TABLE-3.1: Comparison of the FEA Models 76

TABLE-3.2: Dimensions (mm) and Excitation Values (Ampere – Turns) 77

TABLE-3.3: Comparison of Calculated Inductances 77

TABLE-3.4: Comparison of Calculated Forces (N/m) on Conductors for Open Circuit (OC) and Short Circuit (SC) 77

TABLE-5.1: Dimensions of the Machine and Cross Machine Direction Specimens 119

TABLE-5.2: Calculated Elastic and Plastic Poisson's Ratios, v_{12}, with Strain Gauges and DIC 124

TABLE-5.3: Calculated Elastic and Plastic Poisson's Ratios, v_{21}, with Strain Gauges and DIC 127

TABLE-6.1: Dimensions, Loads and Material Properties Used in Comparison 138

TABLE-6.2: Comparison of Elasticity Modulus (MPa) – DIC and Load Deflection Curve 146

TABLE-6.3: Calculated Shear Modulus- G_{13} (MPa) and Elasticity Modulus-E_{11} (MPa) 154

TABLE-6.4: Calculated Shear Modulus- G_{23} (MPa) and Elasticity Modulus-E_{22} (MPa) 155

TABLE-6.5: Interlaminar Shear Strength in Machine (MD) and Cross-Machine (CMD) Directions 159

TABLE-7.1: Time (Minutes) to Failure of Transformerboard Tested in Oil and Air at Different Test Temperatures 184

TABLE-7.2: Time (Minutes) to Failure of Notched and Normal Transformerboard Specimens Tested in Oil at Different Test Temperatures 186

NOMENCLATURE

Nomenclature is divided into three chapters because the chapters 3, 4 and 6 involves formulas and some of the terms used are the same but represent different physical quantities.

- **Chapter-3: Electromagnetic Force Calculations**

  a: Transformer Window Width (m)

  a_0: Constant for Roth's Solution when a Single Permeable Region is Attached to Poisson's Field

  a_2: Polynomial Constant for Laplace's Field in Axial Direction in Region-2

  a_3: Polynomial Constant for Laplace's Field in Radial Direction in Region-3

  a_5: Polynomial Constant for Laplace's Field in Radial Direction in Region-5

  a_6: Polynomial Constant for Laplace's Field in both the Axial and the Radial Directions in Region-6

  a_8: Polynomial Constant for Laplace's Field in Axial Direction in Region-8

  a_{61}: Polynomial Constant for Laplace's Field in Radial Direction in Region-6

  a_{62}: Polynomial Constant for Laplace's Field in Axial Direction in Region-6

  a_{66}: Constant for Roth's Solution when Poisson's Field is Surrounded with Permeable Regions in Region-6

  $a_j \; where \; j = 1,2 \dots number \; of \; winding \; sections$: The Distance between the Core and the Beginning of the Winding Section in Radial Direction (m)

  $a'_j \; where \; j = 1,2 \dots number \; of \; winding \; sections$: The Distance between the Core and the End of the Winding Section in Radial Direction (m)

  A: Magnetic Vector Potential (Wb/m)

  b: Transformer Window Height (m)

  $b_j \; where \; j = 1,2 \dots number \; of \; winding \; sections$: The Distance between the Lower Yoke and the Beginning of the Winding Section in Axial Direction (m)

$b'_j \; where \; j = 1,2 \ldots number \; of \; winding \; sections$: The Distance between the Lower Yoke and the End of the Winding Section in Axial Direction (m)

B: Magnetic Flux Density (Wb/m^2)

B_x: Radial Magnetic Flux Density (Wb/m^2)

B_y: Axial Magnetic Flux Density (Wb/m^2)

B_{turn}: Magnetic Flux Density Actşng on a Single Turn (Wb/m^2)

D: Electric Flux Density (Coulomb/m^2)

E: Electric Field Intensity (Volt/m)

f: Frequency (Hz)

F: Electromagnetic Force (N)

F_x: Radial Electromagnetic Force (N)

F_y: Axial Electromagnetic Force (N)

$F_{Dynamic}$: Dynamic electromagnetic Forces

H: Magnetic Field Intensity (Ampere/m)

$I:$ Current (Ampere)

I_{pss}: Steady State Peak Current Amplitude (Ampere)

J: Current Density (Ampere/m^2)

l_{mean}: Mean Length of Windings (m)

L: Inductance (Henry)

$L_{leakage}$: Leakage Inductance (Henry)

$m_i = \frac{\pi}{a} i \quad i = 0,1 \ldots \infty$: Constants Associated with Circular Functions in Fourier Series in Roth's Solution in Radial Direction

$n_k = \frac{\pi}{b} k \quad k = 0,1 \ldots \infty$: Constants Associated with Circular Functions in Fourier Series in Roth's Solution in Axial Direction

M: Mutual Inductance (Henry)

N: Number of Turns

NI: Ampere-Turns (Ampere)

R: Resistance (Ohm)

t: Time (s)

U_k: Short Circuit Reactance (%)

V: Voltage Drop (Volts)

V_p: Peak Voltage Drop (Volts)

W: Magnetic Energy (Joule)

x_1: Radius of the Core (m)

x_2: Diameter of the Return Limb (m)

X: Reactance (Ohm)

$X_{leakage}$: Leakage Reactance (Ohm)

y_1: Diameter of the Lower Yoke (m)

y_2: Diameter of the Upper Yoke (m)

ε: Permittivity (Farad/m)

μ: Permeability of Free Space (Henry /m)

μ_1: Relative Permeability of the Core

μ_2: Relative Permeability of the Air/oil

μ_r: Relative Permeability (Henry /m)

ρ_v: Total Charge Density (Coulomb/m^3)

σ: Conductivity (Siemens/m)

φ: Phase Angle

- **Chapter-4: Structural Integrity of Transformer Active Part**

a: Transformer Window Width (m)

$a_j \; where \; j = 1,2 \ldots number \; of \; winding \; sections$: The Distance between the Core and the Beginning of the Winding Section in Radial Direction (m)

$a'_j \; where \; j = 1,2 \ldots number \; of \; winding \; sections$: The Distance between the Core and the End of the Winding Section in Radial Direction (m)

A: Area of the Conductor (m^2)

b: Transformer Window Height (m)

$b_j \; where \; j = 1,2 \ldots number \; of \; winding \; sections$: The Distance between the Lower Yoke and the Beginning of the Winding Section in Axial Direction (m)

$b'_j \; where \; j = 1,2 \ldots number \; of \; winding \; sections$: The Distance between the Lower Yoke and the End of the Winding Section in Axial Direction (m)

c^*: Damping Coefficient of the Upper Clamping Ring (kg/s)

c^{**}: Damping Coefficient of the Lower Clamping Ring (kg/s)

$c_n \; where \; n = 1,2..number \; of \; turns$: Damping Coefficient of the Radial Spacers or Insulation Material at that Turn (kg/s)

CTC: Continuously Transposed Cable

$D_{mean_n} \; where \; n = 1,2 \ldots number \; of \; turns$: Mean Diameter of the turns (m)

$F_{R,i,L}$: Radial Applied Electromagnetic Forces on i'th turn of L'th layer of the Winding (N)

h: Height of a Cable or Conductor (mm)

h_{strand}: Height of a Strand (mm)

$i_{SC}(t)$: Dynamic Short Circuit Current (Ampere)

I: Second Moment of Area of the Cable (m^4)

I_{pss}: Steady State Peak Current Amplitude (Ampere)

k^*: Stiffness of the Upper Clamping Ring (kg/s^2)

k^{**}: Stiffness Coefficient of the Lower Clamping Ring (kg/s^2)

$k_n\ where\ n = 1,2..number\ of\ turns$: Stiffness of the Radial Spacers or Insulation Material at that Turn (kg/s^2)

n_{cabRad}: The Number of Cables in Radial Direction

n_{cabAx}: The Number of Cables in Axial Direction

n_{rad}: The Number of Strands in a Cable in Radial Direction

n_T: Total Number of Strands in a CTC Bundle

$m_n\ where\ n = 1,2..number\ of\ turns$: Mass of the Turn (kg)

M_0: Bending Moment at the Point of Symmetry on the Winding (N)

N_0: Normal Reaction Forces at the Point of Symmetry on the Winding (N)

N_{Stick}: Number of Axial Sticks Around the circumference of the Winding

q: Radial Distributed Electromagnetic Forces Acting on a Winding (N/m)

R: Mean Radius of the Winding (m)

Rz: Resistance of the winding (Ohm)

L: Inductance of the Winding (Henry)

t: Time (s)

t_{strand}: Thickness of the Strand in a Cable (mm)

U_B: Strain energy due to Bending (J)

U_S: Strain Energy due to Shear forces (J)

U_T: Total Strain Energy (J)

U_{ST}: Strain Energy in the Axial Sticks (J)

X: Reaction Force Action on an Axial Stick (N)

Y_n: A Parameter Developed to Separate Magnetic flux Density from the Short circuit current. Hence, Magnetic Flux Density can be treated as Constant Parameter [N/(Ampere)^2]

α: Half the Angle between two Axial Sticks (deg)

β: The Factor for Maximum Shear Forces which Depends on the Geometry and the Cross-Sectional Properties of the Conductor

μ_0: Permeability of Free Space (Henry /m)

$\sigma_{Hoop,max}$: Maximum Hoop Stress Acting on a Turn along the Transformer (MPa)

$\sigma_{Hoop,i,L}$: Radial Applied Hoop Stress on i'th turn of L'th layer of the Winding (MPa)

$\sigma_{N,Max}$: Maximum Normal Stresses Acting on the winding (MPa)

τ: The Shear Force Acting on Winding (N)

τ_{max}: Maximum Shear forces Acting on Winding (MPa)

ψ: An Arbitrary Angle between the Axial Stick and the Point of Symmetry (deg)

- **Chapter-6: Bending Tests of Transformerboard**

a: The Length of the Beam (mm)

A: Polynomial Constant

B: Polynomial Constant

d: Depth of the Beam (mm)

d_1: The Length of the Applied Distributed Load (mm)

d_2: The Length of the Support (mm)

E_1: Elasticity Modulus in Direction-1 (MPa)

E_2: Elasticity Modulus in Direction-2 (MPa)

E_{xxB}: Bending Modulus (MPa)

F: Applied Force (N)

G_{12}: Shear Modulus in 1-2 Plane (MPa)

h: The Height of the Beam (mm)

I: Second moment of Area (m^4)

k_1: The Distance between the Applied Load and Mid-Plane of the Beam (mm)

k_2: The Distance between the Support and Mid-Plane of the Beam (mm)

M: Bending Moment (Nm)

P: The applied force (N)

y: The Distance between the Neutral Axis and some Arbitrary Point (mm)

γ_{12}: Shear Strain

δ: Deflection (mm)

ε_{11}: Strain in Direction-1

ε_{22}: Strain in Direction-2

σ_{11}: Stress in Direction-1 (MPa)

σ_{22}: Strain in Direction-2 (MPa)

σ_{SA11}: Stress in direction-1 for Symmetric-Asymmetric Case (MPa)

σ_{SA22}: Stress in direction-2 for Symmetric-Asymmetric Case (MPa)

σ_{SS11}: Stress in direction-1 for Symmetric-Symmetric Case (MPa)

σ_{SS22}: Stress in direction-2 for Symmetric-Symmetric Case (MPa)

υ_{12}: Poisson's Ratio in 1-2 Plane

τ_{12}: Shear Strain (MPa)

τ_{SA12}: Shear Stress for Symmetric-Asymmetric Case (MPa)

τ_{SS12}: Shear Stress for Symmetric-Symmetric Case (MPa)

ϕ_{T}: Total Stress Function of the System

ϕ_{SA}: Stress Function for Symmetric – Asymmetric Case

ϕ_{SS}: Stress Function for Symmetric – Symmetric Case

1-INTRODUCTION

Power transformers are one of the most expensive components of power generation and transmission. Failure causes capital losses as well as undelivered energy. As the power demand increased over the past years, power rating of modern transformers has increased and new winding and manufacturing techniques have been developed. Short circuit forces generated by the power transformers have increased and as a result, the mechanical integrity of a power transformer has become more important than it used to be because of increased power rating.

The most important part of the power transformer is the active part where windings, laminated silicon sheet metals and insulation materials, including clamping structures, are assembled. Among these, insulation materials are very important because they provide both electrical insulation and mechanical integrity. Although these materials have been used in industry for more than 40 years, even simple elastic properties, such as shear modulus or Poisson's ratio are not available. Ageing and electrical properties are very well defined on the other hand. Without defining and determining the mechanical properties of these materials, dynamic short circuit and seismic behaviour of the assembled active part cannot be fully understood.

One of the challenges and aims of this research is to determine necessary material properties and mechanical behaviour of insulation materials, namely, transformerboard. Techniques such as Fast Speed Photography and Digital Image Correlation will be used to map the strain distribution.

Determination of the dynamic behaviour of winding assembly requires determining electromagnetic forces correctly. Great efforts have been performed by researchers in the past to determine the distribution and magnitude of these forces. However, all these methods neglect the permeability of the core material. Inductances and properties related to open circuit condition cannot be determined with these methods. A new method will be introduced to calculate the properties of power transformers related to magnetic field. The method is capable of calculating the open and short circuit related properties. The force values calculated with the developed method are much more accurate because the method considers the permeability of the core.

Dynamic representation of power transformer windings will be studied and a method to calculate shear stresses will be introduced.

Figure1.1 shows typical winding arrangements and position of conductors and insulation materials such as spacers and sticks. These windings are for large power transformers where the diameter is approximately 1.5 meters and the length is 2 meters. Transformer winding is composed of conductors, transformerboard and insulation papers. Total thickness of insulation paper along the winding is smaller compared to other constituents and their stiffness will be assumed to be the same as that of transformerboard through the research.

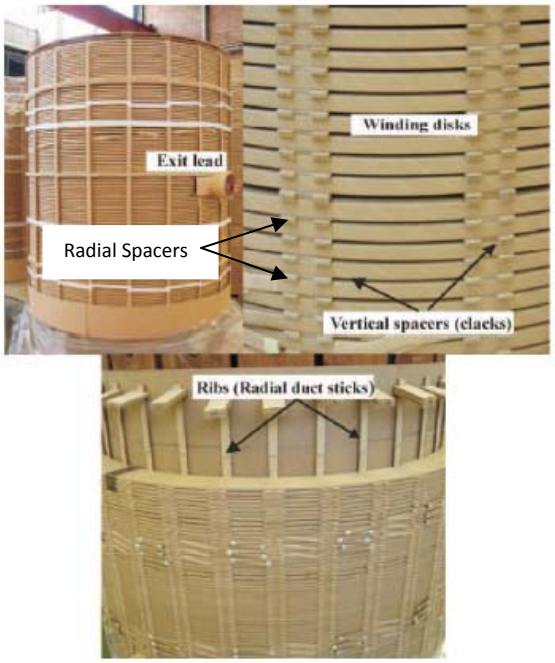

***FIGURE-1.1**: Typical Winding Arrangement*

Axial sticks, or radial duct sticks, are used to increase the buckling strength of the inner windings. Their size and number along the circumference should be determined so that the winding has sufficient strength against buckling and the cooling capacity of the channel between the windings is not reduced. Too many axial sticks will provide perfect strength against buckling because the span length will reduce but cooling capacity will be reduced and the hot spot temperature can be exceeded which will eventually cause failure.

Spacers are always working under compressive loadings. Considerable pre-stress is applied on winding to increase the natural frequency of the system and to enable winding to withstand axial forces. Pre-stress combined with short circuit forces increase compressive

forces acting on spacers. Pre-stress is applied on the upper clamping ring directly during manufacturing and axial short circuit forces generate bending moments. Bending forces combined with compressive forces are acting on the upper clamping ring. Therefore, compressive, tensile and bending behaviour of the transformerboard should be determined properly in order to understand the short circuit phenomenon.

The pre-stress phase starts before the oil filling phase and is always applied on untreated transformerboard. Short circuit forces, on the other hand, are applied on dried and oil impregnated material. Tests to determine material behaviour and properties will be performed on both cases in this research to simulate real loading conditions.

A new method will be introduced in Chapter-3 to calculate short circuit forces and magnetic properties of the power transformers. In Chapter-4, mechanical failure of the transformer winding due to short circuit forces will be investigated and new methods to calculate radial bending stress and dynamic response will be introduced. In Chapter-5 and Chapter-6, behaviour of transformerboard under tensional and bending loading conditions will be studied using Digital Image Correlation technique. Design of a creep test setup and the response of transformerboard at different temperatures in oil bath and in air will be shown in Chapter-7.

This thesis is aimed at determining the properties and the behaviour of the insulation materials used in the modern large power transformers. DIC and fast speed photography techniques are used widely because these techniques can record failure initiation and can map the strain distribution. These distributions then will be compared to the analytical techniques developed. Some material properties of insulation materials are not available in the literature and these material properties will be determined. With the solution techniques developed and the obtained test data, mechanical stress calculations of large power transformers can be made more accurately.

2-LITERATURE REVIEW

2.1 Analytical and Numerical Techniques to Calculate Electromagnetic Field and Force

Before modern numerical techniques and calculation methods were developed in order to calculate reactance and force components acting on transformer windings, approximate and numerical methods were used to estimate the leakage field occurring in transformer window. The magnetic flux density in the radial and the axial directions are calculated based on these limitations and forces are calculated using the Lorentz Law. Radial forces acting on transformer windings result from axial flux between the windings and are used to calculate the reactance (Figure-2.1).

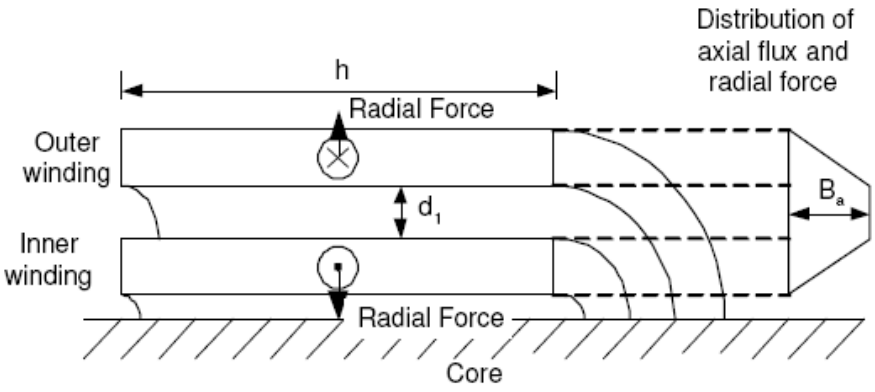

***FIGURE-2.1**: Radial Magnetic Flux and Forces in Concentric Windings [From-Ref.1]*

Waters [1], [38] summarized the solutions for the radial and axial forces using these approximations. The solution for radial forces is achieved by calculating the axial flux density but, axial flux lines fringes at winding ends as shown in Figure-3.9. Force per unit length will be almost uniform over the greatest part of the winding and it can be calculated with great accuracy. This approximation can be used with great accuracy for cases where Low Voltage (LV) and High voltage (HV) windings are equal in height and magnetic centers are aligned. Radial axial forces acting on each winding can be calculated using the formulae below.

$$P_r = \frac{2\pi(NI)^2 D_w}{h10^{11}}\ tons$$

Where h is the height of the winding, D_w is the mean diameter, N is the number of turns and NI is the ampere-turn of the winding. NI is calculated using peak asymmetric short circuit current and current is given by [1],

$$I = \frac{1.8\sqrt{2}MVA}{\sqrt{3}EU_k}\ 10^6 Ampere$$

Here, MVA is the power rating, E is line-to-line voltage, U_k is the leakage impedance of the transformer. Radial forces calculated with approximate methods provide good agreement with more sophisticated methods such as Roth's method [5] or Rabins' method [7].

Axial forces in a transformer with concentric windings cannot be calculated with great accuracy by elementary methods. The curvature of the windings cannot be taken into account without using sophisticated solution techniques and computers. One of the oldest techniques to calculate axial forces follows H.O. Stephen's [3] Residual Ampere-Turn method. In this technique, ampere-turns of the windings are split into two groups. Each group has balanced ampere-turns and ampere-turns acting in the radial direction which are assumed to generate radial flux causing axial forces. Radial ampere-turns acting at any point are calculated by summing primary and secondary ampere-turns between the points (Figure-2.2).

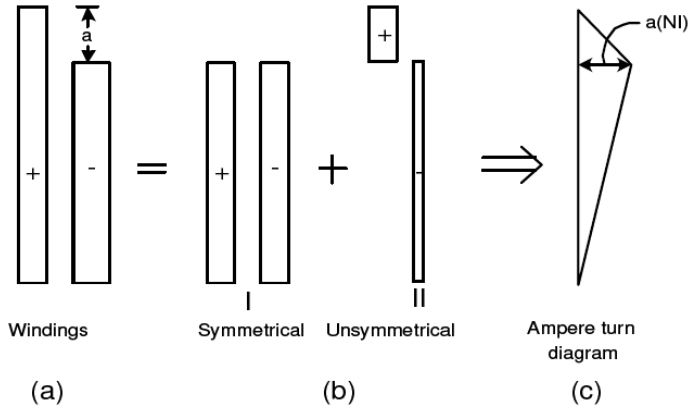

FIGURE-2.2*: Determination of Residual Ampere-Turn Diagram for a Winding Tapped at one end [From- Ref.1]*

The two arrangements I and II of Figure-2.2b are both balanced ampere-turns groups which are then superimposed to produce the given winding arrangement. Figure-2.2c shows the

radial ampere-turn distribution of the windings. This method cannot be applied to the simplest case of two windings having balanced ampere-turns and equal height because in this case there are no residual ampere-turns.

To calculate axial forces, the effective length of path for the radial flux for all points is required. Previously, the assumption has been made that this length is constant and did not vary with axial position of the winding. Although a rough approximation which generates simple results, tests showed that flux does follow a triangular shape [1].

Magnetic flux density acting on the radial direction, B_r, generates forces in axial direction, P_a. Magnetic flux density and axial forces can be calculated using the residual ampere-turn distribution method for winding arrangement shown in Figure-2.2 as;

$$B_r = \frac{4\pi}{10}\frac{a(NI)}{2h_{eff}}\ Gauss$$

$$P_a = \frac{2\pi}{10^{11}}\frac{a(NI)^2}{h_{eff}}\ Tons$$

Different winding arrangements were studied by the researchers using this method to provide a solution for axial forces. Waters provided solutions for widely used winding arrangements [1].

Rogowski [4] was the first to attempt to provide a solution for reactance calculations in a scientific way. In his original work, current density distribution was expressed in terms of Fourier series and solutions to Laplace and Poisson's Equations were provided. In a transformer window, current-carrying conductors possess a current density and Maxwell's equation, in terms of vector potential, reduces to Poisson's equation.

$$\nabla^2 A = -\mu J$$

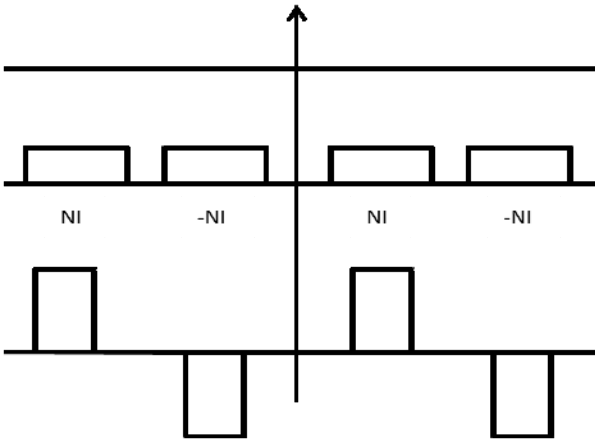

***FIGURE-2.3**: Conductor (top figure) and Current Density (bottom figure) Distributions for Rogowski Model*

$$J = \frac{4J_0}{\pi} \sum_{m=1,3,5.....}^{\infty} \frac{1}{m} \cos(mka) \sin mkx$$

The above equation is the current density expressed in terms of a Fourier series. Rogowski solution gives good results for cases where the windings are perfectly balanced and windings are in line. Winding should line their ends directly on to the yokes and this arrangement is very simple compared to commercial winding design. Moreover, windings never rest their ends on the yokes. This solution method is valuable when the current distribution is periodic.

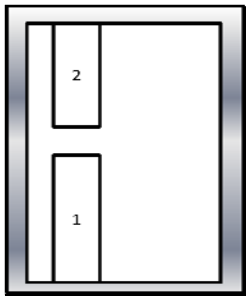

***FIGURE-2.4**: Rogowski's Transformer Model*

Roth [5] took up Rogowski's method under more general conditions. He obtained a solution in terms of double Fourier series which defines the whole window. Current density and vector potential are assumed to flow in the z direction, which is a reasonable assumption. In establishing the solution, a function is first found satisfying the boundary conditions and constants of the function are then chosen to satisfy the field equation. The form of the

vector potential of this method is to replace infinitely permeable boundaries with infinite number of images in both x and y directions. The problem is solved in the x-y plane by considering infinitely long conductors in z direction. This solution does not take the effect of curvature into account and because double Fourier series are involved in the solution, a computer program is needed. Roth's solution finds a single function satisfying both the Laplace's and Poisson's equations and it is easier to derive the final vector potential equations.

Roth's solution, using a double Fourier Series, was compared to the method of separation of variables in reference [6]. Slow convergence of the double Fourier Series compared to a single Fourier Series and simplicity of deriving the final vector potential formulation with Roth's method was shown. Limitation of Roth's solution when boundary conditions are not Neumann's type, where the derivative of the vector potential vanishes at the boundaries, was shown and it was concluded that the solution can only be used for certain boundary conditions. Roth's attempts to replace the iron core with current distribution on the iron surface was shown and discussed.

In [7], an extension of Roth's solution was given. In this method, tangential flux density can take any value at the boundaries and the solution was obtained using transform techniques. Although, the solution gives correct values within the boundary, the solution does not converge to the specified values at the boundary.

Roth's work was spread over a number of papers and was not translated. Billig [8] translated and summarized Roth's work and provided simpler solutions in order to decrease the computational labour and drawing general considerations.

Although most applications of Roth's method have been concerned with rectangles placed parallel to boundaries within the slot, there is little restriction on conductor shape. In this method, there is no requirement for the conductors to be parallel to boundaries. On Rogowski's method on the other hand, rectangular elements must be parallel to the boundaries. In Roth's method, any mathematically definable curve can be solved. Pramanik obtained a solution for triangular conductor [9].

Billig [8] used the theorem developed by Roth and Kouskoff to contract the series involved in original Roth's solution and obtained a simpler vector potential function. Using stored magnetic energy and simplified mean vector potential formulations, he expressed the total inductance as sum of three terms. The first term is balanced term and represents a transformer with equal windings and aligned magnetic centers. Second term gives rise to inductance if magnetic centers are misaligned and third component occurs if a difference exists in the axial heights of the windings.

Billig [8] expressed the axial short circuit forces in terms of second component of total inductance. This is because the second term exists only if magnetic centers of the windings are misaligned and the end thrust vanishes for windings with equal height and aligned magnetic centers. The final result is;

$$F_y = \frac{4\pi(NI)^2 l}{d}\left[1 + \frac{\pi}{2}\frac{h}{d}\left(1 + \sinh\frac{\pi a}{d}\right)\right]\frac{\beta}{a}$$

$$h = \frac{2a}{3} - \left(2\bar{a} + \frac{c}{3}\right) + \frac{\overline{a_1}^2 + \overline{a_2}^2}{a} + \frac{{c_1}^2 + {c_2}^2}{6a}$$

Where β is the difference between magnetic centers, a is the width of the window and d is the height of the windings. Billig also concluded that short circuit forces always tend to increase the total inductance of the windings because any difference between magnetic centers result in axial repulsive forces and these forces increase the difference in magnetic centers. This gives rise to a second component of the inductance term and increases the inductance of the system. Radial forces are expressed in terms of first component of inductance only. Billig reported that second and third components have little effect on radial forces and can be neglected. However, they can be added to calculations in order to increase the accuracy. Radial forces can be calculated by this simplified theory as below.

$$F_x = \frac{2\pi(NI)^2 l}{d}\bar{v}$$

where $\bar{v}$ is the mean potential function, l is the mean diameter between the windings and d is the distance between two windings.

Billig's work is simplified version of vector potential solution and gives more insight into short circuit problems. This is because the forces and inductances are expressed in terms of

dimensions and mean potential functions. Effect of these quantities can be easily understood and conclusions can be easily drawn.

Rabins [10] introduced a solution in axisymmetric coordinates using single Fourier series with coefficients which were Bessel and Struve functions. Therefore, this solution is much more challenging than previous works. Rabins used this solution for reactance calculations but, it can be extended to electromagnetic force calculations because the solution is in terms of vector potential. Rabins' method assumes that the transformer window is unbounded in the radial direction. This method takes axial ampere-turn discontinuities into account and expresses the axial ampere-turn discontinuity in terms of a Fourier series as in Rogowski's work. Figure-2.5 shows the axial distribution of current density for one winding.

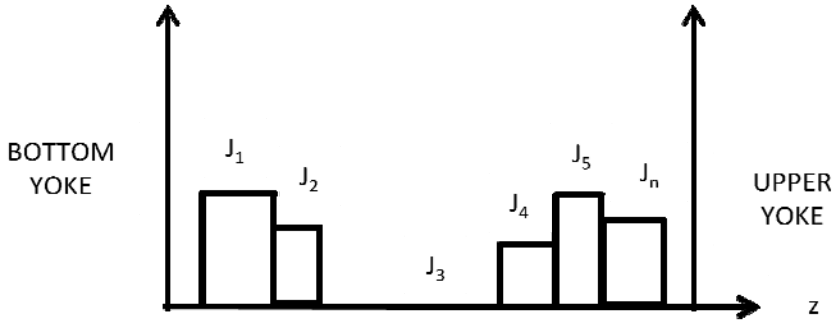

***FIGURE-2.5**: Current Density Distribution for Rabin's Method*

Current density can be written as a Fourier series with fundamental spatial period of L as,

$$J = J_0 + \sum_{n=1}^{\infty} J_n \cos\left(\frac{n\pi z}{L}\right)$$

$$J_0 = \frac{1}{L_0}\int_0^L J dz$$

$$J_n = \frac{2}{L}\int_0^L J \cos\left(\frac{n\pi z}{L}\right) dz$$

Any gaps in the winding treated as sections of winding but with zero current density. Vector potential is then solved for three regions. First region is between the core and the winding, second region is the winding itself and the third region is the space between winding and the

outer cylindrical boundary. In multi winding problems, the solution is obtained by superposition.

Vein [11] used Rabins' method to determine force distribution and end thrusts in terms of force density functions for several winding arrangements. This paper is a summary of Rabins' solution and extends the work to include several interesting and widely encountered winding arrangements.

CIGRE study committee 12 [12] studied the differences of some short circuit force calculation methods for various winding arrangements. The results are compared to finite elements results. The most interesting arrangement studied by the committee was the windings outside the transformer window.

Theoretical results calculated with different techniques are in close agreement and match with finite elements results. Suggestions to calculate short circuit forces were made when the tank walls provided with electromagnetic screenings or magnetic shunts. Magnetic shunts will be saturated during short circuit because they are designed for normal operation conditions. The study committee 12 suggested neglecting the effect of magnetic shunts under short circuit conditions and choosing a large distance between the limb and tank wall. If the magnetic screenings are designed to absorb the magnetic flux under short circuit conditions, the tank wall can be considered as a boundary.

The calculation of forces, eddy losses, and leakage reactance of transformers using the finite element method is given in reference [13] where a solution was obtained using cylindrical coordinates. Unlike Rabins' method, the field is bounded in a radial direction. However, the effect of the permeable core was not taken into consideration and the rest of the boundary conditions were kept the same as those of Rabins' method.

In [14], tangential forces acting on windings ends were discussed. Forces trying to twist and turn winding ends due to interaction of radial and axial components of the current were shown. Tangent forces at the transitions between the coil and the leads were calculated.

Patel [15] studied the axial stability of winding conductors under dynamic short circuit conditions for helical and barrel coils. He accounted for the dynamic considerations in his design and developed a method to calculate resonance frequency. This is actually a different

conductor tilting mode. He successfully defined a new failure mode called half-tilting for helical and barrel type windings. This technique also adapted to disc windings. Calculated strength for half-tilting mode was found to be 10% lower than full-tilting mode and tilting strength decreases inversely as the square of the coil diameter. Mechanical resonance frequency is much higher than exciting frequency for this mode. Critical strength and resonance frequency for helical coils in half-tilting mode was given by the following formulas.

$$F = \frac{\pi}{2Rh}\left(3EI + GI_p\right) + \frac{mbcd^3}{12h}$$

$$f_{cr} = \frac{E}{14}\left(\frac{h}{R}\right)^2 + \frac{mbcd^2}{12\pi Rh^2}$$

where E is the elasticity modulus of the copper, I is the moment of inertia of a single strand, R is the mean radius of the winding, h is the height of the strand, m is the number of the radial spacers, b is the width of the radial spacers and c is the constant of elasticity of the spacer material.

Tournier et al [16] were the first to attempt to characterize the dynamic behaviour of the transformer winding at short circuit conditions. LV winding is assumed motionless during short circuit and dynamic displacements occurring in HV winding were calculated. 33.3 MVA test transformer was manufactured to simulate the short circuit test. Detector units are placed to measure the displacement of the turns and end insulations as shown in Figure-2.6.

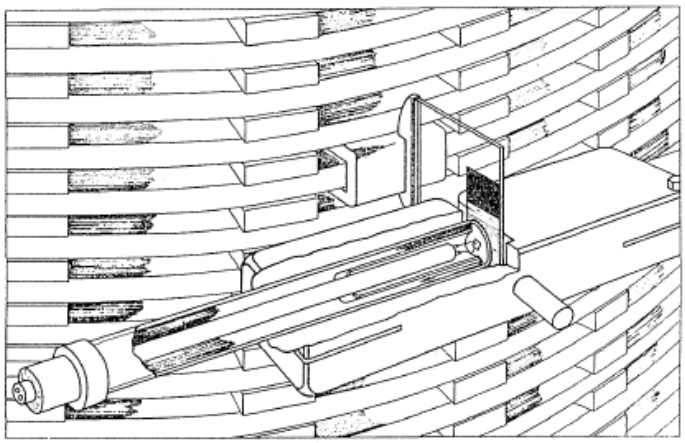

FIGURE-2.6*: Detector Unit used in Short Circuit Test (From Ref.11)*

Three dynamic models were proposed. First model considered the HV winding as a rigid block and end insulations as a linear deformable spring element. Cumulative axial dynamic short circuit forces are applied to rigid winding and displacements occurring at end insulations are calculated. Effect of damping was included in equations and damping calculated from the test data. Second model assumed every conductor along the winding as a rigid block and spacers as springs. Damping effect is neglected and numerical solution techniques were adopted in the final solution. Third model assumed the winding as being composed of an infinitely distributed mass. The effect of damping was neglected. Tests were performed in air and in oil and comparisons were made. Effect of pre-stress on dynamic behaviour was investigated. Resultant forces recorded by dynamometer and calculated forces by first and second model were in agreement in general form however, calculated amplitudes were different from those measured. The difference between theoretical and experimental values was caused by approximate constants according to authors. Elastic behavior of insulation material under dynamic loading was reported as one of the constants needs to be studied by the authors. It was reported that exciting frequency is dominant for a transformer with lower pre-stress value whereas, double exciting frequency component is dominant for a transformer with higher pre-stress value at transient period. Double exciting frequency is the dominant component in the steady state. This is an expected result because dynamic short circuit forces have an exciting frequency component with coefficient higher than double exciting component and decreasing exponentially after 5 to 8 periods. Because applied pre-stress is less, which means that the natural frequency of the winding is closer to exciting frequency, exciting frequency component is dominant. Double exciting frequency is dominant for steady-state since exciting frequency is decreasing exponentially with time. The difference in oscillations when the windings are in air and in oil was found to be small by the authors.

Patel [17] considered transformer winding as an elastic column between end insulations, modeled as springs. Patel assumed linear spring characteristics for the end insulation and sufficient pre-stress on windings to avoid separation between the conductor and end insulation. Displacement and dynamic load at any point was calculated as well as natural frequencies of the system. His theory breaks down in principle when the insulation material has non-linear characteristics. All previous researchers assumed clamping beams as rigid

structures. Patel assumed tank walls as rigid structures in vertical direction and flexible for rotation and foundation is assumed as rigid. The effect of oil on the dynamics of the clamp was found to be crucial. Oil behaves like a large hydrodynamic mass to the system. He also pointed out that dynamic forces can be completely different from the applied electromagnetic forces. The mathematical model of Patel's work is shown in Figure-2.7. K_1, K_2 and K_3 are the equivalent stiffness of the windings representing the phases and F_1, F_2 and F_3 are the friction forces.

In a separate paper, Patel [18] studied the non-linear dynamic characteristics of transformer winding and clamping beams as a combined system. He mentioned the difficulties encountered with modern insulation materials like clamping rings under dry and oil impregnated conditions. That is, when sudden compressive loads applied to oil impregnated insulation materials the oil residing in the material is pressurized and it will flow out and will meet some resistance. In Figure-2.8, K_v is the bulk elasticity of the composite cellulose and oil, K_s is the static elasticity of the insulation material and R is the resistance offered to the oil flow by the cellulose material.

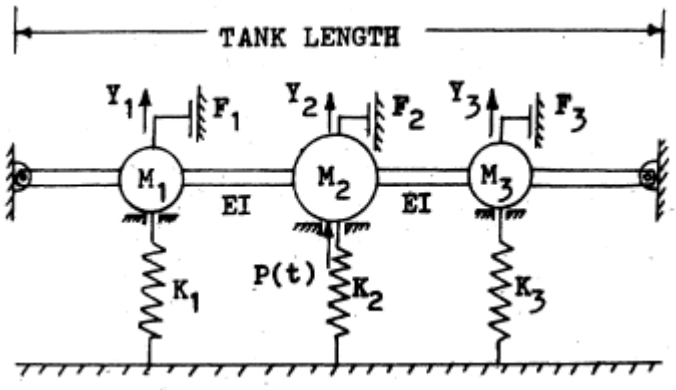

***FIGURE-2.7**: Mathematical Model for three Phase Transformer, Fault on Middle Phase*

The load will be taken by pressboard's static elasticity after all the oil inside the material is flowed out. This phenomenon was shown by mathematical viscoelastic model as;

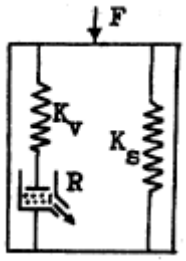

***FIGURE-2.8**: Mathematical Model Representing Oil Impregnated Insulation Material*

Equation of motion for complete winding and clamping arrangements model was given below.

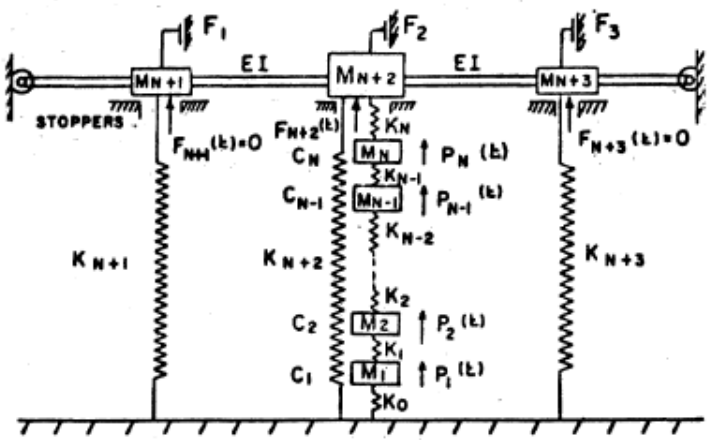

***FIGURE-2.9**: Complete Winding and Clamp Model, Fault on Middle Phase*

In this model oil plays two important roles. It influences the insulation stiffness and it provides hydrostatic mass effect to some moving parts. These results contradict the previous work of Tournier at al. The dynamic forces again found to be different were waveshape and magnitude from the applied electromagnetic forces. The importance of pre-stress on the dynamic respond was discussed by Patel. His results in terms of pre-stress effect are different from the previous researchers. For large power transformers he suggested to apply a moderate pre-stress as large values of pre-stress could cause resonance.

In [19], the forces acting on split windings are studied using field-circuit coupled nonlinear transient finite elements models. The winding configuration that the authors studied were middle entry HV winding with two secondary outputs. The paper considers the short circuit on one winding while other winding is left open circuited. They concluded that the effect of short circuit current share between upper HV and lower HV winding is 5% and 95% when upper LV winding is short circuited and this is because when upper part is short circuited the

leakage flux flows between HV and upper LV winding and this causes saturation on upper part of the core. As a result, upper LV winding experiences heavy short circuit forces.

The finite element method was implemented to study the buckling strength of low voltage transformer winding under short circuit conditions in [20]. The analysis considered large deformations and several manufacturing techniques was compared. A test setup was designed and analytical and test results were compared. The uneven distribution of radial electromagnetic forces was considered. The authors concluded that bending deformation of the windings occurs very easily and the buckling strength becomes very small. Therefore, the buckling strength can be calculated to ensure that no tearing occurs, due to the large deformation of the conductors under bending type loading, on insulation materials.

The tilting strength of conductor and natural frequencies for various winding configurations under the dynamic short circuit forces was shown in [21]. The authors showed that the critical tilt angle can decide whether the winding is stable or unstable and failure in transformers due to tilting after a number of short-circuits is a result of the increase in critical tilting angle.

2.2 Material Properties of the Transformerboard

Not much research has been carried out on transformerboard. This is because this material is treated mainly in terms of its electrical properties. It is obvious that it should satisfy all the electrical properties on the other hand these materials are often used in order to clamp the windings. Therefore, these materials are required to withstand potentially devastating short circuit forces.

Moser [2] studied the mechanical behaviour of these materials. Because the material properties depend upon moisture content of the transformerboard, tests are performed on dry and oil impregnated specimens. The first outcome of the tests was the dependence of the strength on density of the specimen. As the specimen density increases, strength increases. This is because fibres per volume increase which eventually increases the strength of the transformerboard. Oil impregnated specimens have greater strength as this shows the effect of moisture on transformerboard.

The influence of ageing on tensile strength is also observed by Moser [2]. Tensile strength and elongation decrease as a result of ageing and the decrease of tensile strength caused by increased temperature consist of three phases. Tests performed by Moser showed that a decrease in strength occurs within the first 10 hours followed by stability of the ageing process. This period depends upon the temperature. It lasts 100 hours for 130^0C and 50 hours for 150^0C. The actual decrease in strength occurs after this phase. These test data are useful to determine the working temperature of the transformer because over this temperature, significant loss in strength occurs and mechanical durability of the transformer cannot be maintained.

As opposed to previous researchers, Moser pointed out that the stability of the spacer depend more on the manufacturing process rather than density. He concluded that the fibre density has a definite effect on strength of the transformerboard under static loading however, the manufacturing process has more effect on transformerboard's strength.

Waters [1] collected many researchers' results in his book. This book is very valuable as a reference book and explained the outcome of these researches. He mentioned about the importance of spacers and end insulation design in terms of static and dynamic requirements and described their mechanical characteristics based on previous researcher's data. He suggested studying the insulation material's stress-strain relationship after drying and treatment to take operation conditions into account. After explaining the research and test data exist for insulation materials, he concluded that more research is needed to determine its mechanical properties although this material does not exhibit certain properties like copper conductors.

Knaack [22] performed tests on transformerboard and paper materials to study the effect of successive loading. When stacks of paper and transformerboard were subjected to successive loading, the properties tended towards to constant value and the process is called mechanical stabilization (Figure-2.10). Knaack observed that the first pressing results a remarkable permanent set and only after subsequent loading and unloading, elastic behaviour observed. He also observed that the total change in length depends to a great extent on specific weight of the material (Figure-2.11). This shows that porous paper material becomes denser than a previously densified paper. Total change in height on the

other hand, depends on specific weight than elastic compressibility. He also concluded that the thickness of the paper has little effect on this behaviour.

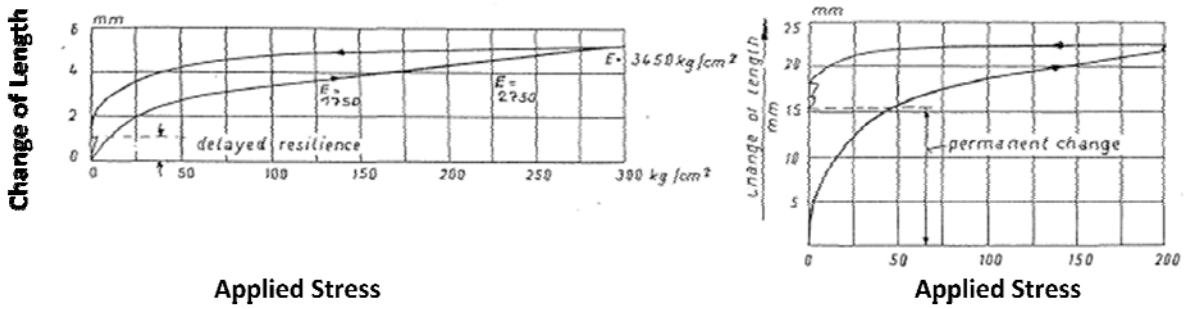

FIGURE-2.10: *Decrease in Residual Length after Several and First Pressing*

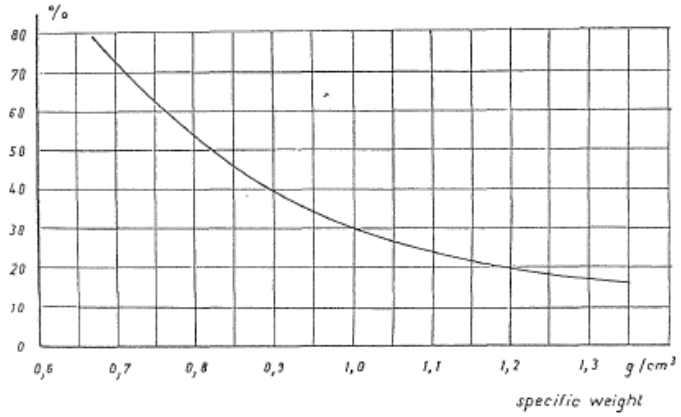

FIGURE-2.11*: Ratio of Residual Length Change to Total Length Change vs Specific Weight after the First Pre-stress with 200 kg/cm^2*

When the pressure on transformerboard is suddenly released in air and in oil, there was a spontaneous and delayed resilience occurred. Delayed resilience was found to be more pronounced in air than in oil.

Lur'e and Mil'man [23] attached strain gauges to complete 1000kVA transformer winding to study the mechanical characteristics of insulation oil. They found that the compression curve was completely determined by insulation materials and conductor has no effect. In other words, conductor is incompressible for the winding arrangement. Effect of friction between spacers and the bars was negligible. Authors also found that the denser the insulation material, lesser the permanent set and compressibility. This outcome matches with previous results. Pre-stressed material is much more resistant to compression and relaxes less under stress than normal material. The authors also concluded that the reduction in

compressibility after the number of cycles of loading and unloading is due to the increase in density of the material.

Waters concluded that based on these research findings, the mechanical properties of all type of transformerboard tend to approach one another as compressive stress increases. At high grades of the applied stress, mechanical properties will be almost similar.

Lur'e and Mil'man [24] also obtained a stress-strain graph by applying a stress of 50kg/cm^2 and removing the load, 100kg/cm^2 and so on up to 200kg/cm^2 for untreated and pre-stressed transformerboard. Pre-stressed transformerboard was loaded and unloaded in three cycles with 200kg/cm^2. At final unloading, the treated specimen underwent very little permanent deformation comparing with untreated specimen. In the report it was also stated that short circuit forces can cause considerable relaxation of the transformerboard and paper and generates a loss of clamping pressure. However, creep recovery might occur but this was not mentioned in the report.

Lur'e and Mil'man concluded that the material exhibits non-linear stress strain characteristic and elasticity modulus increases with the applied stress. Also, untreated material shows large permanent deformation and this can be reduced significantly by cyclic loading and unloading. Internal friction determines the damping oscillations and axial short circuit forces cause loss of clamping ring. The authors also suggested applying a final pressure after the drying phase of the transformer and the magnitude of pressure suggested being one and a half to twice the compressive forces generated by the short circuit. If this is not possible, two to three cycles of loading and unloading is suggested. Authors also suggested that the internal pressure should not exceed 50kg/cm^2.

Swihart and Wright [25] measured the dynamic stiffness of the transformerboard and compared the results with static stiffness. They extended the work of Patel and included the effect of pre-stress, temperature and dynamic stress levels. They designed a test rig (Figure-2.12) where the test specimen was in oil to simulate the real operation conditions and temperature and pre-stress valves were adjustable. In order to investigate the size effects of the transformerboard, the specimen with the larger area was also tested and the results yielded that the increase in area does not have an effect on dynamic behaviour of the transformerboard. It was found that below the pre-stress point, the stiffness is much less

than the point above it and except for high pre-stress levels, the curve below pre-stress follows the static stress-strain curve. The authors pointed out that the squeezed oil in the material will be pressurized during short circuit however, the resistance to flow is so high that it will be trapped in the material for short loadings. Because the highest asymmetrical peaks occur in the first milliseconds during short circuit loadings, the oil will be trapped in the material.

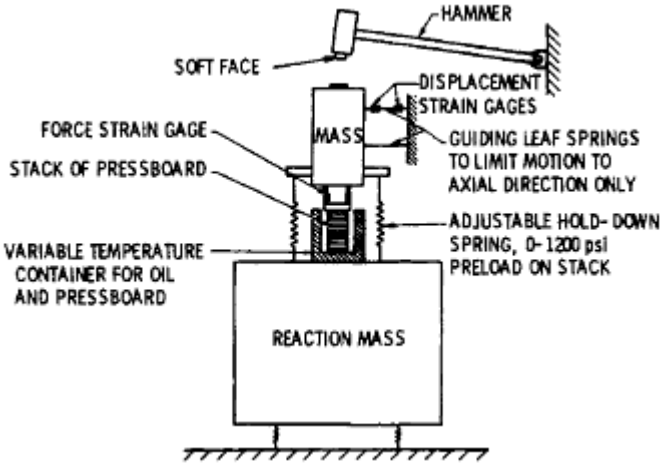

FIGURE-2.12: *Test Rig to Test Transformerboard*

2.3 Digital Image Correlation (DIC) Technique

The DIC technique is used to map strain distribution by comparing a series of images captured at various levels of deformation. A random paint pattern can be applied on the specimen surface if the specimen to be tested does not have distinguishing features on it. An initial image is captured by the cameras and used as the reference image throughout the process. All the subsequent images are compared to the initial image. To achieve a higher degree of accuracy, correlations are based on squares of pixels, known as facets, rather than using individual pixel tracing. These facets have an array of greyscale values corresponding to the pattern, thus allowing tracking through the subsequent image stages [26, 27]. Facets are overlapped to increase the correlation accuracy. Strains ranging from 0.1% to 100% can be measured.

In [28], the DIC technique is used to determine flexural properties of a sandwich beam material, a widely used material in wind turbine industry, having different thicknesses. The sandwich structure was a polymeric foam material strengthened with composite layers at

the top and bottom. The authors provided strain maps under three and four point bending tests and compared the DIC readings at various cross-sections to displacement transducer readings and concluded that the results obtained from the DIC correlated well.

In [29], 3-D image correlation using digital high speed cameras was studied. The accuracy of 3D image correlation system with high speed cameras was thoroughly determined in both field and laboratory conditions. Data acquisition rates were up to 10000 to 27000 frames per second. The advantages of using DIC technique to strain gauge measurements were shown. The application of the DIC technique to ballistic impact investigations was investigated. Figure-2.13 shows the major strain distribution where the black outline indicates the position of the strain gauge attached at the back surface. Figure-2.13 clearly shows the highest strain gradient a short distance away from the attached strain gauge. The authors concluded that the strain gauges can be misleading and might not show the highest strain.

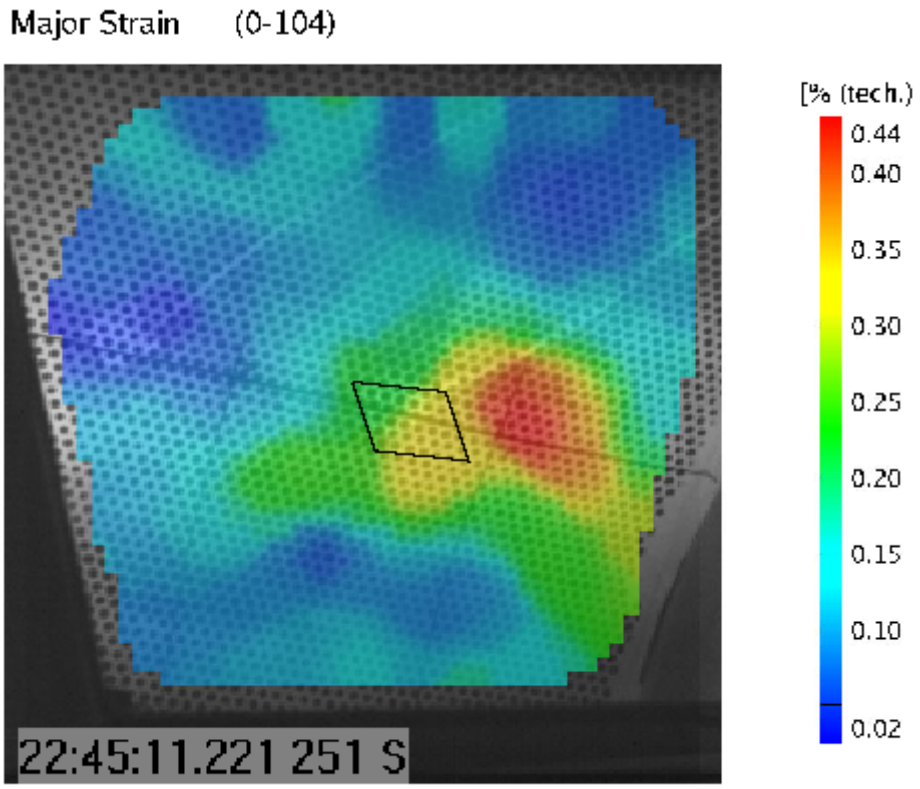

***FIGURE-2.13**: Image correlation full-field principal strain map with strain gauge location indicated by black outline (From [54])*

3-ELECTROMAGNETIC FORCE CALCULATIONS

3.1 Introduction

Electromagnetic fields exert forces on conducting and insulating components in service within micro-electronics components, transmission lines and transformers. Reliable design and prediction of durability of engineering assemblies and structures that are subjected to electromagnetic loading remain a challenging task.

In order to ensure that the design of the windings withstands the mechanical stresses, electromagnetic forces need to be calculated accurately. Electromagnetic forces are generated by either permanent magnets or current carrying conductors. In this research, the forces generated by current carrying conductors will be taken into consideration because the forces acting on transformer windings are a result of conductors carrying current. The electromagnetic forces on current carrying conductors [34] therefore can be calculated using Lorentz Law.

$$F = \int (JxB)dv \quad (\mathbf{3.1})$$

where J is the current density and B is the magnetic flux density.

Power transformers are expected to work for a period of twenty to twenty-five years and during service life, external or internal faults might occur which generates short circuits. External short circuits give rise to asymmetrical short circuit currents which are much higher in magnitude than the service currents and lead to devastating short circuit forces. The magnitude of the short circuit current is a function of several parameters. These are short circuit impedance, leakage inductance, power rating of the transformer and asymmetry factor. Accurate calculation of forces requires determining these parameters precisely.

The force calculation procedure can be summarized as follows;

- Short circuit current calculation from the study of the system
- The electromagnetic force calculations based on the short circuit currents
- Resultant mechanical forces and strength of windings

3.2 Short Circuit Currents

It will be explained and derived in the next chapters that the short circuit forces are proportional to the square of the short circuit currents. When an external fault occurs in the transmission line, the symmetrical currents are 10 to 30 times the normal operation currents. The forces are therefore, 100 to 900 times the normal operation depending on the electrical and physical parameters of the transformer such as power rating, voltage level and dimensions of the windings. Understanding the fault current is a crucial step to calculate and understand the nature of the dynamic and static electromagnetic forces.

When a current versus time graph is plotted during normal operation of the transformer, it draws out a shape of sine wave and it is symmetrical to the zero axes as shown in Figure-3.1. This is called the symmetrical current. During the fault on the other hand, reactive loads supplied by the system can cause a DC offset. When DC offset is added to the system, the line is not symmetrical to the zero axis line and this is called the asymmetrical current. The effect of the DC offset is that the peak values of the current can be higher than the symmetrical case. The highest current is reached at the first peak and during a fault the effect of the DC offset lasts only a few milliseconds and reaches a symmetrical steady state.

The ratio of the first peak asymmetrical current value to symmetrical current value is called asymmetry factor. Symmetrical components should therefore be multiplied by an asymmetry factor when calculating the short circuit current to add the effect of asymmetry. The asymmetry factor is between 1.8 and 1.9 based on the power rating of the power transformer. In practice, if the power rating of the transformer is below 100MVA the asymmetry factor is taken as 1.8, otherwise it is taken as 1.9.

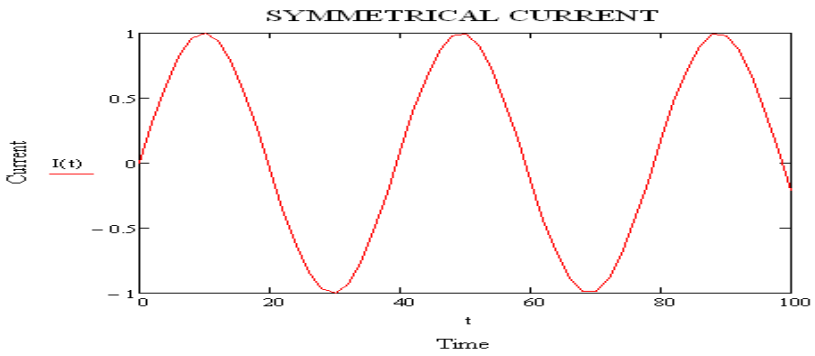

***FIGURE-3.1**: Symmetrical Current*

Complete and more accurate short circuit currents can be calculated from the electrical circuit theory. Figure-3.2 shows the equivalent circuit when transformer is short circuited at time t=0. Here, R and X are the leakage resistance and leakage reactance of the transformer. The applied voltage is sinusoidal and given by

$$V(t) = V_p \sin(wt + \varphi) \quad (\mathbf{3.2})$$

w is the angular velocity and equal to $w = 2\pi f$ where f is the frequency. φ is the phase angle and can have any value because the fault can occur any time during the voltage cycle.

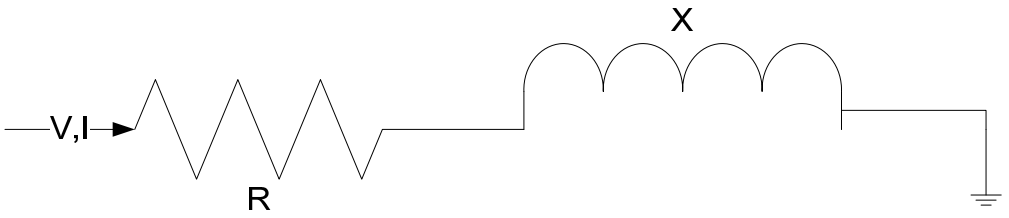

***FIGURE-3.2**: Equivalent Circuit at Short Circuit*

The circuit equation is therefore;

$$V_p \sin(wt + \varphi) = RI + L\frac{dI}{dt}$$

L is the leakage inductance and is related to the leakage reactance through the equation $X = wL$

Solution to the above differential equation can be obtained using Laplace transformations and the final equation is given by [35]

$$I(t) = \frac{V_p}{\sqrt{R^2 + X^2}}\left[\sin(\beta - \varphi)\left(e^{-\frac{R}{L}t} - \cos wt\right) + \cos(\beta - \varphi)\sin wt\right] \quad (\mathbf{3.3})$$

$$\beta = \tan^{-1}\left(\frac{X}{R}\right) \quad (\mathbf{3.4})$$

The term $\sqrt{R^2 + X^2}$ is the leakage impedance (Z) of the transformer and $\frac{V_p}{\sqrt{R^2+X^2}}$ is the steady state peak current amplitude (I_{pss}). The magnitude of the short circuit current is also a function of the phase angle but the maximum value of this current is of interest.

Therefore, the value of phase angle which causes the short circuit current needs to be found by differentiating (3.3) and setting it to zero.

$$e^{-\frac{R}{L}t} - \frac{X}{R}\sin wt - \cos wt = 0 \ (\mathbf{3.5})$$

$$\tan(\beta - \varphi) = \frac{X}{R} \ (\mathbf{3.6})$$

For power transformers *X* is very large compared to R and for this reason equation (3.6) is satisfied when $\varphi = 0$ therefore the maximum amplitude is obtained when the phase angle is equal to zero. The time at which the maximum amplitude occurs can be found by solving equation (3.5).

When the above results are substituted back into equation (3.3), the maximum asymmetrical fault current amplitude can be obtained.

$$\frac{I_{max}}{\mathrm{I_{pss}}} = \sqrt{1 + \left(\frac{X}{R}\right)^2}\ \sin wt \ \ (\mathbf{3.7})$$

where $\mathrm{I_{pss}}$ is the steady state peak current.

The above equation is the asymmetry factor over steady state peak amplitude.

As the reactance to resistance ratio increases, peak asymmetric current increases and eventually reaches its maximum value of 2. This is one of the reasons why power transformers are subjected to higher short circuit forces during service life than distribution transformers, as the ratio of reactance to resistance is very high for power transformers.

Using the rms value of the current when the phase angle is equal to 0, equation (3.3) reduces to;

$$I(t) = \frac{\sqrt{2}\mathrm{I_{pss}}}{\sqrt{1 + \left(\frac{X}{R}\right)^2}}\left[\frac{X}{R}\left(e^{-\frac{R}{L}t} - \cos wt\right) + \sin wt\right] \ (\mathbf{3.8})$$

This is the current function for short circuit conditions and the graph is plotted in Figure-3.3. It can be seen from the Figure-3.3 that the short circuit current reaches a peak value and the

amplitude decays as time increases and reaches a steady state. The asymmetry exists only a few milliseconds and the peak value can be found by equation (3.7).

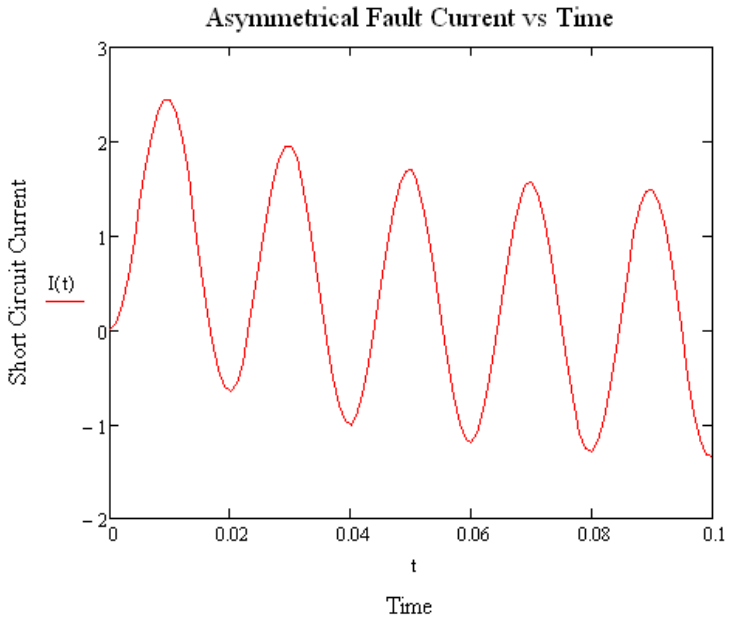

***FIGURE-3.3**: Asymmetrical Fault Current vs Time*

Equation (3.8) can be further simplified when the reactance to resistance ratio is assumed to be infinity, which is a reasonable assumption as this ratio is high for power transformers. From equation (3.6), β is found as $\frac{\pi}{2}$ when the ratio of $\frac{X}{R}$ is infinity.

$$I(t) = \sqrt{2}\mathrm{I}_{\mathrm{pss}}\left[e^{-\frac{R}{L}t} - \cos(wt)\right] \quad (\mathbf{3.9})$$

The above equation will be used to calculate dynamic short circuit forces and resultant mechanical forces and stresses.

3.3 Current Density

In Electromagnetics, current density is defined as current per unit area and given by the formula below. With this definition, the current density is defined at a point and the current through any surface can be calculated.

$$I = \int J ds$$

Figure-3.4 shows the cross section of a simplified transformer window. The current flowing in LV winding and HV winding are in opposite directions. The total current in the winding cross section is N*I ampere-turns where N is the number of turns. Blue lines represent the ferromagnetic core material which completes the magnetic circuit. It is a well known fact that the ampere-turns are equal but flowing in opposite directions for LV and HV windings of a transformer under short circuit conditions.

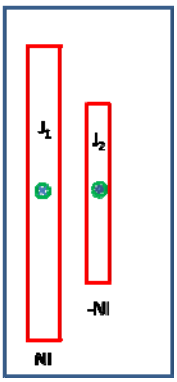

***FIGURE-3.4**: Cross Section of Simplified Transformer Window*

The coupling between electric and magnetic field is based on Faraday's experimental law. A time-dependent magnetic field generates a time-dependent electric field and vice versa. A time-dependent field produces an electric field and that, in turn, inducing currents in conducting materials. This is called induced or Eddy currents and these currents are minimised in transformers because they generate additional losses on conductors and increase the total copper loses. But transformer winding is designed to minimise eddy current losses.

If forces acting on transformer windings are to be calculated when short circuit current reaches its maximum value, it can be assumed that static DC currents are flowing through the windings even though transformer is an AC device. This assumption brings an advantage of eliminating the induced currents through the windings because static current does not generate a time-dependent magnetic field. Eliminating induced currents provides uniform current density distribution and current density J can be found by the simple formula;

$$J = \frac{NI}{Cross\ Sectional\ Area\ of\ the\ Winding}$$

In real operation and short circuit conditions, induced currents are acting on transformer windings and the distribution of current density is not uniform as a result of time-dependent magnetic field. However, in transformer design, stranded and isolated conductors are used to minimise the copper losses generated by induced currents and the above formula can also be used to calculate the current density when transient and harmonic currents are flowing through the windings.

3.4 Review of Maxwell's Equations and Vector Potential

Maxwell equations are given below.

$$\nabla . B = 0, \nabla x H = J + \frac{\partial D}{\partial t}, \nabla . D = \rho_v, \nabla x E = -\frac{\partial B}{\partial t} \ (\mathbf{3.10})$$

Here B is magnetic flux density, H is magnetic field intensity, J current density, D electric flux density and E is electric field intensity.

And constitutive equations;

$$B = \mu H, D = \varepsilon E, J = \sigma E$$

μ is permeability, ε is permittivity and σ is conductivity.

The term $\frac{\partial D}{\partial t}$ is called displacement current. The most important implications of the displacement current are the existence and finite speed of electromagnetic waves. In transformers, this term can be neglected for the reasons below.

- In transformers the frequency is very low. It is either 50 or 60 Hertz.
- The distance between conductors is low. As an example, for a transformer with 380kV HV voltage level, the distance between LV and HV winding is only 92mm.
- The current of the conductor is much higher than the displacement current.

Neglecting this term in second equation of (3.10) leads to;

$$\nabla x H = J \ (\mathbf{3.11})$$

This is the Ampere's Law and this relation will be used to calculate the magnetic flux density distribution within the transformer window.

It is known from mathematics that, divergence of curl of a vector is equal to zero. Therefore, magnetic flux density B can be considered as a curl of a vector. If this vector is denoted as A, from the first equation of Maxwell,

$$\nabla . B = 0 = \nabla . (\nabla \mathrm{xA}) = 0, B = \nabla \mathrm{xA} \ (\mathbf{3.12})$$

A is called magnetic vector potential and has a mathematical meaning. It is used by many researches to simplify the Maxwell's Equations. To define a vector quantity properly, its curl and divergence should be defined. The curl of A is defined above and it is valid for both static and time-dependent fields. The divergence of A, on the other hand, is not defined uniquely because the vector potential field is not unique and requires a gauge. For this solution, coulomb gauge will be used. $\nabla . A = 0$

Substitution of equation (3.12) into equation (3.11) and using the constitutive relations

$$\nabla(\nabla . A) - \nabla^2 A = \mu J$$

$$\nabla^2 A = -\mu J \ (\mathbf{3.13})$$

3.5 Methods Developed to Calculate Magnetic Properties of Transformers

Different analytical and numerical methods are developed to calculate electromagnetic forces, leakage, self and mutual inductances of transformers. All these analytical methods assume an infinitely permeable core. As a result of this assumption, flux lines enter the core at right angles. In other words, the tangential component of magnetic flux density vanishes at the boundary. The infinitely permeable core assumption gives reasonable results when calculating leakage inductance and short circuit forces on the other hand it fails to yield correct results when calculating self and mutual inductances.

Recent trends in transformer design utilizes both 2-D and 3-D finite elements analysis to calculate design parameters and magnetic properties. However, FEA solutions require modelling, meshing and post-processing operations which can be time-consuming. For these reasons and to calculate short circuit forces even more accurately, a new solution technique will be developed here in 2-D Cartesian coordinates taking finite permeability of the core into account which can be introduced in software codes to calculate the magnetic properties of power transformers. Poisson's field in the developed solution utilizes Roth's solution and therefore, it will be explained first.

3.6 Magnetic flux Density and Vector Potential Calculations with Roth's Method

The method of solution to calculate short circuit forces was introduced by Roth. In this method, a solution was obtained by solving the Poisson's equation using double Fourier series. Figure-3.5 shows a transformer window and an arrangement of rectangular conductors. The lower left-hand corner of the boundary is chosen to be the origin of coordinates. General field equation for the vector potential over the section of any winding is

$$\nabla^2 A = -\mu J$$

And within the window where there are no current flowing is

$$\nabla^2 A = 0$$

Some assumptions are needed to provide solution. These are;

1. Relative permeability of the copper conductors and air/oil is equal to 1. In reality, the permeability of these materials is also very close to 1.
2. Permeability of the boundary, ferromagnetic core, is assumed to be infinity. With this assumption the flux lines will be at right angles to boundary lines.
3. Current distribution along the winding is constant and this assumption was discussed in the previous chapter.
4. Infinitely permeable boundaries will be replaced by infinite set of images both in X and Y dimensions so the desired function defining the field inside the window will be periodic with both coordinates (Figure-3.5).
5. The windings will be regarded as parallel bars of length l corresponding to their mean length of turns. No end effects need to be considered as in the case of real transformers due to circular shape.
6. Current density vector is in z direction and therefore, the vector potential is also in z direction.

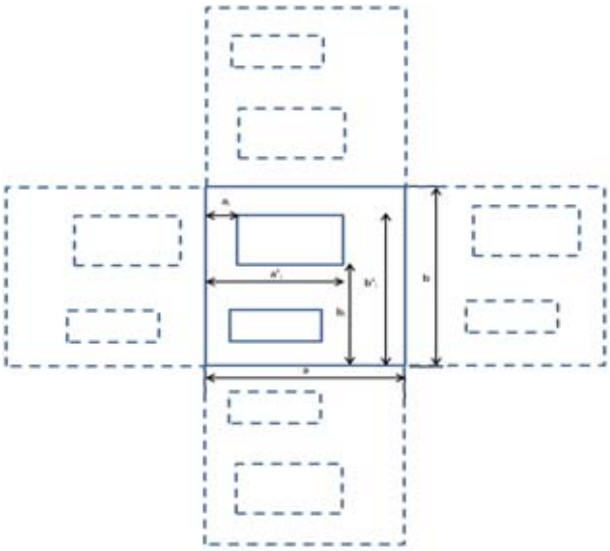

FIGURE-3.5 *Images of Transformer Window in x and y Directions*

Components of magnetic flux density can be found from curl of A. Using the sixth assumption, components of magnetic flux density is,

$$B = CurlA = \begin{bmatrix} i & j & k \\ \frac{\partial}{\partial x} & \frac{\partial}{\partial y} & \frac{\partial}{\partial z} \\ 0 & 0 & A_z \end{bmatrix}$$

$$B_x = \frac{\partial A_z}{\partial y} \; and \; B_y = -\frac{\partial A_z}{\partial x}$$

A_z will be denoted as A hereafter.

General solution can be given by the product of two Fourier series in x and y directions.

$$A = \sum_m \sum_n B_1 \cos mx \cos ny \sum_m \sum_n B_2 \cos mx \sin ny + \sum_m \sum_n B_3 \sin mx \cos ny \sum_m \sum_n B_4 \sin mx \sin ny$$

Assumption 4 brings 4 boundary conditions and because of the assumed infinite permeability at the boundaries, tangential component of flux does not exist.

$$\left(\frac{\partial A}{\partial x}\right)_{x=0} = 0 \, , \left(\frac{\partial A}{\partial y}\right)_{y=0} = 0 \, , \left(\frac{\partial A}{\partial x}\right)_{x=a} = 0 \, , \left(\frac{\partial A}{\partial y}\right)_{y=b} = 0$$

Differentiating A and substituting in first two boundary conditions results;

$$B_2 = B_3 = B_4 = 0$$

And vector potential reduces to;

$$A = \sum_m \sum_n B_{m,n} \cos mx \cos ny$$

Constants m and n can be found from the remaining two boundary conditions.

$$m_i = \frac{\pi}{a} i \quad i = 0,1 \dots \infty, n_k = \frac{\pi}{b} k \quad k = 0,1 \dots \infty$$

$$A = \sum_{i=0}^{\infty} \sum_{k=0}^{\infty} B_{i,k} \cos \frac{\pi x}{a} i \cos \frac{\pi y}{b} k$$

Substituting in Poisson's equation yields;

$$\sum_{i=0}^{\infty} \left[\sum_{k=0}^{\infty} ({m_i}^2 + {n_k}^2) B_{m,n} \cos \frac{\pi x}{a} i \right] \cos \frac{\pi y}{b} k = \mu J \quad (\mathbf{3.14})$$

The problem is reduced to determine the amplitude $\mathrm{B_{m,n}}$. Mathematically, the method is identical with that used for the determination of individual members in any Fourier series. Multiplying both sides with $\cos \frac{\pi x}{a} \mathrm{i}\, \mathrm{dx}$ and integrating the left side of the equation between 0 and a and the left side between aj and a'j ,because the current is only flowing within the winding, and performing the same procedure with multiplying the equation with $\cos \frac{\pi y}{b} \mathrm{k}\, \mathrm{dy}$ and integrating the left side of the equation between 0 and b and the left side between bj and b'j yields;

$$B_{i,k} = \frac{16\pi}{ab} \frac{1}{m_i n_k ({m_i}^2 + {n_k}^2)} \sum_{j=1}^{p} J_j \left(\sin m_i a'_j - \sin m_i a_j \right) \left(\sin n_k b'_j - \sin n_k b_j \right)$$

When the values of mi and nk are equal to zero, the solution becomes indefinite. To obtain a solution for A0k, for example, set mi 0 in equation (3.13) and multiply both sides with dx and integrate as above. The final solution is therefore;

$$A = A_0 + A_{0k} + A_{i0} + A_{ik} \ (\mathbf{3.15})$$

$$A_0 = constant$$

$$A_{0k} = \frac{2\mu_0}{ab}\sum_{j=1}^{p}\frac{N_j I_j}{d_j}\sum_{k=1}^{\infty}\frac{\left(\sin n_k b'_j - \sin n_k b_j\right)}{{n_k}^3}\cos n_k y$$

$$A_{i0} = \frac{2\mu_0}{ab}\sum_{j=1}^{p}\frac{N_j I_j}{c_j}\sum_{k=1}^{\infty}\frac{\left(\sin m_i a'_j - \sin m_i a_j\right)}{{m_i}^3}\cos m_i x$$

$$A_{ik} = \frac{4\mu_0}{ab}\sum_{i=1}^{\infty}\sum_{k=1}^{\infty}\frac{\cos m_i x \cos n_k y}{m_i n_k({m_i}^2 + {n_k}^2)}\sum_{j=1}^{p} J_j\left(\sin m_i a'_j - \sin m_i a_j\right)\left(\sin n_k b'_j - \sin n_k b_j\right)$$

p is the number of conductors, c is the width and d is the height of the conductor within the window. The constant term depends on the magnetization of the ferromagnetic core material and does not contribute to magnetic flux density because its differentiation is equal to zero.

Vector potential solution gives the equipotential lines within the window and potential at any point in the slot can be determined and plotted. Lorentz Law requires determining the current density and magnetic flux density in order to find the electromagnetic forces. The components of magnetic flux density Bx and By can now be determined from the vector potential solution using equation (3.15) and the forces can be calculated.

This solution strategy can be employed to any number and arrangement of conductors within the boundary.

3.7 Proposed Method Taking Finite Permeability of the Core into Account

Previous developed methods shares a common assumption, the permeability of the core material is infinity and as a result of this assumption, the flux enters the core at right angles. This assumption provides simplifications to calculate the magnetic flux within the transformer window because the derivative of vector potential with respect to appropriate coordinates vanishes and as a result, boundary conditions can be taken as Neumann's type. However, these methods can only be employed for short circuit conditions and fails to provide accurate results for open circuit condition. A method is developed below to calculate magnetic properties of power transformers for open and short circuit conditions. With this method, self and mutual inductances of the windings can also be calculated.

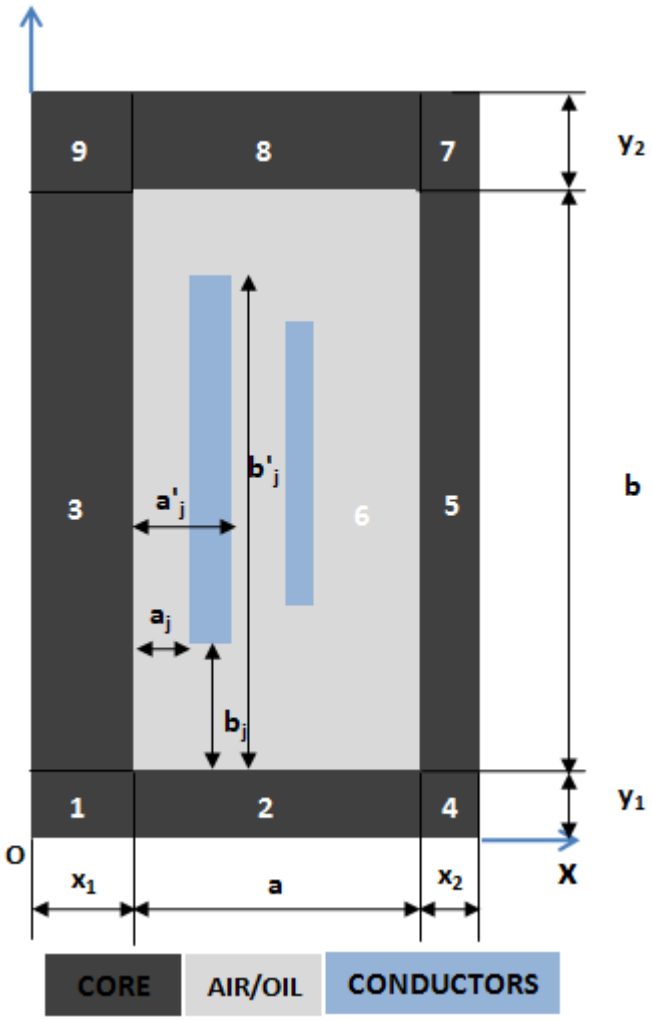

FIGURE-3.6 *Transformer Window Including Core*

Figure-3.6 shows the position of the core and conductors of a transformer window. Dimension x_1 is the radius of the core, μ_1 is the permeability of the core and μ_2 is the permeability of the conductors and air/oil.

At the outer boundary of the core, magnetic vector potential is assumed to have a value of zero. Transformer window is divided into nine regions and each region is connected to neighbour regions with appropriate boundary conditions. Region 6 is the only region which contains the source, current density for this problem. Therefore all the regions except region 6 are governed by the Laplace Equation. Because of the assumed linearity, region 6 can be divided into Poisson's and Laplace fields. Poisson's field takes sources into account with flux normal boundary conditions just as Roth's solution requires and Laplace Field takes the values of magnetic vector potential at the boundaries into account. Superposition of these two fields gives the required vector potential field.

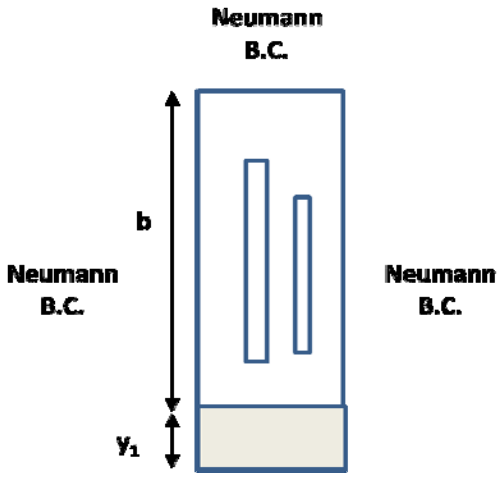

FIGURE-3.7 *Transformer Window Neighbours to Highly Permeable Core*

Poisson's field solution for region 6 can be calculated with Roth's method however, Roth's solution is not sufficient for this problem when total current density inside the transformer window is not zero or during open circuit condition. Some additional polynomial terms may be required to represent the true field inside the window. Figure-3.7 shows a particular case where one side of the boundary is attached to region with different permeability. In this case;

$$a_0\left(\frac{y^2}{2} - y(y_1 + b)\right) + Roth's\ Solution$$

is the solution for vector potential because the first term satisfies all the boundary conditions and $\nabla^2 A = -\mu J$. Constant a_0 can be found by substituting above equation in $\nabla^2 A = -\mu J$ and after zero order Fourier Transform,

$$a_0 = -\mu \sum_{j=1}^{P} \frac{NI}{ab}$$

Under short circuit conditions, constant a_0 disappears because of balanced ampere-turn. Similarly, Laplace fields may involve polynomials satisfying Laplace Equation and boundary conditions. When deriving the equations for the Laplace field, flux normal boundary conditions should be used because Poisson's and Laplace fields will be superimposed to take non-zero values at the boundary in Region-6. Final solution for region 6 can be written for Laplace and Poisson's fields separately.

$$A_{6,Poission}(x,y) = a_{66}\left[\frac{x^2}{2} - x(x_1 + a + x_2) + \frac{y^2}{2} - y(y_1 + b + y_2)\right] + Eq(3.15)$$

When using Roth's solution, y should be replaced with (y-y_1) and x should be replaced with (x-x_1) because of the choice of the origin for this problem.

Constants $a_{61}$and $a_{62}$are added to Laplace field because original Roth's solution involves uniform fields in x and y direction due to Neumann boundary conditions and Laplace field may also involve these terms. A polynomial is required to couple the field in x and y directions and constant a_6 is added for this reason. If a_6 is not added, vector potential at the interface of two regions, such as A6=A2 at y=y1, will be continuous in either x or y directions however, solution requires vector potential to be continuous in both directions. Final Laplace field for Region 6 can be written as below.

$$A_{6,Laplace}(x,y) = a_{61}x + a_{62}y + a_6(x^2 - y^2) + A_{6-1} + A_{6-2} + A_{6-3} + A_{6-4}$$

$$A_{6-1}(x,y) = \sum_{k=1}^{\infty} Y_k Cos\left[\frac{\pi k}{b}(y - y_1)\right]\left[Sinh\left[\frac{\pi k}{b}(x - x_1)\right] - \coth\left(\frac{\pi k}{b}a\right) Cosh\left[\frac{\pi k}{b}(x - x_1)\right]\right]$$

$$A_{6-2}(x,y) = \sum_{s=1}^{\infty} Z_s Cos\left[\frac{\pi s}{a}(x - x_1)\right]\left[Sinh\left[\frac{\pi s}{a}(y - y_1)\right] - \coth\left(\frac{\pi s}{a}b\right) Cosh\left[\frac{\pi s}{a}(y - y_1)\right]\right]$$

$$A_{6-3}(x,y) = \sum_{k=1}^{\infty} W_k Cos\left[\frac{\pi k}{b}(y - y_1)\right] Cosh\left[\frac{\pi k}{b}(x - x_1)\right]$$

$$A_{6-4}(x,y) = \sum_{s=1}^{\infty} V_s Cos\left[\frac{\pi s}{a}(x - x_1)\right] Cosh\left[\frac{\pi s}{a}(y - y_1)\right]$$

Laplace field for Region-2 will be derived as an example and the Laplace fields for remaining regions will be written without derivation but the method is the same. Region-2 can be divided into three regions as shown in Figure-3.8. Superposition of these fields gives the required field for Region-2. The only polynomial satisfying the final Laplace equation and boundary conditions is a_2y and it should be added to final Laplace Equation. This term gives rise to the uniform field.

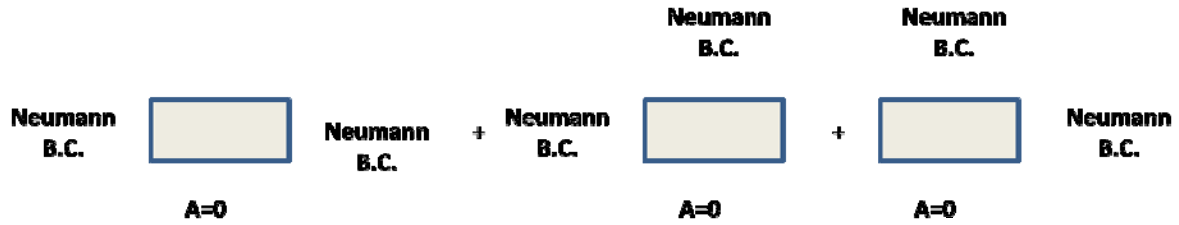

FIGURE-3.8 *Superposition of Laplace Field based on the Boundary Conditions*

$$A_2(x,y) = a_2 y + A_{2-1} + A_{2-2} + A_{2-3}$$

$$A_{2-1}(x,y) = \sum_{s=1}^{\infty} E_s Cos\left[\frac{\pi s}{a}(x - x_1)\right] Sinh\frac{\pi s}{a} y$$

$$A_{2-2}(x,y) = \sum_{k=1}^{\infty} C_k Sin\left[\frac{\pi}{2y_1}(2k-1)y\right] Cosh\left[\frac{\pi}{2y_1}(2k-1)(x - x_1)\right]$$

$$A_{2-3}(x,y) = \sum_{k=1}^{\infty} D_k Sin\left[\frac{\pi}{2y_1}(2k-1)y\right]\left[Sinh\left[\frac{\pi}{2y_1}(2k-1)(x - x_1)\right]\right.$$
$$\left. - \text{Coth}\left(\frac{\pi}{2y_1}(2k-1)a\right) Cosh\left[\frac{\pi}{2y_1}(2k-1)(x - x_1)\right]\right]$$

Areas 1, 4, 7, and 9 do not require polynomial terms because the vector potential needs to be zero at two perpendicular boundaries.

$$A_1(x,y) = A_{1-1} + A_{1-2}$$

$$A_{1-1}(x,y) = \sum_{s=1}^{\infty} A_s Sin\left[\frac{\pi}{2x_1}(2s-1)x\right] Sinh\left[\frac{\pi}{2x_1}(2s-1)y\right]$$

$$A_{1-2}(x,y) = \sum_{k=1}^{\infty} B_k Sin\left[\frac{\pi}{2y_1}(2k-1)y\right] Sinh\left[\frac{\pi}{2y_1}(2k-1)x\right]$$

$$A_3(x,y) = a_3 x + A_{3-1} + A_{3-2} + A_{3-3}$$

$$A_{3-1}(x,y) = \sum_{s=1}^{\infty} F_s Sin\left[\frac{\pi}{2x_1}(2s-1)x\right] Cosh\left[\frac{\pi}{2x_1}(2s-1)(y - y_1)\right]$$

$$A_{3-2}(x,y)=\sum_{s=1}^{\infty}H_s Sin\left[\frac{\pi}{2x_1}(2s-1)x\right]\left[Sinh\left[\frac{\pi}{2x_1}(2s-1)(y-y_1)\right]-\text{Coth}\left(\frac{\pi}{2x_1}(2s-1)b\right)Cosh\left[\frac{\pi}{2x_1}(2s-1)(y-y_1)\right]\right]$$

$$A_{3-3}(x,y)=\sum_{k=1}^{\infty}G_k Cos\left[\frac{\pi k}{b}(y-y_1)\right]Sinh\frac{\pi k}{b}x$$

$$A_4(x,y)=A_{4-1}+A_{4-2}$$

$$A_{4-1}(x,y)=\sum_{s=1}^{\infty}I_s Cos\left[\frac{\pi}{2x_2}(2s-1)(x-x_1-a)\right]Sinh\left[\frac{\pi}{2x_2}(2s-1)y\right]$$

$$A_{4-2}(x,y)=\sum_{k=1}^{\infty}JJ_k Sin\left[\frac{\pi}{2y_1}(2k-1)y\right]\left[Cosh\left[\frac{\pi}{2y_1}(2k-1)(x-x_1-a)\right]-\text{Coth}\left(\frac{\pi}{2y_1}(2k-1)x_2\right)Sinh\left[\frac{\pi}{2y_1}(2k-1)(x-x_1-a)\right]\right]$$

$$A_5(x,y)=a_5(x-x_1-a-x_2)+A_{5-1}+A_{5-2}+A_{5-3}$$

$$A_{5-1}(x,y)=\sum_{s=1}^{\infty}K_s Cos\left[\frac{\pi}{2x_2}(2s-1)(x-x_1-a)\right]Cosh\left[\frac{\pi}{2x_2}(2s-1)(y-y_1)\right]$$

$$A_{5-2}(x,y)=\sum_{s=1}^{\infty}L_s Cos\left[\frac{\pi}{2x_2}(2s-1)(x-x_1-a)\right]\left[Sinh\left[\frac{\pi}{2x_2}(2s-1)(y-y_1)\right]-\text{Coth}\left(\frac{\pi}{2x_2}(2s-1)b\right)Cosh\left[\frac{\pi}{2x_2}(2s-1)(y-y_1)\right]\right]$$

$$A_{5-3}(x,y)=\sum_{k=1}^{\infty}M_k Cos\left[\frac{\pi k}{b}(y-y_1)\right]\left[Cosh\left[\frac{\pi k}{b}(x-x_1-a)\right]-\text{Coth}\left(\frac{\pi k}{b}x_2\right)Sinh\left[\frac{\pi k}{b}(x-x_1-a)\right]\right]$$

$$A_7(x,y)=A_{7-1}+A_{7-2}$$

$$A_{7-1}(x,y)=\sum_{k=1}^{\infty}OQ_k Cos\left[\frac{\pi}{2y_2}(2k-1)(y-y_1-b)\right]\left[Cosh\left[\frac{\pi}{2y_2}(2k-1)(x-x_1-a)\right]-\text{Coth}\left(\frac{\pi}{2y_2}(2k-1)x_2\right)Sinh\left[\frac{\pi}{2y_2}(2k-1)(x-x_1-a)\right]\right]$$

$$A_{7-2}(x,y)=\sum_{s=1}^{\infty} OZ_s Cos\left[\frac{\pi}{2x_2}(2s-1)(x-x_1-a)\right]\left[Cosh\left[\frac{\pi}{2x_2}(2s-1)(y-y_1-b)\right]\right.$$
$$\left.-\operatorname{Coth}\left(\frac{\pi}{2x_2}(2s-1)y_2\right)Sinh\left[\frac{\pi}{2x_2}(2s-1)(y-y_1-b)\right]\right]$$

$$A_8(x,y)=a_8(y-y_1-b-y_2)+A_{8-1}+A_{8-2}+A_{8-3}$$

$$A_{8-1}(x,y)=\sum_{s=1}^{\infty} OO_s Cos\left[\frac{\pi s}{a}(x-x_1)\right]\left[Cosh\left[\frac{\pi s}{a}(y-y_1-b)\right]\right.$$
$$\left.-\operatorname{Coth}\left(\frac{\pi s}{a}y_2\right)Sinh\left[\frac{\pi s}{a}(y-y_1-b)\right]\right]$$

$$A_{8-2}(x,y)=\sum_{k=1}^{\infty} OP_k Cos\left[\frac{\pi}{2y_2}(2k-1)(y-y_1-b)\right]\left[Sinh\left[\frac{\pi}{2y_2}(2k-1)(x-x_1)\right]\right.$$
$$\left.-\operatorname{Coth}\left(\frac{\pi}{2y_2}(2k-1)a\right)Cosh\left[\frac{\pi}{2y_2}(2k-1)(x-x_1)\right]\right]$$

$$A_{8-3}(x,y)=\sum_{k=1}^{\infty} OR_k Cos\left[\frac{\pi}{2y_2}(2k-1)(y-y_1-b)\right]Cosh\left[\frac{\pi}{2y_2}(2k-1)(x-x_1)\right]$$

$$A_9(x,y)=A_{9-1}+A_{9-2}$$

$$A_{9-1}(x,y)=\sum_{s=1}^{\infty} OV_s Sin\left[\frac{\pi}{2x_1}(2s-1)x\right]\left[Cosh\left[\frac{\pi}{2x_1}(2s-1)(y-y_1-b)\right]\right.$$
$$\left.-\operatorname{Coth}\left(\frac{\pi}{2x_1}(2s-1)y_2\right)Sinh\left[\frac{\pi}{2x_1}(2s-1)(y-y_1-b)\right]\right]$$

$$A_{9-2}(x,y)=\sum_{k=1}^{\infty} OW_k Cos\left[\frac{\pi}{2y_2}(2k-1)(y-y_1-b)\right]Sinh\left[\frac{\pi}{2y_2}(2k-1)x\right]$$

At the interface of two regions, normal and tangential components of magnetic flux density is related as follows,

$$B_{1,n}=B_{2,n}\ or\ A_{1,n}=A_{2,n}\ ,\ \frac{B_{1,t}}{\mu_1}=\frac{B_{2,t}}{\mu_2}$$

Using tangential component of magnetic boundary conditions at the interface of two regions;

$$D_k = B_k Cosh\left[\frac{\pi}{2y_1}(2k-1)x_1\right], H_s = A_s Cosh\left[\frac{\pi}{2x_1}(2s-1)y_1\right]$$

$$C_k = -JJ_k \frac{Coth\left[\frac{\pi}{2y_1}(2k-1)x_2\right]}{Sinh\left[\frac{\pi}{2y_1}(2k-1)a\right]}, L_s = I_s Cosh\left[\frac{\pi}{2x_2}(2s-1)y_1\right]$$

$$K_s = -OZ_s \frac{Coth\left[\frac{\pi}{2x_2}(2s-1)y_2\right]}{Sinh\left[\frac{\pi}{2x_2}(2s-1)b\right]}, F_s = -OV_s \frac{Coth\left[\frac{\pi}{2x_1}(2s-1)y_2\right]}{Sinh\left[\frac{\pi}{2x_1}(2s-1)b\right]}$$

$$OW_k = \frac{OP_k}{Cosh\left[\frac{\pi}{2y_2}(2k-1)x_1\right]}, OR_k = -OQ_k \frac{Coth\left[\frac{\pi}{2y_2}(2k-1)x_2\right]}{Sinh\left[\frac{\pi}{2y_2}(2k-1)a\right]}$$

$$Y_k = \frac{\mu_2}{\mu_1} G_k Cosh\frac{\pi k}{b} x_1 \; and \; a_2 = \frac{\mu_1}{\mu_2}[a_{62} - 2a_6 y_1 - a_{66}(b + y_2)]$$

$$W_k = -\frac{\mu_2}{\mu_1} M_k \frac{Coth\frac{\pi k}{b} x_2}{Sinh\frac{\pi k}{b} a} \; and \; a_8 = \frac{\mu_1}{\mu_2}[a_{62} - 2a_6(y_1 + b) - a_{66} y_2]$$

$$Z_s = \frac{\mu_2}{\mu_1} E_s Cosh\frac{\pi s}{a} y_1 \; and \; a_3 = \frac{\mu_1}{\mu_2}[a_{61} + 2a_6 x_1 - a_{66}(a + x_2)]$$

$$V_s = -\frac{\mu_2}{\mu_1} OO_s \frac{Coth\frac{\pi s}{a} y_2}{Sinh\frac{\pi s}{a} b} \; and \; a_5 = \frac{\mu_1}{\mu_2}[a_{61} + 2a_6(x_1 + a) - a_{66} x_2]$$

From boundary condition A2=A1 at x=x_1

$$\sum_{k=1}^{\infty}\left[C_k - D_k Coth\left[\frac{\pi}{2y_1}(2k-1)a\right] - B_k \,\mathrm{Sinh}\left[\frac{\pi}{2y_1}(2k-1)x_1\right]\right] Sin\left[\frac{\pi}{2y_1}(2k-1)y\right]$$
$$= -a_2 y - \sum_{s=1}^{\infty} E_s Sinh\left(\frac{\pi s}{a} y\right) + \sum_{s=1}^{\infty} A_s (-1)^{s+1} Sinh\left[\frac{\pi}{2x_1}(2s-1)y\right]$$

Applying Finite Fourier Sine Transform to above equation and using relations obtained from tangential boundary conditions yields;

$$-JJ_k\frac{Coth\left[\frac{\pi}{2y_1}(2k-1)x_2\right]}{Sinh\left[\frac{\pi}{2y_1}(2k-1)a\right]}-D_k\left[Coth\left[\frac{\pi}{2y_1}(2k-1)a\right]+Tanh\left[\frac{\pi}{2y_1}(2k-1)x_1\right]\right]$$

$$=-a_2\frac{8y_1(-1)^{k+1}}{[\pi(2k-1)]^2}-\sum_{s=1}^{\infty}\frac{Z_s\frac{\pi s}{a}\frac{\mu_1}{\mu_2}\frac{2}{y_1}(-1)^{k+1}}{\left[\frac{\pi}{2y_1}(2k-1)\right]^2+\left(\frac{\pi s}{a}\right)^2}+\sum_{s=1}^{\infty}\frac{H_s\frac{\pi}{2x_1}(2s-1)\frac{2}{y_1}(-1)^{k+s}}{\left[\frac{\pi}{2y_1}(2k-1)\right]^2+\left[\frac{\pi}{2x_1}(2s-1)\right]^2}$$

It is easier to handle these equations in matrix and vector form because coefficients appear in Fourier Series, such as J_k and D_k, can simply be found using matrix relations. When all equations are derived, the final solution can be written in $\{Coeffs\}=[.]^{-1}\{.\}$ form. Here, $[.]$ represents matrix and $\{.\}$ represents vector. Therefore, above equation will be written as below.

$$-JJ_k\alpha 1_k-D_k\alpha 2_k=-a_2\alpha 3_k-\alpha 4_{k,s}Z_s+\alpha 5_{k,s}H_s$$

$$\alpha 1_k=\frac{Coth\left[\frac{\pi}{2y_1}(2k-1)x_2\right]}{Sinh\left[\frac{\pi}{2y_1}(2k-1)a\right]},\alpha 2_k=Coth\left[\frac{\pi}{2y_1}(2k-1)a\right]+Tanh\left[\frac{\pi}{2y_1}(2k-1)x_1\right]$$

$$\alpha 3_k=\frac{8y_1(-1)^{k+1}}{[\pi(2k-1)]^2},\alpha 4_{k,s}=\frac{\frac{\pi s}{a}\frac{\mu_1}{\mu_2}\frac{2}{y_1}(-1)^{k+1}}{\left[\frac{\pi}{2y_1}(2k-1)\right]^2+\left(\frac{\pi s}{a}\right)^2},$$

$$\alpha 5_{k,s}=\frac{\frac{\pi}{2x_1}(2s-1)\frac{2}{y_1}(-1)^{k+s}}{\left[\frac{\pi}{2y_1}(2k-1)\right]^2+\left[\frac{\pi}{2x_1}(2s-1)\right]^2}$$

From boundary condition A2=A4 at $x=x_1+a$ after applying Finite Fourier Sine Transform;

$$JJ_k\beta 1_k+D_k\beta 2_k=a_2\alpha 3_k+\beta 3_{k,s}Z_s-\beta 4_{k,s}L_s$$

$$\beta 1_k=1+Coth\left[\frac{\pi}{2y_1}(2k-1)x_2\right]Coth\left[\frac{\pi}{2y_1}(2k-1)a\right],\beta 2_k=\frac{1}{Sinh\left[\frac{\pi}{2y_1}(2k-1)a\right]}$$

$$\beta 3_{k,s}=\frac{\frac{\pi s}{a}\frac{\mu_1}{\mu_2}\frac{2}{y_1}(-1)^{k+1+s}}{\left[\frac{\pi}{2y_1}(2k-1)\right]^2+\left(\frac{\pi s}{a}\right)^2},\beta 4_{k,s}=\frac{\frac{\pi}{2x_2}(2s-1)\frac{2}{y_1}(-1)^{k+1}}{\left[\frac{\pi}{2y_1}(2k-1)\right]^2+\left[\frac{\pi}{2x_2}(2s-1)\right]^2}$$

From boundary condition A1=A3 at $y=y_1$ after applying Finite Fourier Sine Transform;

$$-OV_s\gamma 1_s-H_s\gamma 2_s=-a_3\gamma 3_k+\gamma 4_{s,k}D_k-\gamma 5_{s,k}Y_k$$

$$\gamma 1_s = \frac{Coth\left[\frac{\pi}{2x_1}(2s-1)y_2\right]}{Sinh\left[\frac{\pi}{2x_1}(2s-1)b\right]}, \gamma 2_s = Coth\left[\frac{\pi}{2x_1}(2s-1)b\right] + Tanh\left[\frac{\pi}{2x_1}(2s-1)y_1\right]$$

$$\gamma 3_s = \frac{8x_1(-1)^{s+1}}{[\pi(2s-1)]^2}$$

$$\gamma 4_{s,k} = \frac{\frac{\pi}{2y_1}(2k-1)\frac{2}{x_1}(-1)^{k+s}}{\left[\frac{\pi}{2y_1}(2k-1)\right]^2 + \left[\frac{\pi}{2x_1}(2s-1)\right]^2}, \gamma 5_{s,k} = \frac{\frac{\pi k}{b}\frac{\mu_1}{\mu_2}\frac{2}{x_1}(-1)^{s+1}}{\left(\frac{\pi k}{b}\right)^2 + \left[\frac{\pi}{2x_1}(2s-1)\right]^2}$$

From boundary condition A9=A3 at y=y_1+b after applying Finite Fourier Sine Transform;

$$OV_s\delta 1_s + H_s\delta 2_s = a_3\gamma 3_k + \delta 3_{s,k}Y_k - \delta 4_{s,k}OP_k$$

$$\delta 1_s = 1 + Coth\left[\frac{\pi}{2x_1}(2s-1)y_2\right]Coth\left[\frac{\pi}{2x_1}(2s-1)b\right], \delta 2_s = \frac{1}{Sinh\left[\frac{\pi}{2x_1}(2s-1)b\right]}$$

$$\delta 4_{s,k} = \frac{\frac{\pi k}{b}\frac{\mu_1}{\mu_2}\frac{2}{x_1}(-1)^{k+s+1}}{\left(\frac{\pi k}{b}\right)^2 + \left[\frac{\pi}{2x_1}(2s-1)\right]^2}, \delta 5_{s,k} = \frac{\frac{\pi}{2y_2}(2k-1)\frac{2}{x_1}(-1)^{s+1}}{\left[\frac{\pi}{2y_2}(2k-1)\right]^2 + \left[\frac{\pi}{2x_1}(2s-1)\right]^2}$$

From boundary condition A4=A5 at y=y_1 after applying Finite Fourier Cosine Transform;

$$-L_s\varepsilon 1_s - OZ_s\varepsilon 2_s = -a_5\varepsilon 3_s - \epsilon 4_{s,k}M_k + \varepsilon 5_{s,k}JJ_k$$

$$\varepsilon 1_s = Coth\left[\frac{\pi}{2x_2}(2s-1)b\right] + Tanh\left[\frac{\pi}{2x_2}(2s-1)y_1\right], \varepsilon 2_s = \frac{Coth\left[\frac{\pi}{2x_2}(2s-1)y_2\right]}{Sinh\left[\frac{\pi}{2x_2}(2s-1)b\right]}$$

$$\varepsilon 3_s = -\frac{8x_2}{[\pi(2s-1)]^2}$$

$$\varepsilon 4_{s,k} = \frac{\frac{\pi k}{b}\frac{2}{x_2}Coth(\frac{\pi k}{b}x_2)}{\left(\frac{\pi k}{b}\right)^2 + \left[\frac{\pi}{2x_2}(2s-1)\right]^2}, \varepsilon 5_{s,k} = \frac{\frac{\pi}{2y_1}(2k-1)\frac{2}{x_2}(-1)^{k+1}Coth\left[\frac{\pi}{2y_1}(2k-1)x_2\right]}{\left[\frac{\pi}{2y_1}(2k-1)\right]^2 + \left[\frac{\pi}{2x_2}(2s-1)\right]^2}$$

From boundary condition A7=A5 at y=y_1+b after applying Finite Fourier Cosine Transform;

$$L_s\theta 2_s + OZ_s\theta 1_s = a_5\varepsilon 3_s + \theta 3_{s,k}M_k - \theta 4_{s,k}OQ_k$$

$$\theta 1_s = 1 + Coth\left[\frac{\pi}{2x_2}(2s-1)y_2\right]Coth\left[\frac{\pi}{2x_2}(2s-1)b\right], \theta 2_s = \frac{1}{Sinh\left[\frac{\pi}{2x_2}(2s-1)b\right]}$$

$$\theta 3_{s,k} = \frac{\frac{\pi k}{b}\frac{2}{x_2}Coth(\frac{\pi k}{b}x_2)(-1)^k}{\left(\frac{\pi k}{b}\right)^2 + \left[\frac{\pi}{2x_2}(2s-1)\right]^2}, \theta 4_{s,k} = \frac{\frac{\pi}{2y_2}(2k-1)\frac{2}{x_2}Coth\left[\frac{\pi}{2y_2}(2k-1)x_2\right]}{\left[\frac{\pi}{2y_2}(2k-1)\right]^2 + \left[\frac{\pi}{2x_2}(2s-1)\right]^2}$$

From boundary condition A7=A8 at x=x_1+a after applying Finite Fourier Cosine Transform;

$$OQ_k\eta 1_k + OP_k\eta 2_k = a_8\eta 3_k + \eta 4_{k,s}OO_s - \eta 5_{k,s}OZ_s$$

$$\eta 1_k = 1 + Coth\left[\frac{\pi}{2y_2}(2k-1)x_2\right]Coth\left[\frac{\pi}{2y_2}(2k-1)a\right], \eta 2_k = \frac{1}{Sinh\left[\frac{\pi}{2y_2}(2k-1)a\right]}$$

$$\eta 3_k = -\frac{8y_2}{[\pi(2k-1)]^2}$$

$$\eta 4_{k,s} = \frac{\frac{\pi s}{a}\frac{2}{y_2}Coth(\frac{\pi s}{a}y_2)(-1)^s}{\left(\frac{\pi s}{a}\right)^2 + \left[\frac{\pi}{2y_2}(2k-1)\right]^2}, \eta 5_{k,s} = \frac{\frac{\pi}{2x_2}(2s-1)\frac{2}{y_2}Coth\left[\frac{\pi}{2x_2}(2s-1)y_2\right]}{\left[\frac{\pi}{2y_2}(2k-1)\right]^2 + \left[\frac{\pi}{2x_2}(2s-1)\right]^2}$$

From boundary condition A9=A8 at x=x_1 after applying Finite Fourier Cosine Transform;

$$OQ_k\vartheta 1_k + OP_k\vartheta 2_k = a_8\eta 3_k + \vartheta 3_{k,s}OO_s - \vartheta 4_{k,s}OV_s$$

$$\vartheta 1_k = \frac{Coth\left[\frac{\pi}{2y_2}(2k-1)x_2\right]}{Sinh\left[\frac{\pi}{2y_2}(2k-1)a\right]}, \vartheta 2_k = Coth\left[\frac{\pi}{2y_2}(2k-1)a\right] + Tanh\left[\frac{\pi}{2y_2}(2k-1)x_1\right]$$

$$\vartheta 3_{k,s} = \frac{\frac{\pi s}{a}\frac{2}{y_2}Coth(\frac{\pi s}{a}y_2)}{\left(\frac{\pi s}{a}\right)^2 + \left[\frac{\pi}{2y_2}(2k-1)\right]^2}, \vartheta 4_{k,s} = \frac{(-1)^{s+1}\frac{\pi}{2x_1}(2s-1)\frac{2}{y_2}Coth\left[\frac{\pi}{2x_1}(2s-1)y_2\right]}{\left[\frac{\pi}{2y_2}(2k-1)\right]^2 + \left[\frac{\pi}{2x_1}(2s-1)\right]^2}$$

Boundary conditions A2=A6 at y=y_1, A8=A6 at y=y_1+b, A3=A6 at x=x_1 , A5=A6 at x=x_1+a are much more complex than previous boundary conditions because these conditions also involve zero order transforms and constant terms. These terms appear due to flux normal boundary conditions. If boundary conditions were of flux parallel type, no constant or polynomial terms would have appeared when representing magnetic vector potential in terms of Fourier Series as vector potential for flux parallel boundary condition is A=0. Arranging the terms for final solution for the first boundary condition will be given in detail only.

From boundary condition A2=A6 at y=y_1 A2 is equal to;

$$A2(x,y1) = a_2 y_1 + \sum_{s=1}^{\infty} E_s \operatorname{Cos}\left[\frac{\pi s}{a}(x-x1)\right] \operatorname{Sinh}\left(\frac{\pi s}{a} y_1\right) - \sum_{k=1}^{\infty} JJ_k \frac{\operatorname{Coth}[n_k x_2]}{\operatorname{Sinh}[n_k a]} (-1)^{k+1} \operatorname{Cosh}[n_k (x-x1)]$$
$$+ \sum_{k=1}^{\infty} D_k (-1)^{k+1} [\operatorname{Sinh}[n_k (x-x1)] - \operatorname{Coth}[n_k a] \operatorname{Cosh}[n_k (x-x1)]]$$

$$where\ n_k = \frac{\pi}{2y_1}(2k-1)$$

A6 will be divided into three components; constant and polynomial terms, series solution from Laplace and Poisson's equations. It should be noted that A_{0k} from Roth's solution will become constant after substituting y=y_1.

$$A6_{poly}(x,y_1) = A_0 + a_{66}\left[\frac{x^2}{2} - x(x_1 + a + x_2) - \frac{{y_1}^2}{2} - y_1(b + y_2)\right] + a_{61}x + a_{62}y_1$$
$$+ a_6(x^2 - {y_1}^2) + \frac{2\mu_0}{ab}\sum_{j=1}^{p}\frac{N_j I_j}{d_j}\sum_{k=1}^{\infty}\frac{\left(\sin\frac{\pi k}{b} b'_j - \sin\frac{\pi k}{b} b_j\right)}{\left(\frac{\pi k}{b}\right)^3}$$

$$A6_{Poisson}(x,y_1) = \frac{2\mu_0}{ab}\sum_{j=1}^{p}\frac{N_j I_j}{c_j}\sum_{s=1}^{\infty}\frac{\left(\sin\frac{\pi s}{a} a'_j - \sin\frac{\pi s}{a} a_j\right)}{\left(\frac{\pi s}{a}\right)^3}\cos\frac{\pi s}{a}(x-x1)$$
$$+ \frac{4\mu_0}{ab}\sum_{s=1}^{\infty}\sum_{k=1}^{\infty}\frac{\cos\frac{\pi s}{a}(x-x1)}{\frac{\pi s}{a}\frac{\pi k}{b}\left[\left(\frac{\pi s}{a}\right)^2 + \left(\frac{\pi k}{b}\right)^2\right]}\sum_{j=1}^{p} J_j\left(\sin\frac{\pi s}{a} a'_j - \sin\frac{\pi s}{a} a_j\right)\left(\sin\frac{\pi k}{b} b'_j - \sin\frac{\pi k}{b} b_j\right)$$

$$A6_{Laplace}(x,y_1) = \sum_{k=1}^{\infty} Y_k\left[Sinh\left[\frac{\pi k}{b}(x-x_1)\right] - \operatorname{Coth}\left(\frac{\pi k}{b} a\right) Cosh\left(\frac{\pi k}{b}(x-x_1)\right)\right] - \sum_{s=1}^{\infty} Z_s Cos\left[\frac{\pi s}{a}(x-x_1)\right]\operatorname{Coth}\left(\frac{\pi s}{a} b\right)$$
$$+ \sum_{k=1}^{\infty} W_k\, Cosh\left[\frac{\pi k}{b}(x-x_1)\right] + \sum_{s=1}^{\infty} V_s Cos\left[\frac{\pi s}{a}(x-x_1)\right]$$

$$A6(x,y_1) = A6_{Laplace}(x,y_1) + A6_{Poisson}(x,y_1) + A6_{poly}(x,y_1)$$

Collecting terms contain $\cos\frac{\pi s}{a}(x-x_1)$ on right hand side and all the other terms on left hand side;

$$\sum_{s=1}^{\infty}\left[\left[E_s \operatorname{Sinh}\left(\frac{\pi s}{a}y_1\right) - V_s + Z_s \operatorname{Coth}\left(\frac{\pi s}{a}b\right)\right]\cos\frac{\pi s}{a}(x-x_1)\right] - A6_{Poisson}(x,y_1)$$

$$= A6_{poly}(x,y_1) + \sum_{k=1}^{\infty} Y_k\left[Sinh\left[\frac{\pi k}{b}(x-x_1)\right] - \operatorname{Coth}\left(\frac{\pi k}{b}a\right)Cosh\left[\frac{\pi k}{b}(x-x_1)\right]\right]$$

$$+ \sum_{k=1}^{\infty} W_k\, Cosh\left[\frac{\pi k}{b}(x-x_1)\right] + \sum_{k=1}^{\infty} JJ_k \frac{\operatorname{Coth}[n_k x_2]}{\operatorname{Sinh}[n_k a]}(-1)^{k+1}\operatorname{Cosh}[n_k(x-x_1)]$$

$$- \sum_{k=1}^{\infty} D_k(-1)^{k+1}[\operatorname{Sinh}[n_k(x-x_1)] - \operatorname{Coth}[n_k a]\operatorname{Cosh}[n_k(x-x_1)]]$$

Constant terms disappear after Finite Fourier Cosine Transform applied to above equation. Results can be written in matrix form after substituting the equations obtained from tangential boundary conditions.

$$Z_s\lambda 1_s + OO_s\lambda 2_s = a_{61}\lambda 3_s + a_6\lambda 4_s + a_{66}\lambda 5_s + \lambda 6_s + \lambda 7_{s,k}D_k - \lambda 8_{s,k}Y_k + \lambda 9_{s,k}JJ_k - \lambda 10_{s,k}M_k$$

$$\lambda 1_s = Coth\left(\frac{\pi s}{a}b\right) + \frac{\mu_1}{\mu_2}Tanh\left(\frac{\pi s}{a}y_1\right),\ \lambda 2_s = \frac{\mu_2}{\mu_1}\frac{Coth\left(\frac{\pi s}{a}y_2\right)}{Sinh\left(\frac{\pi s}{a}b\right)}$$

$$\lambda 3_s = \frac{2a}{(\pi s)^2}[(-1)^s - 1],\ \lambda 4_s = \frac{4a}{(\pi s)^2}[x_1[(-1)^s - 1] + a(-1)^s]$$

$$\lambda 5_s = -\frac{2a}{(\pi s)^2}[x_2(-1)^s - a - x_2], a_{66} = -\mu_0\sum_{j=1}^{P}\frac{NI}{2ab}$$

$$\mu_0 = 4\pi 10^{-7}\frac{H}{m}, NI = Ampere - Turns\ and\ p =\ number\ of\ conductors\ within\ the\ slot$$

$$\lambda 6_s = \sum_{\mathrm{j=1}}^{\mathrm{p}}\frac{\frac{N_j I_j}{c_j}\frac{2\mu_0}{ab}\left(\sin\frac{\pi s}{a}a'_j - \sin\frac{\pi s}{a}a_j\right)}{\left(\frac{\pi s}{a}\right)^3} + \sum_{k=1}^{\infty}\frac{\frac{4\mu_0}{ab}\sum_{j=1}^{p}J_j\left(\sin\frac{\pi s}{a}a'_j - \sin\frac{\pi s}{a}a_j\right)\left(\sin\frac{\pi k}{b}b'_j - \sin\frac{\pi k}{b}b_j\right)}{\frac{\pi s}{a}\frac{\pi k}{b}\left[\left(\frac{\pi s}{a}\right)^2 + \left(\frac{\pi k}{b}\right)^2\right]}$$

$$\lambda 7_{s,k} = \frac{\frac{\pi}{2y_1}(2k-1)\frac{2}{a}(-1)^{k+1}}{\left(\frac{\pi s}{a}\right)^2 + \left[\frac{\pi}{2y_1}(2k-1)\right]^2},\ \lambda 8_{s,k} = \frac{\frac{\pi k}{b}\frac{2}{a}}{\left(\frac{\pi k}{b}\right)^2 + \left(\frac{\pi s}{a}\right)^2}$$

$$\lambda 9_{s,k} = \frac{\frac{\pi}{2y_1}(2k-1)\frac{2}{a}(-1)^{k+s+1}Coth\left[\frac{\pi}{2y_1}(2k-1)x_2\right]}{\left(\frac{\pi s}{a}\right)^2 + \left[\frac{\pi}{2y_1}(2k-1)\right]^2},\ \lambda 10_{s,k} = \frac{\frac{\pi k}{b}\frac{2}{a}\frac{\mu_2}{\mu_1}(-1)^s Coth\left(\frac{\pi k}{b}x_2\right)}{\left(\frac{\pi k}{b}\right)^2 + \left(\frac{\pi s}{a}\right)^2}$$

Zero Order Transform yields;

$$a_2 y_1 = A_0 + C_1 + a_{61}\frac{(a+2x_1)}{2} + a_{62}y_1 + a_6\left(\frac{a^2}{3} + x_1(x_1+a) - {y_1}^2\right) - \sum_{k=1}^{\infty}\frac{b}{a\pi k}Y_k$$
$$- \sum_{k=1}^{\infty}\frac{\mu_2}{\mu_1}\frac{b}{a\pi k}Coth\left(\frac{\pi k}{b}x_2\right)M_k + \sum_{k=1}^{\infty}D_k\frac{(-1)^{k+1}}{n_k a} + \sum_{k=1}^{\infty}JJ_k\frac{\mathrm{Coth}(n_k x_2)}{n_k a}(-1)^{k+1}$$

And the constant term C_1 is;

$$C_1 = a_{66}\left[\int_{x_1}^{x_1+a}\left(\frac{\frac{x^2}{2} - x(x_1+a+x_2)}{a}\right)dx - \frac{{y_1}^2}{2} - y_1(b+y_2)\right] + \frac{2\mu_0}{ab}\sum_{j=1}^{p}\frac{N_j I_j}{d_j}\sum_{k=1}^{\infty}\frac{\left(\sin\frac{\pi k}{b}b'_j - \sin\frac{\pi k}{b}b_j\right)}{\left(\frac{\pi k}{b}\right)^3}$$

From boundary condition A8=A6 at y=y_1+b after Finite Fourier cosine Transform,

$$OO_s\xi 1_s + Z_s\xi 2_s = a_{61}\lambda 3_s + a_6\lambda 4_s + a_{66}\lambda 5_s + \xi 3_s + \xi 4_{s,k}OP_k - \xi 5_{s,k}Y_k + \xi 6_{s,k}OQ_k - \xi 7_{s,k}M_k$$

$$\xi 1_s = 1 + \frac{\mu_2}{\mu_1}Coth\left(\frac{\pi s}{a}y_2\right)Coth\left(\frac{\pi s}{a}b\right),\ \xi 2_s = \frac{1}{Sinh\left(\frac{\pi s}{a}b\right)}$$

$$\xi 3_s = \sum_{\mathrm{j}=1}^{\mathrm{p}}\frac{\frac{N_j I_j}{c_j}\frac{2\mu_0}{ab}\left(\sin\frac{\pi s}{a}a'_j - \sin\frac{\pi s}{a}a_j\right)}{\left(\frac{\pi s}{a}\right)^3} + \sum_{k=1}^{\infty}\frac{\frac{4\mu_0}{ab}\sum_{j=1}^{p}J_j\left(\sin\frac{\pi s}{a}a'_j - \sin\frac{\pi s}{a}a_j\right)\left(\sin\frac{\pi k}{b}b'_j - \sin\frac{\pi k}{b}b_j\right)(-1)^k}{\frac{\pi s}{a}\frac{\pi k}{b}\left[\left(\frac{\pi s}{a}\right)^2 + \left(\frac{\pi k}{b}\right)^2\right]}$$

$$\xi 4_{s,k} = \frac{\frac{\pi}{2y_2}(2k-1)\frac{2}{a}}{\left(\frac{\pi s}{a}\right)^2 + \left[\frac{\pi}{2y_2}(2k-1)\right]^2},\ \xi 5_{s,k} = \frac{\frac{\pi k}{b}\frac{2}{a}(-1)^k}{\left(\frac{\pi k}{b}\right)^2 + \left(\frac{\pi s}{a}\right)^2}$$

$$\xi 6_{s,k} = \frac{\frac{\pi}{2y_2}(2k-1)\frac{2}{a}(-1)^s Coth\left[\frac{\pi}{2y_2}(2k-1)x_2\right]}{\left(\frac{\pi s}{a}\right)^2 + \left[\frac{\pi}{2y_2}(2k-1)\right]^2},\ \xi 7_{s,k} = \frac{\frac{\pi k}{b}\frac{2}{a}\frac{\mu_2}{\mu_1}(-1)^{s+k}Coth\left(\frac{\pi k}{b}x_2\right)}{\left(\frac{\pi k}{b}\right)^2 + \left(\frac{\pi s}{a}\right)^2}$$

Zero Order Transform yields;

$$a_2(y_1+b) = A_0 + C_2 + a_{61}\frac{(a+2x_1)}{2} + a_{62}(y_1+b) + a_6\left(\frac{a^2}{3} + x_1(x_1+a) - (y_1+b)^2\right)$$
$$- \sum_{k=1}^{\infty}\frac{b(-1)^k}{a\pi k}Y_k - \sum_{k=1}^{\infty}\frac{\mu_2}{\mu_1}\frac{b(-1)^k}{a\pi k}Coth\left(\frac{\pi k}{b}x_2\right)M_k + \sum_{k=1}^{\infty}OP_k\frac{2y_2}{\pi(2k-1)a}$$
$$+ \sum_{k=1}^{\infty}OQ_k\frac{2y_2}{\pi(2k-1)a}\mathrm{Coth}\left[\frac{\pi(2k-1)}{2y_2}x_2\right]$$

$$C_2 = a_{66}\left[\int_{x_1}^{x_1+a}\left(\frac{x^2}{2} - x(x_1+a+x_2)}{a}\right)dx + \frac{(y_1+b)^2}{2} - (y_1+b)(y_1+b+y_2)\right]$$

$$+\frac{2\mu_0}{ab}\sum_{j=1}^{p}\frac{N_j I_j}{d_j}\sum_{k=1}^{\infty}\frac{(-1)^k\left(\sin\frac{\pi k}{b}b'_j - \sin\frac{\pi k}{b}b_j\right)}{\left(\frac{\pi k}{b}\right)^3}$$

From boundary condition A3=A6 at x=x_1 after Fourier Transforms;

$$Y_k\phi 1_k + M_k\phi 2_k = a_{62}\phi 3_k - a_6\phi 4_k + a_{66}\phi 5_k + \phi 6_k + \phi 7_{k,s}H_s - \phi 8_{k,s}Z_s - \phi 9_{k,s}OO_s + \phi 10_{k,s}OV_s$$

$$\phi 1_k = Coth\left(\frac{\pi k}{b}a\right) + \frac{\mu_1}{\mu_2}Tanh\left(\frac{\pi k}{b}x_1\right), \phi 2_k = \frac{\mu_2}{\mu_1}\frac{Coth\left(\frac{\pi k}{b}x_2\right)}{Sinh\left(\frac{\pi k}{b}a\right)}$$

$$\phi 3_k = \frac{2b}{(\pi k)^2}\left[(-1)^k - 1\right], \phi 4_k = \frac{4b}{(\pi k)^2}\left[y_1\left[(-1)^k - 1\right] + b(-1)^k\right]$$

$$\phi 5_k = -\frac{2b}{(\pi k)^2}\left[y_2(-1)^k - b - y_2\right]$$

$$\phi 6_k = \sum_{\mathrm{j}=1}^{\mathrm{p}}\frac{\frac{N_j I_j}{d_j}\frac{2\mu_0}{ab}\left(\sin\frac{\pi k}{b}b'_j - \sin\frac{\pi k}{b}b_j\right)}{\left(\frac{\pi k}{b}\right)^3} + \sum_{s=1}^{\infty}\frac{\frac{4\mu_0}{ab}\sum_{j=1}^{p}J_j\left(\sin\frac{\pi s}{a}a'_j - \sin\frac{\pi s}{a}a_j\right)\left(\sin\frac{\pi k}{b}b'_j - \sin\frac{\pi k}{b}b_j\right)}{\frac{\pi s}{a}\frac{\pi k}{b}\left[\left(\frac{\pi s}{a}\right)^2 + \left(\frac{\pi k}{b}\right)^2\right]}$$

$$\phi 7_{k,s} = \frac{\frac{\pi}{2x_1}(2s-1)\frac{2}{b}(-1)^{s+1}}{\left(\frac{\pi k}{b}\right)^2 + \left[\frac{\pi}{2x_1}(2s-1)\right]^2}, \phi 8_{k,s} = \frac{\frac{\pi s}{a}\frac{2}{b}}{\left(\frac{\pi k}{b}\right)^2 + \left(\frac{\pi s}{a}\right)^2}$$

$$\phi 9_{k,s} = \frac{\frac{\mu_2}{\mu_1}\frac{\pi s}{a}\frac{2}{b}(-1)^k Coth\left(\frac{\pi s}{a}y_2\right)}{\left(\frac{\pi s}{a}\right)^2 + \left(\frac{\pi k}{b}\right)^2}, \phi 10_{k,s} = \frac{\frac{\pi}{2x_1}(2s-1)\frac{2}{b}(-1)^{s+k+1}Coth\left[\frac{\pi}{2x_1}(2s-1)y_2\right]}{\left(\frac{\pi k}{b}\right)^2 + \left[\frac{\pi}{2x_1}(2s-1)\right]^2}$$

Zero Order Transform yields;

$$a_3x_1 = A_0 + C_3 + a_{62}\frac{(b+2y_1)}{2} + a_{61}x_1 + a_6\left({x_1}^2 - \frac{b^2}{3} - y_1(y_1+b)\right) - \sum_{s=1}^{\infty}\frac{a}{b\pi s}Z_s$$

$$-\sum_{s=1}^{\infty}\frac{\mu_2}{\mu_1}\frac{a}{b\pi s}Coth\left(\frac{\pi s}{a}y_2\right)OO_s + \sum_{s=1}^{\infty}\frac{H_s 2x_1(-1)^{s+1}}{\pi(2s-1)b}$$

$$+\sum_{s=1}^{\infty}OV_s\frac{2x_1(-1)^{s+1}}{\pi(2s-1)b}Coth\left[\frac{\pi}{2x_1}(2s-1)y_2\right]$$

And the constant term C_3 is;

$$C_3 = a_{66}\left[-\frac{{x_1}^2}{2} - x_1(a+x_2) + \int_{y_1}^{y_1+b}\left(\frac{y^2}{2} - y(y_1+b+y_2)}{b}\right)dy\right] + \frac{2\mu_0}{ab}\sum_{j=1}^{p}\frac{N_j I_j}{c_j}\sum_{s=1}^{\infty}\frac{\left(\sin\frac{\pi s}{a}a'_j - \sin\frac{\pi s}{a}a_j\right)}{\left(\frac{\pi s}{a}\right)^3}$$

From boundary condition A5=A6 at x=x_1+a after Fourier Transforms;

$$Y_k\chi 1_k + M_k\chi 2_k = a_{62}\phi 3_k - a_6\phi 4_k + a_{66}\phi 5_k + \chi 3_k + \chi 4_{k,s}L_s - \chi 5_{k,s}Z_s - \chi 6_{k,s}OO_s + \chi 7_{k,s}OZ_s$$

$$\chi 1_k = \frac{1}{Sinh\left(\frac{\pi k}{b}a\right)}, \chi 2_k = 1 + \frac{\mu_2}{\mu_1}Coth\left(\frac{\pi k}{b}x_2\right)Coth\left(\frac{\pi k}{b}a\right)$$

$$\chi 3_k = \sum_{\mathrm{j}=1}^{\mathrm{p}}\frac{\frac{N_j I_j}{d_j}\frac{2\mu_0}{ab}\left(\sin\frac{\pi k}{b}b'_j - \sin\frac{\pi k}{b}b_j\right)}{\left(\frac{\pi k}{b}\right)^3} + \sum_{s=1}^{\infty}\frac{\frac{4\mu_0}{ab}\sum_{j=1}^{p}J_j\left(\sin\frac{\pi s}{a}a'_j - \sin\frac{\pi s}{a}a_j\right)\left(\sin\frac{\pi k}{b}b'_j - \sin\frac{\pi k}{b}b_j\right)(-1)^s}{\frac{\pi s}{a}\frac{\pi k}{b}\left[\left(\frac{\pi s}{a}\right)^2 + \left(\frac{\pi k}{b}\right)^2\right]}$$

$$\chi 4_{k,s} = \frac{\frac{\pi}{2x_2}(2s-1)\frac{2}{b}}{\left(\frac{\pi k}{b}\right)^2 + \left[\frac{\pi}{2x_1}(2s-1)\right]^2}, \chi 5_{k,s} = \frac{\frac{\pi s}{a}\frac{2}{b}(-1)^s}{\left(\frac{\pi k}{b}\right)^2 + \left(\frac{\pi s}{a}\right)^2}$$

$$\chi 6_{k,s} = \frac{\frac{\mu_2}{\mu_1}\frac{\pi s}{a}\frac{2}{b}(-1)^{s+k}Coth\left(\frac{\pi s}{a}y_2\right)}{\left(\frac{\pi s}{a}\right)^2 + \left(\frac{\pi k}{b}\right)^2}, \chi 7_{k,s} = \frac{\frac{\pi}{2x_2}(2s-1)\frac{2}{b}(-1)^k Coth\left[\frac{\pi}{2x_2}(2s-1)y_2\right]}{\left(\frac{\pi k}{b}\right)^2 + \left[\frac{\pi}{2x_2}(2s-1)\right]^2}$$

Zero Order Transform yields;

$$a_3(x_1+a) = A_0 + C_4 + a_{62}\frac{(b+2y_1)}{2} + a_{61}(x_1+a) + a_6\left((x_1+a)^2 - \frac{b^2}{3} - y_1(y_1+b)\right)$$
$$- \sum_{s=1}^{\infty}\frac{a(-1)^s}{b\pi s}Z_s - \sum_{s=1}^{\infty}\frac{\mu_2}{\mu_1}\frac{a(-1)^s}{b\pi s}Coth\left(\frac{\pi s}{a}y_2\right)OO_s + \sum_{s=1}^{\infty}\frac{L_s 2x_2}{\pi(2s-1)b}$$
$$+ \sum_{s=1}^{\infty}OZ_s\frac{2x_2}{\pi(2s-1)b}Coth\left[\frac{\pi}{2x_2}(2s-1)y_2\right]$$

And the constant term C_4 is;

$$C_4 = a_{66}\left[\frac{(x_1+a)^2}{2} - (x_1+a)(x_1+a+x_2) + \int_{y_1}^{y_1+b}\left(\frac{y^2}{2} - y(y_1+b+y_2)}{b}\right)dy\right]$$

$$+\frac{2\mu_0}{ab}\sum_{j=1}^{p}\frac{N_j I_j}{c_j}\sum_{s=1}^{\infty}\frac{\left(\sin\frac{\pi s}{a}a'_j - \sin\frac{\pi s}{a}a_j\right)(-1)^s}{\left(\frac{\pi s}{a}\right)^3}$$

All boundary conditions are applied, all Fourier Transforms are performed and final matrix is ready to be constructed. However, these equations still contain constant terms such as a_2, a_8. It is easier to write these constant terms in terms of Fourier coefficients. To be able do this, correlation between constant terms will be derived from zero order Fourier Transforms and tangential boundary conditions. Substitute the equations for a_2, a_3, a_5, a_8 from tangential boundary conditions into Zero Order Fourier Transforms,

$$a_{62}\kappa_1 - a_6\kappa_2 = A_0 + Coef_1 + a_{61}\kappa_{12} + S_1 \ (\mathbf{3.16})$$

$$a_{62}\kappa_3 - a_6\kappa_4 = A_0 + Coef_2 + a_{61}\kappa_{12} + S_2 \ (\mathbf{3.17})$$

$$a_{61}\kappa_5 - a_6\kappa_6 = A_0 + Coef_3 + a_{62}\kappa_{23} + S_3 \ (\mathbf{3.18})$$

$$a_{61}\kappa_7 - a_8\kappa_8 = A_0 + Coef_4 + a_{62}\kappa_{23} + S_4 \ (\mathbf{3.19})$$

$$Coef_1 = C_1 + a_{66}\frac{\mu_1}{\mu_2}(b+y_2)y_1\,, Coef_2 = C_2 - a_{66}\frac{\mu_1}{\mu_2}{y_2}^2$$

$$Coef_3 = C_3 + a_{66}\frac{\mu_1}{\mu_2}(a+x_2)x_1\,, Coef_4 = C_4 - a_{66}\frac{\mu_1}{\mu_2}{x_2}^2$$

$$\kappa_1 = y_1\left(\frac{\mu_1}{\mu_2}-1\right), \kappa_2 = {y_1}^2(2\frac{\mu_1}{\mu_2}-1) + \frac{a^2}{3} + {x_1}^2 + ax_1, \kappa_{12} = \frac{a+2x_1}{2}$$

$$\kappa_5 = x_1\left(\frac{\mu_1}{\mu_2}-1\right), \kappa_6 = {x_1}^2\left(-2\frac{\mu_1}{\mu_2}+1\right) - \frac{b^2}{3} - by_1 - {y_1}^2, \kappa_{23} = \frac{b+2y_1}{2}$$

$$\kappa_3 = -\frac{\mu_1}{\mu_2}y_2 - y_1 - b,\ \kappa_4 = -2\frac{\mu_1}{\mu_2}y_2(y_1+b) - (y_1+b)^2 + \frac{a^2}{3} + {x_1}^2 + ax_1$$

$$\kappa_7 = -\frac{\mu_1}{\mu_2}x_2 - x_1 - a,\ \kappa_8 = 2\frac{\mu_1}{\mu_2}x_2(x_1+a) + (x_1+a)^2 - \frac{b^2}{3} - {y_1}^2 - by_1$$

$$S_1 = -\sum_{k=1}^{\infty}\frac{b}{a\pi k}Y_k - \sum_{k=1}^{\infty}\frac{\mu_2}{\mu_1}\frac{b}{a\pi k}Coth\left(\frac{\pi k}{b}x_2\right)M_k + \sum_{k=1}^{\infty}D_k\frac{(-1)^{k+1}}{n_k a} + \sum_{k=1}^{\infty}JJ_k\frac{\mathrm{Coth}(n_k x_2)}{n_k a}(-1)^{k+1}$$

$$S_2 = -\sum_{k=1}^{\infty} \frac{b(-1)^k}{a\pi k} Y_k - \sum_{k=1}^{\infty} \frac{\mu_2}{\mu_1} \frac{b(-1)^k}{a\pi k} Coth\left(\frac{\pi k}{b} x_2\right) M_k + \sum_{k=1}^{\infty} OP_k \frac{2y_2}{\pi(2k-1)a}$$
$$+ \sum_{k=1}^{\infty} OQ_k \frac{2y_2}{\pi(2k-1)a} \mathrm{Coth}\left[\frac{\pi(2k-1)}{2y_2} x_2\right]$$

$$S_3 = -\sum_{s=1}^{\infty} \frac{a}{b\pi s} Z_s - \sum_{s=1}^{\infty} \frac{\mu_2}{\mu_1} \frac{a}{b\pi s} Coth\left(\frac{\pi s}{a} y_2\right) OO_s + \sum_{s=1}^{\infty} \frac{H_s 2x_1(-1)^{s+1}}{\pi(2s-1)b}$$
$$+ \sum_{s=1}^{\infty} OV_s \frac{2x_1(-1)^{s+1}}{\pi(2s-1)b} Coth\left[\frac{\pi}{2x_1}(2s-1)y_2\right]$$

$$S_4 = -\sum_{s=1}^{\infty} \frac{a(-1)^s}{b\pi s} Z_s - \sum_{s=1}^{\infty} \frac{\mu_2}{\mu_1} \frac{a(-1)^s}{b\pi s} Coth\left(\frac{\pi s}{a} y_2\right) OO_s + \sum_{s=1}^{\infty} \frac{L_s 2x_2}{\pi(2s-1)b}$$
$$+ \sum_{s=1}^{\infty} OZ_s \frac{2x_2}{\pi(2s-1)b} Coth\left[\frac{\pi}{2x_2}(2s-1)y_2\right]$$

From Eq(3.16),

$$A_0 = a_{62}\kappa_1 - a_6\kappa_2 - Coef_1 - a_{61}\kappa_{12} - S_1$$

And substitute above equation in Eq(3.17),

$$a_{62}\kappa_3 - a_6\kappa_4 = a_{62}\kappa_1 - a_6\kappa_2 - Coef_1 - S_1 + Coef_2 + S_2$$

$$a_{62} = \frac{a_6(\kappa_2 - \kappa_4) + Coef_1 - Coef_2 + S_1 - S_2}{(\kappa_1 - \kappa_3)}$$

Subtracting Eq(3.18) from Eq(3.19) gives;

$$a_{61} = \frac{a_6(\kappa_6 - \kappa_8) + Coef_3 - Coef_4 + S_3 - S_4}{(\kappa_5 - \kappa_7)}$$

Substitute above equations back in Eq(3.18) and Eq(3.19);

$$a_{61}(\kappa_5 + \kappa_{12}) - a_6\left[(\kappa_6 - \kappa_2) + \frac{(\kappa_1 + \kappa_{23})(\kappa_2 - \kappa_4)}{(\kappa_1 - \kappa_3)}\right]$$
$$= Coef_3 - Coef_1 + S_3 - S_1 + \frac{(\kappa_1 + \kappa_{23})(Coef_1 - Coef_2)}{(\kappa_1 - \kappa_3)} + \frac{(\kappa_1 + \kappa_{23})(S_1 - S_2)}{(\kappa_1 - \kappa_3)}$$

$$a_{61}(\kappa_7+\kappa_{12})-a_6\left[(\kappa_8-\kappa_2)+\frac{(\kappa_1+\kappa_{23})(\kappa_2-\kappa_4)}{(\kappa_1-\kappa_3)}\right]$$
$$=Coef_4-Coef_1+S_4-S_1+\frac{(\kappa_1+\kappa_{23})(Coef_1-Coef_2)}{(\kappa_1-\kappa_3)}+\frac{(\kappa_1+\kappa_{23})(S_1-S_2)}{(\kappa_1-\kappa_3)}$$

Solving these equations gives the required form for a_6 in terms of constants and series.

$$a_6=\frac{Constant1}{Constant2}+SC_1(S_1-S_2)+\frac{S_4}{Constant2}-SC_2S_3+SC_3S_1$$

$$Constant1=Coef_4-Coef_1+\frac{(\kappa_1+\kappa_{23})(Coef_1-Coef_2)}{(\kappa_1-\kappa_3)}$$
$$-\frac{(\kappa_7+\kappa_{12})}{(\kappa_5+\kappa_{12})}\left[(Coef_3-Coef_1)\frac{(\kappa_1+\kappa_{23})(Coef_1-Coef_2)}{(\kappa_1-\kappa_3)}\right]$$

$$Constant2=\frac{(\kappa_7+\kappa_{12})}{(\kappa_5+\kappa_{12})}\left[(\kappa_6-\kappa_2)\frac{(\kappa_1+\kappa_{23})(\kappa_2-\kappa_4)}{(\kappa_1-\kappa_3)}\right]-\left[(\kappa_8-\kappa_2)\frac{(\kappa_1+\kappa_{23})(\kappa_2-\kappa_4)}{(\kappa_1-\kappa_3)}\right]$$

$$SC_1=\frac{1}{Constant2}\frac{(\kappa_1+\kappa_{23})(\kappa_5-\kappa_7)}{(\kappa_1-\kappa_3)(\kappa_5+\kappa_{12})}$$

$$SC_2=\frac{1}{Constant2}\frac{(\kappa_7+\kappa_{12})}{(\kappa_5+\kappa_{12})}$$

$$SC_3=\frac{1}{Constant2}\left[\frac{(\kappa_7+\kappa_{12})}{(\kappa_5+\kappa_{12})}-1\right]$$

All the constant coefficients can now be written in terms of series and known constant terms. Substituting the final form for a_2, a_8, a_3, a_5, a_6, a_{61} and a_{62} gives the structure for final matrix. For example, for a_2 after substituting a_{62} and a_6,

$$a_2=\frac{\mu_1}{\mu_2}\left[\left(SC_1(S_1-S_2)+\frac{S_4}{Constant2}-SC_2S_3+SC_3S_1\right)\left(\frac{(\kappa_2-\kappa_4)}{(\kappa_1-\kappa_3)}-2y_1\right)+\frac{S_1-S_2}{\kappa_1-\kappa_3}+T_c\right]$$

$$T_c=-a_{66}(b+y_2)+\frac{Coef_1-Coef_2}{(\kappa_1-\kappa_3)}+\left(\frac{(\kappa_2-\kappa_4)}{(\kappa_1-\kappa_3)}-2y_1\right)\frac{Constant1}{Constant2}$$

Only the last term, T_c, does not contribute to series because it is constant term. After substituting for S_1, S_2, S_3 and S_4, additional terms in series form will occur and will be added to the equations derived earlier. However, terms from S_1 and S_2 will occur in vector form whereas terms from S_3 and S_4 will occur in matrix form for a_2. For example, additional term for Z_s is;

$$\frac{\mu_1}{\mu_2}\left(\frac{(\kappa_2-\kappa_4)}{(\kappa_1-\kappa_3)}-2y_1\right)\frac{8y_1(-1)^{k+1}}{[\pi(2k-1)]^2}\sum_{s=1}^{\infty}\frac{a}{b\pi s}\left[SC_2-\frac{(-1)^s}{Constant2}\right]Z_s$$

Or

$$Z_{add_{k,s}}=\frac{\mu_1}{\mu_2}\left(\frac{(\kappa_2-\kappa_4)}{(\kappa_1-\kappa_3)}-2y_1\right)\frac{8y_1(-1)^{k+1}}{[\pi(2k-1)]^2}\frac{a}{b\pi s}\left[SC_2-\frac{(-1)^s}{Constant2}\right]Z_s$$

This additional term can easily be added to $\alpha 4_{k,s}Z_s$ term obtained from A2=A1 boundary condition as both of these equations are in matrix form. Additional term for D_k is;

$$\frac{\mu_1}{\mu_2}\left[\left(\frac{(\kappa_2-\kappa_4)}{(\kappa_1-\kappa_3)}-2y_1\right)(SC_1+SC_3)+\frac{1}{\kappa_1-\kappa_3}\right]\frac{8y_1(-1)^{k+1}}{[\pi(2k-1)]^2}\sum_{k=1}^{\infty}D_k\frac{2y_1(-1)^{k+1}}{\pi(2k-1)a}$$

Above equation should be added to the term $D_k\alpha 2_k$. This can be possible by changing the summation parameter and converting above equation from vector form to matrix form. Therefore,

$$\frac{\mu_1}{\mu_2}\left[\left(\frac{(\kappa_2-\kappa_4)}{(\kappa_1-\kappa_3)}-2y_1\right)(SC_1+SC_3)+\frac{1}{\kappa_1-\kappa_3}\right]\frac{8y_1(-1)^{k+1}}{[\pi(2k-1)]^2}\sum_{s=1}^{\infty}D_s\frac{2y_1(-1)^{s+1}}{\pi(2s-1)a}$$

Or

$$D_{add_{k,s}}=\frac{\mu_1}{\mu_2}\left[\left(\frac{(\kappa_2-\kappa_4)}{(\kappa_1-\kappa_3)}-2y_1\right)(SC_1+SC_3)+\frac{1}{\kappa_1-\kappa_3}\right]\frac{8y_1(-1)^{k+1}}{[\pi(2k-1)]^2}D_s\frac{2y_1(-1)^{s+1}}{\pi(2s-1)a}$$

Terms, such as $D_k\alpha 2_k$, can easily be written in matrix form. This is achieved by writing $\alpha 2_k$ as diagonal matrix. Final summation is,

$$[Diagonal(-\alpha 2_k)]\{D_k\}+\left[D_{add_{k,s}}\right]\{D_k\}=\left([Diagonal(-\alpha 2_k)]+\left[D_{add_{k,s}}\right]\right)\{D_k\}$$

Where $Diagonal(-\alpha 2_k)$ represents diagonal matrix.

Final matrix can now be constructed applying the technique described above to constants a_2, a_8, a_3, a_5, a_6, a_{61} and a_{62}. The final matrix and its constituents are given in Appendix-A.

Fourier series needs to be truncated when desired level of accuracy is reached. If the series is truncated after HH_{tr} terms, first HH_{tr} terms in the coefficient vector are the required constants related to D and from HH_{tr}+1 to $2HH_{tr}$ are the terms for H and so on. All the remaining constants can now be determined and problem is solved.

3.8 Comparison of the Proposed Method with FEA and Roth's Solution

Proposed method is compared to FEA results in order to test the accuracy. The series was truncated after the first 35 terms. 2-D, 8 node planar quadratic triangular elements are used. The model consists of 36702 elements and 73837 nodes. In order to test the accuracy of the FEA results, a model with coarser mesh consisting 9174 elements and 18565 nodes and a model with finer mesh consisting 146808 elements and 294481 nodes were used. Table-3.1 shows the comparison where the model with 9174 elements is denoted as Model1, the model with 36702 elements is denoted as Model2 and the model with 146808 elements is denoted as Model3. It can be seen that the results approach to the theoretical findings in Tables-3.3 and 3.4 with the refined mesh. Flux lines are plotted and forces and inductances calculated by FEA, Roth's Method and the proposed theory are given below.

	Self Inductance		**Mutual Inductance**	**Short-Circuit Forces in Direction X**		**Short-Circuit Forces in Direction Y**	
	LV	**HV**		**LV**	**HV**	**LV**	**HV**
Model1	1.377	347.79	21.887	-21305	20938	-252.37	-53.058
Model2	1.378	347.88	21.893	-21338	20971	-257.48	-57.616
Model3	1.3782	347.92	21.895	-21338	20971	-257.47	-57.610

TABLE-3.1: *Comparison of the FEA Models*

Table-3.2 shows the dimensions of the transformer window, position of the conductors and excitation values used. These values are taken from a generator transformer in service. Table-3.3 shows the inductances calculated with the proposed method and FEA. The inductances are calculated using ANSYS LMATRIX built-in macro. Roth's solution is not given in Table-3.3 as the Roth's solution gives unreasonable results to calculate the inductances because it wasn't developed to calculate open circuit properties.

x_1	y_1	x_2	y_2	a	b	μ_1	μ_2
480	480	480	480	516	2460	5500	1
Winding	a_j	a'_j	b_j	b'_j	**NI (Ampere-Turns)**		**N**
LV	19	112	102.5	2229.5	-276190		54
HV	205	357	110	2222	276190		858

TABLE-3.2: *Dimensions (mm) and Excitation Values (Ampere – Turns)*

Winding	**Self Inductance**		**Mutual Inductance**	
	FEA	**THEORY**	**FEA**	**THEORY**
LV	1.378	1.3787	21.893	21.9
HV	347.88	348.02		

TABLE-3.3: *Comparison of Calculated Inductances*

Table-3.4 compares the forces for open and short circuit conditions for the developed method, Roth's solution and FEA. Roth's solution fails to provide accurate results for open condition. In short circuit condition, the agreement between the Roth's solution and other methods are close but still a difference of 3% to 6% exists. Near to perfect agreement between the proposed method and FEA can be seen from these tables for both open and short circuit conditions.

Winding	**FEA**				**Developed Theory**				**ROTH's Method**			
	Force-x		**Force-y**		**Force-x**		**Force-y**		**Force-x**		**Force-y**	
	OC	**SC**	**OC**	**SC**	**OC**	**SC**	**OC**	**SC**	**OC**	**SC**	**OC**	**SC**
LV	-5264.8	-21338	-3576.4	-257.48	-5264.81	-21337.8	-3576.52	-257.348	-15905.6	-21343	-5057.65	-264.92
HV	0	20971	0	-57.616	0	20971.2	0	-58.4	0	20971	0	-62.03

TABLE-3.4: *Comparison of Calculated Forces (N/m) on Conductors for Open Circuit (OC) and Short Circuit (SC)*

Figure-3.9 shows the flux lines obtained from FEA and the proposed method for short circuit condition and Figures 3.10 to 3.12 show vector potential values at some distances to compare the techniques.

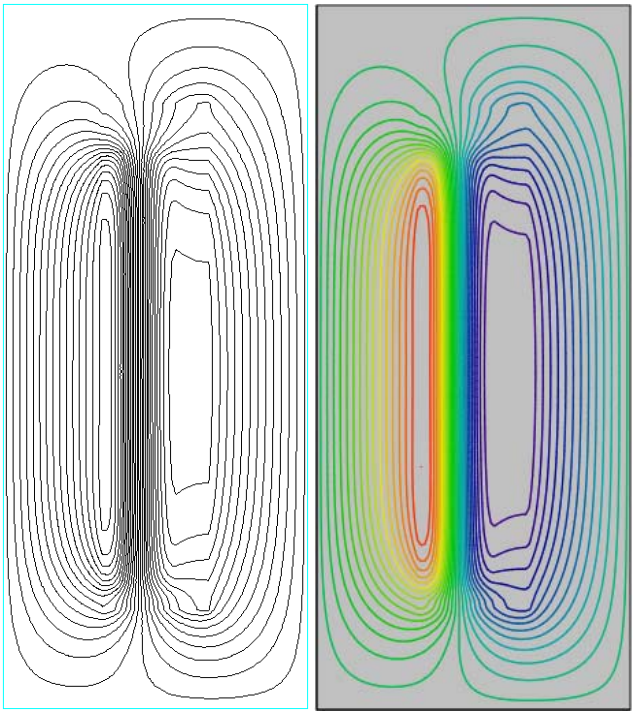

FIGURE-3.9 *Flux Lines – Open Circuit Condition FEA – Proposed Theory*

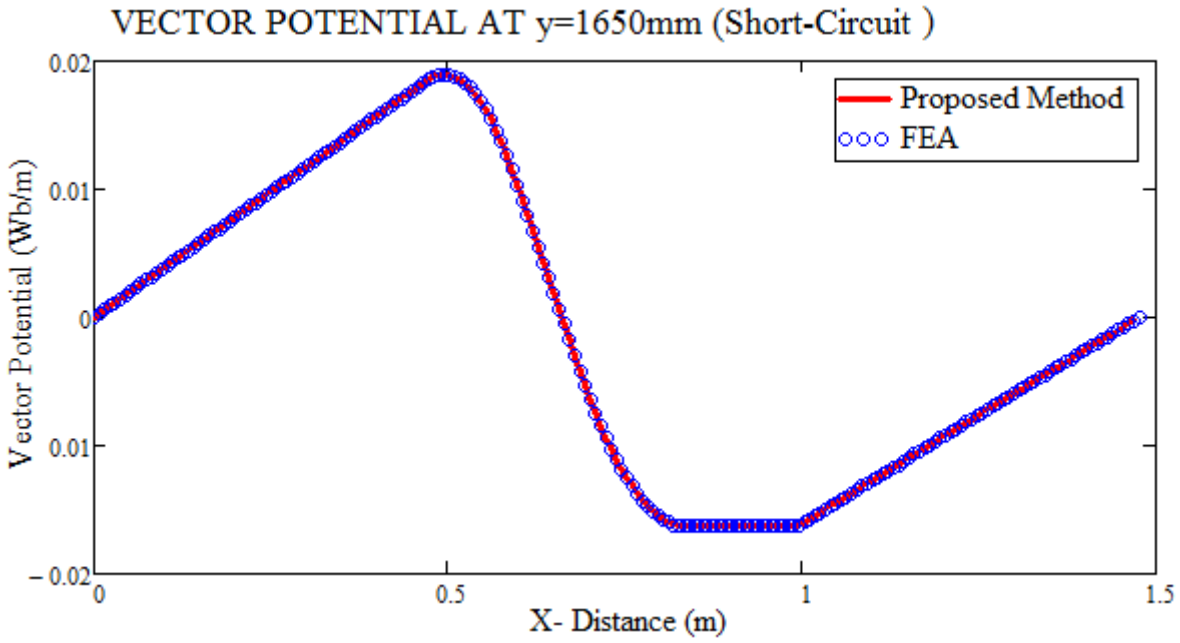

FIGURE-3.10 *Comparison of Vector Potential Values – Short Circuit Condition at y=1650mm*

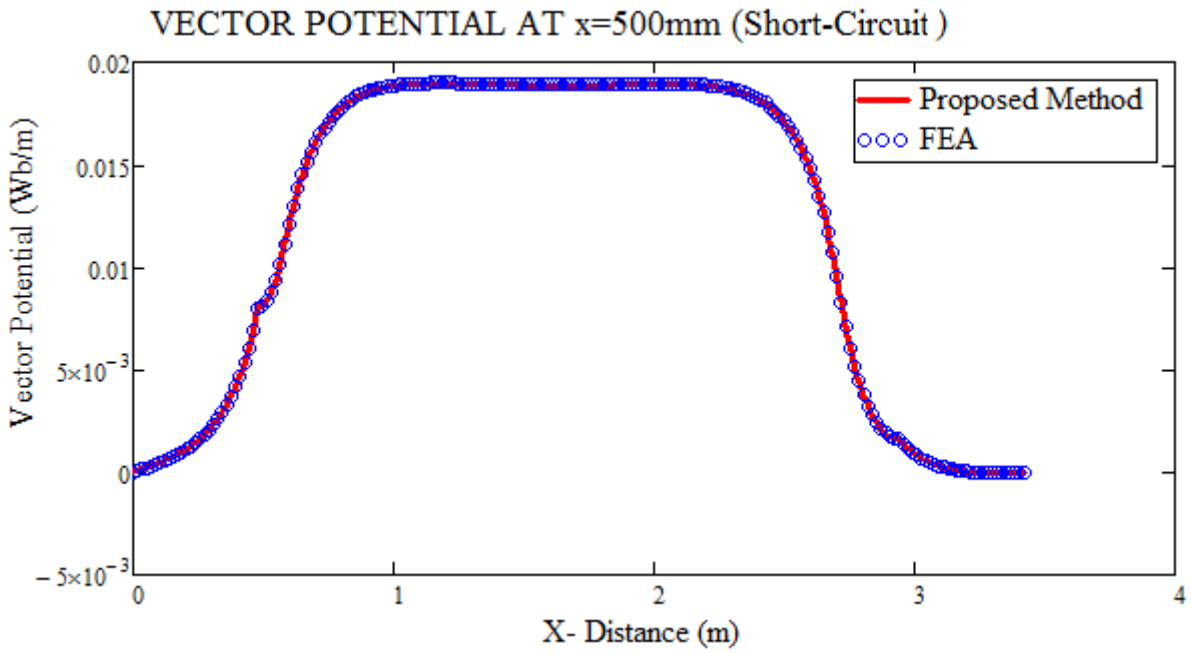

FIGURE-3.11 *Comparison of Vector Potential Values – Short Circuit Condition at x=500mm*

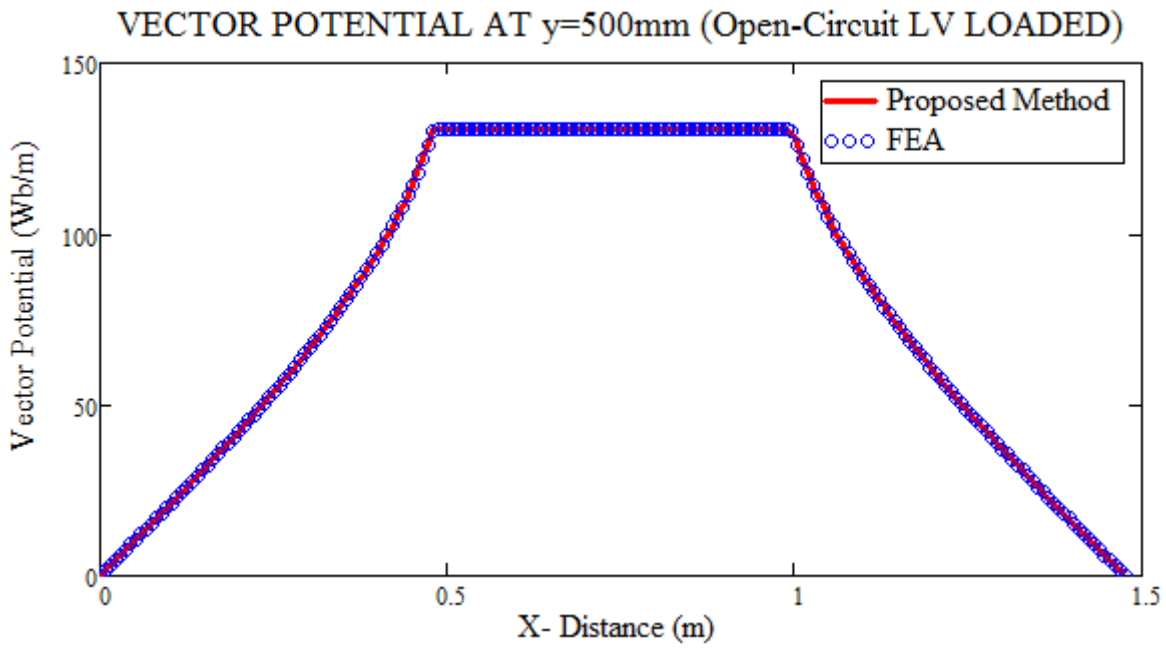

FIGURE-3.12 *Comparison of Vector Potential Values – Open Circuit Condition at y=500mm*

An analytical method is developed to calculate the magnetic properties of transformer taking finite permeability of the core into account and implementation of this on a PC is demonstrated. All the previous methods neglects the effects of the permeable core and as a result of this assumption, properties related to the open circuit condition cannot be determined with great accuracy and numerical methods have been used. Here, a full

mathematical solution to handle magnetic field problems with multiple regions using transform techniques and matrix operations is shown. Determining the constant and polynomial terms required satisfying boundary conditions, how to interpret them in series form and converting into matrix form are demonstrated. The method can also be very useful in cases where disc to disc or turn to turn mutual inductances are needed, for instance, lumped parameter model for transient voltage distribution because determination of the self and mutual inductances of the power transformers with the FEA can be quite complex as each turn or disc needs to be modelled and meshed. Most FEA software require the input parameters of a disc or a turn as a table before the inductance calculations and each turn or disc needs to be identified or flagged in the software. Then the FEA software needs to be run n+1 times, if the code provides a built-in macro like ANSYS LMATRIX, in order to determine the inductances where n represents number of turns or discs. The first run is necessary to determine short circuit properties. Moreover, if the developed method is inserted into a PC code, the magnetic properties can be determined during detailed design phase without further need for an FE analysis. Hence, the solution time can be reduced with the method introduced.

It seems difficult to employ the developed solution into a PC however, the matrix solution in Appendix-A gives all the Fourier constants needed and the constant and polynomial terms were given in Chapter-3.5. The solution strategy and formulas are lengthy however, once introduced in programming codes the solution can be obtained in several seconds. Especially, self and mutual inductance calculations can be performed in a short time using the method introduced. Magnetic properties of three and five limb three phase transformers can be calculated with the developed technique in the same sense of other methods, for instance Roth's or Rabins' methods.

The method calculates following properties of the power transformers.

- Magnetic Flux Density and Electromagnetic Forces
- Magnetic Energy
- Induced EMF
- Flux Linkage, Main flux and No-Load Current
- Self and Mutual Inductances

• Leakage Inductance and %Short Circuit Impedance

The method shows how to solve multiple connected permeable regions using the transform techniques. The effects of the permeability can be determined with the developed technique. In open circuit calculations, the flux is assumed to increase linearly within the core in x direction. This assumption can be valid for the regions close to the mid-plane of the core. The proposed solution shows that the flux does not increase linearly as shown in Figure-3.12, especially in the regions away from the mid-plane of the core.

3.9 Electromagnetic Force Calculations

Electromagnetic forces can be calculated using Lorentz Law. Current density J has only one component in the z direction and magnetic flux density has two components in the x and y directions. Performing the cross-product results;

$$JxB = \begin{bmatrix} i & j & k \\ 0 & 0 & J \\ B_x & B_y & 0 \end{bmatrix} = \left(-JB_y\right)i + (JB_x)j$$

Force has two components in the radial (x) and axial (y) directions. Magnetic flux density in the radial direction generates forces in axial direction and magnetic flux density in axial direction generates force component in radial direction.

Vector potential formulation contains the current density J. Force calculation also contains J and these two current density components are multiplied according to Lorentz Law and therefore, forces are proportional to square of current. This is an important outcome of the force calculations because it enforces the importance of the correct asymmetric current calculations. Force components are;

$$F_y = l_{mean} J \int B_x dxdy = l_{mean} J \int \frac{\partial A}{\partial y} dxdy$$

$$F_x = -l_{mean} J \int B_y dxdy = -l_{mean} J \int \frac{\partial A}{\partial x} dxdy$$

$$where\ dv = l_{mean} dxdy$$

The integration above can be performed over the cross-section of the winding to determine net bulk forces acting on that winding or can be performed turn-by-turn in axial direction to

determine the forces acting on each turn to study the distribution of the forces along the winding.

Axial force distribution along the winding can be complex and this is caused by several reasons. One of the most important reasons is due to the tapping arrangements that exist in modern transformers. If a transformer is designed with 380kV HV winding and 154kV LV winding, the requirement from that transformer is that it supplies 154kV from its LV side. However, transmission lines do not always carry the exact voltage level. To provide constant LV output, some turns on the HV winding are live and some not based on the voltage supplied from the transmission line. Ampere-turn balance on the other hand is kept constant for all cases. Tapping arrangement can be placed anywhere along the winding however, the position of the tapping can change the magnetic flux distribution and gives rise to more devastating axial forces. Some examples of tapping arrangement are shown in Figure-3.13.

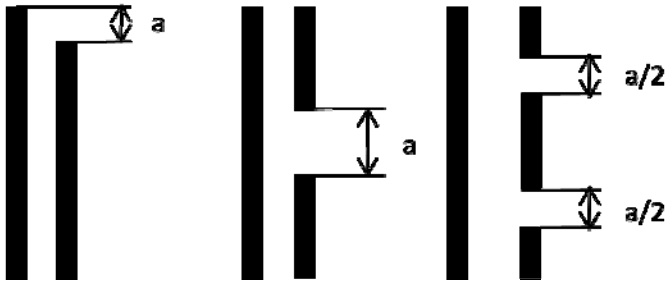

***FIGURE-3.13**: Some Tapping Arrangements on HV Winding*

Another imperfection increasing the axial forces is the misalignment of the windings with respect to mid plane. Magnetic centers of the windings are not aligned and this gives rise to axial forces. Billig [8] shown that misalignment of the windings increases the leakage inductance of the system and proved that short circuit forces always tend to increase the leakage inductance.

Turns of windings are separated by cellulose based insulation materials called spacers. During short circuit, these materials are under compressive forces and can fail based on the magnitude of the force acting on them. To find the magnitude of the electromagnetic forces acting on these materials, magnitude and direction of the forces need to be determined. Let a turn denoted as K to be placed somewhere close to middle of the winding. A turn of a

winding can push its neighbor but cannot pull it. If, as a result of magnetic field and current, a force exerted on K is directed upward this force will be transmitted through the winding and will contribute to compression on any upper turn. If it is directed downwards, K has no effect on the contribution on the upper part. However, the force exerted on K directed downwards and a force with higher magnitude exerted to K from the turns located downwards, the total vector sum of the forces contribute the compression on upper turns. In order to find the exact distribution, axial force density F(y) should be determined first. Force density can be found from the below formula.

$$F(y) = \frac{dF_y}{dy}$$

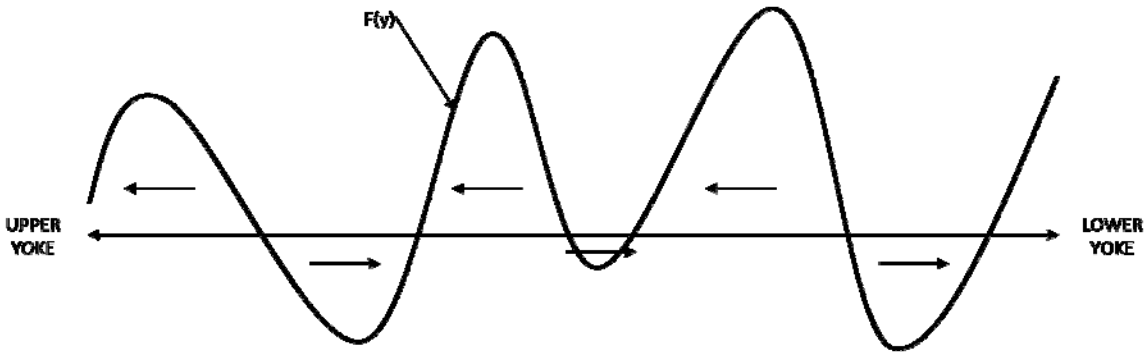

***FIGURE-3.14**: Force Density Distribution through the Winding Height*

Figure-3.14 shows a distribution of force density of a winding. Points intersecting the zero line are the points where the force density is zero. Integrating the force density function between each point, those intersect the zero line, gives the basic thrusts and since the direction is known, the problem is now reduced to simply addition/subtraction.

This procedure is very important because it also enables one to calculate the correct magnitude of the forces acting on upper clamping ring because one of the objectives of this research is to investigate the effect of delamination on the upper clamping ring. Moreover, the correct magnitude of forces and their direction acting on spacers is now determined because this is also one of the failure modes of a power transformer under short circuit forces.

If no electromagnetic thrust is exerted on a point in a winding, this point is called a point of separation. It was shown by Vein [11] that there is at least one point of separation in each

winding including the end points. If a transformer has LV and HV windings equal in height, the ampere-turns are balanced and uniformly distributed, and windings are symmetric in window with respect to the mid-plane, the points of separation are the upper and lower end points. Figure-3.15 shows the force density distribution of such a winding where the cumulative forces acting from the upper and the lower sections of the winding are equal in magnitude and opposite in sign. Net force exerted to upper or lower clamping rings are zero and both ends are the points of separation.

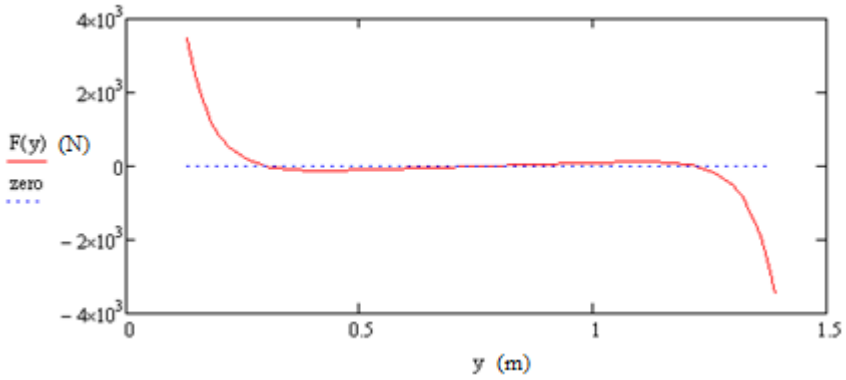

***FIGURE-3.15**: Force Density Distribution of an Example Winding*

When basic thrusts are calculated according to the procedure explained above, it can be found that the upper and lower end points are the points of separation for this winding configuration.

Figure-3.15 also gives the electromagnetic forces acting on each turn of the winding. It can be seen from Figure-3.15 that forces are larger at end turns of the winding but in opposite direction and the magnitude of the forces are decreasing and reaches a value of zero at the middle turn. However, cumulative forces are maximum at the middle and largest compression forces are acting the spacers located at the mid of winding.

This procedure will be used when modeling a dynamic short circuit forces on a transformer throughout the research.

In reality, transformer windings are pre-stressed through the upper clamping ring to withstand short circuit forces during manufacturing phase. The above procedure does not include the effect of the pre-stress but the pre-stress effect can be superimposed on to

above calculated forces. This is a normal and reasonable procedure because, in order to calculate the magnitude of the pre-stress, electromagnetic forces need to be determined.

3.10 Dynamic Electromagnetic Force Calculations

Windings cannot move in large magnitudes during short circuit. If they do, this will give rise to leakage inductance and eventually to magnetic flux density and much higher short circuit forces. Failure is obvious in this case. Therefore, it is reasonable to assume small displacements in the windings which will enable an important assumption for dynamic short circuit calculations. If the displacements are small enough to neglect the change in magnetic flux density during dynamic short circuit, magnetic flux density can be assumed constant at each point of the winding. Moreover, according to International Electrotechnical Commission (IEC) [43], the change in inductance before and after successful short circuit test should not exceed 1%. Because inductance is a parameter of dimensions only, very little winding displacement is allowed.

It was shown in the previous chapters that dynamic short circuit forces are proportional to square of the short circuit current. Therefore, with the assumption of constant magnetic flux density, short circuit force diagram, directions and magnitudes can be easily drawn. Using the simplified asymmetric short circuit current equation (3.9), dynamic short circuit force acting on each turn is drawn and shown in Figure-3.16.

Using the Roth's method to calculate direction, magnitude of forces and magnetic flux density, dynamic electromagnetic forces acting on each turn can be determined. Square of the short circuit current is given below. Force has two unidirectional components. One constant and one is decreasing exponentially with time. Two alternating components are of fundamental frequency decreasing exponentially with time and double frequency with smaller amplitude. There is a possibility of resonance if the windings, together with upper and lower clamping rings, have a natural frequency closer to these frequencies.

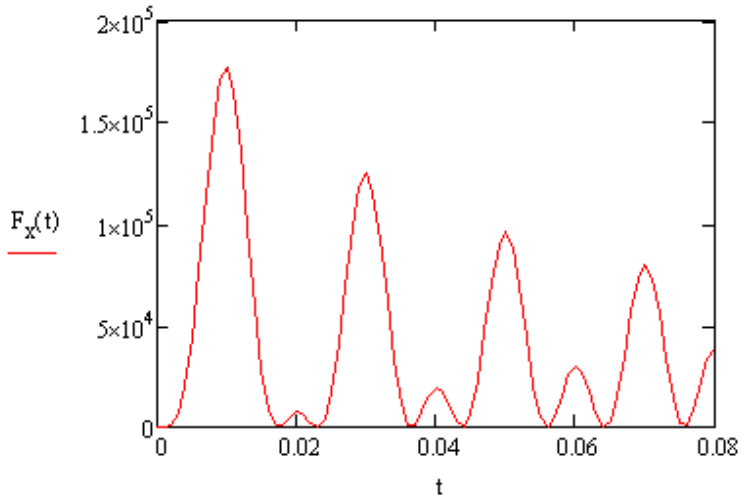

***FIGURE-3.16**: Dynamic Short Circuit Forces Acting on Turn of a Transformer Winding*

$$I(t)^2 = 2\mathrm{I_{pss}}^2\left[\frac{1}{2} + e^{-2\frac{R}{L}t} - 2e^{-\frac{R}{L}t}\cos wt + \frac{1}{2}\cos 2wt\right]$$

To model mechanical dynamic response of each turn, magnetic flux density acting on that turn should be calculated. Because the current passing through the turns is the same, calculated magnetic flux density on that turn can be multiplied by the above formula. This is very simple method to calculate dynamic electromagnetic exciting forces acting on that turn. Final equation can be written as below.

$$F_{Dynamic} = B_{turn}I(t)^2$$

3.11 Inductance, Reactance and Magnetic Energy Calculations

Steady state peak current calculations require calculating leakage reactance of the system. Leakage reactance is related to leakage inductance and leakage inductance of the winding can be calculated from magnetic energy of the system. Magnetic energy of the system is calculated from the below equation.

$$W = \frac{1}{2}\int HBdv$$

The relation between the magnetic energy and self and mutual inductances is for a linear system is;

$$W = \frac{1}{2}\sum_{i} L_i {I_i}^2 + \sum_{i<j} M_{ij} I_i I_j$$

And leakage inductance referring primary winding can be found by;

$$L_{leakage} = \frac{2W}{{I_1}^2} \; and \; Leakage \; Reactance \; X_{leakage} = 2\pi f L_{leakage}$$

Self and mutual inductances of the system can also be found using vector potential solution. To calculate the self inductance of a winding, other windings are assumed to be short circuited and vector potential is calculated only for that winding. Mutual inductance can be calculated from the difference between total inductance of that winding when all the windings are active and self inductance of that winding.

3.12 Electromagnetic Finite Elements Solutions

Low frequency electromagnetic finite elements solutions can be divided in to 3 main categories. These are;

- Static magnetic analysis
- Harmonic analysis
- Transient analysis

Static magnetic analysis is suitable for time-independent magnetic solutions. Solution is obtained by solving Ampere's Law. Solution in terms of magnetic vector potential or scalar potential is obtained and magnetic properties, such as magnetic flux density, magnetic field intensity, are obtained from magnetic vector potential. Loads are applied as current density and in ANSYS software, conductors or the components where electromagnetic cumulative force magnitudes are needed, should be flagged. In 2-D applications, the vector potential has only one component in z axis or circumferential axis because current density has one component in 2-D applications. Material properties of ferromagnetic core can be entered as constant or B-H curve data.

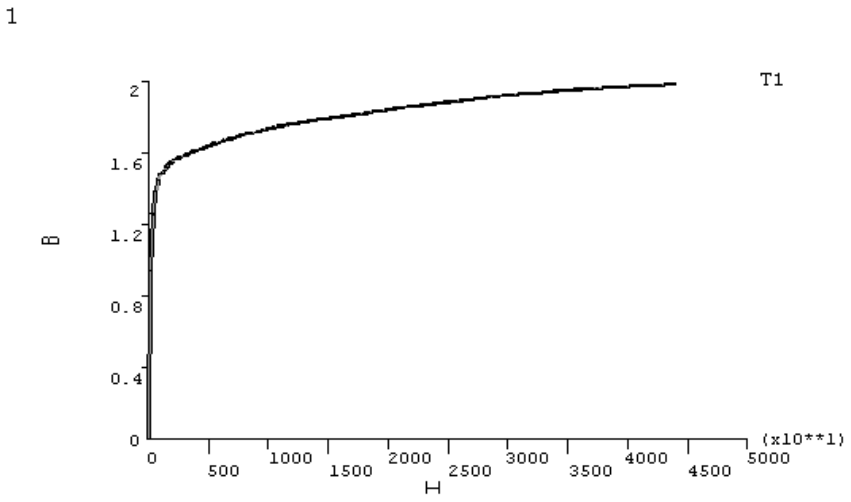

***FIGURE-3.17**: Typical B-H curve for FEA Analysis from ANSYS Documentation*

There are two types of boundary conditions in 2-D analysis. These are Drichlet and Neumann boundary conditions. Drichlet boundary condition assumes that the flux lines are parallel to the boundary whereas Neumann boundary conditions assume flux lines are perpendicular to the boundary.

Harmonic solutions take induced currents into consideration because of changing magnetic field caused by sinusoidal exciting current. Two options are available for conductor modelling, stranded or massive conductor. Stranded conductors are formed by many wires and the wires are insulated between them in order to eliminate the effect of eddy currents. Massive conductors, on the other hand, are suitable to model the effect of eddy currents. These conductors can be current fed or voltage fed. Harmonic analysis gives results in terms of real and imaginary solutions because sinusoidal loading can be represented in complex coordinates and this is how electromagnetic FEA packages handle harmonic problems.

Windings can be connected to circuit elements such as resistor, inductor, stranded coil, and the winding can be loaded through these elements. ANSYS provides a circuit element, stranded coil, where the properties of the winding is entered and assigned to this element and the solution for winding is obtained. Dynamic short circuit forces can be calculated this way by assigning short circuited circuit element to secondary side and applying the voltage through circuit elements to primary side.

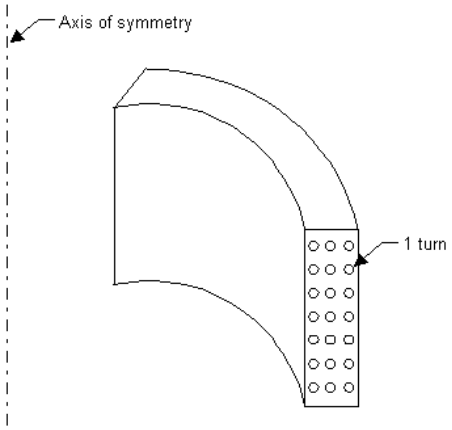

***FIGURE-3.18**: Cross-section of Stranded Coil, from ANSYS Documentation*

For 3-D analysis, vector potential and current density loading is more complex than 2-D analysis because these vector quantities can have values in different coordinates.

3.13 Conclusions

Correct determination of the short circuit forces requires the correct determination of the short circuit currents as the electromagnetic forces are proportional to the square of the short circuit currents. In this thesis, only the three-phase to ground short circuit case is considered as this case usually generates the highest short circuit currents. Autotransformers or YNynd connected three-phase, three winding transformers might generate higher short circuit currents in the single phase to ground fault conditions and the magnitude of the short circuit fault currents can be determined as explained in [55].

Many methods are developed to calculate the short circuit forces acting on transformer windings during the fault conditions. Image method, Rabins' method or Roth's method are the widely used ones. All these methods share a common assumption, the ferromagnetic core is infinitely permeable and as a result of this assumption, flux enters the core at right angles due to the magnetic continuity conditions. All these developed methods calculate the magnetic properties related to the short circuit condition with reasonable accuracy however, they fail to give reasonable results in the open circuit condition. A method developed in Chapter-3.7 to calculate both the open and the short circuit properties of the power transformers. Roth's method is used to calculate the Poissons' field in the solution because of its simplicity. Extension of Roth's method when a highly permeable region is

connected to the Poisson's region is given. The ferromagnetic core can take any permeability value and the assumption of infinitely permeable core is suppressed and as a result, the properties related to the short circuit condition can be calculated with greater accuracy compared to the methods developed earlier. The method can also calculate the properties related to the open circuit condition and especially turn to turn or disc to disc self and mutual inductances can be determined. The developed method was compared to the FEA and near to perfect agreement was shown. Advantages of using the method rather than FEA were discussed. The solution also shows how to treat multiply connected highly permeable regions with flux normal boundary conditions, the choice of the polynomial and the constant terms. This case is the most difficult case because of the choice of the boundary conditions.

Calculation of the electromagnetic forces and the concept of the force density function are given. The difference between the cumulative forces and the end forces are introduced and the calculation methods using the force density function are given. Dynamic electromagnetic force calculations are given using the dynamic short circuit current calculated in Chapter-3.2. Inductance, reactance and magnetic energy calculations are given briefly.

Accurate determination of the mechanical stresses acting on the power transformer components requires the accurate determination of the electromagnetic forces in the radial and the axial directions. In this chapter, a new and more accurate solution strategy is developed to calculate the electromagnetic forces acting on the power transformer components.

4-STRUCTURAL INTEGRITY OF TRANSFORMER ACTIVE PART

4.1 Introduction

The complexity of electromagnetic force calculations was discussed and a new method to calculate properties related to magnetic field of power transformers was introduced in the previous chapter. Although the exerted forces are a result of short circuit currents, integrity of the transformer windings depends on the materials used and the geometry of the transformer windings. The active part contains ferromagnetic core material, windings and insulation materials and short circuit forces are acting on these elements.

In power transformer technology, the materials used are determined based on their electrical properties. Electrical conductivity, dielectric constant and electrical breakdown strength are the major concerns when designing the active part of the transformer and this is the major restriction from mechanical point of view in terms of materials used in the active part. In power transformers, copper is the conductive metal used [36]. The dimensions of the copper are determined by the current density and the load losses. In order to reduce the eddy currents on the copper conductor, the thickness of the conductors is chosen to be small or the conductor is divided into a number of smaller conductors. The first method cannot always be employed because the axial length of the winding can become longer, which will eventually affect the short circuit impedance as the area of the conductor is determined by the current density. In the second method, the conductors are insulated from each other by covering the surfaces with enamel. The conductors are also transposed continuously to eliminate the occurrence of circulating current. To prevent the electrical discharge during transient lightning impact, the conductors are covered with several layers of insulation papers. This type of conductor is called Continuously Transposed Cable or CTC. There may be more than one layer of CTC in radial and axial directions in order to achieve the desired current density value. Figure-4.1 shows a typical CTC conductor used in transformer windings.

Insulation materials are natural cellulose based materials due to their perfect electrical properties. Two types of insulation materials are used namely, transformerboard and laminated wood. In order to achieve better mechanical performance, the density of the insulation material is increased by pressing the material through the thickness direction for

laminated wood or by increasing the fiber density for transformerboard. Elasticity modulus of 15GPa can be achieved by such an operation. More information regarding the mechanical properties of insulation materials and their manufacturing technology will be given in the next chapters.

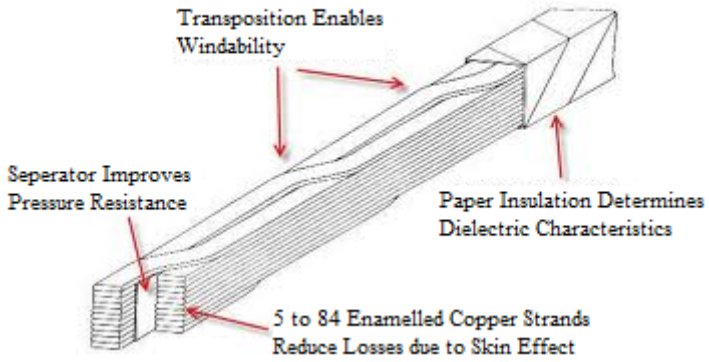

***FIGURE-4.1**: Continuously Transposed Cable*

Electromagnetic forces are dynamic forces and the resulting mechanical effects should be treated from a dynamics point of view. However, this is computationally expensive and to determine the real damping constants for a particular transformer is a challenging task. Electromagnetic forces can be treated statically. This can be achieved by determining the maximum force acting on the system. Maximum electromagnetic forces are acting when the short circuit currents reach their maximum value. Figure-4.2 shows the typical short circuit current and the short circuit forces acting on the system. Static force calculations will be performed considering the peak value of the dynamic electromagnetic forces, the calculation method to find the peak electromagnetic force was shown in the previous chapter.

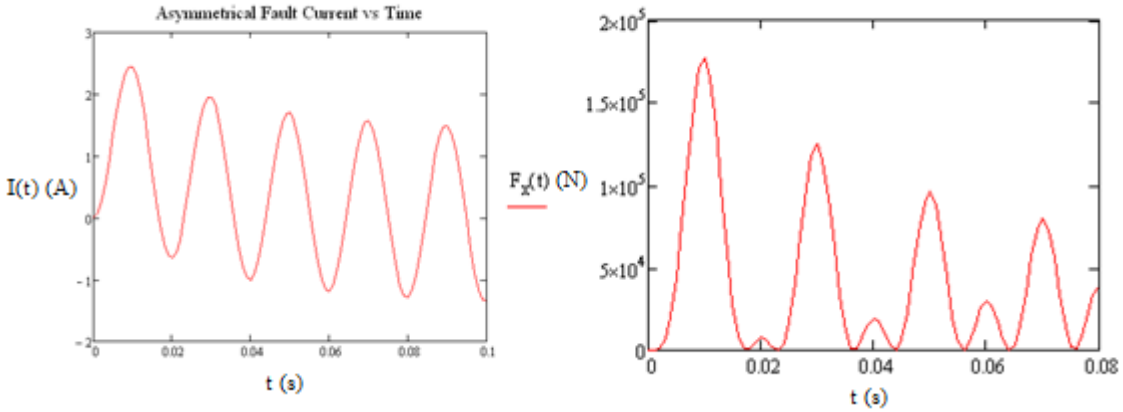

***FIGURE-4.2**: Short Circuit Current and Dynamic Short Circuit Force Respectively*

4.2 Radial and Axial Electromagnetic Forces

Electromagnetic forces are divided into two components, namely, radial and axial components and the failure mechanisms in radial and axial directions differ from each other. Low voltage (LV) and high voltage (HV) windings repel each other in both radial and axial directions under short circuit conditions because the current flows in opposite directions whereas turns of a winding attracts each other in axial direction. Figure-4.3 shows one limb of a three phase transformer and the direction of the radial forces generated by short circuit condition. The inner winding (LV) is forced to collapse and hoop stress is stretching the outer (HV) winding. The distribution of radial forces along the winding is shown in Figure-4.4a. At the top and bottom parts of the winding, the magnitude of the radial forces is smaller than the middle section of the winding because the flux fringes at the top and the bottom. Therefore, the stress calculations should be performed based on the maximum radial force in radial direction because the forces are acting on each turn and the stability or maximum stresses generated differ at every turn. The magnitude of the radial forces acting at a turn of the winding can be found using the theory developed and the mechanical stresses can be determined.

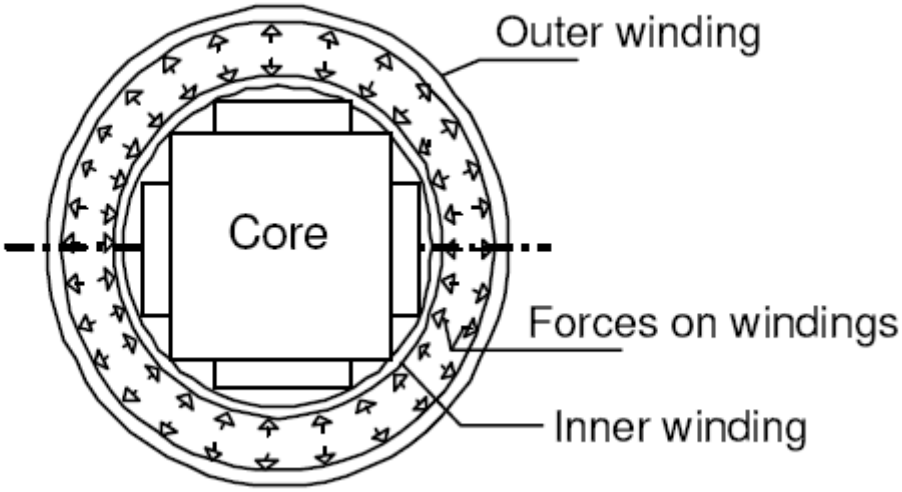

***FIGURE-4.3**: Electromagnetic Forces Acting on Outer and Inner Windings*

In the axial direction, the distribution of forces is much more complicated due to several reasons. Complexity is caused by misalignment of magnetic centres of LV and HV windings in the axial direction, tapping arrangements and differences in the lengths of the windings. Therefore, axial force distribution changes for different configurations. In [12], axial force

distributions for several interesting cases are shown. Also, the method proposed in Chapter 3 can be used to plot these distributions. Figure-4.4.b shows a case where the HV winding is shorter than the LV winding and the distribution of axial forces along the winding is shown. For this particular case, axial forces reach a maximum at the top and the bottom ends and the magnitude decreases towards to mid section of the winding, where the magnetic centre of the winding is. At some points, no electromagnetic axial forces are acting because the directions of axial forces along the winding change their sign.

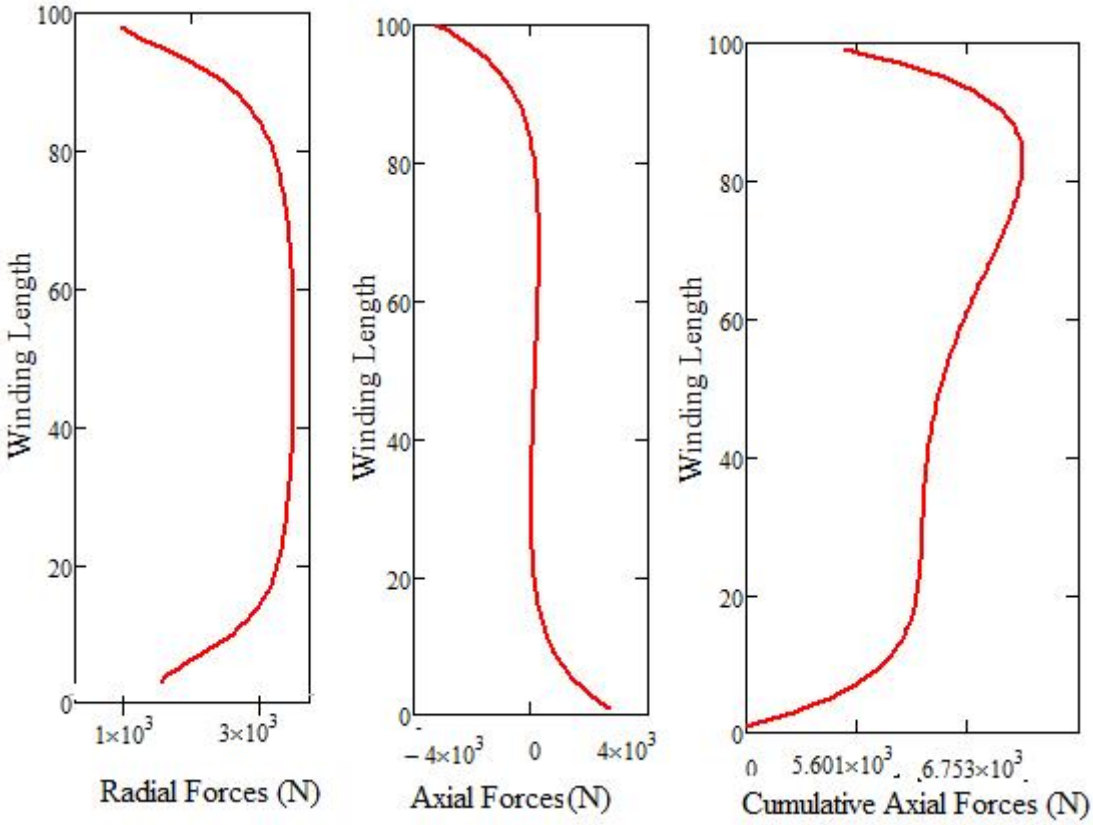

***FIGURE-4.4**: Distribution of Electromagnetic Forces along the Winding **a)** Radial Forces **b)** Axial Forces **c)** Cumulative Axial Forces*

Axial forces are acting at every turn and based on the direction of the forces, their cumulative effect varies through the winding and gives rise to compressive forces. Figure-4.5 shows the directions of the axial forces acting at every turn of a winding comprises of 5 turns and the method to calculate the compressive forces. In Figure-4.4.c distribution of the compressive forces along the winding is shown and it can be concluded that the position of the maximum compressive forces are different than the electromagnetic forces exerted by the short circuit current.

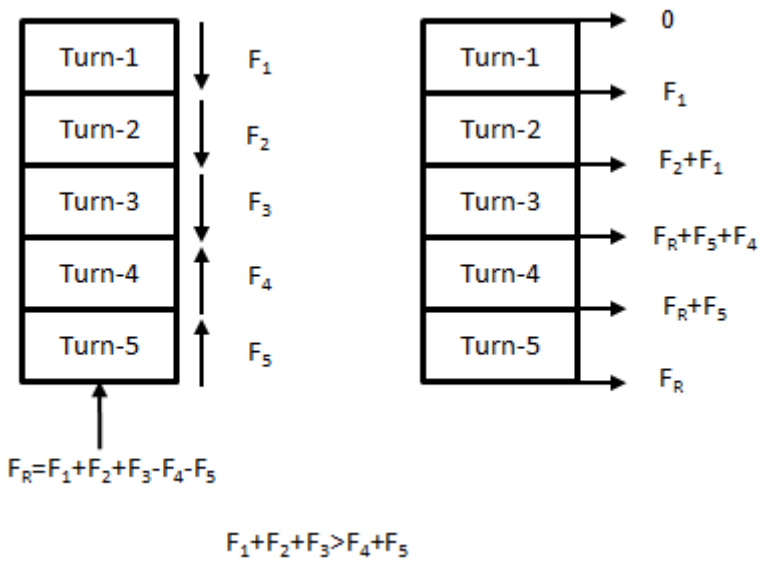

***FIGURE-4.5**: Example of Electromagnetic Axial Forces Acting on a Winding Consists of 5 Turns and Their Cumulative Effect*

Windings can be wound using several techniques according to their lightning voltage withstand level or cooling capacity. Based on the technology used, electromagnetic force and stress calculations should be performed according to winding's geometry. Layer winding configuration is shown in Figure-4.6 as an example.

In layer windings, the conductors are wound on each other in axial directions without a gap and in order to increase the windings cooling capacity and to prevent the electrical discharge between neighbouring layers, a gap is required in radial direction. Every layer should be treated as a separate winding where the current flows in the same direction with an ampere-turns of 1/(layer number) of the total ampere-turns. The geometrical position of the layers within a slot should be considered taking the gaps between the layers into account. This is necessary as the main flux, which generates electromagnetic forces, reaches their maximum values between the low and high voltage windings. Therefore, inner layer of outer winding and outer layer of inner winding experiences higher radial forces than other layers. Stress calculations should be performed at these layers in order to calculate the stresses accurately. If the winding is treated as an entity, without dividing it into layers, the calculated forces will be average forces and the calculated stresses will be lower. It can be concluded that if there are axial or radial gaps in the winding, these gaps should be considered and the winding should be separated into layers or discs in order to increase the accuracy of the force and stress calculations.

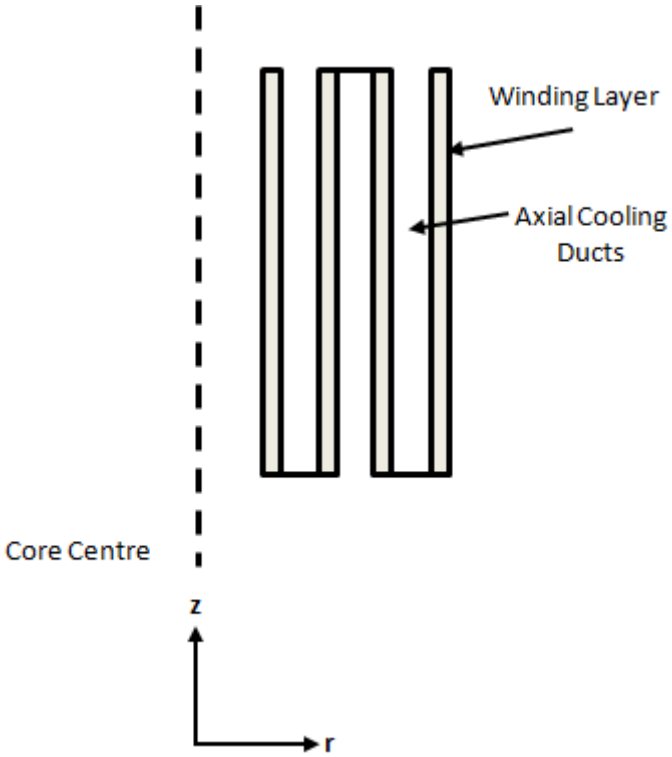

***FIGURE-4.6**: Layer Winding Configuration*

4.3 Radial Failure Modes and the Integrity of the Windings

Radial electromagnetic forces are stretching the outer winding according to Figure-4.3. Outer winding can be modelled as a cylinder subjected to internal pressure and as a result, the stresses generated are hoop stresses. Thickness to radius ratio of power transformers are very small and the thin cylinder assumption is suitable which provides further simplifications when calculating the stresses generated by electromagnetic forces. The stresses should be calculated for a turn, along the winding, where maximum radial electromagnetic forces are acting and the magnitude of these forces can be calculated using the theory developed in Chapter-3. The hoop stress is then;

$$\sigma_{Hoop,i,L} = \frac{F_{R,i,L}R}{2\pi t}, \quad \sigma_{Hoop,max} = \max_{i,L}(\sigma_{Hoop,i,L})$$

Here, $F_{R,i,L}$ is the radial applied electromagnetic forces on i'th turn of L'th layer calculated using the theory developed in Chapter-3, R is the mean radius of the outer winding and t is the thickness of the winding. If magnet wires are used, t can be found using below formula.

$$t = n_{rad} * t_{strand} * n_{cabRad}$$

If CTC's are used

$$t = \frac{n_T - 1}{2} * t_{strand} * n_{cabRad}$$

where n_{rad} is the number of strands in a cable in radial direction, t_{strand} is the thickness of the strand in a cable, n_T is the total number of strands in a CTC bundle and n_{cabRad} is the number of cables in radial direction. The number of strands in a CTC bundle is always an odd number and the cross section of CTC bundle is shown in Figure-4.7. In above formulation, the outer strand is neglected in calculations.

***FIGURE-4.7**: CTC Cross-Section*

Maximum hoop stress can be used to determine the proof stress of the outer winding's conductor. Winding comprises of insulation paper and conductor copper and the dimensions of the copper should be taken into account when calculating the hoop stresses because the load carrying capacity of the insulating paper is very small compared to copper.

Transformer windings are supported by axial sticks made of cellulose based insulation materials as shown in Figure-4.8. Axial sticks are used to prevent buckling of the inner windings in radial direction and acts as a support to prevent excessive bending in radial direction. The failure modes of inner windings are the free buckling of the winding, the forced buckling of the winding and the yielding as a result of radial bending stresses. Free buckling assumes that the supports are soft and negligible whereas forced buckling considers the effect of the axial sticks. The turn at which the maximum radial compressive forces are acting should be selected for calculations. Forced buckling can be used to calculate the minimum number of axial sticks according to formula by [37] where R is the mean radius of the winding.

$$N_{Stick} = R \sqrt{\frac{\sigma_{Hoop,i,L}}{E \frac{{n_{rad}}^3 {t_{strand}}^2}{12}}}$$

For CTC and magnet wires, n_{rad} should be selected as 1 because the strands can slide over each other and the buckling strength is determined by the strength of a single strand. In order to increase the buckling resistance of the CTC, strands can be bonded to their neighbouring strands using epoxy. This type of CTC is called epoxy bonded CTC and n_{rad} for this type can be selected as;

$$n_{rad} = \frac{n_T - 1}{2}$$

Epoxy bonded CTC bonds all the strands in the bundle and as a result, the entire strands act as an entity and the buckling strength is determined by the strength of all the strands in radial direction. Therefore, to prevent buckling of inner winding either the number of sticks needs to be increased or epoxy bonded CTC can be used.

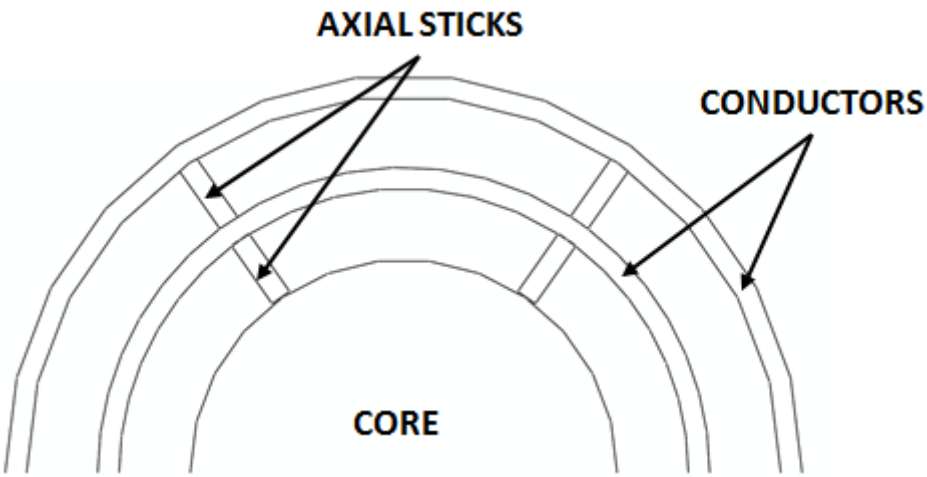

***FIGURE-4.8**: Position of Axial Sticks*

4.3.1 Radial Bending

Axial sticks are used to prevent buckling phenomenon and bending of conductor in the radial direction. Bending in radial direction resembles the bending of an arch subjected to uniform loading. If epoxy bonded CTC is used, shear force acting at the cross-section will generate an interlaminar shear stress between the strands. When the critical stress level is reached, the epoxy between the strands will break resulting a decrease in buckling strength and will give rise to radial bending stresses. Therefore, a theory is needed to calculate shear stresses acting between the strands.

In [38], normal and bending stresses acting along the arch subjected to uniform loading is given however, the effects of shear stresses was not given. An extension of the method developed by [38] is given below.

Figure-4.9 shows the portion and the free body diagram of the arch that will be analyzed. Due to symmetry, half the length of the conductor between two axial sticks is depicted. X is the reaction force in radial direction, R is the mean radius of the winding, q is the radial electromagnetic forces, N_0 and M_0 are the normal force in tangential direction and bending moment respectively. No shear force is acting and the amount of rotation is zero at the left and right ends due to symmetry.

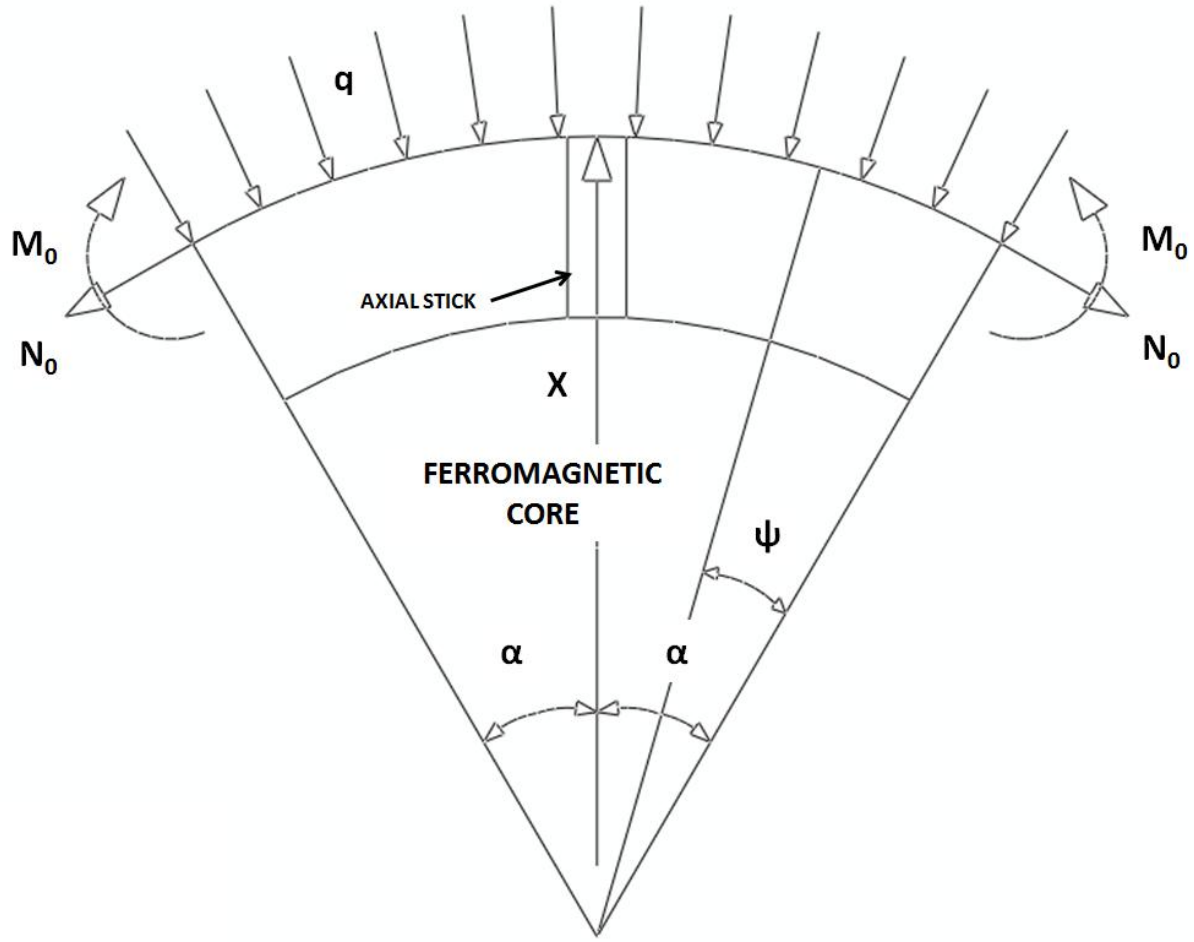

***FIGURE-4.9**: Free Body Diagram of Inner Winding*

This problem is statically indeterminate and Castigliano's Theorem will be used to determine the unknown reaction forces. Balancing the forces in vertical direction,

$$N_0 = \frac{X}{2Sin(\alpha)} - qR \qquad (4.1)$$

At any cross section ψ, bending moment acting at that cross section can be found using static equilibrium requirements as shown in Figure-4.10. Taking the moment of the system shown in Figure-4.10;

$$M(\psi) = M_0 - N_0 R[1 - Cos(\psi)] - \int_0^{\psi} qR^2 Sin(\psi - \psi')d\psi'$$

Performing the integral and substituting (4.1) yields,

$$M(\psi) = M_0 + \frac{XR}{2Sin(\alpha)}[Cos(\psi) - 1] \qquad (4.2)$$

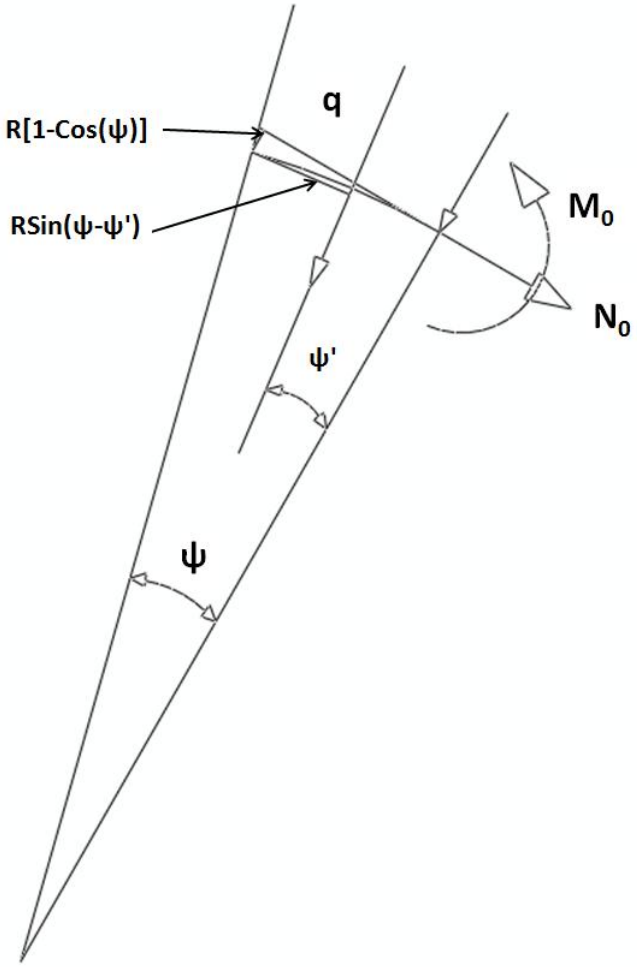

***FIGURE-4.10**: Distances to Consider for Moment Relations*

Static equilibrium of normal forces yields,

$$N(\psi) = N_0 Cos(\psi) - \int_0^{\psi} qRSin(\psi - \psi')d\psi'$$

Performing the integral and substituting (4.1) yields,

$$N(\psi) = \frac{XCos(\psi)}{2Sin(\alpha)} - qR \qquad (4.3)$$

Static equilibrium in radial direction yields,

$$\tau(\psi) = N_0 Sin(\psi) + \int_0^{\psi} qRCos(\psi - \psi')d\psi'$$

Performing the integral and substituting (4.1) yields,

$$\tau(\psi) = \frac{XSin(\psi)}{2Sin(\alpha)} \qquad (4.4)$$

Reaction forces X and M_0 will be found using Castigliano's Theorem. Total strain energy of the system is;

$$U_T = U_B + U_N + U_S + U_{ST}$$

U_B is the strain energy due to bending, U_N is the strain energy due to normal forces, U_S is the strain energy due to shear forces and U_{ST} is the strain energy in the axial sticks.

$$U_T = 2\int_0^{\alpha} \frac{M^2 R d\psi}{2EI} + 2\int_0^{\alpha} \frac{N^2 R d\psi}{2EA} + 2\int_0^{\alpha} \beta \frac{\tau^2 R d\psi}{2AG} + \frac{X^2 L}{2A_{ST}E_{ST}}$$

Here β is the factor for maximum shear forces and depends on the geometry and cross-sectional properties of the conductor. For CTC β can be taken between 1.15...1.2. A_{ST} and E_{ST} are the area and elasticity modulus of the axial stick. Because the ends do not rotate, due to symmetry, derivative of the total strain energy with respect to M_0 is zero and at the fixed end, the displacement of the axial stick is zero.

$$\frac{\partial U_T}{\partial M_0} = 0 \; and \; \frac{\partial U_T}{\partial X} = 0$$

$$M_0 = \frac{XR}{2}\left(\frac{1}{Sin(\alpha)} - \frac{1}{\alpha}\right) \quad (4.5)$$

$$X = \frac{qR}{f_1(\alpha) + \frac{AR^2}{I}\left[f_1(\alpha) - \frac{1}{2\alpha}\right] + \frac{AE}{A_{ST}E_{ST}} + \frac{E\beta}{4GSin(\alpha)^2}\left(\alpha - \frac{1}{2}Sin(2\alpha)\right)} \quad (4.6)$$

$$f_1(\alpha) = \frac{1}{4Sin(\alpha)^2}\left(\alpha + \frac{Sin(2\alpha)}{2}\right) \quad (4.7)$$

The last term in the denominator of equation (4.6) is due to shear force and the addition of shearing effect to radial bending of transformer winding conductor is found. In these calculations, centroidal axis and neutral axis is assumed to coincide for rectangular cross section as the radius to thickness ratio is large for power transformers and this assumption can be applied with great accuracy.

All stress components reach their maximum values at the axial support. Bending and normal stresses can be added to find maximum normal stress acting to the system. Normal stress is always negative because of the compressive forces. On the other hand, bending stresses can reach their maximum values at the top and bottom fibers. When finding maximum normal stresses acting at the support, bending stress should be selected so that the total stress is maximized.

$$\sigma_{N,Max} = Max\left[\left(\frac{M(\alpha)\frac{h}{2}}{I} + \frac{N(\alpha)}{A}\right), \left(-\frac{M(\alpha)\frac{h}{2}}{I} + \frac{N(\alpha)}{A}\right)\right]$$

Shear stress is then can be calculated by;

$$\tau_{max} = \frac{\tau(\alpha)}{2I}\left(\frac{h^2}{4} - y^2\right)$$

$$I = \frac{2h_{strand}\left[\left(\frac{n_T - 1}{2}t_{strand}\right)^3\right]}{12}, h = \frac{n_T - 1}{2}t_{strand}$$

CTC's always possess odd number of conductors as shown in Figure-4.7. Shear stress distribution is parabolic and reaches its maximum value at the middle. However, the shear stress value required is not at the mid-plane due to geometrical shape of the CTC. It can reasonably be assumed that the distance between neutral axis and required plane is ¼ of thickness of the strand. Therefore,

$$\tau_{max} = \frac{3\tau(\alpha)}{4h_{strand}t_{strand}\left(\frac{n_T - 1}{2}\right)^3}[(n_T - 1)^2 - 0.25] \quad (4.8)$$

A theoretical formula is developed to calculate shear stress distribution and maximum shear stress acting in the epoxy bonded CTC. Normal and bending stresses are corrected by adding the effect of shearing forces.

4.4 Axial Failure Modes and the Integrity of the Windings

The failure modes due to axial short circuit forces are the tilting of the conductors, stresses on the tie-bars, compressive forces on the radial spacers, axial bending of the conductor between two radial spacers and bending of clamping ring. Figure-1.1 shows the application of radial spacers in high voltage winding technology.

Axial bending of the conductor between two radial spacers can be treated as a beam with clamped boundary conditions at both ends and subjected to uniform loading due to axial electromagnetic forces. Every turn of the transformer winding should be modelled. The maximum value of the calculated axial electromagnetic force acting on the turns has to be considered in the calculations. Figure-4.11 shows statically indeterminate axial bending of the conductor. This system can easily be solved and maximum bending stress can be found. Moment of resistance for CTC and epoxy bonded CTC is;

$$I = \frac{n_{cabRad}\left(\frac{n_T - 1}{2}\right) t_{strand} 2 n_{cabAx} (h_{strand})^3}{12}$$

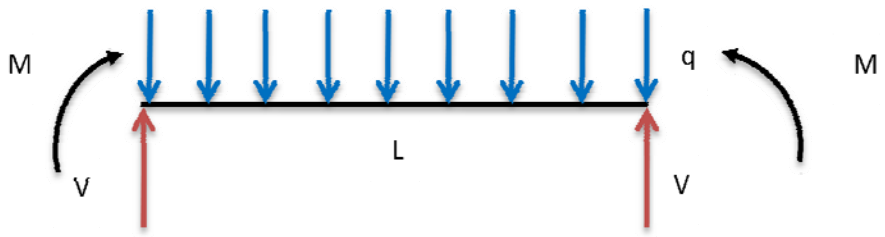

***FIGURE-4.11**: Axial Bending of Conductor between two Radial Spacers*

Compressive stresses on radial spacers and tilting of conductors should be calculated using the cumulative axial forces as shown in Figure-4.4.c. If CTC is epoxy bonded, tilting strength of the conductor is very high and can be neglected. Detailed information on tilting of conductors can be found in [1], [39] and [40].

In order to calculate the stresses in the tie-bars and clamping rings, net axial short circuit forces needs to be considered. This can be achieved by obtaining the force density function along the winding as described in Chapter-3 and summing the results algebraically. Net axial electromagnetic force can be directed to upwards, downwards or both based on the tapping arrangement.

All these calculations assume that the electromagnetic forces are static forces but in reality, they are dynamic. Dynamic representation of the transformer winding will be attempted to determine the dynamic forces acting on transformer winding. The movement of the high voltage (HV) winding is considered only and low voltage (LV) winding is assumed motionless during the short circuit. This assumption is introduced because the LV winding is smaller in diameter and closer to the core and the position of the metal nuts and stoppers, which applies the pre-stress on the winding stack, is closer to the LV winding due to electrostatic considerations. Hence, larger percentage of the applied compressive forces is acting on the LV winding. However, LV winding can also be inserted into the equations below but the size of the matrix will increase. Figure-4.12 shows the dynamic representation of transformer winding. Each turn is represented as a mass and radial spacers and paper insulation is represented as springs. Top and bottom rings' stiffness are denoted as K* and K** respectively and C is the damping coefficient. Equation of motion of this discrete system is constructed below.

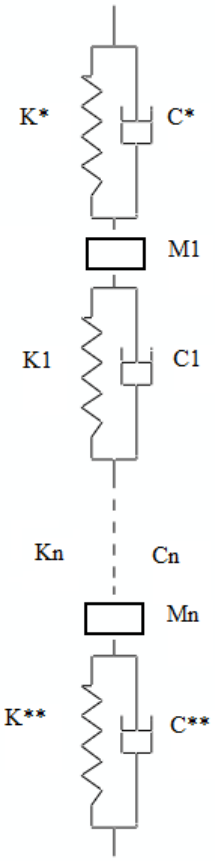

***FIGURE-4.12**: Discrete Representation of Transformer Winding*

$$m_1\ddot{u}_1 + c^*\dot{u}_1 + (k^* + k_1)u_1 - k_1u_2 = F_1(t)$$

$$m_2\ddot{u}_2 + c_2\dot{u}_2 + (k_1 + k_2)u_2 - k_1u_1 - k_2u_3 = F_2(t)$$

$$m_{n-1}\ddot{u}_{n-1} + c_{n-1}\dot{u}_{n-1} + (k_{n-2} + k_{n-1})u_{n-1} - k_{n-2}u_{n-2} - k_{n-1}u_n = F_{n-1}(t)$$

$$m_n\ddot{u}_n + c^{**}\dot{u}_n + (k_{n-1} + k^{**})u_n - k_{n-1}u_{n-1} = F_n(t)$$

Electromagnetic forces are acting on each turn and the magnitude of the dynamic force is a function of both the short circuit current and the magnetic flux density acting on that turn according to Lorentz Law, Equation 3.1. Short circuit forces are proportional to the square of the short circuit current and therefore, the result of this integration can be written in the form;

$$F_n(t) = [i_{SC}(t)]^2 Y_n \quad (4.9)$$

$i_{sc}(t)$ is the short circuit current given by Equation 3.9. It is advantageous to write the dynamic short circuit forces in the form of Equation 4.9 because magnetic flux density is not a function of time and can be treated as a constant parameter. The forcing function on the right hand side of the equation of motion can then be separated and equation of motion can be solved. k_n is found by performing the integral in Equation 3.1 as below. Definitions of the terms used in the below equations are given in Chapter-3.

$$Y_n = \frac{2\mu_0 D_{mean_n}}{ab}\frac{Y1(t) + Y2(t)}{J(t)_n}\left(\sqrt{2}\mathrm{I}_{\mathrm{pss}}\right)^2 \quad (4.10)$$

$$Y1(t) = (a'_n - a_n)\sum_{k=1}^{\infty}\left[\sum_{j=1}^{p} J(t)_j\left(a'_j - a_j\right)\frac{\left(\sin nn_k b'_j - \sin nn_k b_j\right)}{{nn_k}^3}\right](\cos nn_k b'_n - \cos nn_k b_n)$$

$$Y2(t) = 2\sum_{i=1}^{\infty}\sum_{k=1}^{\infty}\frac{(\sin m_i a'_n - \sin m_i a_n)(\cos nn_k b'_n - \cos nn_k b_n)}{{m_i}^2 nn_k({m_i}^2 + {nn_k}^2)}\sum_{j=1}^{p} J(t)_j\left(\sin m_i a'_j - \sin m_i a_j\right)\left(\sin nn_k b'_j - \sin nn_k b_j\right)$$

$$m_i = \frac{\pi}{a}i \quad i = 0,1 \ldots \infty \quad nn_k = \frac{\pi}{b}k \quad k = 0,1 \ldots \infty \quad J(t)_n = \frac{NI(t)_n}{(a'_n - a_n)(b'_n - b_n)}$$

In order to solve the equation of motion, square of the short circuit current needs to be found. Taking the square of the short circuit current and using trigonometric relations,

$$[i_{SC}(t)]^2 = \frac{1}{2} + e^{-2\frac{Rz}{L}t} - 2e^{-\frac{Rz}{L}t}Cos(wt) + \frac{1}{2}Cos(2wt) \quad (4.11)$$

The solution to linear dynamic system can be obtained by superposition of complementary and particular solutions. If damping matrix is proportional type, there will be n uncoupled and independent equations. However, the system in Figure-4.12 can be constructed so that the damping matrix is non-proportional type after pre and post multiplied by the modal matrix. The solution to non-proportional case will be considered as this is more general form. Complementary solution for non-proportional case is given in [41] and it will be extended to cover particular solution. Equation of motion can be written in below form,

$$[M](\dot{u}) - [M](\dot{u}) = (0)$$

$$[M](\ddot{u}) + [C](\dot{u}) + [K](u) = (F)$$

or in more general form,

$$\begin{bmatrix}[0] & [M]\\ [M] & [C]\end{bmatrix}\begin{pmatrix}(\ddot{u})\\ (\dot{u})\end{pmatrix} + \begin{bmatrix}[-M] & [0]\\ [0] & [K]\end{bmatrix}\begin{pmatrix}(\dot{u})\\ (u)\end{pmatrix} = \begin{pmatrix}(0)\\ (F)\end{pmatrix}$$

where [.] represents $n_x n$ matrix and (.) represents $n_x 1$ vector.

or,

$$[A](\dot{x}) + [B](x) = (F') \quad (4.12)$$

$$[A] = \begin{bmatrix}[0] & [M]\\ [M] & [C]\end{bmatrix}, [B] = \begin{bmatrix}[-M] & [0]\\ [0] & [K]\end{bmatrix}, (F') = \begin{pmatrix}(0)\\ (F)\end{pmatrix} \; and \; (x) = \begin{pmatrix}(\dot{u})\\ (u)\end{pmatrix}$$

Equation 4.12 is referred to as to reduced equation of motion. Matrices A and B are both symmetrical matrices of order 2n and both the eigenvalues and the eigenvectors are complex form and in conjugate pairs. Setting the right hand side of equation 4.12 to zero and assuming the solution of the form $(x) = (v)e^{st}$ represents a standard eigenproblem of order 2n where v are the eigenvectors and s are the eigenvalues. Eigenvectors are orthogonal to matrices [A] and [B].

$$[-A]^{-1}[B](v) = s(v)$$

Modal matrix, [V], can be constructed from 2n eigenvectors and the conditions of orthogonality are;

$$[V^T][-A][V] = [I] and\ [V^T][B][V] = [S]$$

Here, S is the spectral matrix and I is the identity matrix. Transforming the displacements to modal coordinates using the relation $(x) = [V](y)$ substituting these conditions to equation 4.12 yields,

$$-(\dot{y}) + [S](y) = [V^T](F') \quad (4.13)$$

Equation of motion for non-proportional case is now uncoupled. Complementary solution can now be found by setting the right hand side of equation 4.13 to zero. Equation 4.13 has a solution of the form of $y_n = d_n s^{s_n t}$ where d_n can be determined from initial conditions. First n terms in vector d are the initial velocities and from n+1 to 2n terms are the initial displacements. The response in physical coordinates can be found using the relation $(x) = \sum_{n=1}^{2n} d_n s^{s_n t}\,(v_n)$.

s_n is in a+ib form and therefore can be written as;

$$(x) = \sum_{n=1}^{2n} d_n e^{a_n t}[\cos(b_n t) + i sin(b_n t)]\,(v_n)$$

Particular solution of the equation of motion can be solved in four steps. The first step is to find a solution to constant term in Equation 4.11.

$$-(\dot{y}) + s(y) = [V^T](F1') = (F1'') \quad (4.14)$$

From 1 to n rows of the vector F1' are zero and from n+1 to 2n rows are equal to (1/2)Y_n where Y_n is given by equation 4.10.

The solution to the above equation is;

$$y_n = Constant_n$$

Substitute above in Equation 4.14,

$$Constant_n = \frac{F1''_n}{s_n} \quad (4.15)$$

The second step involves finding a solution to $e^{-2\frac{R}{L}t}$ term

$$-(\dot{y}) + s(y) = [V^T](F2') = (F2'') \quad (4.16)$$

From 1 to n rows of the vector F2' are zero and from n+1 to 2n rows are equal to Y_n.

The solution to the above equation is;

$$y_n = T_n e^{-2\frac{R}{L}t}$$

Substitute above in Equation 4.16,

$$T_n = \frac{F2''_n}{s_n + 2\frac{R}{L}} \quad (4.17)$$

The third step involves finding a solution to $\frac{1}{2}Cos(2wt)$ term

$$-(\dot{y}) + s(y) = [V^T](F3') = (F3'') \quad (4.18)$$

From 1 to n rows of the vector F3' are zero and from n+1 to 2n rows are equal to (1/2)Y_n.

The solution to the above equation is;

$$y_n = P_n Cos(2wt + \lambda_n)$$

Substitute above in Equation 4.18,

$$P_n = \frac{F3''_n}{\sqrt{(4w)^2 + (s_n)^2}} \quad \lambda_n = Atan\left(\frac{2w}{s_n}\right) \quad (4.19)$$

The fourth step involves finding a solution to $-2e^{-\frac{R}{L}t}Cos(wt)$ term

$$-(\dot{y}) + s(y) = [V^T](F4') = (F4'') \quad (4.20)$$

From 1 to n rows of the vector F4' are zero and from n+1 to 2n rows are equal to -2Y_n.

The solution to the above equation is;

$$y_n = J_n e^{-\frac{R}{L}t}Cos(wt + \chi_n)$$

Substitute above in Equation 4.21,

$$J_n = \frac{F4''_n}{\sqrt{(w)^2 + \left(s_n + \frac{R}{L}\right)^2}} \quad \chi_n = Atan\left(\frac{w}{s_n + \frac{R}{L}}\right) \quad (4.22)$$

Both the complementary and particular solution is found. The final solution can now be constructed by superposing these solutions.

$$(x) = \begin{pmatrix} \dot{u} \\ u \end{pmatrix} = \sum_{n=1}^{2n} d_n e^{a_n}[\cos(b_n t) + isin(b_n t)] + \frac{F1''_n}{s_n} + T_n e^{-2\frac{R}{L}t} + P_n Cos(2wt + \lambda_n) + J_n e^{-\frac{R}{L}t} Cos(wt + \chi_n) \quad (4.23)$$

Constant d_n can be determined from the initial conditions. At t=0, both the velocity and the displacement is zero.

$$d_n = -\frac{F1''_n}{s_n} - T_n - P_n Cos(\lambda_n) - J_n Cos(\chi_n) \quad (4.24)$$

First n rows of the derivative of equation 4.23 are the accelerations of the masses, accelerations of the turns of the winding for the current problem. The method introduced treats the short circuit as a dynamic event and the effects of resonance are taken into account.

As an example, a transformer having a low voltage winding consists of 5 layers in radial direction and a high voltage winding consists of 60 turns in axial direction will be considered. Each turn is 204kg and the elasticity modulus of insulation material is taken as 400MPa and 800MPa to compare the effect of the choice of insulation material. Damping coefficient is taken from [16], 1520 kgs/m. Resistance to inductance ratio of the transformer is 10.585 which results 1.9 asymmetry factor for short circuit current and the frequency of the exciting current is 50Hz.

Figure-4.13 and Figure-4.14 show the displacements of top and bottom turns, top and bottom clamping rings. During transient phase, 50Hz component of the electromagnetic force is the dominant component for the winding with lower insulation stiffness. As the stiffness increases, 100Hz component plays an as important role as 50Hz component during transient phase. 100Hz component is the dominant component for all cases during steady

state phase because 50Hz component of the electromagnetic force decays exponentially as the time increases.

Static calculations predict 0.27mm displacement at peak short circuit force on the top turn for the insulation material with 400MPa elasticity modulus on the other hand dynamic calculations predict that the displacement reaches 0.443mm maximum displacement and the dynamic amplification factor is found to be 1.64 for this case.

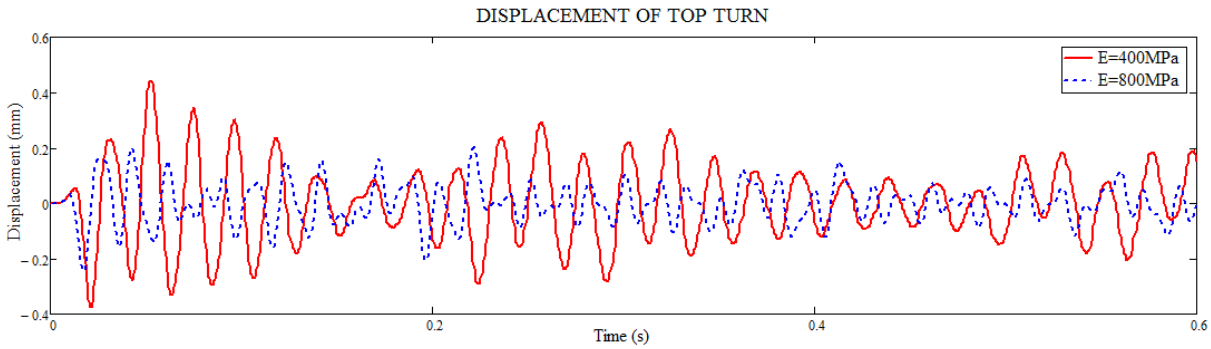

***FIGURE-4.13**: Displacement of Top Turn*

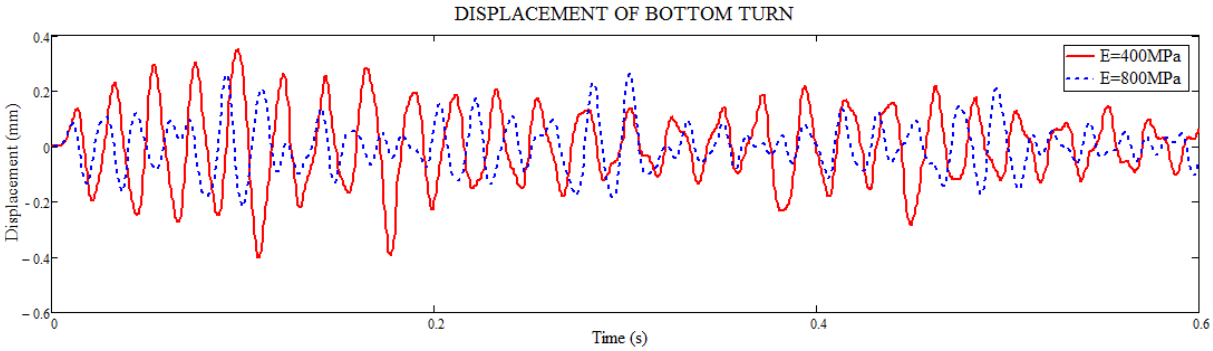

***FIGURE-4.14**: Displacement of Bottom Turn*

Maximum compressive forces on insulation material and copper can be found in order to determine the stresses on the radial spacers and the tilting strength of the copper by taking the dynamic amplification factors into account using the developed method.

4.5 Conclusions

A brief explanation of radial and axial forces exerted by electromagnetic forces is introduced. A method is developed to calculate the shear stress on epoxy bonded CTC's by extending the existing solution developed by [39]. The developed solution can also calculate the normal and bending stresses more accurately than previous methods because it takes shear forces into account. Application of the developed formulas to CTC structure based on the winding

design parameters is introduced. This method can be used to determine the number of axial sticks used in transformer winding.

In order to determine dynamic forces, the transformer is modelled as spring-mass-dashpot system with non-proportional damping. A method to separate dynamic short circuit current from axial dynamic short circuit forces is introduced in Equation-4.10. This separation greatly simplifies the solution because the terms from integration of magnetic flux density can be treated as a multiplication factors for dynamic short circuit currents.

Free vibration solution of equation of motion for multi degree of freedom system with non-proportional damping is used as given in [41]. A solution to the forced vibration case is developed by solving the equation of motion as given in Equation-4.23 and 4.24. This is achieved by separating the forcing term, proportional to short circuit current, into its constituent components. Final solution is constructed by superposing the complementary and particular solutions. The dynamic model is much more accurate to validate the number and dimensions of radial spacers and tilting strength because the dynamic effects can be taken into account.

5- BEHAVIOUR OF TRANSFORMERBOARD UNDER TENSION LOADING

5.1 Introduction

Transformerboard can be treated as an orthotropic material formed by stacking very thin sheets together under hot pressing. The manufacturing process is identical to paper manufacturing at the beginning of the process. Cellulose is dispersed in water and the individual fibers are crushed and refined to expose additional surface area. The strength of the transformerboard is determined by the bonding forces between fibers and the magnitude of the stress generated by these forces are far below the breaking point of fibers. Wet sheets are pressed, dried and compressed in hot presses and become cross-linked. The result is a transformerboard stronger than pressboard and its resistance to both flexural and tensile loading is increased.

The complexity of the structure of the transformerboard is caused by the dominance of the short fibers on one plane and by stacking very thin sheets which forms cross linked fibers through the thickness direction. A simple load-deflection curve can provide valuable data for instance, ultimate tensile strength and elongation at failure. However, these data are not enough to understand the true behaviour of the transformerboard under tensile loading conditions. In order to understand the effect of short fibers and cross linked fibers through the thickness direction, the stress or strain map along the specimen need to be determined.

5.2 Description of Test Setup and Digital Image Correlation Post-processing Procedure

The mechanical properties of the transformerboard are given in [1] and [2]. Tensile strength, elongation and influence of ageing of the transformerboard on tensile strength in machine and cross machine direction based on specific weight are given. Apart from these data, the effect of fibers in directions perpendicular to loading and through the thickness is not given. In order to study the strain distribution on the material, Digital Image Correlation (DIC) technique will be used. Figure-5.1 shows the tensile test specimen. On the 1-2 plane, short cellulose fibers are dominant and these fibers are aligning themselves in the machine direction during manufacturing. Transformerboard is made by extracting the fibers of the wood material. These fibers are then crushed and refined in order to increase the surface

area of the fibers. The manufacturing process is similar to the paper manufacturing process at the beginning. Fibers are kept in a container and a belt is moving below this container. Fibers are then released from the container to the belt and due to the movement of the belt fibers tend to align themselves towards to one direction. This direction is called machine direction (MD). The direction 90^0 to the belt's movement is the cross machine direction (CMD). The 1-3 plane is the thickness direction where very thin sheets are stacked together under a hot press. The surface of the transformerboard was cleaned with a small amount of isopropyl alcohol and the surfaces were sanded with emery paper before the strain gauges were glued to the surfaces using wood glue. Vishay made 125TG model general purpose, 90^0 tee rosettes with high resistance grid strain gauges were attached at the back surfaces of the specimen. Each section of the strain gauges has a separate electrical connection and each section can be connected to the strain indicator and recorder instruments separately. Vishay made P3 Model portable, battery operated strain indicator and recorder unit was used. This instrument is capable of simultaneously record 4 quarter bridge strain gauge circuits. Each section of the strain gauges is 3.18mm in length and the overall length of the strain gauges are 12.7mm. Resistance of the strain gauge is 350 ± 0.2% ohms and the gauge factors of the strain gauges were 2.09. These strain gauges measure elongation along the loading and perpendicular to the loading directions. Surfaces where these strain gauges were attached are shown in Figure-5.1. Using these strain gauges, Poisson's ratios v_{12} and v_{13} can be measured. Poisson's ratio v_{21} and v_{23} can be obtained simply by cutting the specimen along the cross machine direction and interchanging the coordinate axes 1 and 2 in Figure-5.1. Every strain gauge is connected to the strain indicator and recorder unit by quarter bridge circuit arrangement. Once the quarter bridge connections were made, the strain gauges were calibrated simply by using the zero balancing and calibration option available in the P3 Model measuring instrument. Therefore, readings for strain gauges can be obtained from four quarter bridge circuit arrangements and Poisson's ratios can simply be determined.

DIC setup used in these experiments possesses a laser pointer. Using the laser pointer, left and right cameras can be adjusted so that the cameras are directed to the same point. Measuring distance and the distance between the cameras can be chosen with the help of DIC software manual. The next step involves adjusting the focus and the aperture of the lenses. Once the cameras are directed to the same point and fixed to their support, the

cameras were calibrated using the calibration blocks. Panel calibration object was suggested by the DIC manual considering the size of the test specimen dimensions. Automatic calibration option was chosen from the DIC software. This option step by step shows and explains how to position the calibration object. After following the instructions and taking images of the calibration object at different positions, software automatically calculates the error involved during the calibration process. If the calibration is successful, the calibration can be saved and the process is completed.

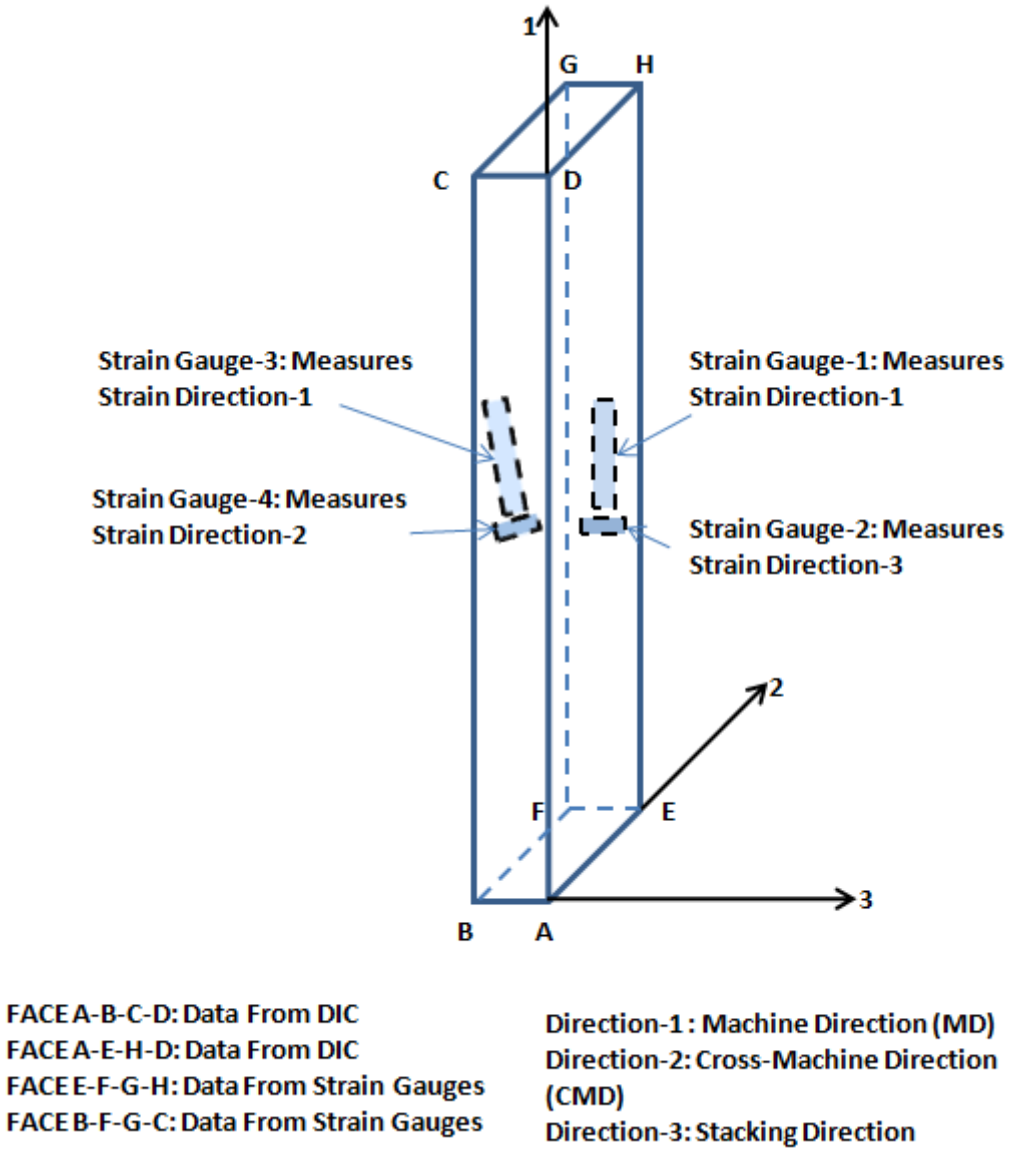

***FIGURE-5.1**: Planes where Strain Gauges are Attached and Speckle Patterns are Created for DIC Measurement*

A speckle pattern is created on front surfaces of the test specimen as shown in Figure-5.1 to determine the strain map from DIC cameras under tensile loading condition. Test data obtained from DIC and strain gauges can now be compared.

This test setup is necessary to compare strain gauge data and DIC data because strain gauges need to be glued on the surfaces as shown in Figure-5.1. This can change the state of strain especially through the thickness direction because in this plane very thin sheets are stacked together under hot press without any bonding agent to achieve better performance under electrical field. When these thin sheets are glued together to bond the strain gauges, the response of the material can change. To investigate the effect of the glue used to attach strain gauges on the surfaces, readings obtained from DIC and strain gauges will be compared. Effects of the bonding agent on the 1-2 plane, where short fibers are dominant, are also of interest and will be compared.

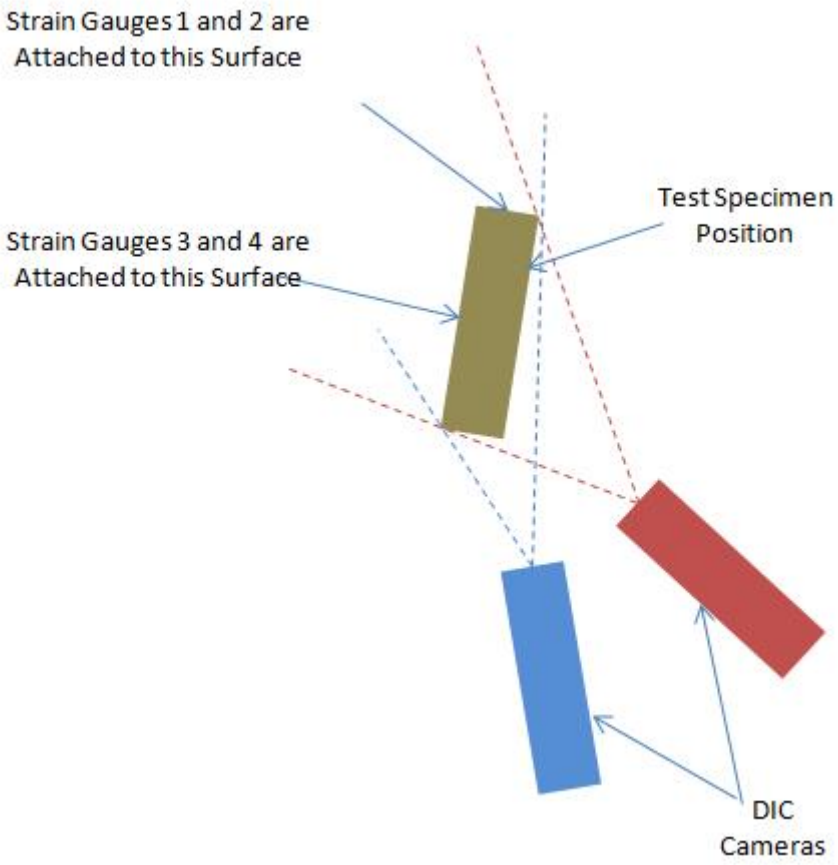

***FIGURE-5.2**: Position of the Test Specimen and DIC Cameras for 3-D DIC Measurements*

In order to capture the strain map on faces ABCD and AEHD using ARAMIS DIC cameras, 3-D measurements have to be performed. Figure-5.2 shows the test arrangement employed to capture strain distribution on the two faces, where the speckle pattern is created, of the test specimen. The cameras are calibrated so that the deformation on the two faces of the test specimen will be captured by each camera. Therefore, Poisson's ratios can be calculated from both DIC and strain gauges simultaneously. At the back surfaces, four strain gauges are attached and connected to strain indicators using four quarter bridge circuit.

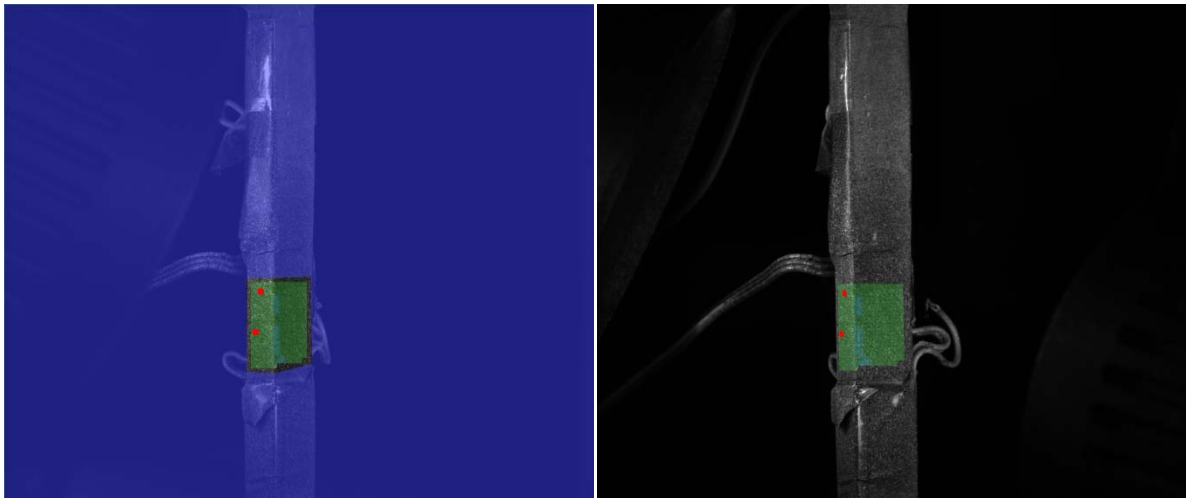

***FIGURE-5.3**: Test Specimen Images- Left and Right Camera Respectively*

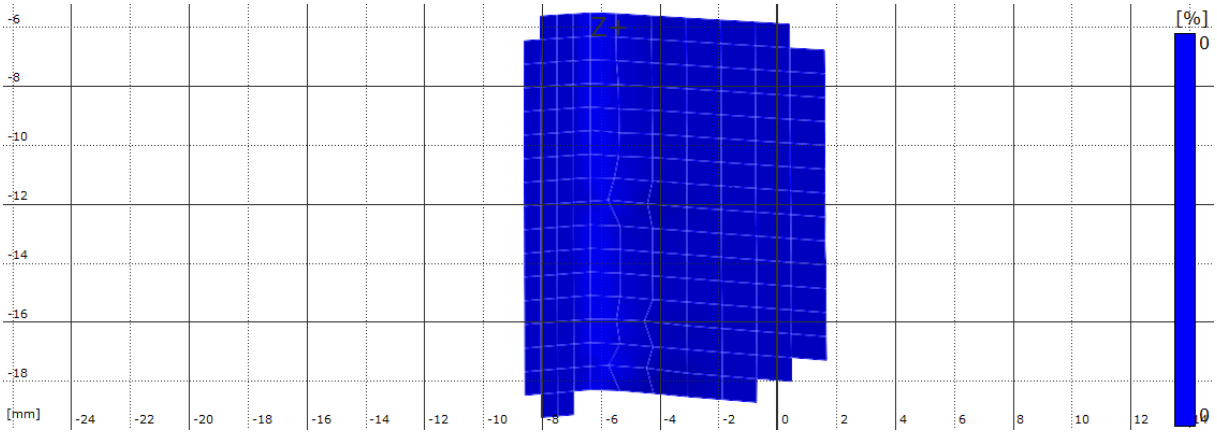

***FIGURE-5.4**: Image Obtained from 3-D ARAMIS DIC Software – Right Camera*

Figure-5.3 shows the test specimen pictures captured by the left and right cameras respectively and Figure-5.4 shows the DIC result processed by the ARAMIS software at the beginning of the test, prior to application of the tensile loading. Both surfaces, 1-2 plane and 1-3 plane, can be clearly distinguished. In order to study the strains or extensions occurring during loading conditions, two techniques can be employed. The first technique is to

generate lines using ARAMIS software as shown in Figure-5.5. The software automatically calculates the strain or extension values at these lines at every stage. These data can then be saved as text file and can be processed with appropriate software such as EXCEL, MATHCAD or MATLAB. The beauty of this method is its simplicity during post-processing operations.

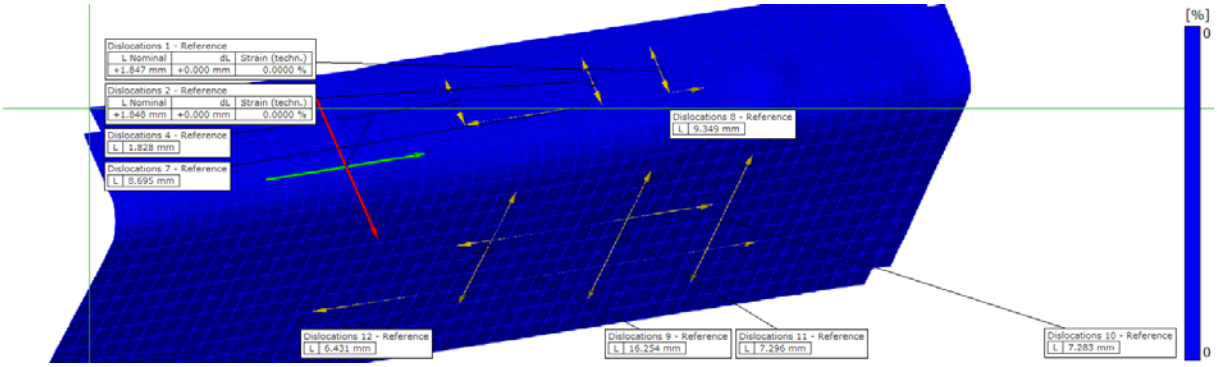

***FIGURE-5.5**: Lines Generated by ARAMIS Software to Study Strains/Extensions*

The second method has to be used if strain distributions on one surface with respect to appropriate coordinate axes need to be studied. For instance, if ε_{11} or ε_{22} need to be studied on the 1-2 plane, coordinate transformation has to be employed. To be able to do this, three pixel points should be created using ARAMIS software where the first point is the origin of the coordinate system, a line from first to second point is the positive Y axis (or direction 2) and the line from first to third point is the positive X axis (or direction 1). Figure-5.6 shows the position of six pixel points created on test specimen using ARAMIS software. Pixel points 1, 2 and 3 are for coordinate transformation on the 1-3 plane and pixel points 4, 5 and 6 are for the 1-2 plane.

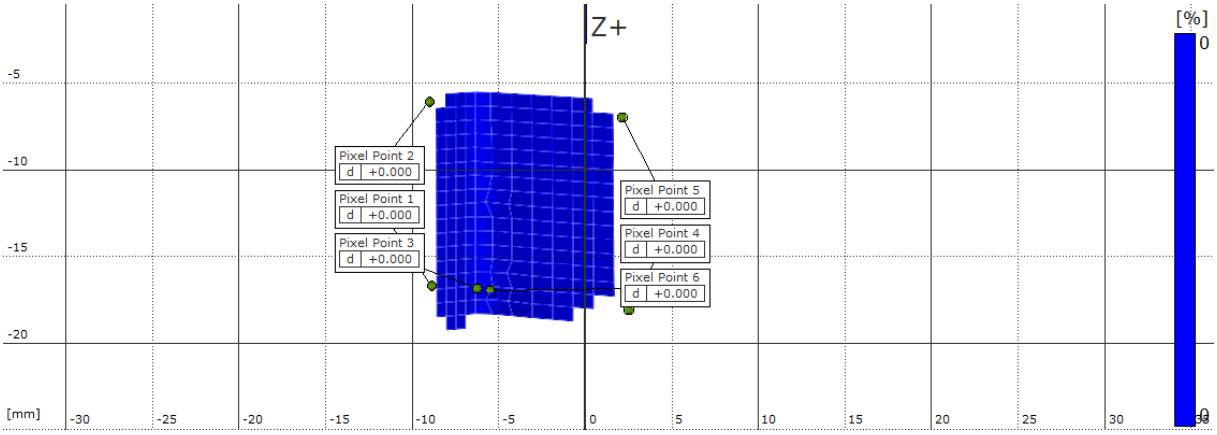

***FIGURE-5.6**: Position of the Pixel Points for Coordinate Transformation*

Once the coordinate transformation is completed for example on the 1-2 plane, all the data points on the 1-3 plane should be selected and deleted. These deleted points can be retrieved whenever needed. The strain distribution ε_{11} or ε_{22} on the 1-2 plane can now be studied. The same procedure should be repeated to study strain distribution on the 1-3 plane. Figure-5.7 shows the 1-3 plane after the above mentioned procedure is applied. Only data points on 1-3 plane are available as required and strains in 1 and 3 directions can now be studied and strain maps can be plotted, if necessary.

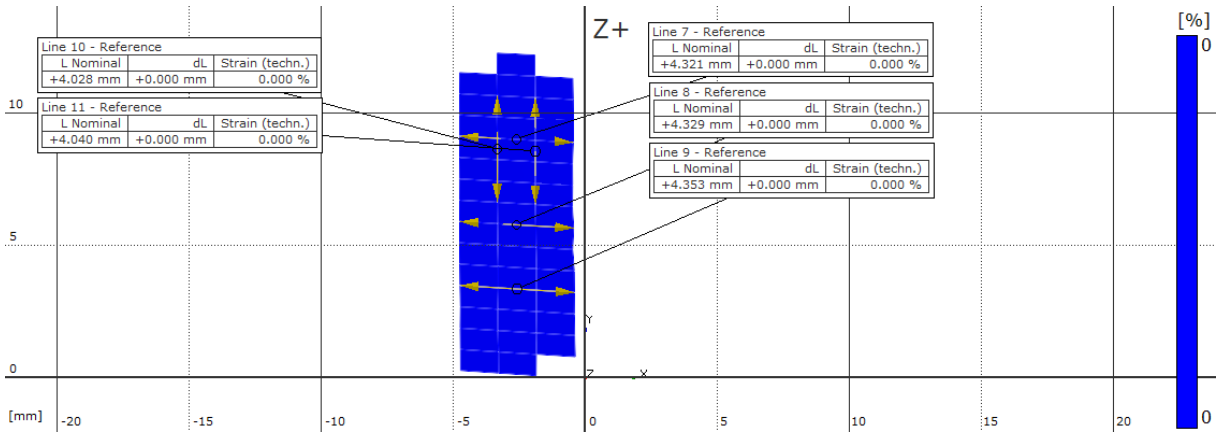

***FIGURE-5.7**: DIC Data Contains Information on 1-3 Plane Only*

5.3 Tensile Tests Performed on Transformerboard in Machine Direction and Cross Machine Direction

Figure-5.8 shows the test specimen configuration used for tensile tests. Metal tabs are attached at the ends of the specimen and dimensions used for specimens cut in machine and cross machine directions are shown in Table-5.1. The results shown are for dried specimens as the material properties at low loading rates for oil-impregnated specimens do not change dramatically. This is because the oil trapped in the transformerboard has time to respond the applied load and time to be released.

Test rate was set to 0.5mm/min, recording interval of the DIC cameras were set to 1 frame per second and data from strain gauges were recorded every second. Test machine, DIC cameras and strain gauges recordings were started manually at the same time. Load-extension curves for MD and CMD test specimen are given first because an important conclusion can be drawn for failure mode of the transformerboard under tensile loading conditions. Figure-5.9 shows the load – extension curves for machine and cross machine direction specimens. All CMD specimens failed at an area close to mid plane of the gauge

length as expected. The test specimen was ruptured and separated into two pieces. The first failure in MD specimens, on the other hand, occurred at the thickness direction, in direction 3 according to Figure-5.1, and part of the specimen was separated. As the load level increased, the failure in thickness direction was propagated along the direction 1 and test specimen was separated into two pieces as shown in Figure-5.10.

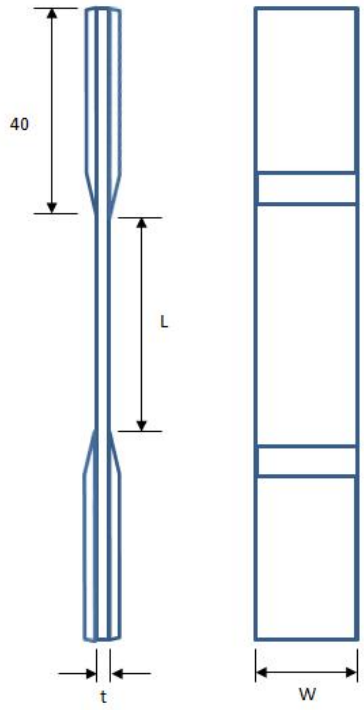

***FIGURE-5.8**: Tensile Test specimen Configuration*

SPECIMEN	t (mm)	W (mm)	L (mm)
MD	5	13	118
CMD	5	25	110

***TABLE-5.1**: Dimensions of the Machine and Cross Machine Direction Specimens*

Poisson's ratio is defined here as the positive value of the ratio of the strain in direction perpendicular to the loading to the strain in direction parallel to loading. Expansions are taken as positive and contractions are taken as negative. In other words, for a MD specimen;

$$\nu_{12} = \frac{\varepsilon_2}{\varepsilon_1}, \nu_{13} = \frac{\varepsilon_3}{\varepsilon_1} \qquad (4.1)$$

and for a CMD specimen;

$$\nu_{21} = \frac{\varepsilon_1}{\varepsilon_2}, \nu_{23} = \frac{\varepsilon_3}{\varepsilon_2} \qquad (4.2)$$

Therefore if a MD specimen is contracting in direction 3 and elongating in direction 1, the Poisson's ratio v_{13} is negative and if it is expanding, the Poisson's ratio is positive.

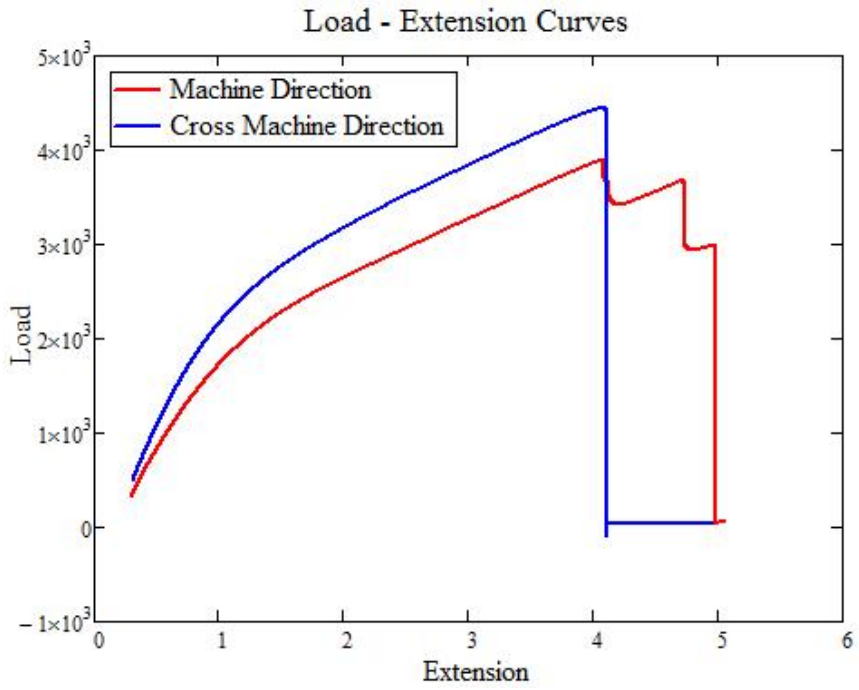

***FIGURE-5.9**: Load (N) – Extension (mm) Curves for Dry Machine & Cross Machine Direction Specimens*

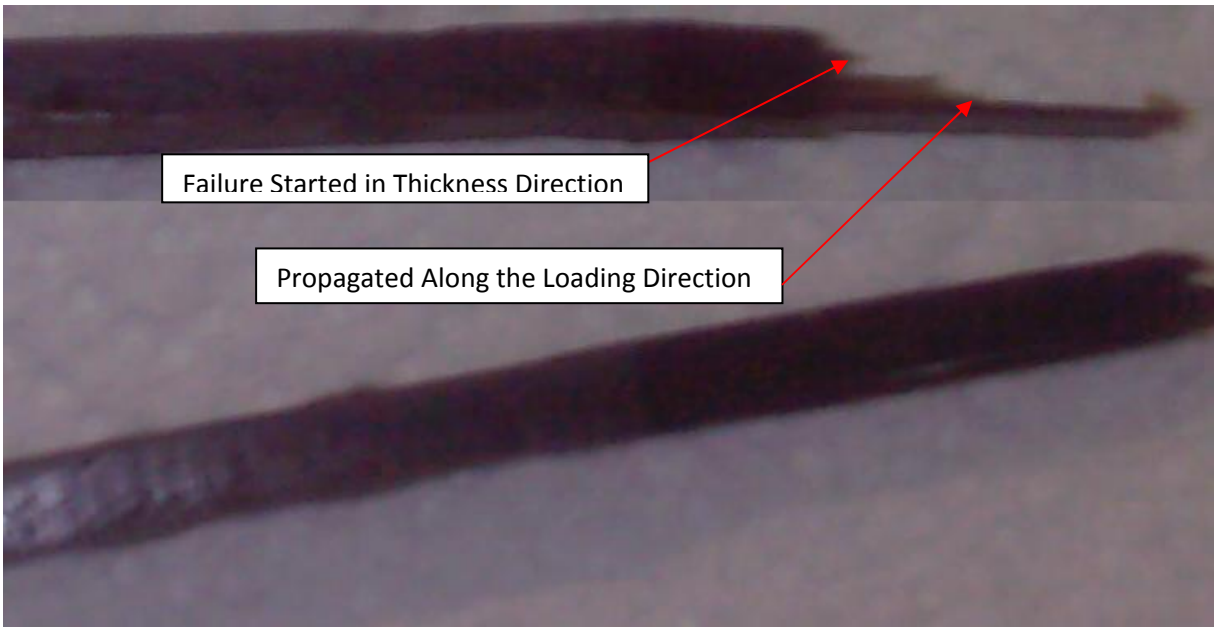

***FIGURE-5.10**: Failure Mechanism of Machine Direction Specimens – Oil Impregnated*

Based on the observations obtained from failure mechanism of the transformerboard, following comments can be concluded. Bonding forces generated by cellulose fibers in the

thin sheets are weaker than the bonding forces generated by the cross linked fibers which are present in thickness direction and are generated during hot press operation, when transformerboard is loaded in cross machine direction. All test specimens were failed in an expected way, rupture occurred almost at the mid-plane and no separation in thickness direction was observed. This trend was opposite when transformerboard is loaded in machine direction. The first failure always occurred in thickness direction and propagated through the loading direction. This suggests that in thickness direction transformerboard is expanding rather than contracting under tensile loading. The probable explanation is that the bonding between cross linked fibers is breaking as the load level is increasing and releasing the thin sheets causing an increase in thickness of the specimen. To validate the increase in thickness direction, strain gauge and DIC results are studied.

Figure-5.11.a shows the data obtained from strain gauge 2 in Figure-5.1 and Figure-5.11.b shows the data obtained from DIC for MD specimen. At the beginning of the test both data shows contraction and when the load level reaches a critical point, the thickness starts increasing. For strain gauge data, time to reach this critical load level is higher than DIC data and the reason is the applied glue to bond the strain gauge on the surface. At this critical load level, cross-linked fibers are debonding and thin sheets are separating. This is the probable reason for increase in the thickness of transformerboard under tensional loading conditions. Although the trend in %strain vs time graphs obtained from DIC and strain gauge is similar, the difference in %strain values between two measurements is very large in magnitude. This is due to the effect of bonding agent used to attach strain gauge on the surface. As explained before, bonding agent keeps very thin transformerboard sheets together and generates artificial resistance to deformation between the sheets. Same behaviour is also observed for the CMD test specimen. These results show that transformerboard is expanding in thickness direction when the tensile load reaches critical limit.

In order to obtain the strain values in direction 2 data obtained from strain gauge, DIC and load extension curve from test machine is processed and shown in Figure-5.12. The agreement in strain values in direction 2 between DIC and test data provides additional confidence in the results obtained from DIC technique. Strain gauge data, on the other hand, underestimates the strain values. When strain data obtained from DIC divided to strain

gauge data, the average value is found to be 1.95. Strain gauge data therefore is approximately half the DIC data.

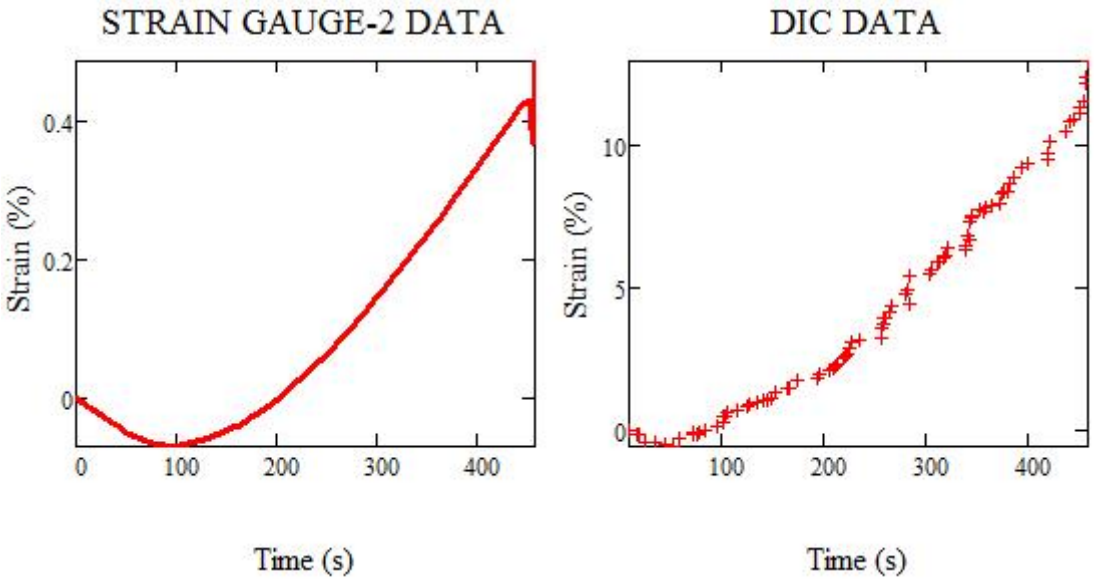

***FIGURE-5.11**: % Strain in Direction-3, MD Specimen **a)** Strain Gauge-2 Data **b)** DIC Data*

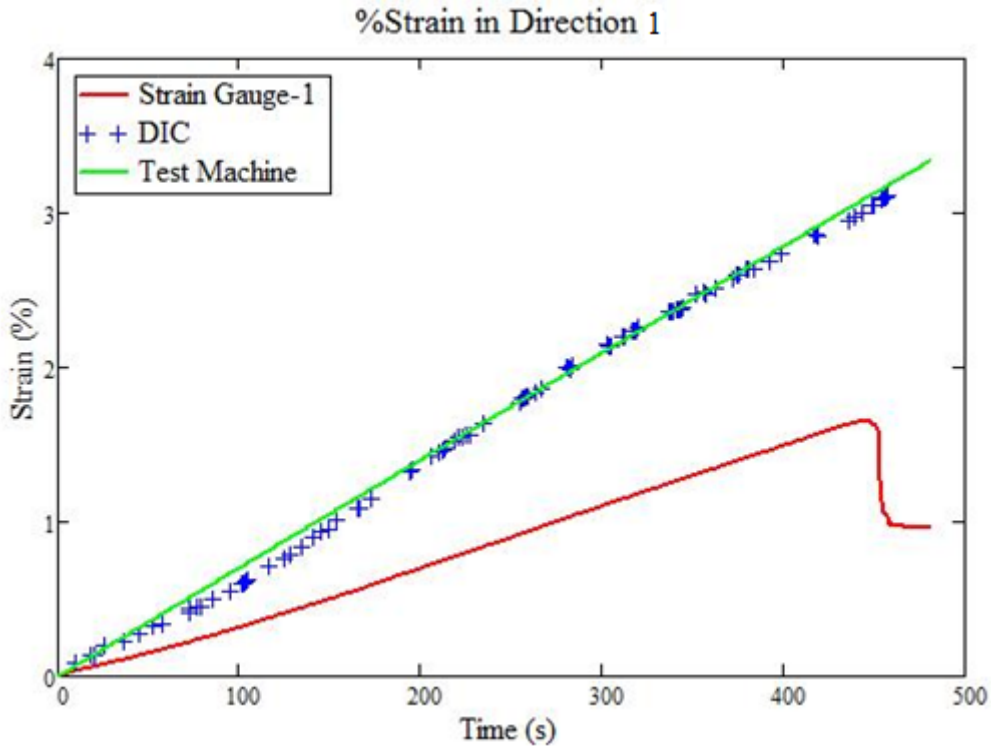

***FIGURE-5.12**: Comparison of %Strain in Direction 1 – MD Specimen*

Using above values, Poisson's ratio v_{13} can be obtained from both DIC and strain gauge data. Figure-5.13a and Figure-5.13b shows the Poisson's ratio data obtained from strain gauge measurements and DIC respectively. Poisson's ratio at this plane takes negative values at the

beginning of the test and when critical limit is reached, increases to very high values. Especially DIC values reach a value of 4 at the end of the test. Therefore, strain rate in the thickness direction is much higher than the loading direction. Constant Poisson's ratio at this plane cannot be considered for transformerboard.

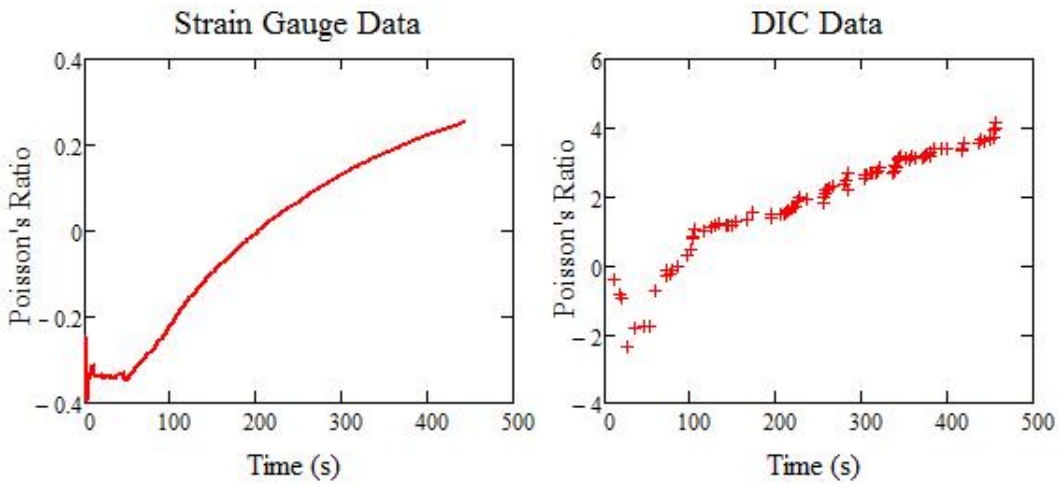

***FIGURE-5.13**: Poisson's Ratio v_{13}, MD Specimen **a)** Strain Gauge-1 Data **b)** DIC Data*

Strain in direction-2 is shown in Figure-5.14. The magnitude of strain in this direction is smaller than others. DIC technique is reliable over 400μe and any strain data found to be smaller than this limit is not considered in the comparisons. The agreement between strain gauge and DIC results are much better on this plane. Strain gauge data is again smaller than the DIC data but the difference is much smaller comparing to previous cases. Strain in this direction always contracts and this is supported by both DIC and strain gauge data.

Poisson's ratio v_{12} calculated from both DIC and strain gauge data is shown in Figure-5.15 where elastic limit and beginning of linearly plastic regions are shown with green dashed vertical lines. DIC data shows some variation when material is loaded elastically and this variation becoming much more pronounced at the transition region. DIC results show almost constant Poisson's ratio at the plastic region. Strain gauge data, on the other hand, show higher Poisson's ratio. This is because the strain gauge data underestimates the strain values in loading direction as shown in Figure-5.12. Calculated average elastic and plastic Poisson's ratios, v_{12}, are listed in Table-5.2. Both elastic and plastic Poisson's ratios calculated with DIC result are smaller than those calculated using strain gauges.

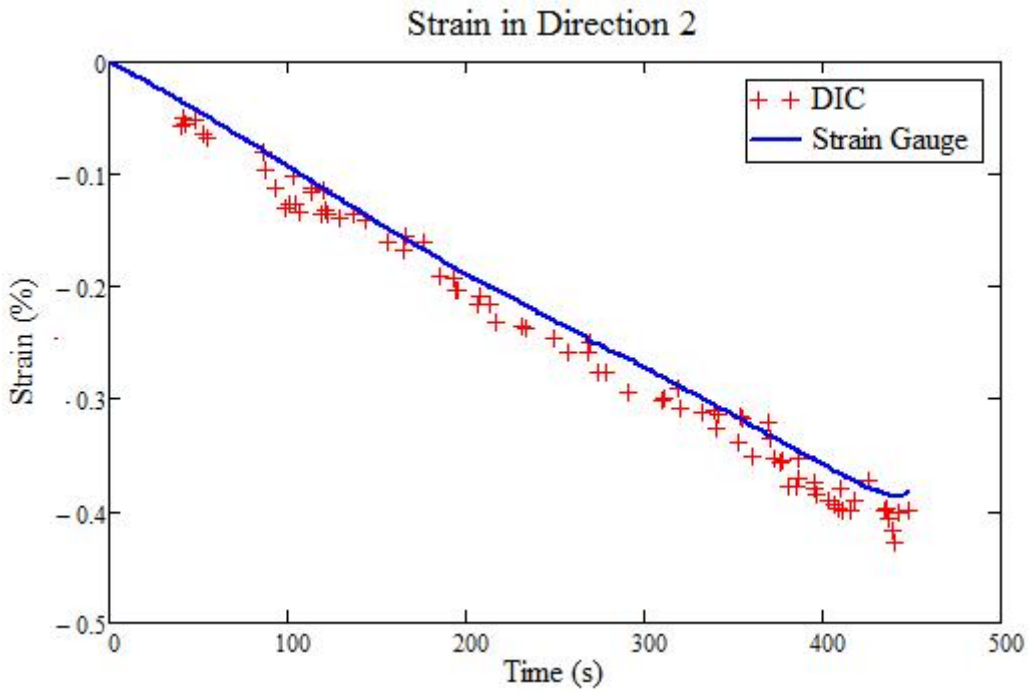

***FIGURE-5.14**: Comparison of Strain in Direction 2 – Strain Gauge and DIC Data*

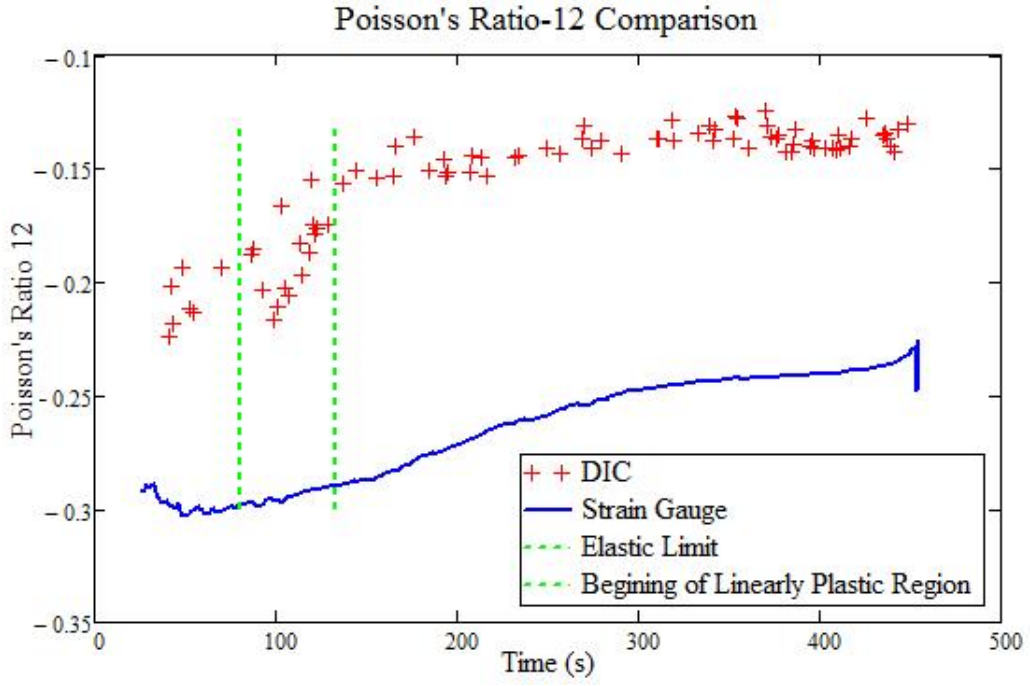

***FIGURE-5.15**: Comparison of Poisson's Ratio v_{12}, MD Specimen – Strain Gauge and DIC Data*

Elastic v_{12} Strain Gauge	**Elastic v_{12} DIC**	**Plastic v_{12} Strain Gauge**	**Plastic v_{12} DIC**
-0.3	-0.2	-.245	-.14

***TABLE-5.2**: Calculated Elastic and Plastic Poisson's Ratios, v_{12}, with Strain Gauges and DIC*

Figure-5.16 shows the %strain in direction-3 for CMD specimen. Transformerboard is expanding in thickness direction and the difference between strain gauge and DIC results are large agreeing with MD specimen tests. Conclusions which were drawn for MD specimen are valid for CMD specimen. Scatter in DIC readings are less than Figure-5.13.b.

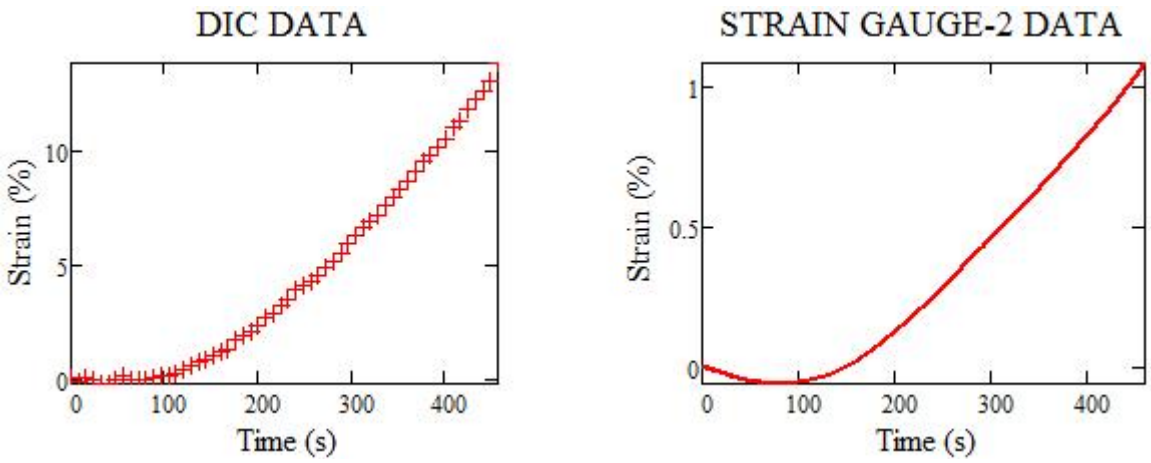

***FIGURE-5.16**: % Strain in Direction-3, CMD Specimen **a)** Strain Gauge-2 Data **b)** DIC Data*

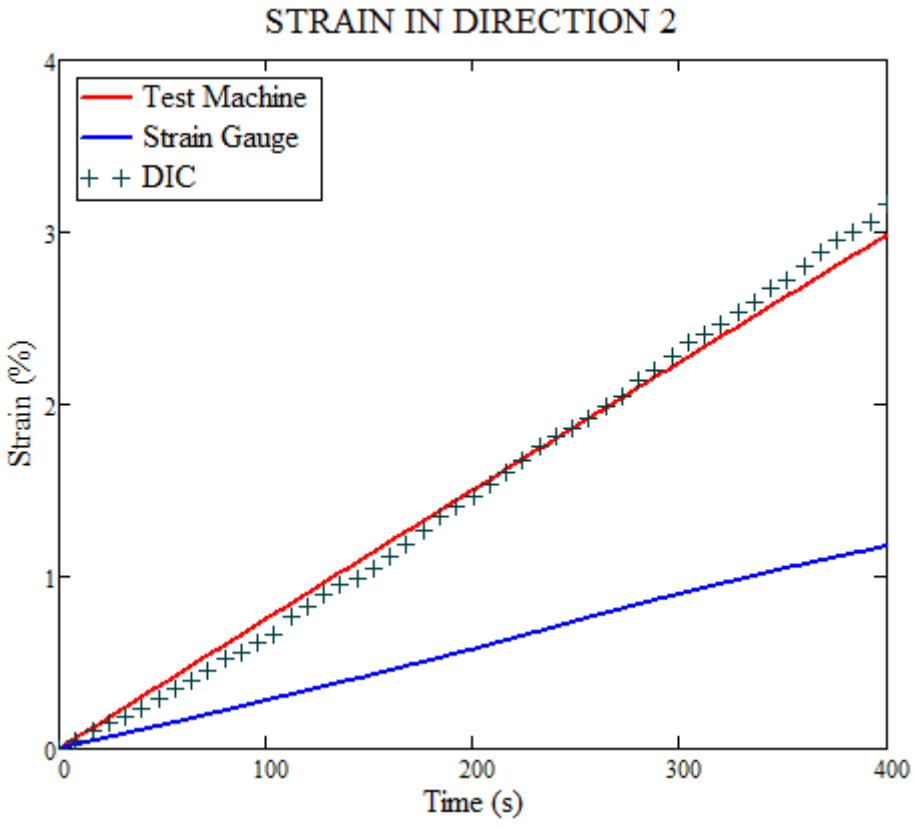

***FIGURE-5.17**: Comparison of %Strain in Direction 2 – CMD Specimen*

Percentage strain in loading direction is shown in Figure-5.17 for CMD specimen and agreement between DIC and test machine data can be observed comparing to strain gauge

data. Strain gauge data again underestimates the strain and the difference is approximately 2.5 times at this loading direction.

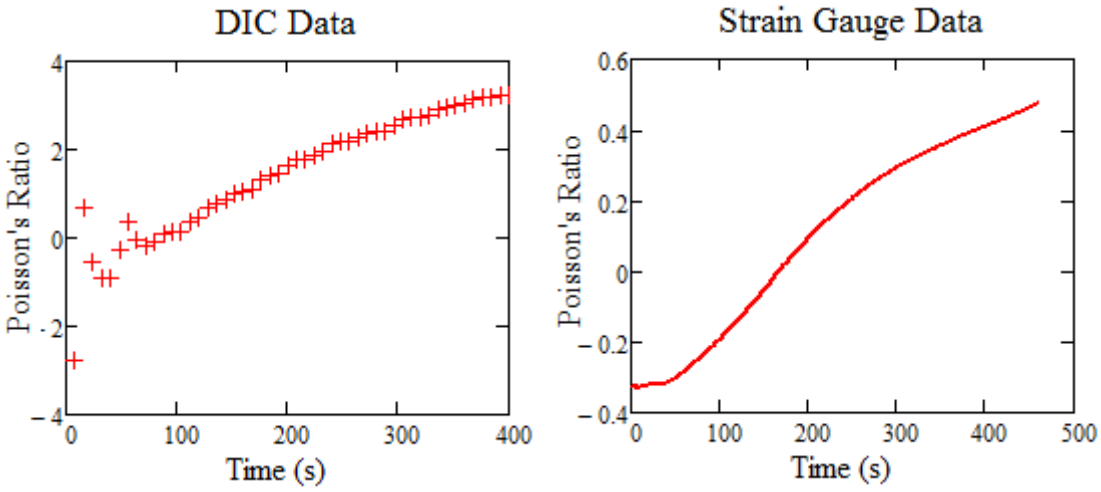

***FIGURE-5.18**: Poisson's Ratio ν_{23}, MD Specimen **a)** Strain Gauge-1 Data **b)** DIC Data*

Calculated Poisson's ratio from DIC and strain gauge data is shown in Figure-5.18. DIC data during elastic loading scatters a lot but as the load level increases, the data show stability.

At direction 1 for CMD specimen, the strain values smaller than 400µe are not considered. Thus, at the beginning of the test where the material's response is almost elastic, no data is extracted from DIC. DIC results scatter much more for the CMD specimen than for the MD specimen. Elastic Poisson's ratio from DIC was not calculated because the strain values were smaller than 400µe.

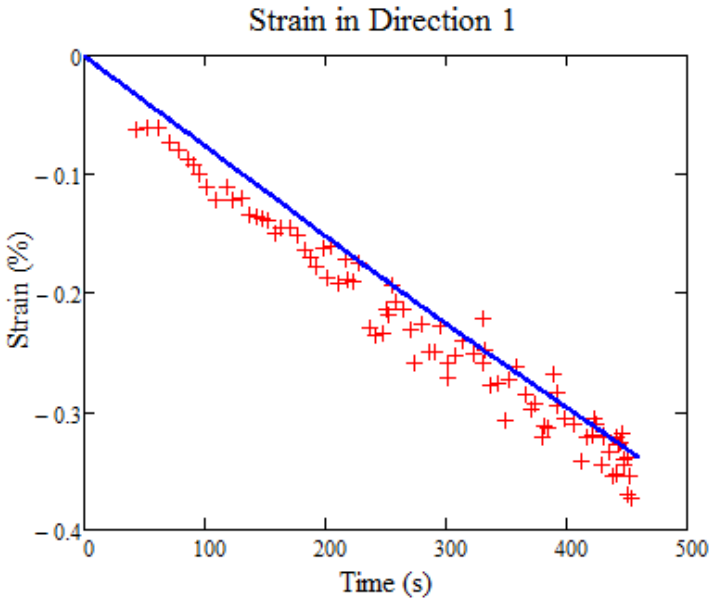

***FIGURE-5.19**: Comparison of Strain in Direction 1 for CMD Specimen– Strain Gauge and DIC Data*

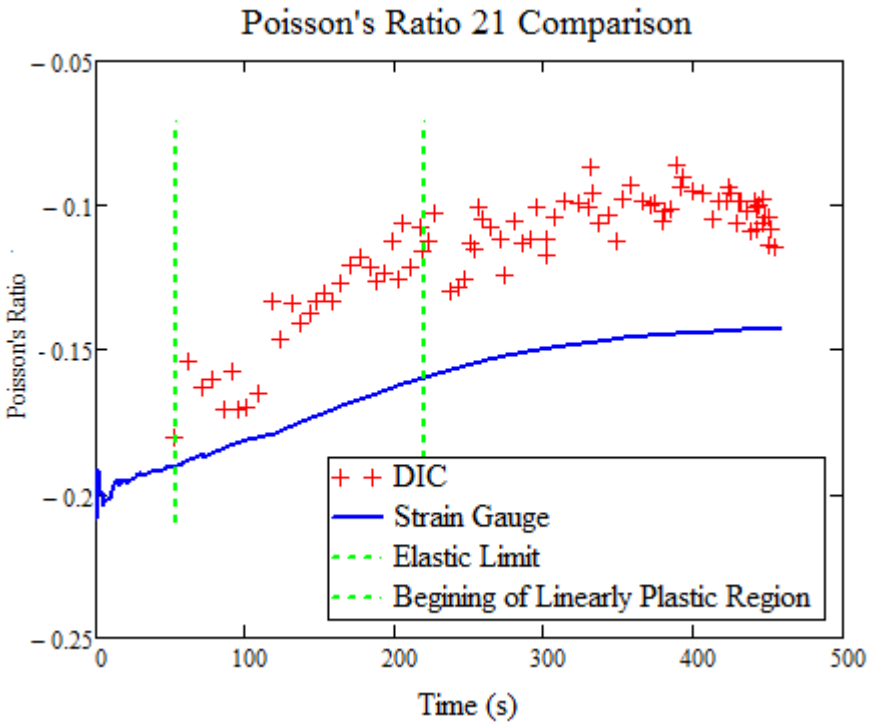

***FIGURE-5.20**: Comparison of Poisson's Ratio v_{21}, CMD Specimen – Strain Gauge and DIC Data*

Elastic v_{21} Strain Gauge	**Elastic v_{21} DIC**	**Plastic v_{21} Strain Gauge**	**Plastic v_{21} DIC**
-0.195	N/A	-.15	-.11

***TABLE-5.3**: Calculated Elastic and Plastic Poisson's Ratios, v_{21}, with Strain Gauges and DIC*

5.4 Conclusions

A test setup is used to calculate the properties of dried and oil-impregnated transformerboard under tensile loadings which compares strain gauge and 3-D DIC data. This test setup is necessary because strain gauges need to be glued on the surfaces of the specimen and application of the glue generates additional resistance to applied loads as explained before. 3-D DIC technique is used because strain gauge and DIC data need to be compared simultaneously and it is an interest to obtain strain values at both surfaces. Therefore, one test will reveal strain data on three principal directions. A method to map strain on each surface is explained and demonstrated before. Failure mechanisms of the MD and CMD specimens are explained based on the observations during the test and the load extension curve. Failure in MD specimen always occurs on thickness direction.

Both MD and CMD specimens shows expansion in thickness direction however, at the beginning of the test material contracts up to a critical level. DIC data shows that this critical level is very short and almost negligible for CMD specimen whereas MD specimen shows much more pronounced contraction. Both time to reach this critical point and the magnitude of the contraction is high for the data obtained from strain gauges because the applied glue keeps very thin sheets together and adds to resistance of cross linked fibers.

Strain in the loading direction was compared to the true strain calculated from the test machine data and agreement between DIC and test machine data provided additional confidence to DIC method. Strain gauges underestimate the strain values and a ratio for MD and CMD specimens calculated.

On the direction perpendicular to loading where short fibers are dominant, data obtained from DIC technique scatters. Also at this direction strain values are small and elastic Poisson's ratio for CMD specimen cannot be calculated with DIC.

Poisson's ratio in the 23 and 32 directions increases with the applied load and no constant value is found on the other hand, Poisson's ratio in 12 and 21 directions are determined by both methods for elastic and linearly plastic regions. Only elastic Poisson's ratio from DIC technique v_{21} was not calculated as the stains were small.

Reliability of DIC method to calculate material properties of transformerboard is shown in this chapter. Using strain gauges can be misleading for this material for the reasons given before. A better understanding of material's response to applied tension load especially in thickness direction is provided and the effect of short fibers upon strain is given. An interesting behaviour of transformerboard, almost linearly increasing positive Poisson's ratio, is shown. Although the results scatter, especially for the plane where short fibers are dominant, practical values for material properties are given and can be a useful design data. The values for elasticity modulus will not be given because this data can be found in manufacturer's data sheets and in [1].

A method can also be used to determine material properties of anisotropic materials with DIC technique. Preparation of strain gauges can be time consuming and DIC technique offers reliable measurements in less time, especially for composite materials made out of

continuous fibers and homogeneous matrix. The cameras need to be calibrated once and materials cut in fiber and cross-fiber directions can be measured to obtain all necessary material properties. If the resolution of the cameras is high enough, some information at the fiber matrix interface can be obtained. Comparing to transformerboard, post-processing is expected to be easier.

6-BENDING TESTS OF TRANSFORMERBOARD

6.1 Introduction

In power transformer design technology clamping rings are frequently used. Axial pressure to stabilize windings is applied through clamping rings made out of transformerboard or densified resin laminated wood because of their perfect electrical insulation capabilities. Because of electrical design constraints, such as the requirement to prevent electrical discharge due to the high electrical field, the pressure is usually maintained by means of small metal components such as metal nuts as shown in Figure-6.1. Because of this arrangement, the clamping ring is subjected to bending therefore the bending behaviour of the material should be examined closely.

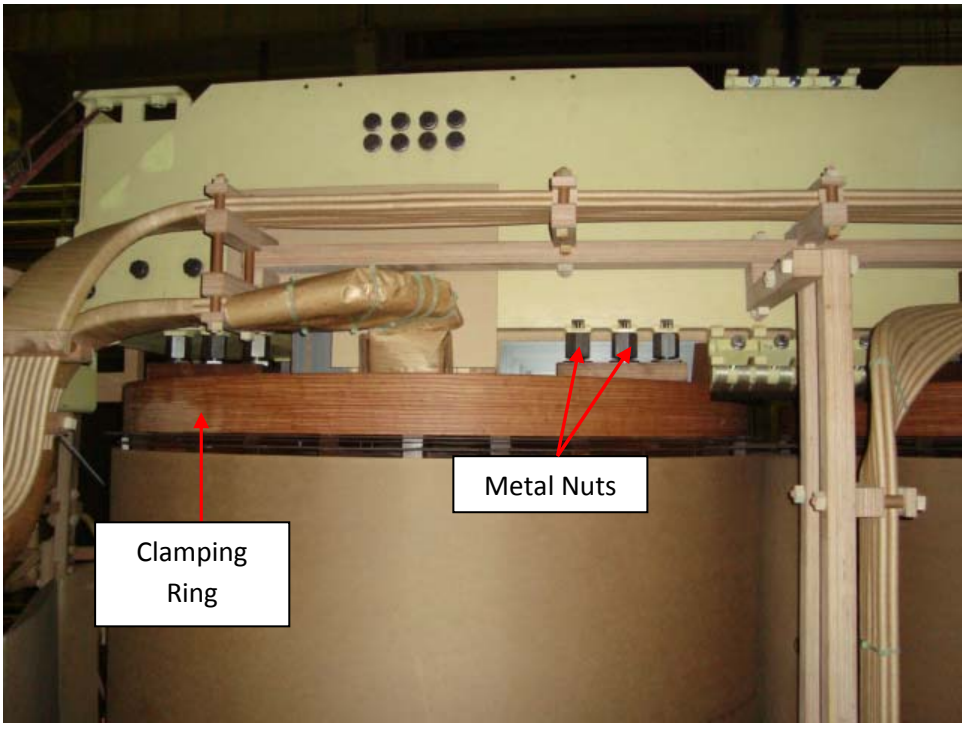

***FIGURE-6.1**: Position of Clamping Ring and Metal Nuts*

It was mentioned in Moser's book [2] that the bending behaviour of transformerboard is not yet investigated properly. Some tests were performed in a manufacturer's plant by Moser in [2] and the basic aim of the research was to compare the transformerboard with resin laminated wood. Delamination between plies was reported but no detailed information was given. The bending strength of the transformerboard was measured up to the delamination point and no information on strain or stress distribution exists in the literature. As expected, transformerboard showed advantages over the resin laminated wood because of its plastic deformation capability.

A complete clamping ring was tested by Moser in [2]. Winding was simulated by a spring bed and the ring was tested according to Figure-6.2. Bending strength was again measured up to delamination and it was suggested that this load level should not be exceeded during the design phase. In [46], some simple formulas were given by treating the ring as a beam between the clamping screws. In order to understand the delamination initiation and to observe in-plane and out of plane bending behaviour of transformerboard, three and four point bending tests are performed on untreated specimens. Dried and oil-impregnated specimens will not be tested in this thesis because the treatment has to be done by a transformer manufacturer in a special facilities and it is recommended to use the specimen within two weeks after the treatment to prevent excessive moisture absorption.

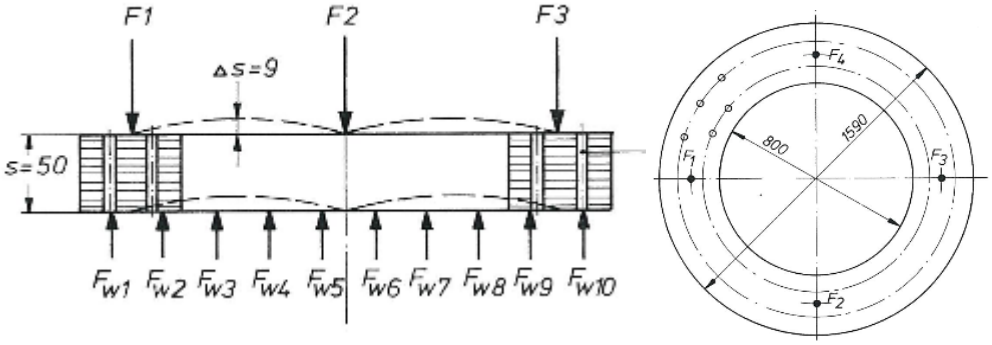

***FIGURE-6.2**: Bending Test Arrangement for Complete Clamping Ring [From Ref.2]*

6.2 Full Analytical Solution to Three and Four Point Bending Tests

Before attempting bending tests, the full solution to three and four point bending tests will be given. Elementary bending theory gives relatively accurate results along the cross-section away from the boundary or loading points but is unable to provide the true strain map on the specimen. One way to provide the strain map is to use finite elements packages. However, whenever loading conditions, material properties or geometry changes a new analysis needs to be run and this is time consuming. Moreover, a full solution can help to identify material properties much more accurately and can give better understanding regarding the material's linearity.

A solution will be attempted for an orthotropic beam. Material linearity is the major assumption in this solution. In [47], the solutions for three and four point bending tests are provided. These solutions used Saint-Venant approximations, the stresses acting along the end of the specimen

are replaced by force and moment relations. The loads and the reaction forces at the supports are expanded into Fourier Series. Therefore, concentrated forces are represented as distributed loads acting on a small area. The solution is represented by hyperbolic functions through the thickness of the beam. In this chapter, a solution will be attempted where force and moment relations at the boundaries at specimen ends are replaced by shear and normal stress relations thus attaining much more accurate solutions. Figure-6.3 shows dimensions and notations used to represent the four point bending test arrangement. Loading can be separated into symmetric-symmetric (SS) and symmetric-asymmetric (SA) components as shown in Figure-6.4 to provide simplifications when solving the bi-harmonic equation. Denoting the stress function for symmetric-symmetric case with Φ_{SS} and symmetric-asymmetric case with Φ_{SA}, final solution is

$$\Phi_T = \Phi_{SS} + \Phi_{SA}$$

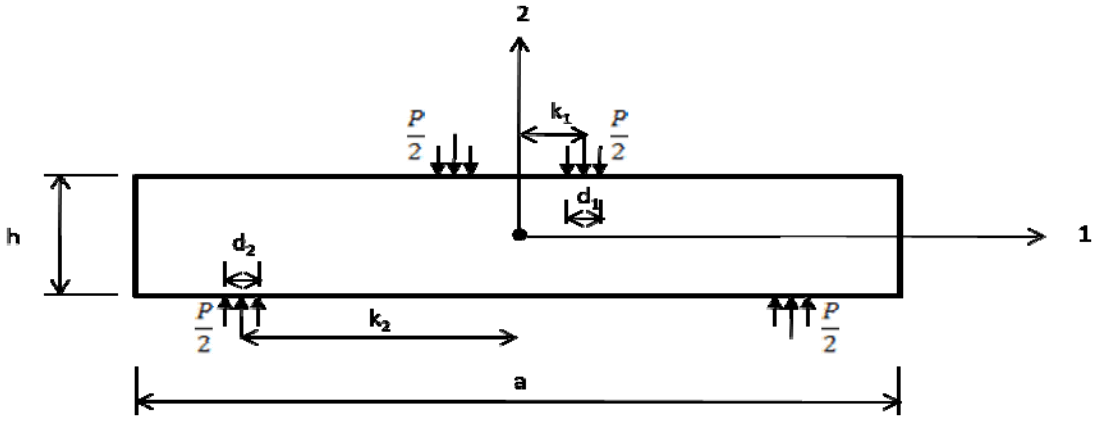

Figure-6.3: *Four-Point Bending Test Arrangement*

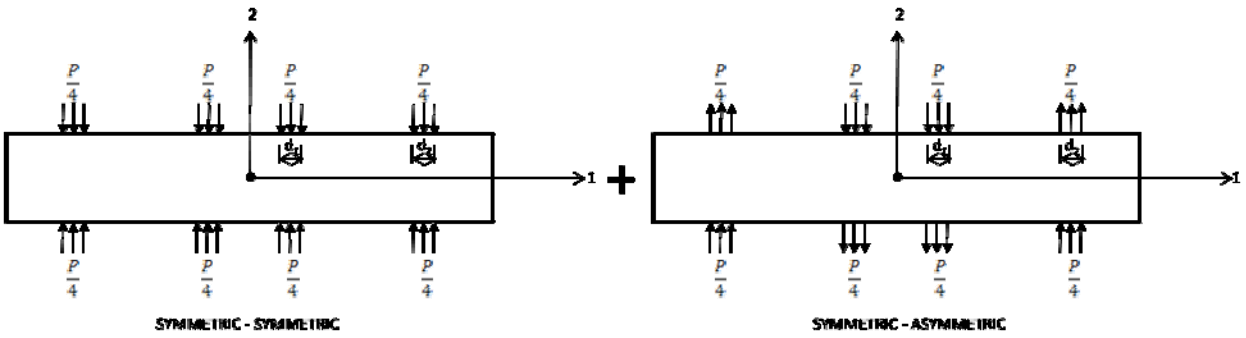

Figure-6.4: *Decomposition of 4PB Test Arrangement*

Compatibility equation for 2-D orthotropic material is given by;

$$S_{11}\frac{\partial^4\Phi}{\partial y^4} + S_{22}\frac{\partial^4\Phi}{\partial x^4} + (S_{66} + 2S_{12})\frac{\partial^4\Phi}{\partial x^2 \partial y^2} = 0 \qquad (6.1)$$

The constant terms which appear in equation (6.1) for plane stress approximation are;

$$S_{11} = \frac{1}{E_1}\,, S_{22} = \frac{1}{E_2}\,, S_{66} = \frac{1}{G_{12}}\,, S_{12} = \frac{-\upsilon_{12}}{E_1} \tag{6.2}$$

The solution to equation (6.1) can be given by;

$$\Phi = \mathrm{A}\frac{\mathrm{x}^2}{2} + \mathrm{B}\frac{\mathrm{y}^2}{2} + \sum_{\mathrm{k}=1}^{\infty}(\mathrm{f_k(x)}\cos(\alpha_\mathrm{k}\mathrm{y}) + \mathrm{h_k(x)}\sin(\alpha_\mathrm{k}\mathrm{y})) + \sum_{\mathrm{j}=1}^{\infty}\left(\mathrm{g_j(y)}\cos\left(\beta_\mathrm{j}\mathrm{x}\right) + \mathrm{r_j(y)}\sin\left(\beta_\mathrm{j}\mathrm{x}\right)\right) \tag{6.3}$$

$$\alpha_\mathrm{k} = \frac{2\pi\mathrm{k}}{\mathrm{h}} \text{ and } \beta_\mathrm{j} = \frac{2\pi\mathrm{j}}{\mathrm{a}} \tag{6.4}$$

Here, polynomial terms with constant coefficients A and B are added to account for constant terms that will appear when representing loads in terms of Fourier series. Further simplifications for the SS case can be obtained because the terms involve $\mathrm{sine}(.)$ will disappear due to symmetry. For the SA case $\sin(\beta_\mathrm{k}\mathrm{x})$ and $\cos(\alpha_\mathrm{k}\mathrm{y})$ terms will disappear due to symmetry in direction 1 and asymmetry in direction 2 respectively. Constant terms will also disappear in (6.3) if equations in (6.5) are used instead of the equations in (6.4). This will also ensure that bending stress in direction 1 will disappear at $x = \pm\frac{a}{2}$ and the boundary condition $\sigma_{11} = 0$ @ $x = \pm\frac{a}{2}$ will be satisfied automatically.

$$\alpha_\mathrm{k} = \frac{\pi(2\mathrm{k}-1)}{\mathrm{h}} \text{ and } \beta_\mathrm{j} = \frac{\pi(2\mathrm{j}-1)}{\mathrm{a}} \tag{6.5}$$

$$\Phi_{\mathrm{SS}} = \sum_{\mathrm{k}=1}^{\infty}\mathrm{f_k(x)}\cos(\alpha_\mathrm{k}\mathrm{y}) + \sum_{\mathrm{j}=1}^{\infty}\mathrm{g_j(y)}\cos(\beta_\mathrm{j}\mathrm{x}) \tag{6.6}$$

$$\Phi_{\mathrm{SA}} = \sum_{\mathrm{j}=1}^{\infty}\mathrm{g_j(y)}\cos(\beta_\mathrm{j}\mathrm{x}) + \sum_{\mathrm{k}=1}^{\infty}\mathrm{h_k(x)}\sin(\alpha_\mathrm{k}\mathrm{y}) \tag{6.7}$$

Assuming $\mathrm{f_k(x)} = \mathrm{F_k}e^{\mu\alpha_\mathrm{k}\mathrm{x}}, \mathrm{g_j(y)} = \mathrm{G_j}e^{\chi\beta_\mathrm{j}\mathrm{y}}$ and $\mathrm{h_k(x)} = \mathrm{H_k}e^{\varphi\alpha_\mathrm{k}\mathrm{x}}$ and substituting these functions in equations (6.3) and (6.1) respectively yields;

$$\mu^4 - \mathrm{A}\mu^2 + \mathrm{B} = 0, \qquad \varphi^4 - \mathrm{A}\varphi^2 + \mathrm{B} = 0, \qquad \chi^4 - \mathrm{C}\chi^2 + \mathrm{D} = 0$$

$$\text{where } A = \frac{(S_{66} + 2S_{12})}{S_{22}}, B = \frac{S_{11}}{S_{22}}, C = \frac{(S_{66} + 2S_{12})}{S_{11}} \; and \;\; D = \frac{S_{22}}{S_{11}} \tag{6.8}$$

$$\mu_{1,2,3,4} = \varphi_{1,2,3,4} = \pm\sqrt{\frac{A \pm \sqrt{A^2 - 4B}}{2}} \text{ and } \chi_{1,2,3,4} = \pm\sqrt{\frac{C \pm \sqrt{C^2 - 4D}}{2}} \tag{6.9}$$

Finally, solution can be written for $f_k(x)$ as;

$$f_k(x) = F_{k1}e^{\mu_1\alpha_k x} + F_{k2}e^{-\mu_1\alpha_k x} + F_{k3}e^{\mu_2\alpha_k x} + F_{k4}e^{-\mu_2\alpha_k x}$$

Or in an alternative form using hyperbolic functions;

$$f_k(x) = \sum_{i=1}^{2}\left(\frac{F1_k \cosh(\mu_i\alpha_k x)}{\cosh\left(\frac{\mu_i\alpha_k a}{2}\right)} + \frac{F2_k \sinh(\mu_i\alpha_k x)}{\cosh\left(\frac{\mu_i\alpha_k a}{2}\right)}\right)$$

Similar results can be found for $g_j(y)$ and $h_k(x)$. In SS case, the terms involving sinh(.) will also disappear resulting in a final stress function of the form (6.10). The term $\cosh\left(\frac{\mu_i\alpha_k a}{2}\right)$ is inserted to provide stability in the calculations.

$$\Phi_{SS} = \sum_{k=1}^{\infty}\sum_{i=1}^{2}\left(\frac{F_{k,i}\cosh(\mu_i\alpha_k x)}{\cosh\left(\frac{\mu_i\alpha_k a}{2}\right)}\right)\cos(\alpha_k y) + \sum_{j=1}^{\infty}\sum_{i=1}^{2}\left(\frac{G_{j,i}\cosh(\chi_i\beta_j y)}{\cosh\left(\frac{\chi_i\beta_j h}{2}\right)}\right)\cos(\beta_j x) \tag{6.10}$$

$$\Phi_{SA} = \sum_{j=1}^{\infty}\sum_{i=1}^{2}\left(\frac{C_{j,i}\sinh(\chi_i\beta_j y)}{\cosh\left(\frac{\chi_i\beta_j h}{2}\right)}\right)\cos(\beta_j x) + \sum_{k=1}^{\infty}\sum_{i=1}^{2}\left(\frac{H_{k,i}\cosh(\mu_i\alpha_k x)}{\cosh\left(\frac{\mu_i\alpha_k a}{2}\right)}\right)\sin(\alpha_k y) \tag{6.11}$$

Stresses can be found using the relationships below.

$$\sigma_{11} = \frac{\partial^2\Phi}{\partial y^2}, \sigma_{22} = \frac{\partial^2\Phi}{\partial x^2}, \tau_{12} = -\frac{\partial^2\Phi}{\partial x \partial y} \tag{6.12}$$

6.3 Solution to Symmetric- Symmetric (SS) Case

Substituting equation (6.10) in (6.12) yields;

$$\sigma_{SS11} = -\sum_{k=1}^{\infty}{\alpha_k}^2\sum_{i=1}^{2}\left(\frac{F_{k,i}\cosh(\mu_i\alpha_k x)}{\cosh\left(\frac{\mu_i\alpha_k a}{2}\right)}\right)\cos(\alpha_k y) + \sum_{j=1}^{\infty}{\beta_j}^2\sum_{i=1}^{2}(\chi_i)^2\left(\frac{G_{j,i}\cosh(\chi_i\beta_j y)}{\cosh\left(\frac{\chi_i\beta_j h}{2}\right)}\right)\cos(\beta_j x) \tag{6.13}$$

$$\sigma_{SS22} = \sum_{k=1}^{\infty}{\alpha_k}^2\sum_{i=1}^{2}\left((\mu_i)^2\frac{F_{k,i}\cosh(\mu_i\alpha_k x)}{\cosh\left(\frac{\mu_i\alpha_k a}{2}\right)}\right)\cos(\alpha_k y) - \sum_{j=1}^{\infty}{\beta_j}^2\sum_{i=1}^{2}\left(\frac{G_{j,i}\cosh(\chi_i\beta_j y)}{\cosh\left(\frac{\chi_i\beta_j h}{2}\right)}\right)\cos(\beta_j x) \tag{6.14}$$

$$\tau_{SS12} = \sum_{k=1}^{\infty} {\alpha_k}^2 \sum_{i=1}^{2} \left(\mu_i \frac{F_{k,i} \sinh(\mu_i \alpha_k x)}{\cosh\left(\frac{\mu_i \alpha_k a}{2}\right)} \right) \sin(\alpha_k y) + \sum_{j=1}^{\infty} {\beta_j}^2 \sum_{i=1}^{2} \left(\chi_i \frac{G_{j,i} \sinh(\chi_i \beta_j y)}{\cosh\left(\frac{\chi_i \beta_j h}{2}\right)} \right) \sin(\beta_j x) \tag{6.15}$$

Boundary conditions are;

$$\sigma_{SS11} = 0 \ @ \ x = \pm \frac{a}{2} \tag{6.16}$$

$$\tau_{SS12} = 0 \ @ \ x = \pm \frac{a}{2} \tag{6.17}$$

$$\tau_{SS12} = 0 \ @ \ y = \pm \frac{h}{2} \tag{6.18}$$

$$\sigma_{SS22} = -\frac{P}{4b}\frac{1}{d_1} - \frac{P}{4b}\frac{1}{d_2} \ , \left(k_1 - \frac{d_1}{2} \le x \le k_1 + \frac{d_1}{2}\right) , \left(k_2 - \frac{d_2}{2} \le x \le k_2 + \frac{d_2}{2}\right), @ \ y = \pm \frac{h}{2} \tag{6.19}$$

where b is the depth of the beam.

From boundary condition (6.16);

$$F_{k,1} + F_{k,2} = 0 \tag{6.21}$$

From boundary condition (6.17), after applying Finite Fourier Sine Transform yields;

$$\sum_{i=1}^{2} \mu_i F_{k,i} \tanh\left(\mu_i \alpha_k \frac{a}{2}\right) = -\frac{4}{h{\alpha_k}^2} \sum_{j=1}^{\infty} {\beta_j}^3 \sum_{i=1}^{2} \left(G_{j,i} \frac{{\chi_i}^2}{\left(\chi_i \beta_j\right)^2 + (\alpha_k)^2} \right) (-1)^{j+k} \tag{6.22}$$

From boundary condition (6.18), after applying Finite Fourier Sine Transform yields;

$$\sum_{i=1}^{2} \chi_i G_{j,i} \tanh\left(\chi_i \beta_j \frac{h}{2}\right) = -\frac{4}{a{\beta_j}^2} \sum_{k=1}^{\infty} {\alpha_k}^3 \sum_{i=1}^{2} \left(F_{k,i} \frac{{\mu_i}^2}{(\mu_i \alpha_k)^2 + \left(\beta_j\right)^2} \right) (-1)^{j+k} \tag{6.23}$$

From boundary condition (6.19), after applying Finite Fourier Cosine Transform yields;

$$\sum_{i=1}^{2} G_{j,i} = \frac{2P}{b}\frac{1}{{\beta_j}^3 a}\left[\frac{1}{d_1}\sin\left(\beta_j \frac{d_1}{2}\right)\cos(\beta_j k_1) + \frac{1}{d_2}\sin\left(\beta_j \frac{d_2}{2}\right)\cos(\beta_j k_2)\right] = K \tag{6.24}$$

Substituting (6.21) and (6.24) into (6.22) and (6.23);

$$F_{k,1} = \frac{-4}{Wh{\alpha_k}^2}\left(\sum_{j=1}^{\infty} {\beta_j}^3 G_{j,1}\left(\frac{(-1)^{j+k}{\chi_1}^2}{\left(\chi_1\beta_j\right)^2 + (\alpha_k)^2} - \frac{(-1)^{j+k}{\chi_2}^2}{\left(\chi_2\beta_j\right)^2 + (\alpha_k)^2}\right) + \sum_{j=1}^{\infty} {\beta_j}^3 \frac{(-1)^{j+k}{\chi_2}^2}{\left(\chi_2\beta_j\right)^2 + (\alpha_k)^2} K\right) \quad (6.25)$$

$$Where\ W = \mu_1 \tanh\left(\mu_1\alpha_k\frac{a}{2}\right) - \mu_2 \tanh\left(\mu_2\alpha_k\frac{a}{2}\right)$$

$$G_{j,1} = -\frac{4}{Ya{\beta_j}^2}\left[\sum_{k=1}^{\infty} {\alpha_k}^3 F_{k,1}(-1)^{j+k}\left(\frac{{\mu_1}^2}{(\mu_1\alpha_k)^2 + \left(\beta_j\right)^2} - \frac{{\mu_2}^2}{(\mu_2\alpha_k)^2 + \left(\beta_j\right)^2}\right)\right] - \frac{\chi_2}{Y}\tanh\left(\chi_2\beta_j\frac{h}{2}\right) K \quad (6.26)$$

$$Where\ Y = \chi_1 \tanh\left(\chi_1\beta_j\frac{h}{2}\right) - \chi_2 \tanh\left(\chi_2\beta_j\frac{h}{2}\right)$$

It is easier to solve equations (6.25) and (6.26) in matrix form. Denoting the first term on the right hand side in equation (6.25) by $\left[Q_{k,j}\right]$ and second term by $\{E_j\}$, where [.] represents matrix and {.} represents a vector, equation (6.25) and (6.26) can be written in the following form.

$$\{F_{k,1}\} = \left[Q_{k,j}\right]\{G_{j,1}\} + \{E_k\} \quad (6.27)$$

$$\{G_{j,1}\} = \left[D_{j,k}\right]\{F_{k,1}\} + \{Z_j\} \quad (6.28)$$

Substitute (6.28) in (6.27),

$$\{F_{k,1}\} = \left([I] - \left[Q_{k,j}\right]\left[D_{j,k}\right]\right)^{-1}\left(\left[Q_{k,j}\right]\{Z_j\} + \{E_k\}\right) \qquad I = Identity\ Matrix \quad (6.29)$$

Remaining constants can be found using equations (6.28), (6.24) and (6.21).

6.4 Solution to Symmetric – Asymmetric (SA) Case

Substituting equation (6.11) in (6.12) yields;

$$\sigma_{SA11} = \sum_{j=1}^{\infty} {\beta_j}^2 \sum_{i=1}^{2} (\chi_i)^2 \left(\frac{C_{j,i}\sinh(\chi_i\beta_j y)}{\cosh\left(\frac{\chi_i\beta_j h}{2}\right)}\right)\cos(\beta_j x) - \sum_{k=1}^{\infty} {\alpha_k}^2 \sum_{i=1}^{2}\left(\frac{H_{k,i}\cosh(\mu_i\alpha_k x)}{\cosh\left(\frac{\mu_i\alpha_k a}{2}\right)}\right)\sin(\alpha_k y) \quad (6.30)$$

$$\sigma_{SA22} = -\sum_{j=1}^{\infty} {\beta_j}^2 \sum_{i=1}^{2}\left(\frac{C_{j,i}\sinh(\chi_i\beta_j y)}{\cosh\left(\frac{\chi_i\beta_j h}{2}\right)}\right)\cos(\beta_j x) + \sum_{k=1}^{\infty} {\alpha_k}^2 \sum_{i=1}^{2}\left((\mu_i)^2\frac{H_{k,i}\cosh(\mu_i\alpha_k x)}{\cosh\left(\frac{\mu_i\alpha_k a}{2}\right)}\right)\sin(\alpha_k y) \quad (6.31)$$

$$\tau_{SA12} = \sum_{j=1}^{\infty} {\beta_j}^2 \sum_{i=1}^{2}\left(\chi_i\frac{C_{j,i}\cosh(\chi_i\beta_j y)}{\cosh\left(\frac{\chi_i\beta_j h}{2}\right)}\right)\sin(\beta_j x) - \sum_{k=1}^{\infty} {\alpha_k}^2 \sum_{i=1}^{2}\left(\mu_i\frac{H_{k,i}\sinh(\mu_i\alpha_k x)}{\cosh\left(\frac{\mu_i\alpha_k a}{2}\right)}\right)\cos(\alpha_k y) \quad (6.32)$$

Boundary conditions (6.16), (6.17) and (6.18) are the same. The last boundary condition becomes;

$$\sigma_{SS22} = -\frac{P}{4b}\frac{1}{\mathrm{d}_1} + \frac{P}{4b}\frac{1}{\mathrm{d}_2}\ , \left(\mathrm{k}_1 - \frac{\mathrm{d}_1}{2} \le x \le \mathrm{k}_1 + \frac{\mathrm{d}_1}{2}\right), \left(\mathrm{k}_2 - \frac{\mathrm{d}_2}{2} \le x \le \mathrm{k}_2 + \frac{\mathrm{d}_2}{2}\right), @\ y = \pm\frac{h}{2} \qquad (6.33)$$

Substituting the boundary conditions in Equations (6.30), (6.31) and (6.32) and using Finite Fourier Transforms when necessary;

$$\mathrm{H}_{\mathrm{k},1} + \mathrm{H}_{\mathrm{k},2} = 0 \qquad (6.34)$$

$$\sum_{\mathrm{i}=1}^{2} \mu_{\mathrm{i}}\, \mathrm{H}_{\mathrm{k,i}} \tanh\left(\mu_{\mathrm{i}}\alpha_{\mathrm{k}}\frac{\mathrm{a}}{2}\right) = \frac{4}{\mathrm{h}\alpha_{\mathrm{k}}} \sum_{\mathrm{j}=1}^{\infty} {\beta_{\mathrm{j}}}^2 \sum_{\mathrm{i}=1}^{2} \left(\mathrm{C}_{\mathrm{j,i}} \frac{\chi_{\mathrm{i}}}{\left(\chi_{\mathrm{i}}\beta_{\mathrm{j}}\right)^2 + (\alpha_{\mathrm{k}})^2}\right)(-1)^{\mathrm{j}+\mathrm{k}} \qquad (6.35)$$

$$\chi_1 \mathrm{C}_{\mathrm{j},1} + \chi_2 \mathrm{C}_{\mathrm{j},2} = 0 \qquad (6.36)$$

$$\sum_{\mathrm{i}=1}^{2} \mathrm{C}_{\mathrm{j,i}} \tanh\left(\chi_{\mathrm{i}}\beta_{\mathrm{j}}\frac{\mathrm{h}}{2}\right) = \mathrm{K2} + \frac{4}{\mathrm{a}\beta_{\mathrm{j}}} \sum_{\mathrm{k}=1}^{\infty} {\alpha_{\mathrm{k}}}^2 \sum_{\mathrm{i}=1}^{2} \left(\mathrm{H}_{\mathrm{k,i}} \frac{{\mu_{\mathrm{i}}}^2}{(\mu_{\mathrm{i}}\alpha_{\mathrm{k}})^2 + \left(\beta_{\mathrm{j}}\right)^2}\right)(-1)^{\mathrm{j}+\mathrm{k}} \qquad (6.37)$$

$$\text{Where } \mathrm{K2} = \frac{2\mathrm{P}}{\mathrm{b}}\frac{1}{{\beta_{\mathrm{j}}}^3 \mathrm{a}}\left[\frac{1}{\mathrm{d}_1}\sin\left(\beta_{\mathrm{j}}\frac{\mathrm{d}_1}{2}\right)\cos\left(\beta_{\mathrm{j}}\mathrm{k}_1\right) - \frac{1}{\mathrm{d}_2}\sin\left(\beta_{\mathrm{j}}\frac{\mathrm{d}_2}{2}\right)\cos\left(\beta_{\mathrm{j}}\mathrm{k}_2\right)\right]$$

Substituting (6.34) and (6.36) into (6.35) and (6.37);

$$\mathrm{H}_{\mathrm{k},1} = \frac{4}{\mathrm{Wh}\alpha_{\mathrm{k}}} \sum_{\mathrm{j}=1}^{\infty} {\beta_{\mathrm{j}}}^2\, \mathrm{C}_{\mathrm{j},1}(-1)^{\mathrm{j}+\mathrm{k}} \left(\frac{\chi_1}{\left(\chi_1\beta_{\mathrm{j}}\right)^2 + (\alpha_{\mathrm{k}})^2} - \frac{\chi_1}{\left(\chi_2\beta_{\mathrm{j}}\right)^2 + (\alpha_{\mathrm{k}})^2}\right) \qquad (6.38)$$

$$\mathrm{C}_{\mathrm{j},1} = \frac{4}{\mathrm{Ma}\beta_{\mathrm{j}}} \sum_{\mathrm{k}=1}^{\infty} {\alpha_{\mathrm{k}}}^2\, \mathrm{H}_{\mathrm{k},1}(-1)^{\mathrm{j}+\mathrm{k}} \left(\frac{{\mu_1}^2}{(\mu_1\alpha_{\mathrm{k}})^2 + \left(\beta_{\mathrm{j}}\right)^2} - \frac{{\mu_2}^2}{(\mu_2\alpha_{\mathrm{k}})^2 + \left(\beta_{\mathrm{j}}\right)^2}\right) + \frac{\mathrm{K2}}{\mathrm{M}} \qquad (6.39)$$

$$Where\ M = \frac{\chi_2 \tanh\left(\chi_1\beta_{\mathrm{j}}\frac{\mathrm{h}}{2}\right) - \chi_1 \tanh\left(\chi_2\beta_{\mathrm{j}}\frac{\mathrm{h}}{2}\right)}{\chi_2}$$

Writing above equations in matrix form;

$$\{H_{k,1}\} = [S_{k,j}]\{C_{j,1}\} \qquad (6.40)$$

$$\{C_{j,1}\} = [U_{j,k}]\{H_{k,1}\} + \{T_j\} \qquad (6.41)$$

Substitute (6.28) in (6.27);

$$\{C_{j,1}\} = \left([I] - [U_{j,k}][S_{k,j}]\right)^{-1}\{T_j\} \qquad I = Identity\ Matrix \tag{6.42}$$

Remaining constants can be found using equations (6.40), (6.36) and (6.34). Final solution can be found by adding SS and SA cases. Strains can be found using Hooke's Law.

$$\begin{pmatrix}\varepsilon_{11}\\ \varepsilon_{22}\\ \gamma_{12}\end{pmatrix} = \begin{bmatrix}\frac{1}{E_1} & \frac{-\upsilon_{21}}{E_2} & 0\\ \frac{-\upsilon_{12}}{E_1} & \frac{1}{E_2} & 0\\ 0 & 0 & \frac{1}{G_{12}}\end{bmatrix}\begin{pmatrix}\sigma_{11}\\ \sigma_{22}\\ \tau_{12}\end{pmatrix} \tag{6.43}$$

Solution to three point bending test can simply be obtained by setting k_1=0.

In order to gain confidence on the method developed, the results of the analysis will be compared to FEA. In FEA analysis, the actual pin sizes used during the tests will be used and the pins will be represented by analytical rigid elements. Therefore, no deformation is allowed in the pins. This is a reasonable assumption as the transformerboard's rigidity is low and some indentation takes place as the load level increases. Dimensions, loads and material properties used in the comparison are given in Table-6.1. All dimensions are in mm and loadings are in Newton.

h(mm)	**Depth(mm)**	**a(mm)**	**k1(mm)**	**k2(mm)**	**d1(mm)**	**d2(mm)**	**P(N)**
20	20	200	0	80	1	1	200
E_{11} (MPa)	**E_{22}(MPa)**	**ν_{12}**	**G_{12}(MPa)**				
16000	6000	0.2	2000				

***TABLE-6.1**: Dimensions, Loads and Material Properties Used in Comparison*

Figure-6.5 shows comparison of bending and shear strain distribution at -40mm, mid-plane between loading and support, and Figure-6.6 show normal and shear strain distribution at -5mm. Near to perfect agreement provides confidence in the theory proposed.

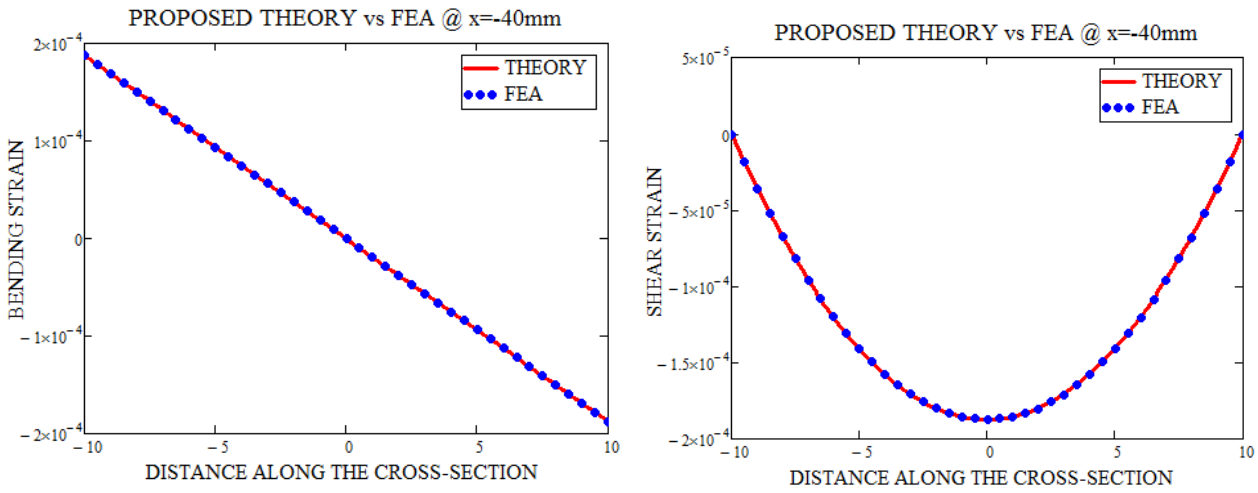

Figure-6.5: *Comparison of Bending and Shear Strain Distribution at -40mm*

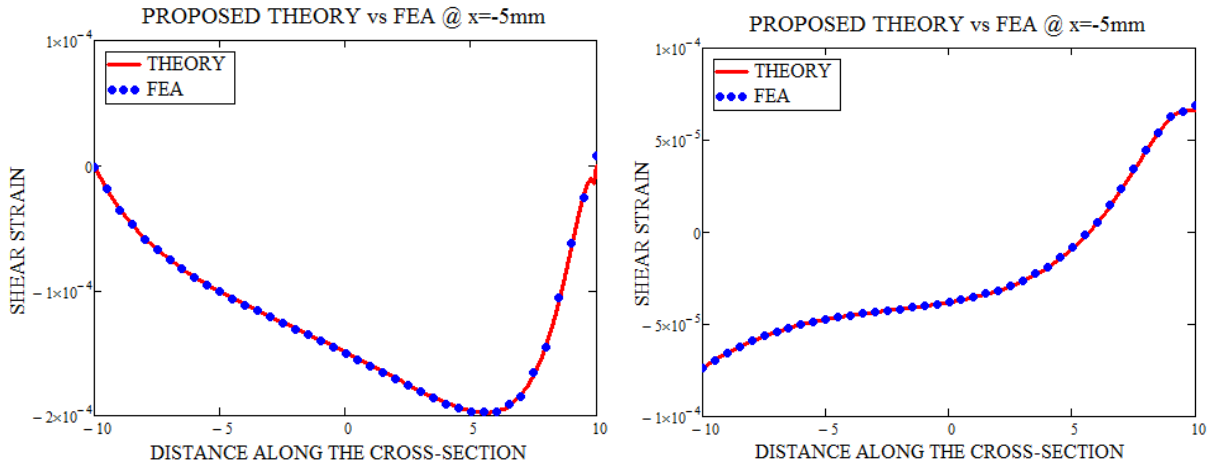

Figure-6.6: *Comparison of Normal and Shear Strain Distribution at -5mm*

The developed method does not consider Saint-Venant approximation and therefore, can be employed to determine the stress and the strain distributions in areas close to the material edges in x direction. In order to test the accuracy at these points, cross-section data obtained by the proposed method at x=-90mm are compared to FEA results. Figure-6.7 shows the agreement. However, at the material edges in y direction, namely at y=10mm and y=-10mm, agreement is clearly spoiled. This is because the applied forces and reaction forces are expressed in terms of Fourier Series. Because the series truncated at some number, the representation of applied forces are not complete in this sense. Moreover, applied forces are also used to define boundary conditions 6.19 and 6.33. The final double series are also truncated at some number and adding all these truncation and Fourier representation errors contributes these differences.

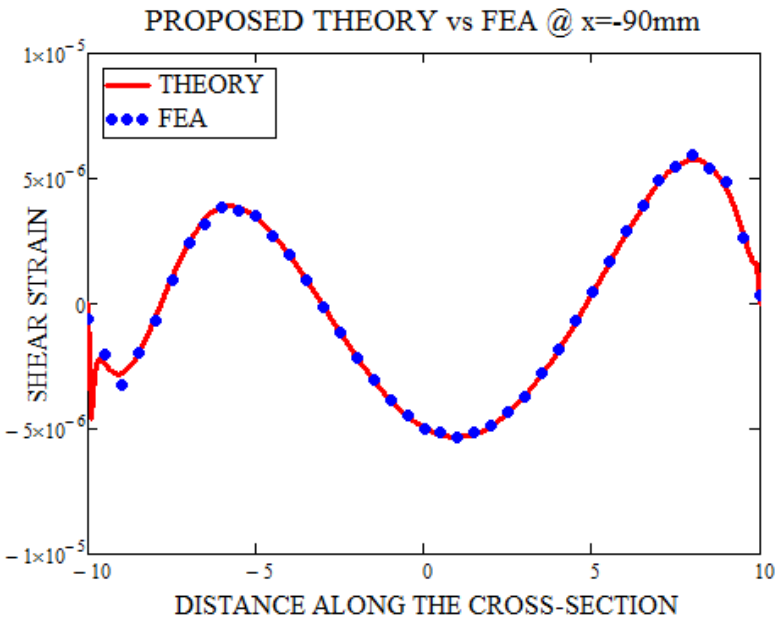

Figure-6.7: *Comparison of Shear Strain Distribution at -90mm*

Lastly, shear and bending strain map on specimen, obtained from the theory developed, will be given in Figure-6.8 and Figure-6.9 respectively.

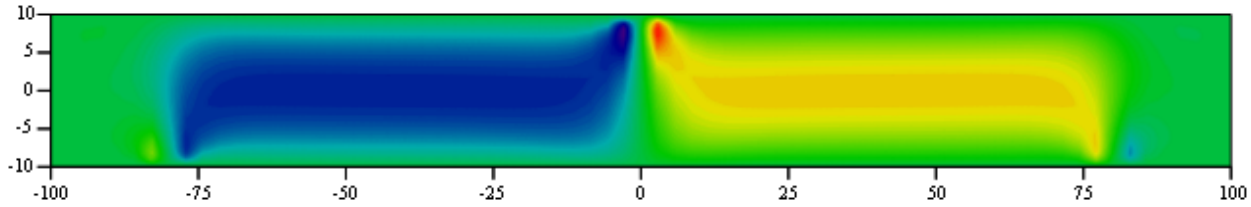

Figure-6.8: *Shear Strain Distribution*

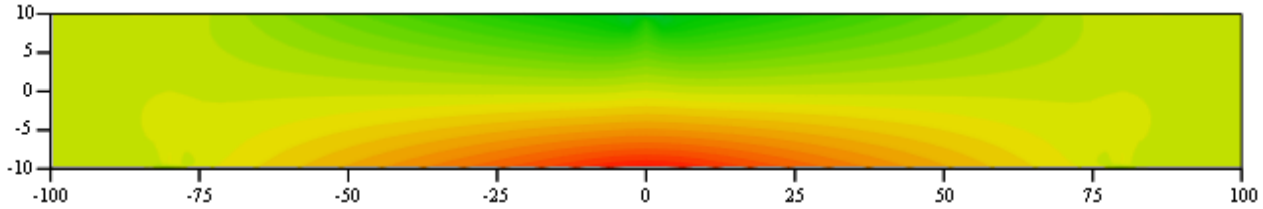

Figure-6.9: *Bending Strain Distribution*

6.5 Three Point Bending Tests

Three point bending test specimen dimensions are shown in Figures-6.10 and 6.11. Specimens are made of 4 layers of 5mm thick transformerboard plies and are subjected to three-point bending loading through pins of 10mm diameter. Tests were performed at 5mm/min test speed for all specimens. Although tests at higher test speeds are performed, these were mainly for the purpose of capturing the initiation of delamination.

Tests were performed on four different specimens. These are listed below. Z direction is the stacking direction.

- Speckle pattern created on the plane as shown in Figure-6.10 and fiber orientation through x direction is machine direction. Variant-1
- Speckle pattern created on the plane as shown in Figure-6.10 and fiber orientation through x direction is cross machine direction. Variant-2
- Speckle pattern created on the plane as shown in Figure-6.11 and fiber orientation through x direction is machine direction. Variant-3
- Speckle pattern created on the plane as shown in Figure-6.11 and fiber orientation through x direction is cross machine direction. Variant-4

DIC technique is used to map the out of plane strain distribution of the specimen. VIC 3-D cameras used during the tests that have DIC and fast speed photography features. Initiation of delamination is captured with high speed photography feature and displacement/strain distribution is mapped.

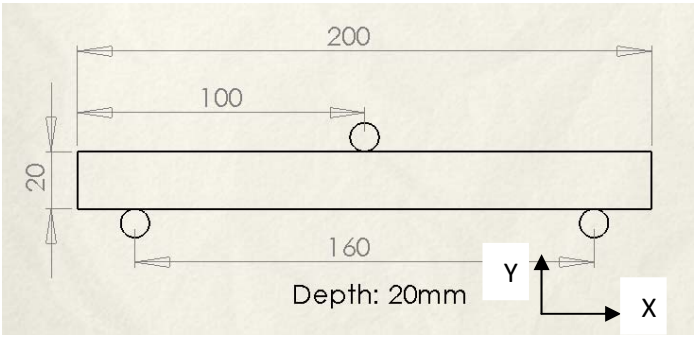

***FIGURE-6.10**: Dimensions of Three-Point Test Specimen for Variants 1 and 2*

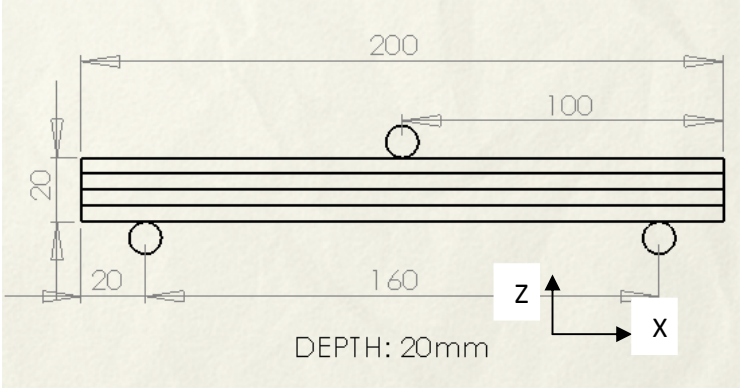

***FIGURE-6.11**: Dimensions of Three-Point Test Specimen for Variants 3 and 4*

6.6 Delamination Initiation

All test specimens of Variant-3 and Variant-4 failed by delamination after some deflection under flexural loading. In order to capture the initiation of the delamination, fast speed photography technique is used. Frame rate was set to 75000 frames per second (fps) and shutter was set to 1/100000. Test machine speed was 200mm/min. One of the three point bending test specimen was not painted and no speckle pattern was created on its surface to observe delamination initiation more accurately without using the DIC option. Figure-6.12 shows the initiation of delamination. Delamination was started between two pins and propagated through the specimen until half of the specimen was separated. The material did not delaminate at the bonding surface but delamination occurred on the transformerboard ply. The delamination plane was very close to mid-plane, bonding region of the test specimen. All the specimens at this loading plane were failed in the same way described above.

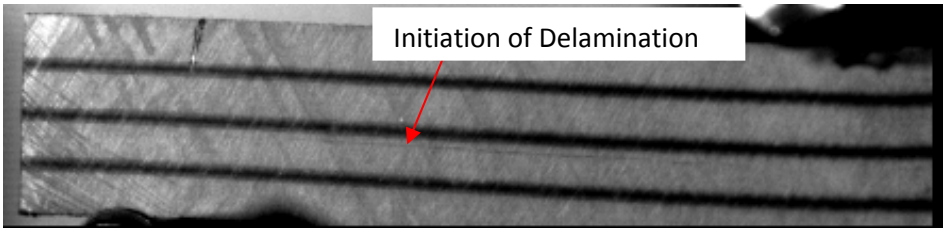

***FIGURE-6.12**: Start of Delamination*

Delamination tends to occur where interlaminar shear stresses reach their maximum value. It is known from conventional bending theory that the shear stress has a parabolic distribution over the cross-section and reaches its peak value at the middle. However, the transformerboard did not fail at the mid-plane. This is due to manufacturing process of the transformerboard. Each lamina of transformerboard is formed by stacking very thin wet sheets containing fibres without any bonding agent to form required thickness. The stack of wet sheets is then compressed and dehydrated in a special hot press. The hot and moist fibres become cross-linked and the bonding is achieved between many layers of sheets and transformerboard lamina is formed. When two laminas are glued, the bonding strength between these two laminas is much higher than the bonding generated by cross-linked fibers and the failure due to interlaminar shear stresses does not occur at the interface where two laminas are glued to each other.

Figure-6.13, using the DIC feature of the cameras, shows the shear strain concentration at the delamination region during four point bending test just before failure which supports the failure

mode. The test speed is the same as before but the camera settings (10000fps and 1/20000 shutter speed) are different in order to increase the resolution of the cameras to capture the whole behavior.

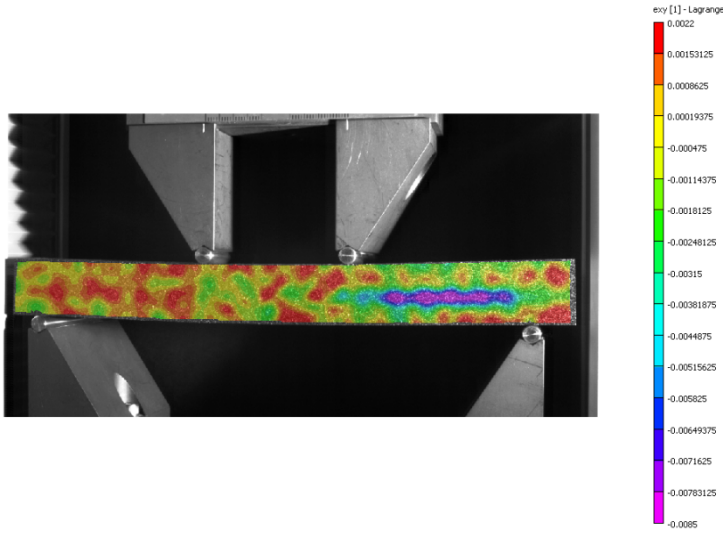

***FIGURE-6.13**: Strain Concentration before Delamination*

Figure-6.14 shows the shear stress distribution just after the delamination occurrence for three point bending specimen. Complete fracture between the pins can be clearly seen. Because the transformerboard split into two parts, high shear stresses are acting at the delaminated region. The DIC technique did not capture the whole strain pattern at the separation points but, the general pattern can be seen clearly.

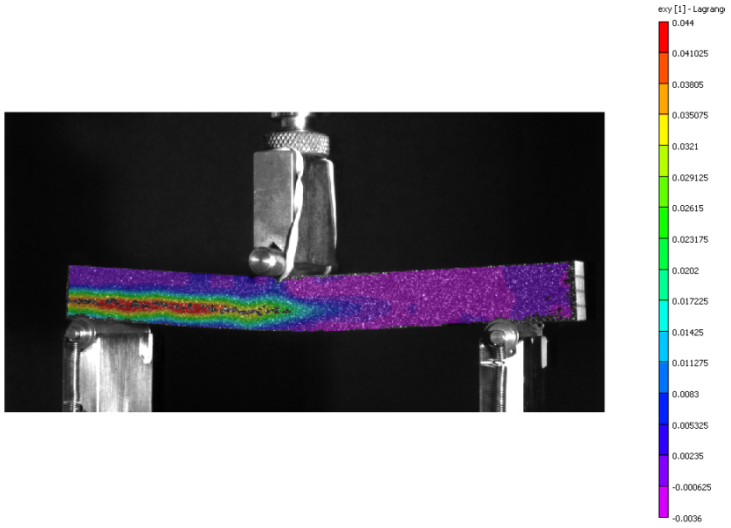

***FIGURE-6.14**: Shear Stress Mapping after Delamination*

6.7 Three Point Bending Test Results of Variant-1 and 2

Tests performed at 5mm/min rate and cameras are set to 50fps frame rate in order to capture the whole test data and shutter was set to 1/frame. Figure-6.15 shows the distribution of the strain component ε_{xx} for Variant-1 at 3 and 5mm crosshead displacements respectively. The maximum bending strain occurs at mid-plane where maximum bending moments act as expected. Transformerboard is not subject to a load at this plane when used in transformers but in order to understand the material's behaviour against different loading conditions, these tests are necessary. Indentation effect at the loading area is much more severe in this case. As the crosshead displacement increases, a local increase in depth of the specimen at loading area was observed. This is because the bonding between cross-linked fibres is broken causing local separation and increase in depth as shown in Figure-6.16. Same behaviour is also observed during tensile tests.

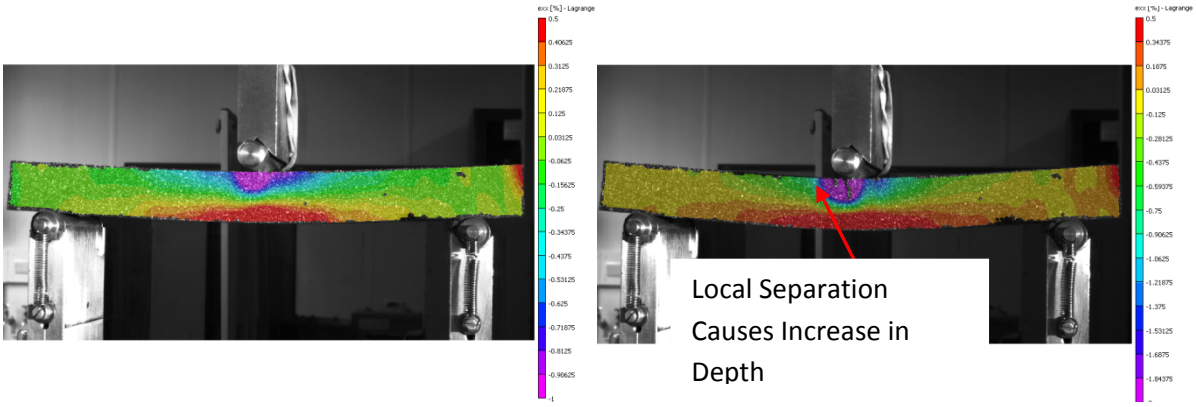

FIGURE-6.15 *DIC Results for Bending Strain at 3 and 5 mm respectively*

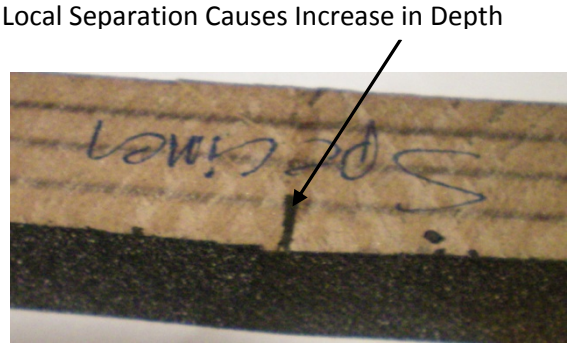

FIGURE-6.16*: Local Separation after Test*

Load-Displacement curve is shown in Figure-6.17. The material shows linearity at the beginning of the test up to 1.4mm crosshead displacement and after this point non-linearity starts. This is

the point at which local separation is observed meaning cross-linked bonding between fibers are starting to break.

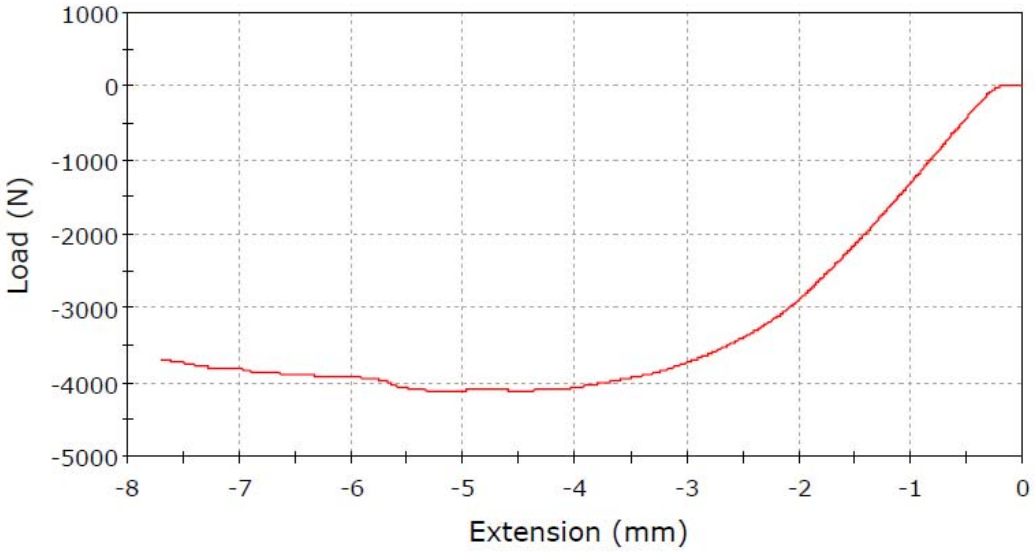

***FIGURE-6.17**: Load-Extension Curve for Variant-1*

In order to gain confidence in the results obtained from DIC, elasticity modulus will be calculated using simple beam theory and the load-displacement curve. These results will be compared to cross-section data obtained from DIC at the mid-plane between the support and the loading point. To calculate bending modulus from load-displacement curve:

$$E_{xxB} = \frac{FL^3}{48\delta I} \quad (6.44)$$

Here, E_{xxB} is the bending modulus, F is the applied load, I is the second moment of area and δ is the deflection. To calculate the elasticity modulus from DIC data at the cross section:

$$\sigma_{xx} = \frac{My}{I}, E_{xx} = \frac{20Fy}{I\varepsilon_{xx}} \quad (6.45)$$

Here, M is the bending moment, E_{xx} is the elasticity modulus and ε_{xx} is the bending strain. Figure-6.18 shows the distribution of the bending strain at the cross-section. It is expected that the bending strain should be zero at the neutral axis but it is not. This is caused by the choice of coordinate axis before processing the results and therefore, the distance should be corrected. This will be achieved by finding the value of the bending strain where it changes its sign from negative to positive and applying linear interpolation between these two points. Calculated point

using linear interpolation gives the position of the neutral axis. Subtracting the value of this point from the original data gives the corrected distance. Figure-6.19 shows the corrected graph and Table-6.2 shows the elasticity modulus obtained from equations 6.44 and 6.45 at different load levels.

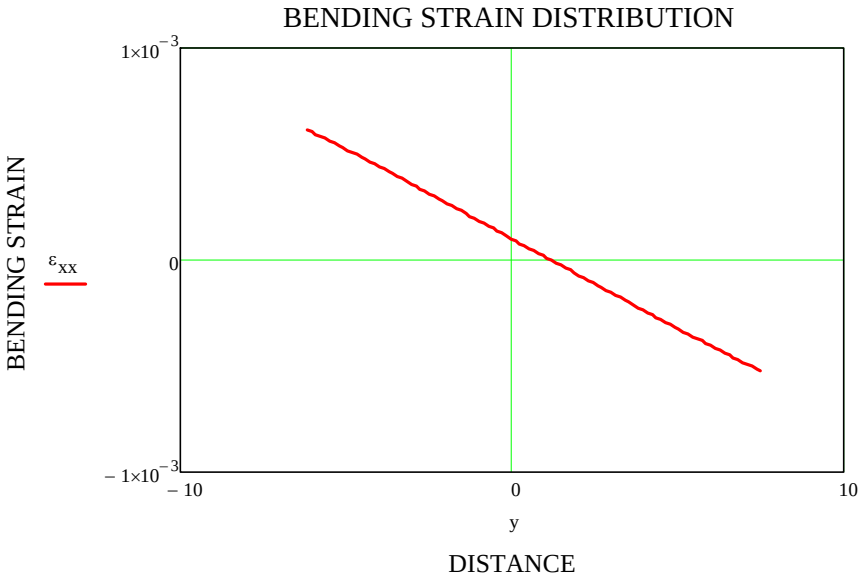

***FIGURE-6.18**: Distribution of the Bending Strain at Mid-Plane- From DIC*

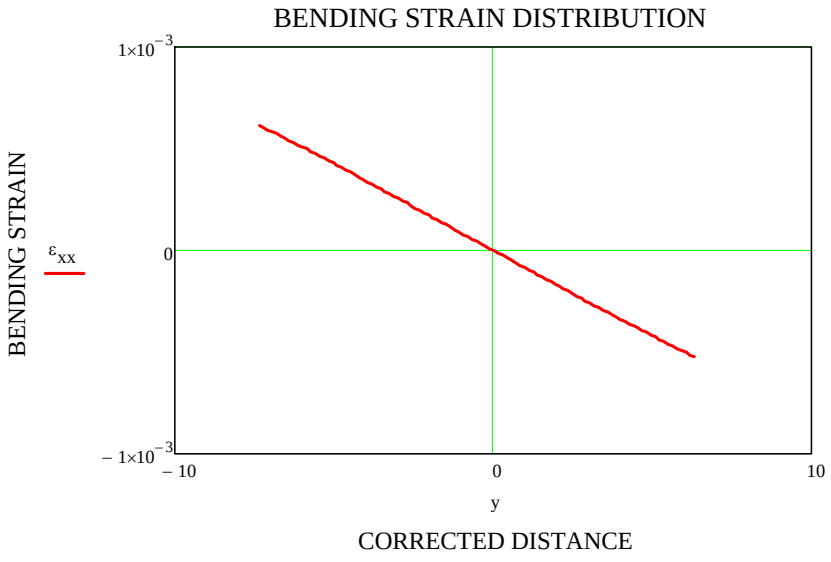

***FIGURE-6.19**: Corrected Distribution of the Bending Strain at Mid-Plane- From DIC at 580N Load*

	580N	**1100N**	**1610N**	**2170N**	**AVERAGE**
DIC	11430	11900	11500	12445	11818
3PB Test	~11000				

***TABLE-6.2** Comparison of Elasticity Modulus (MPa) – DIC and Load Deflection Curve*

Linearity can be observed from both load-deflection curve and DIC cross-section curve in this loading case. The position of the neutral axis is very close to the middle of the cross-section after appropriate correction has been applied. It is known that the position of the neutral axis shifts if elasticity modulus is different in tension and compression. The results obtained from DIC data confirm that the modulus is almost the same in tension and compression. There is a little difference in the calculated values. Several factors can contribute these differences. First of all, the displacement due to shear strain was not included in the analysis. However, it will be shown later that the value of the shear strain is small compared to normal strain in this loading case and the contribution is small. Values can also be affected by the size of the speckle pattern and size of the subset and step size during post-processing operation. Calculated average elasticity modulus is used to compare the cross-section data obtained from DIC and 3PB test as shown in Figure-6.20. Good agreement between the results can be observed.

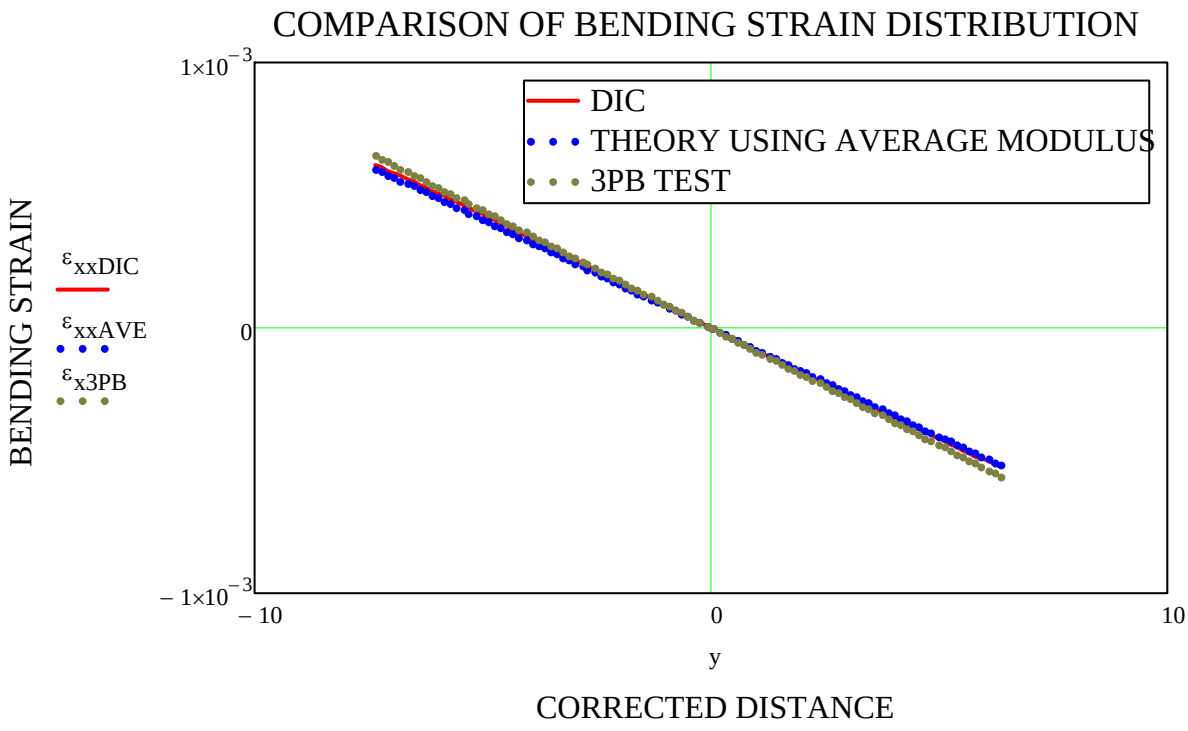

***FIGURE-6.20**: Comparison of Bending Strain at Mid-Plane at 580N*

Shear strain distribution is also of interest. Figure-6.21 shows the distribution of shear strain map on the specimen. This is a random distribution of shear strain and does not resemble to the expected shear strain distribution obtained by the developed theory earlier, Figure-6.8. Shear strain distribution is different at every cross-section and nothing can be deduced about the shear modulus using linear theories.

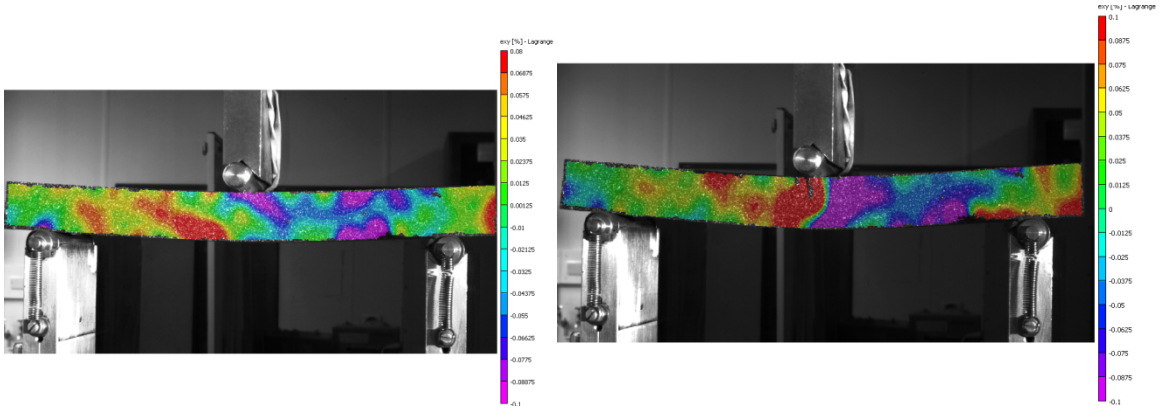

***FIGURE-6.21**: Shear Strain Distribution at 3 and 5mm respectively for Variant-1*

Shear strain distribution along the cross-section at the mid-plane between the support and the loading pin is shown in Figure-6.22

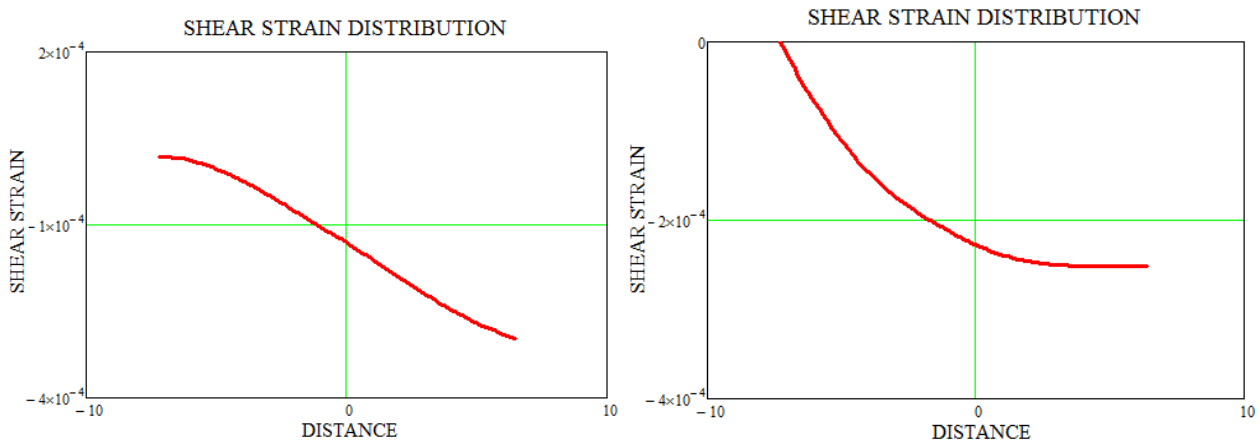

***FIGURE-6.22**: Shear Strain Distribution at 0.9mm and 1.55mm Crosshead Displacement*

The shape of the shear strain distribution changes at different load levels. Shear strain is not zero at specimen edges which is inconsistent with the theory as the shear stress and hence shear strain should vanish at these edges. The value of the shear strain is small comparing to bending strain and the contribution of the shear strain to overall displacement is small. It is difficult to determine or to consider shear modulus at this plane.

Figure-6.23 shows load-extension curve for Variant-2. Material responds non-linearly to applied load. Load carrying capacity is lower and material fails due to tension stresses generated by the flexural loads. In Variant-1, the material's load carrying capacity was reduced gradually due to separation through the thickness. This suggests an important conclusion. When transformerboard loaded in machine direction, the direction at which the fibers tend to align themselves during manufacturing operation, the tensile strength of the fibers are higher than the

bonding strength formed by fibers during hot press operation. The failure is therefore is the separation of the transformerboard through the thickness. Same failure mode is also observed during tensile tests and creep tests at different temperatures. The opposite is true for cross machine direction.

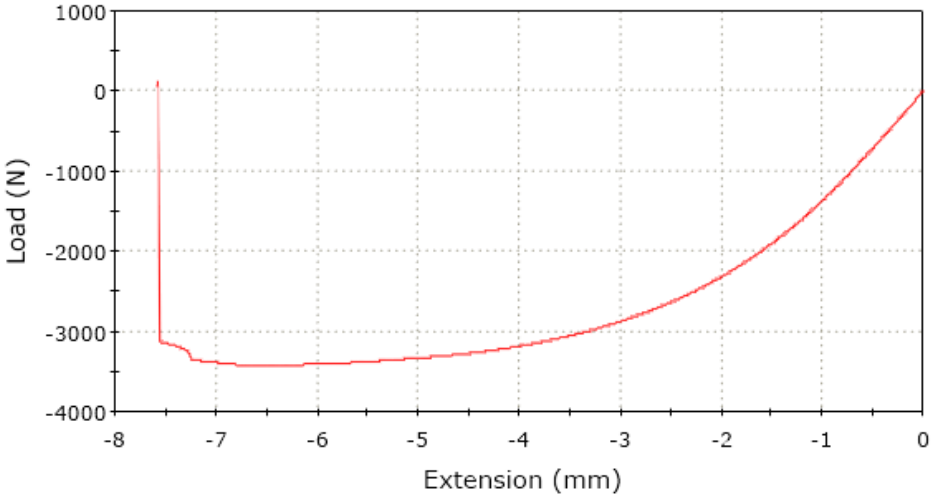

***FIGURE-6.23**: Load-Extension Curve for Variant-2*

Figure-6.24 shows the bending strain distribution along the cross-section at mid-plane between the loading pin and the left support. Distribution is linear.

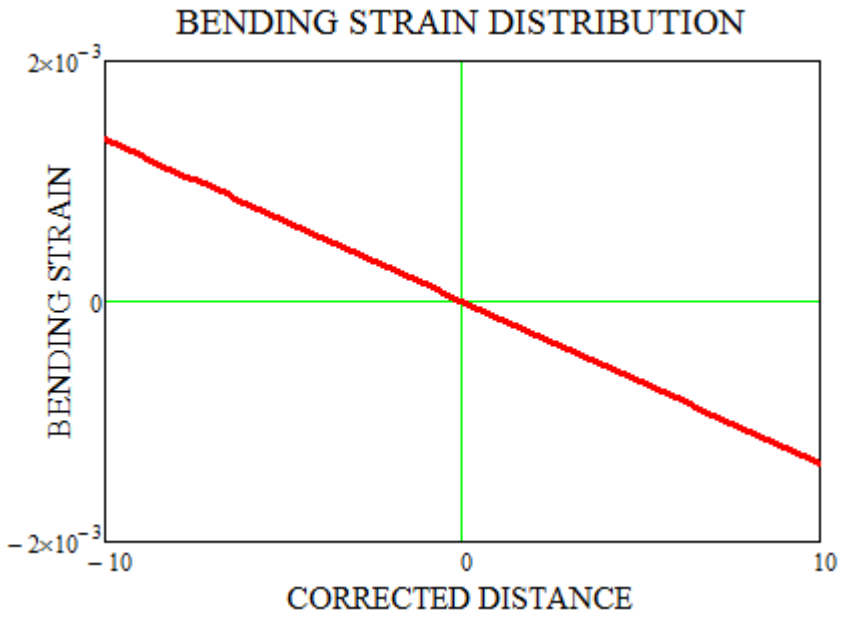

***FIGURE-6.24**: Corrected Distribution of the Bending Strain at Mid-Plane- From DIC at 1300N*

Shear strain distribution again does not follow any pattern and changes at different cross-sections however, the value of the shear strain is higher than previous loading condition.

6.8 Three Point Bending Test Results of Variant-3 and 4

Transformerboard is subjected to flexural loading at this cross-section during operation life. Reaction forces generated after application of pre-stress on the windings and the short circuit forces are the two main reasons of the flexural stresses acting on clamping ring.

Figure 6-25 shows the bending strain and Figure-6.26 shows the shear strain distribution. Shear strain distribution resembles the one obtained by the theory developed.

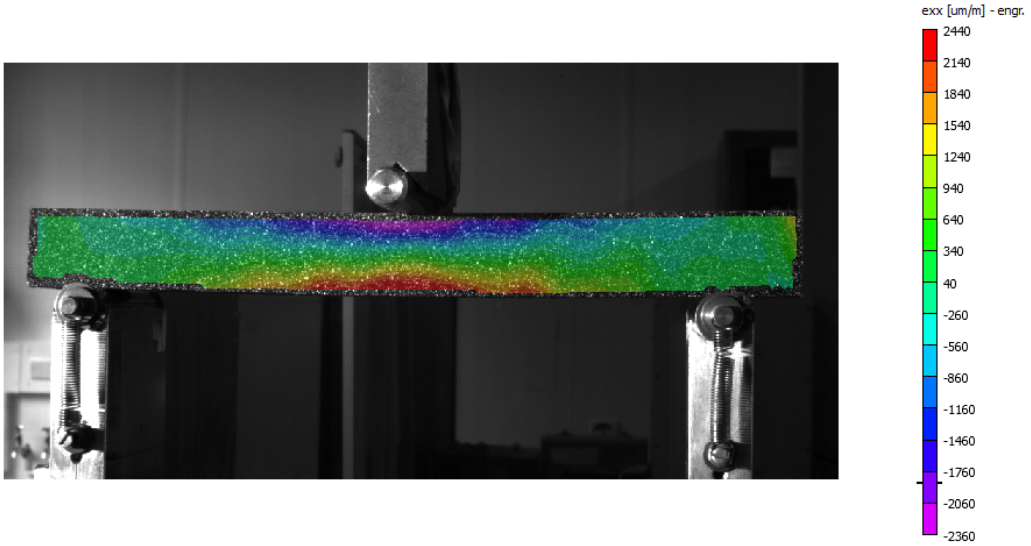

***FIGURE-6.25**: Bending Strain Distribution*

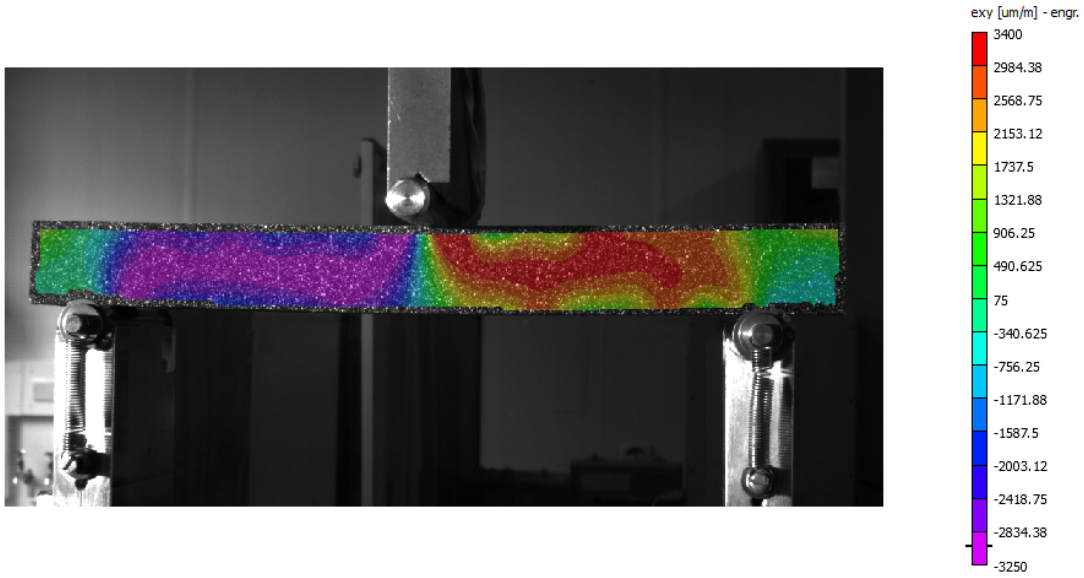

***FIGURE-6.26**: Shear Strain Distribution*

Figure-6.27 shows the load-extension curve. Material fails at approximately 3850N loading and the failure mode is delamination of the transformerboard. Delamination does not take place at mid-plane in y direction but closer to it due to reasons explained below.

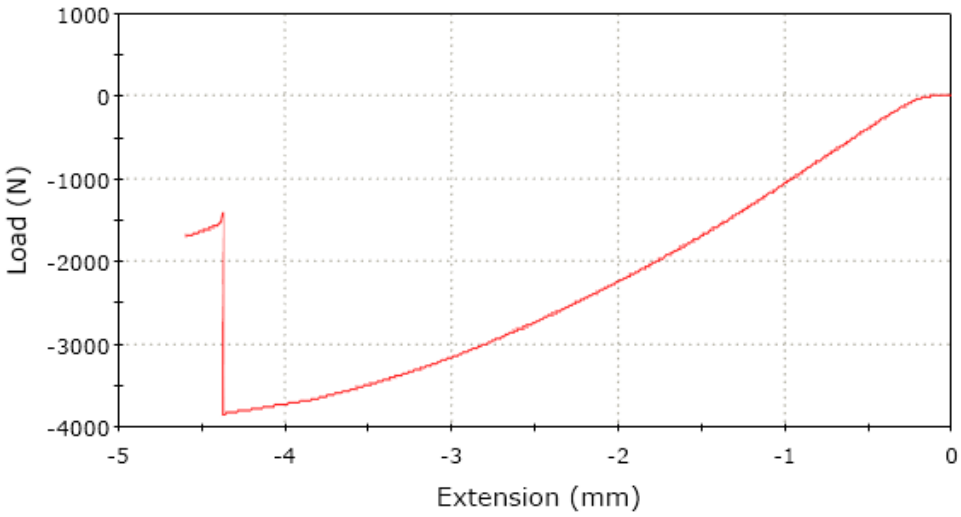

***FIGURE-6.27**: Load-Extension Curve for Variant-3*

The difficulty in determining shear modulus at this loading plane is caused by several factors. One reason is that the transformerboard lamina, each of them is 5mm in thickness, are stacked together by gluing them. The glue propagates through the thickness of a lamina between very thin layers of transformerboard and increases the bonding strength at those areas. Measurements show that the glue propagates 0.5mm in to each lamina resulting higher interlaminar shear strength at those areas. The shear strength is no longer determined by the cross-linked fibers during hot press operation and both elasticity modulus and shear modulus can be affected. Figure-6.28 shows the proposed cross-section geometry and material properties for transformerboard. After the application of the glue, the thickness of the transformerboard lamina is reduced to 4.5mm rather than 5mm. Material properties can be different at the regions where glue is applied and therefore, different material properties are assigned. To validate this with FEA, the result of simple FEA analysis for shear strain distribution is shown in Figure-6-29. The maximum shear strain does not occur at mid-plane. The second difficulty is that the transformerboard is formed by stacking very thin sheets consist of short fibers and fibers tend to align themselves to the machine direction during manufacturing resulting in anisotropy.

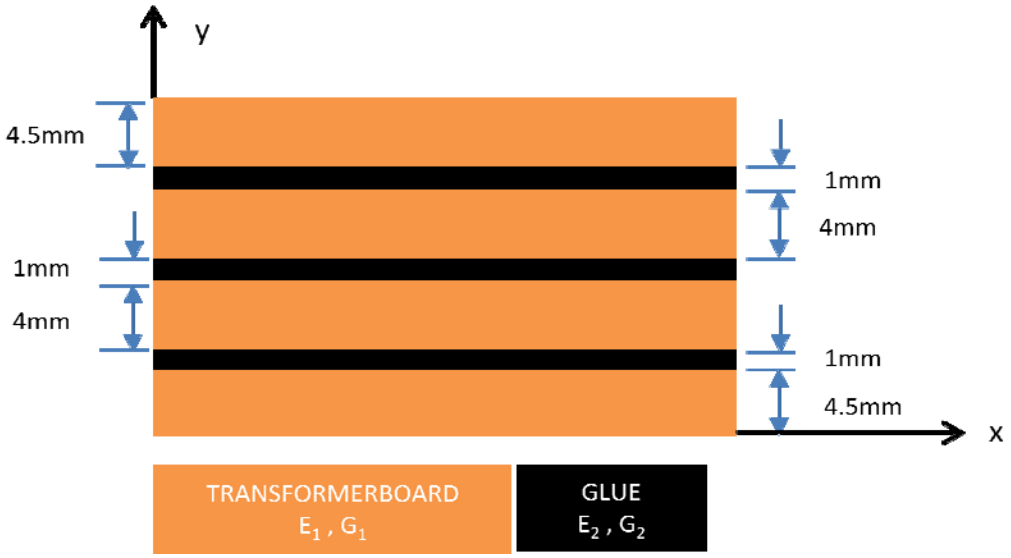

***FIGURE-6.28**: Cross-Section Geometry and Material Properties*

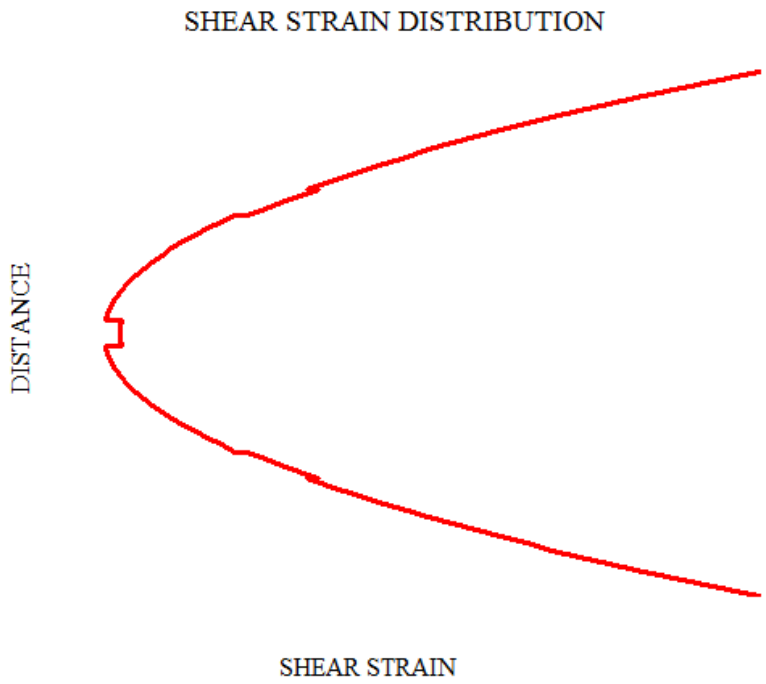

***FIGURE-6.29**: Expected Shear Strain Distribution for Multi-Layer Beam*

Figure-6.30 shows the bending strain distribution along the corrected cross-section at x=-40mm, mid-plane between the loading pin and left support. The position of the neutral axis for this case was not exactly at the middle but at 0.9mm above. Bending strain distribution is not exactly linear and the slope of the curve below and above the neutral line is different. Slope is lesser at the areas where compressive stresses occur but the difference is not very large in magnitude.

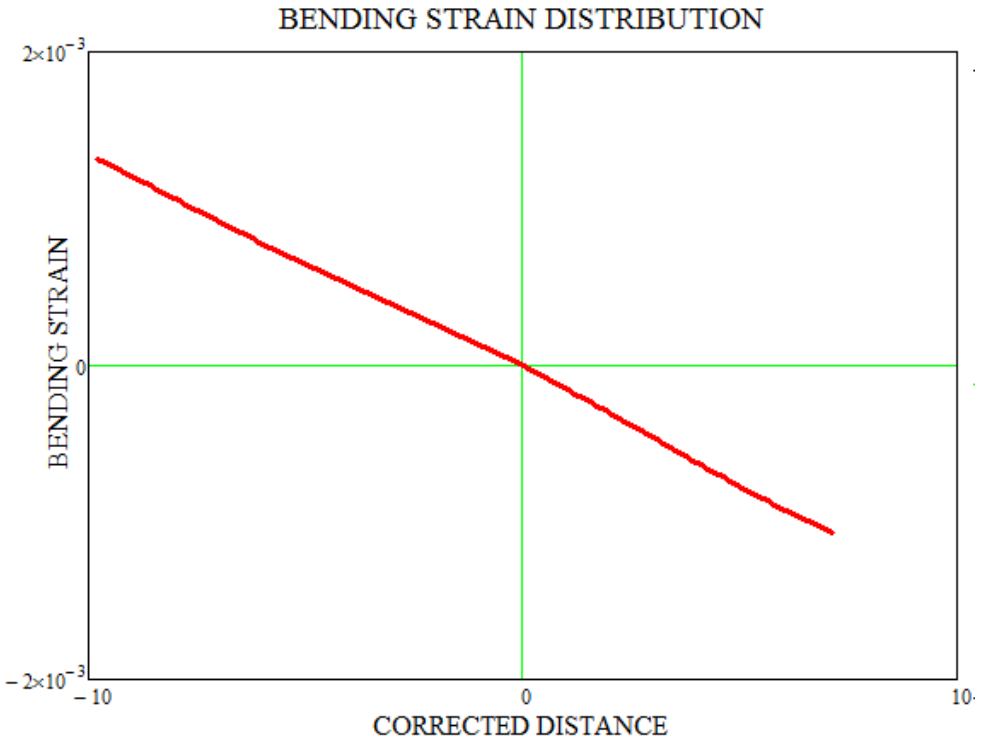

***FIGURE-6.30**: Bending Strain Distribution for Variant-3*

Figure-6.31 shows the comparison of shear strain distribution obtained from DIC and calculated one where shear modulus is calculated using elementary bending theory at x=-40mm.

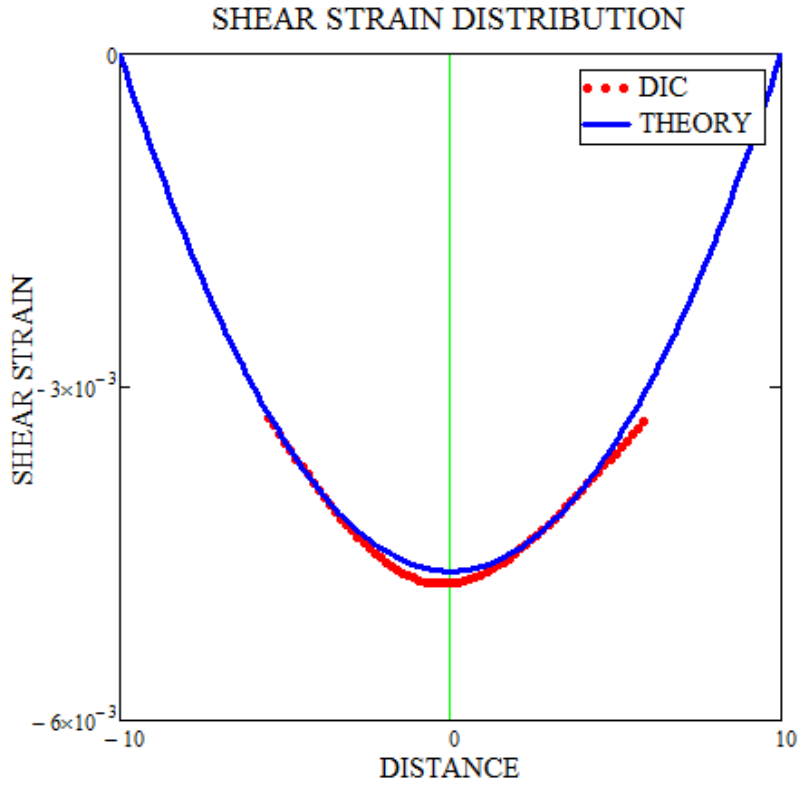

***FIGURE-6.31**: Comparison of Theoretical and Experimental Shear Strain for Variant-3 at 2.38kN*

The measured shear strain distribution from DIC data does not follow a perfect parabolic shape and the maximum shear strain is attained below the neutral axis. Table-6.3 shows the calculated shear modulus at different load levels using elementary theory and average elasticity modulus in machine direction using the cross section data obtained from DIC.

	1670N	**1910N**	**2144N**	**2380N**	**AVERAGE**
Shear Modulus G_{13}(MPa)	940	955	930	940	~940MPa
Elasticity Modulus E_{11} (MPa)	12800				

TABLE-6.3 *Calculated Shear Modulus- G_{13} (MPa) and Elasticity Modulus-E_{11} (MPa)*

Unlike metallic structures, the effects of the shear stress are dominant during the bending of transformerboard and the deflection generated by shear stresses should be taken into consideration. Deflection due to shear should be added to equation 6.44. Using the calculated material properties of the transformerboard and the dimensions of the test setup, the additional effect of the shear stress is found to be 32% using elementary theory.

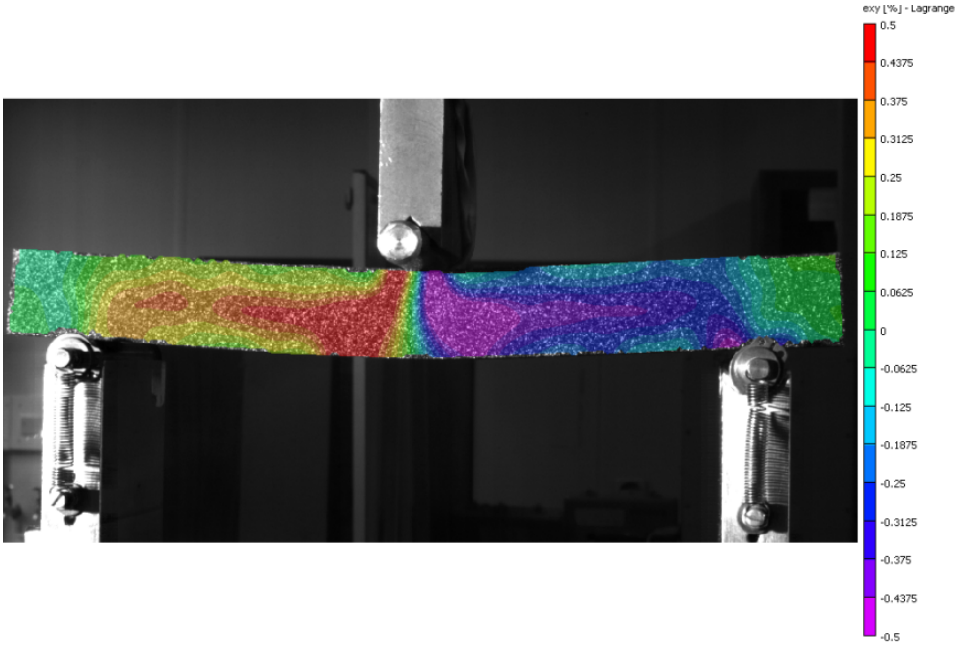

FIGURE-6.32*: Shear Strain Map on Variant-4*

Figure-6.32 shows the shear strain distribution for Variant-4. Shear strain distribution resembles the one obtained from the full solution (Eq 6.43). Same method will be used to calculate the

shear modulus at this plane. Position of the neutral axis is at the middle of the specimen based on the bending strain distribution, consistent with elementary bending theory.

Figure-6.33 shows the shear strain distribution obtained from DIC and calculated one from theory. Shear strain distribution does not follow perfect parabolic shape. An expected shape is one that resembles Figure6-29. The reason for this is that at the middle of the specimen there is a region where glue changes the material properties, especially shear modulus. This region is small in thickness and when post-processing the test data, the value set for facet size was not small enough to contain only glue region but instead contain glue and transformerboard regions. Too small facet size does not contain enough speckles and does not post-process the results. Calculated strains were therefore average strains within the facet size. However, the average distribution is accurate enough for design purposes.

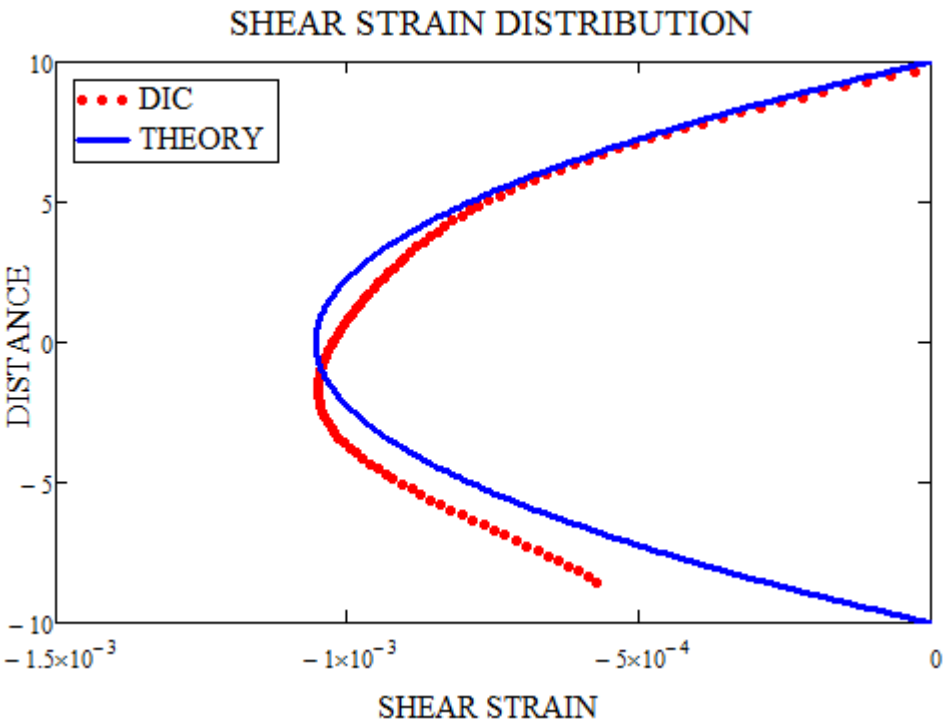

***FIGURE-6.33**: Comparison of Theoretical and Experimental Shear Strain for Variant-4 at 1kN*

	675N	**900N**	**1000N**	**1500N**	**AVERAGE**
Shear Modulus G_{23}(MPa)	1010	1010	1025	1040	~1020MPa
Elasticity Modulus E_{22} (MPa)	~9000				

***TABLE-6.4** Calculated Shear Modulus- G_{23} (MPa) and Elasticity Modulus-E_{22} (MPa)*

Table-6.4 shows the calculated shear modulus G_{23} and elasticity modulus E_{22}. The effects of the shear stress are also dominant at this plane and the deflection generated by shear stresses should be taken into consideration by adding the deflections due to shear strain in equation 6.44. Using the calculated material properties of the transformerboard and the dimensions of the test setup, the additional effect of the shear stress is found to be 21% using elementary theory.

All test specimens loaded at 1-3 and 2-3 planes, failed due to interlaminar shear stresses and the failure mode for transformerboard under flexural loading condition is delamination. Interlaminar shear strength of the transformerboard is also of interest. One way to measure this quantity is to perform a lap shear test. However, this test requires gluing two laminas to each other and the glue will propagate through the transformerboard and will change the shear properties. For this reason, short shear beam test method will be used instead. The advantage of using short shear beam test for transformerboard is that the delamination is the major failure mode, any height to span length ratio will provide failure due to interlaminar shear stresses. The disadvantage is that the delamination occurred at the plastic region in all the tests performed previously and shorter span length may be required. If the tests are performed with shorter span length, the effect of indentation at the regions close to loading pin could spoil the results. Figure-6.34 shows the distribution of shear stresses at x=-1mm, x=-40mm and x=-79mm using the properties in Table-6.1 and the full solution developed. It can be seen that the magnitude of the shear stresses are very large at loading pin and first failure can occur at these areas first.

To prevent these disadvantages, the loading will be supplied through an aluminium seat. The thickness of the aluminium seat is 7.3mm, length is 80mm and the depth is 20mm. All the material properties are determined and will be substituted in the full solution developed to calculate the interlaminar shear strength of the transformerboard. In the full solution, the loading will be considered as uniform pressure acting between -40mm to 40mm because centre of the material is the origin. The test condition at first sight seems different because of the contact between the aluminium seat and transformerboard and in order to validate uniform pressure assumption, FEA analysis and full solution will be compared. Figure-6.35 shows the comparison of shear strain distribution and Figure6-36 shows the comparison of bending strain distribution at x=60mm (mid position between the right support and the end of the seat) obtained from full solution and FEA analysis where the contact between aluminium seat and transformerboard is taken into consideration. Figures 6.35 and 6.36 show that at the cross-

section of interest, where highest interlaminar shear stresses act, the proposed theory and FEA results are very close and the proposed method to calculate interlaminar shear strength can be used reliably.

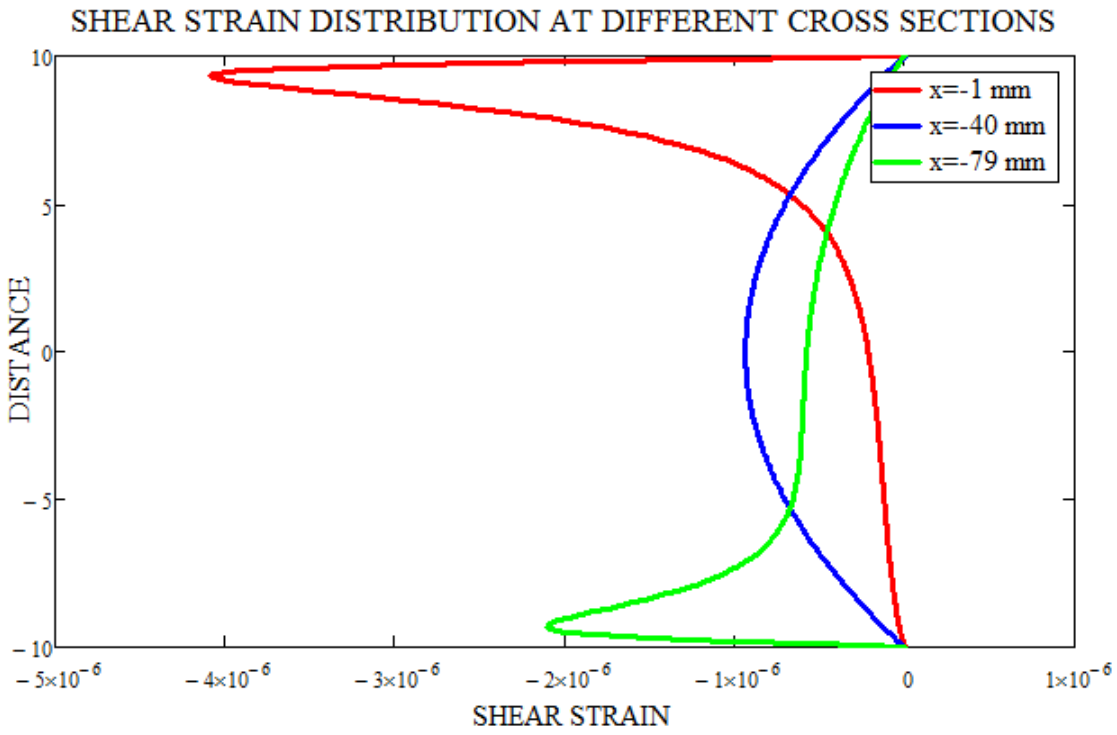

***FIGURE-6.34**: Shear Strain Distribution at Different Cross Sections – Full Solution Results*

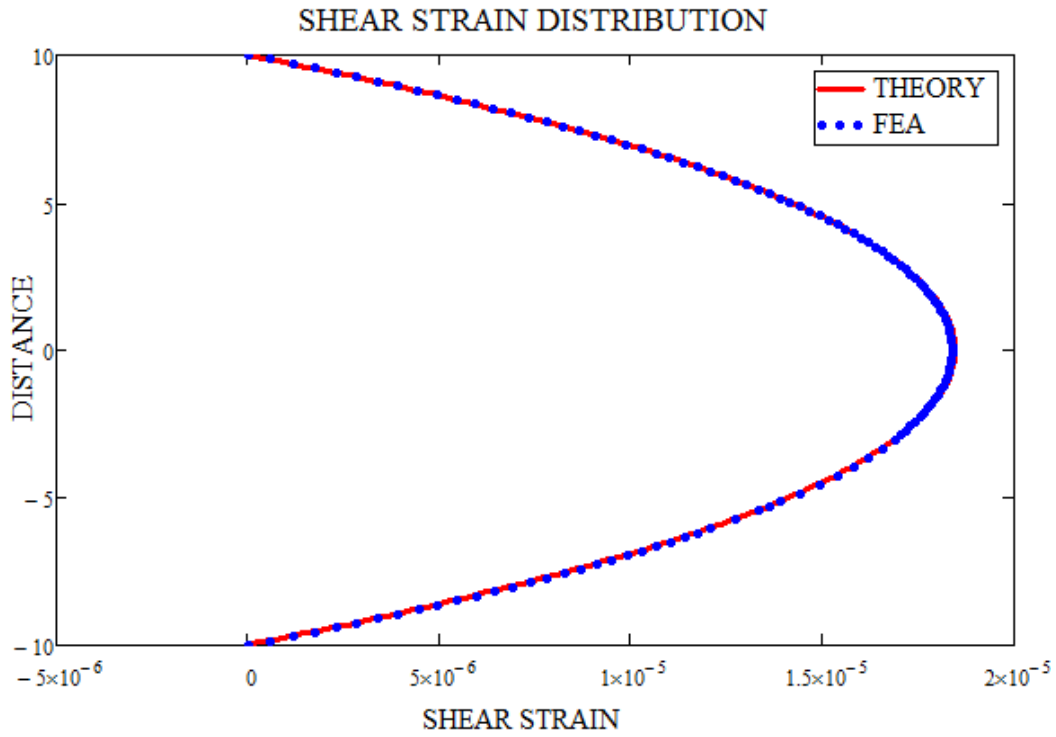

***FIGURE-6.35**: Comparison of Shear Strain Distribution at x=60mm*

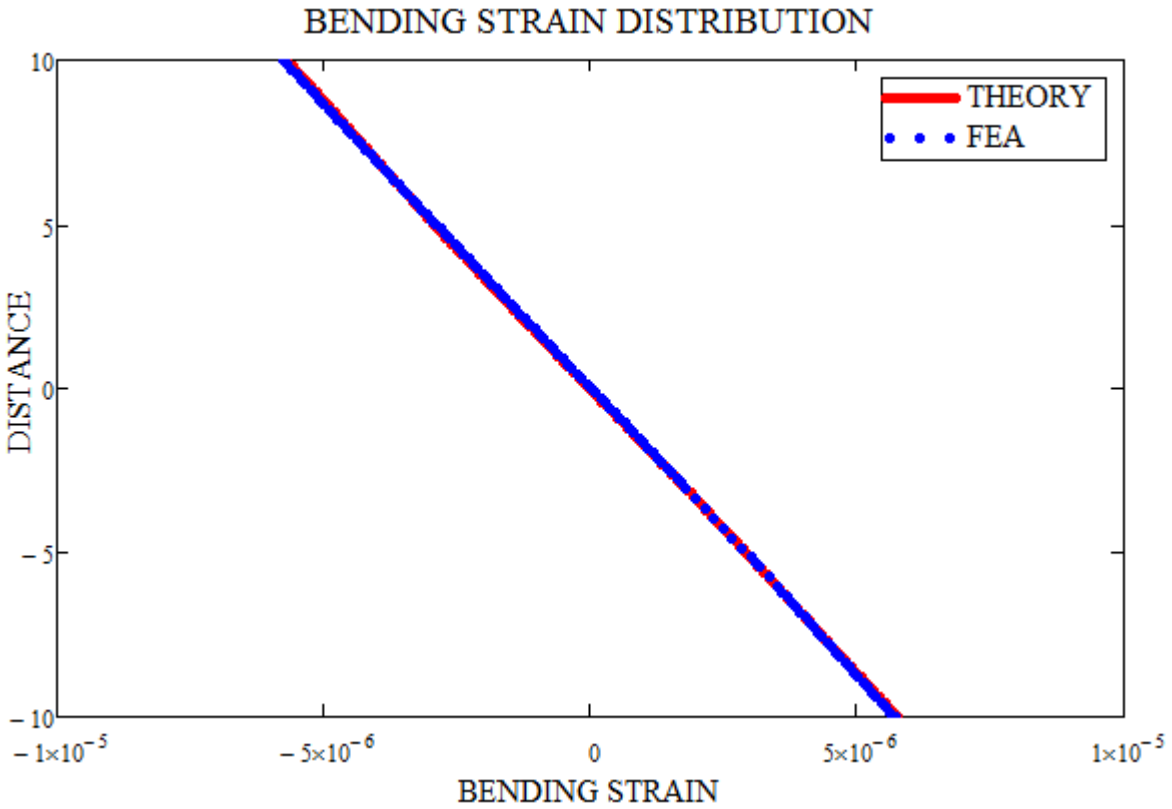

***FIGURE-6.36**: Comparison of Bending Strain Distribution at x=60mm*

Figure-6.37 shows the shear strain distribution prior to failure. High shear strain concentration can be clearly seen. The failure occurred at 4823kN loading and the material's response was elastic according to data from test machine prior to delamination.

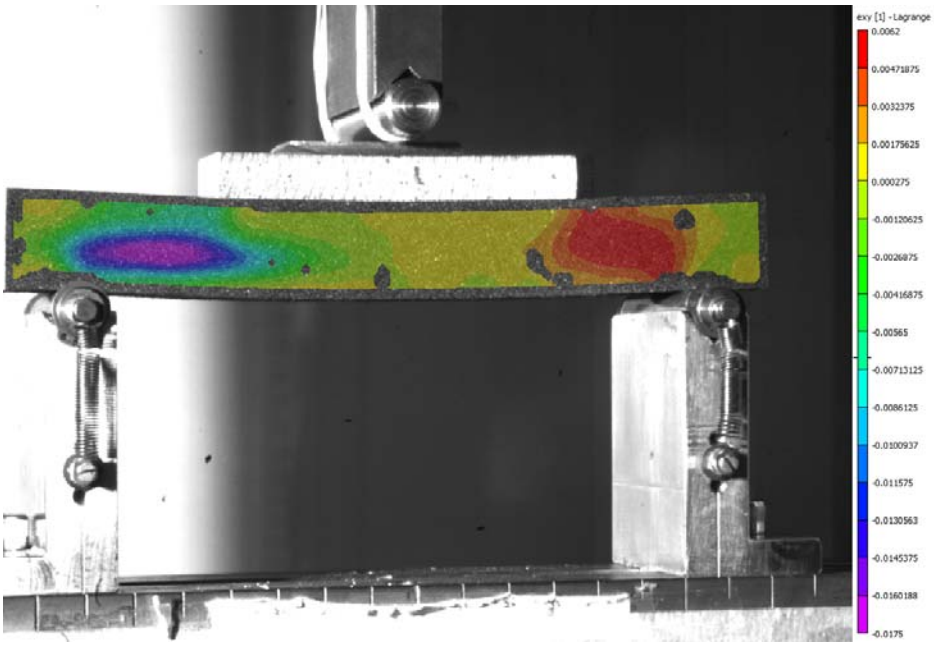

***FIGURE-6.37**: Shear Strain Distribution Prior to Final Failure*

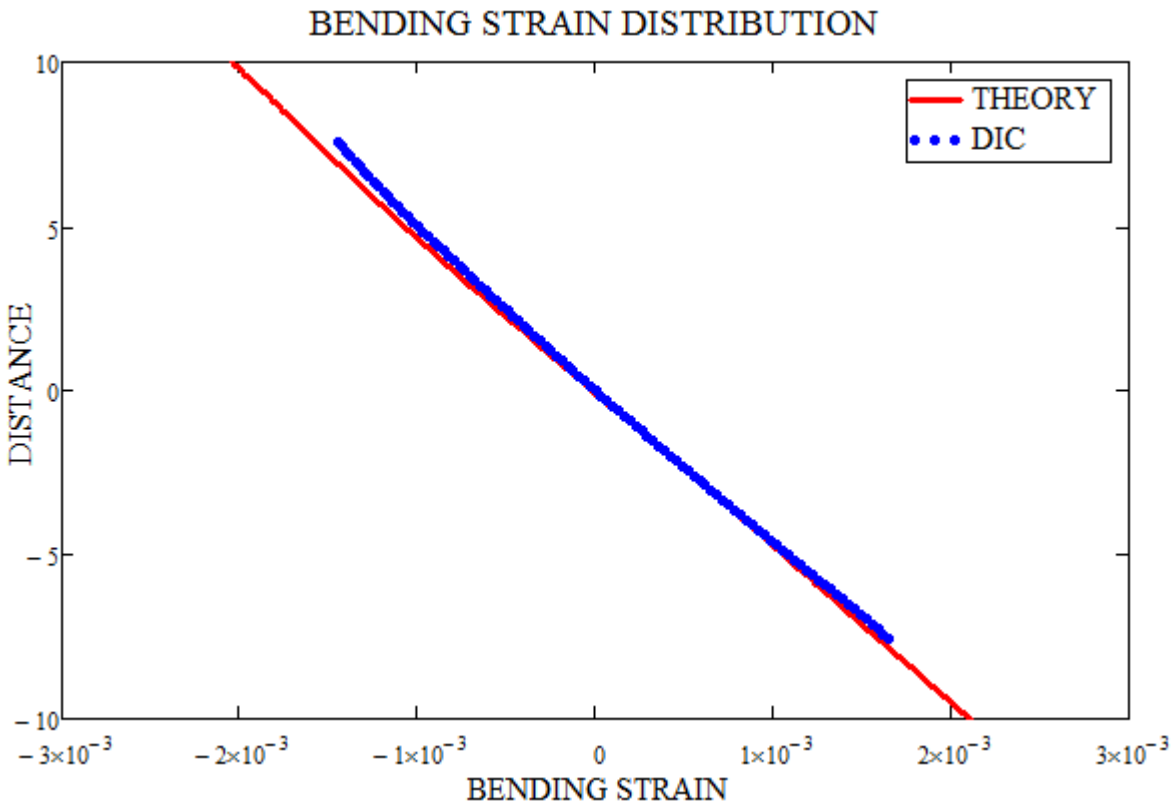

***FIGURE-6.38**: Comparison of Bending Strain Distribution at 4700N Loading – Theory vs DIC*

Figure-6.38 shows the bending strain distribution obtained from the theory developed and DIC at the mid-plane between the end of the seat and the right support at 4700N loading. At the outer fibers, the theoretical results and DIC results do not match perfectly but the agreement is close. This is probably due to plastic deformation taking place at the outer fibers. These results also provide a method to check the accuracy of the material properties found by the tests performed earlier. Shear strain distribution on the other hand still differs from the theory developed due to the effect of the glue. Figure-6.39 shows comparison of the shear strain distribution between DIC and developed theory. The agreement is much better at the areas where tensional stresses act. Maximum shear strain again does not occur at the mid-plane and the shear strain distribution does not follow the parabolic curve where compressive stresses are dominant. Just before the failure, the values of interlaminar shear stress are calculated from the theory developed and listed in Table-6.5.

	TEST-1	**TEST-2**	**AVERAGE**
Shear Strength-MD (MPa)	8.75	8.71	8.73
Shear Strength-CMD (MPa)	8.68	8.93	8.8

***TABLE-6.5** Interlaminar Shear Strength in Machine (MD) and Cross-Machine (CMD) Directions*

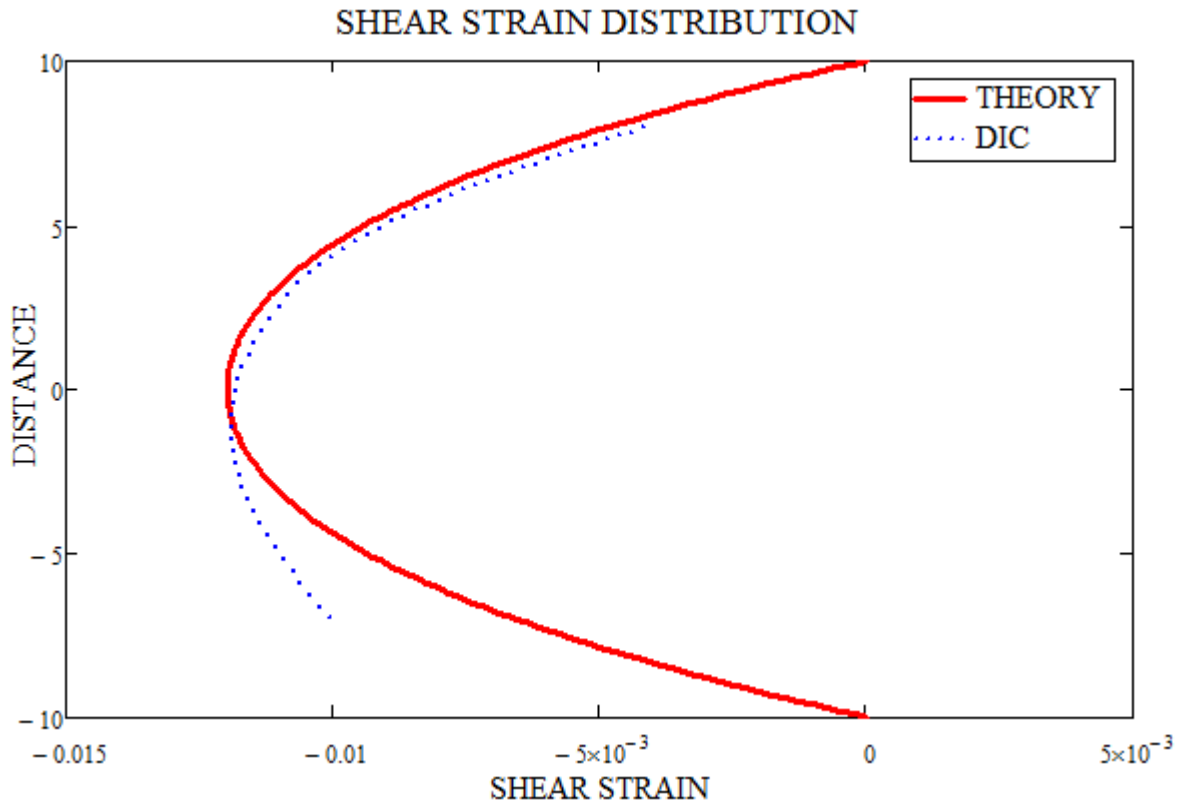

***FIGURE-6.39**: Comparison of Shear Strain Distribution at 4700N Loading – Proposed Theory vs DIC*

6.9 Final Comments on Bending Tests of Transformerboard

A full solution method was developed to calculate stress and strain distributions at any cross-section within the orthotropic specimen for three and four point loading conditions. As long as the loading is symmetric with respect to x axis, any loading distribution can be used as an input with the theory developed. The advantage of the method developed is that force and moment boundary conditions at the material ends replaced with normal and shear stress boundary conditions. This enables the solution to be used with any height to length ratio, providing additional flexibility to the solution. Once correct material properties are found, values of stress and strain can be found at any point with great accuracy.

The digital image correlation (DIC) technique was used to investigate the bending properties of transformerboard. For Variant-1 and Variant-2, it was shown that the bending strain is linear whereas shear strain distribution within the specimen does not follow any pattern and shear strain distribution changes at every cross-section.

For Variant-3 and Variant-4, difficulty arises because the transformerboard is glued together to achieve the desired thickness. Glue propagates through the thickness of the transformerboard

lamina results a change in the material properties. Before application of the glue, very thin transformerboard wet sheets are hot-pressed and this operation creates cross-linked fibers holding very thin sheets together. The addition of the glue generates stronger bonding than that of cross-linked fibers and changes material properties through the thickness. All the specimens loaded by flexural forces failed due to delamination and delamination always occurred at the transformerboard region. The region where the glue is dominant is thinner compared to transformerboard. During DIC post-processing operations, a facet size cannot be set small enough to capture the strain distribution only in glued area but instead the facet contains transformerboard and glue region together. The calculated strains are the average strains within the facet.

Interlaminar shear strength and shear modulus are calculated using the data extracted from DIC tests and the developed theory. The prediction on bending strain is much more accurate than shear strain. However, for design purposes, the calculated values are accurate enough.

6.10 Laminated Wood

A number of tests were performed on laminated wood to investigate the load carrying capacity, failure mode and the effect of temperature on these properties. Oil impregnated specimens were soaked in a treated transformer oil for 44 days at 20, 50 and 90 degrees centigrade. The material used was KP 20222 made from beech veneers. Laminas are dried and bonded together using phenolic resin under high temperature and pressure. Each lamina is 2mm in thickness stacked in (0^0–90^0–0^0-90^0….) layup to form total thickness of 20mm. Here, 0^0 represents the direction where the fibers in the wood are aligned. Total length of the specimen was 150mm, span length was 130mm and depth was 20mm.

Figure-6.40 shows the comparison of load extension curves obtained at three different temperatures. Bending modulus does not change significantly at the beginning of the tests at all temperatures. A significant reduction at the load carrying capacity for a specimen aged at 90 ^{0}C can clearly be seen.

All the laminated wood specimens aged at 20^0C and 50^0C in transformer oil failed due to tensile stresses acting at the outer fibers whereas all the specimens aged at 90^0C failed due to delamination. The failure always occurs on 90^0 laminas closer to the neutral axis.

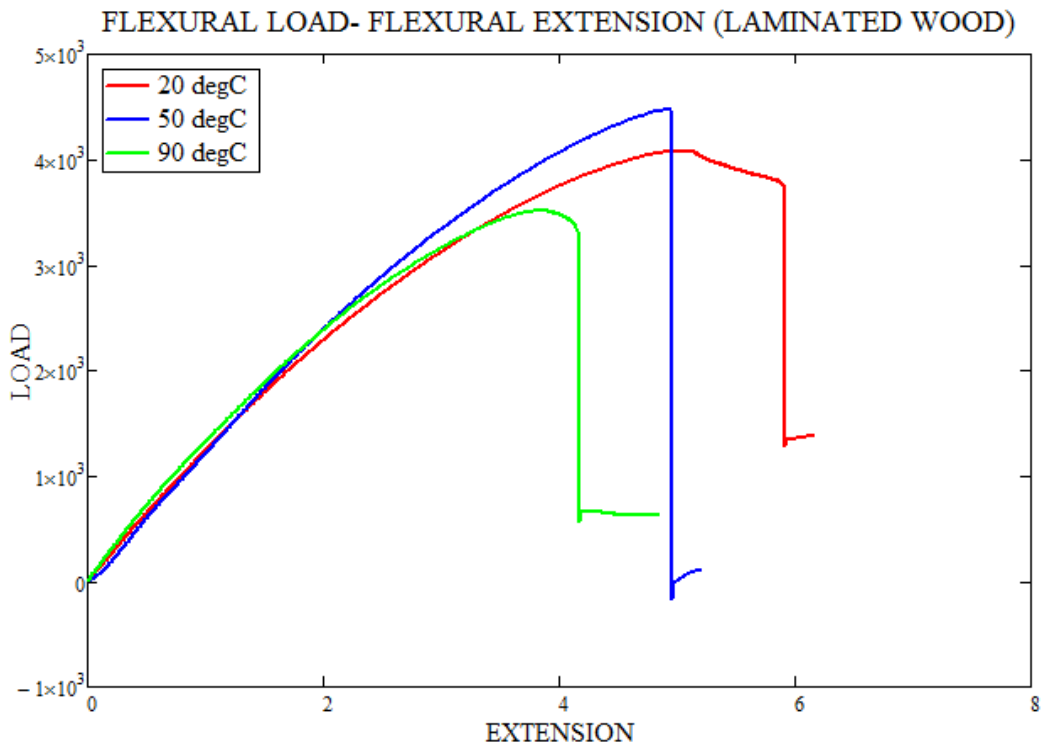

***FIGURE-6.40**: Comparison of Load – Extension curves of Laminated Wood Aged at Three Different Temperatures*

In conclusion, elevated temperatures affect the material properties of the laminated wood and change the failure mode. In transformer design, clamping ring is placed on top of the windings where the transformer oil is hotter and electrical field is high. The combination of these two factors contributes ageing of the laminated wood and eventually causing degradation of the material properties. It is therefore highly suggested to use bending modulus values measured at elevated temperatures during the design to take into ageing affect into account. Ageing of transformerboard will be considered in next chapter.

6.11 Laminated Wood Reinforced with Glass Fibre

A relatively new material, the laminated wood reinforced with glass fibre, is shown in Figure-6.41. Glass fibre reinforcements are inserted between the last two laminates at the top and bottom surfaces to create a sandwich like structure. This configuration is designed for high mechanical performance under flexural forces and typical applications are furnace transformers.

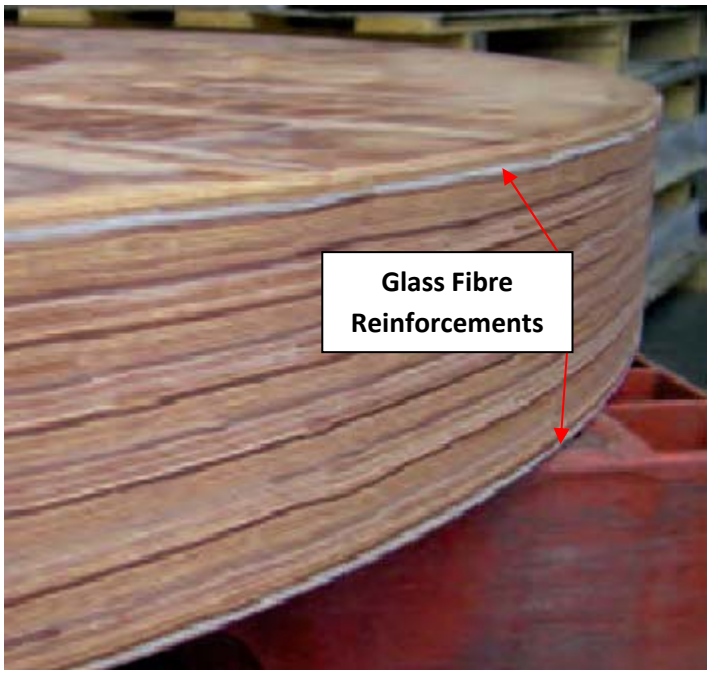

***FIGURE-6.41**: Laminated Wood Reinforced with Glass Fibre*

In order to map the strain distribution within the material and along any cross-section, 3-D DIC technique is used. Specimens are dried and oil impregnated under vacuum.

Figure-6.42 shows the shear strain distribution on the test specimen. Higher shear strains are acting on laminates stacked at 90 degrees whereas laminates stacked at 0 degrees experiences lower shear strain. Figure-6.43 shows the shear strain distribution on the mid-plane between the support and the loading pin. This distribution resembles the one obtained from FEA analysis because of the large difference of the elasticity modulus in fibre and cross fibre directions. At one layer, the shear strain is higher than other layers. This due to the imperfections contained within the raw material especially dominant at cross fibre direction. The effect of the imperfections, resulting non-homogeneity, is much more pronounced in bending strain distribution shown in Figure-6.44. At some local areas, the bending strain is much more in magnitude than the neighbor areas. Bending strain distribution is extracted from the test data at two cross sections as shown in Figure-6.44. Figure-6.45 shows the comparison of the bending strain at two different cross-sections labeled as 1 and 2 in Figure-6.44. The discontinuity in the bending strain is apparent. The effect of discontinuity is much more apparent for oil impregnated specimens, because the hot transformer oil does act as an ageing agent.

Unlike transformerboard, the glue does not propagate within the wood and does not affect the strain distribution. Interlaminar shear strength is higher because thick woods are glued to each other whereas in transformerboard, very thin sheets of fibers hot pressed to form a lamina where the shear strength is determined by the chemical bond between the fibers.

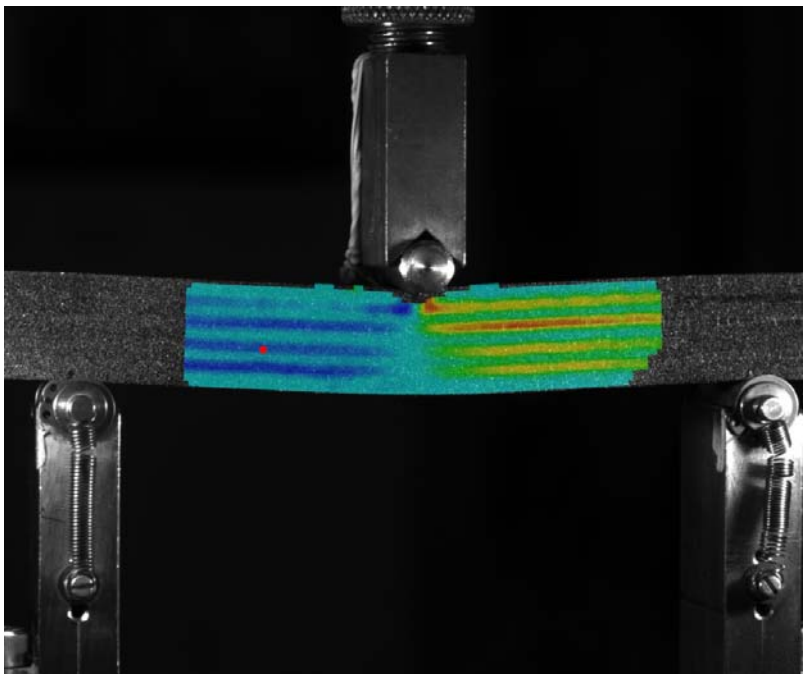

***FIGURE-6.42**: Shear Strain Map on Laminated Wood Reinforced with Glass Fibre Specimen*

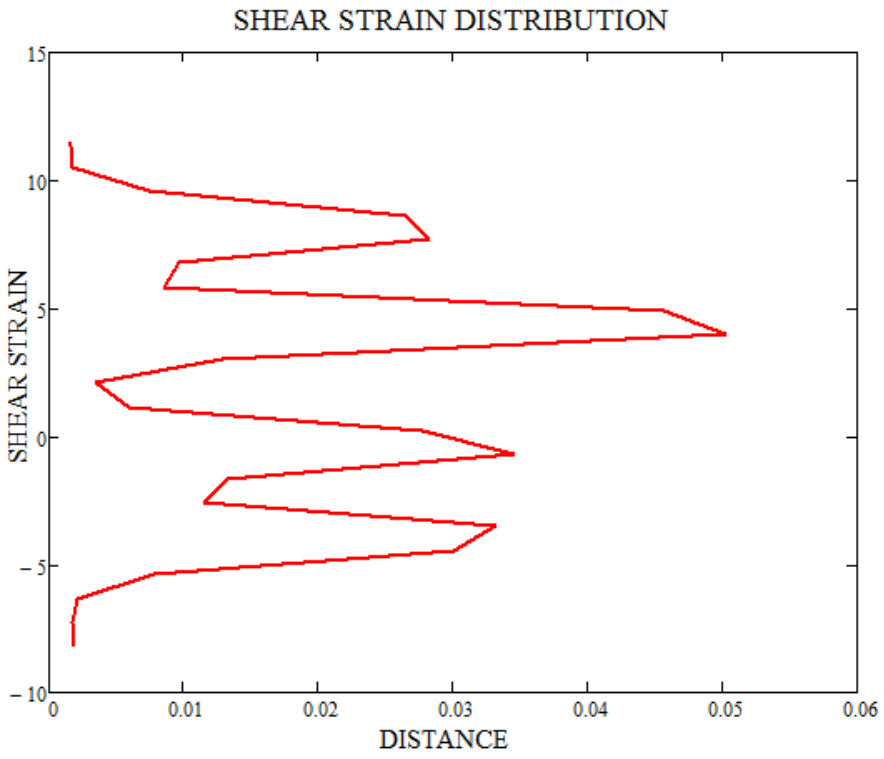

***FIGURE-6.43**: Shear Strain Distribution at Mid-Plane between the Support and Loading Pin*

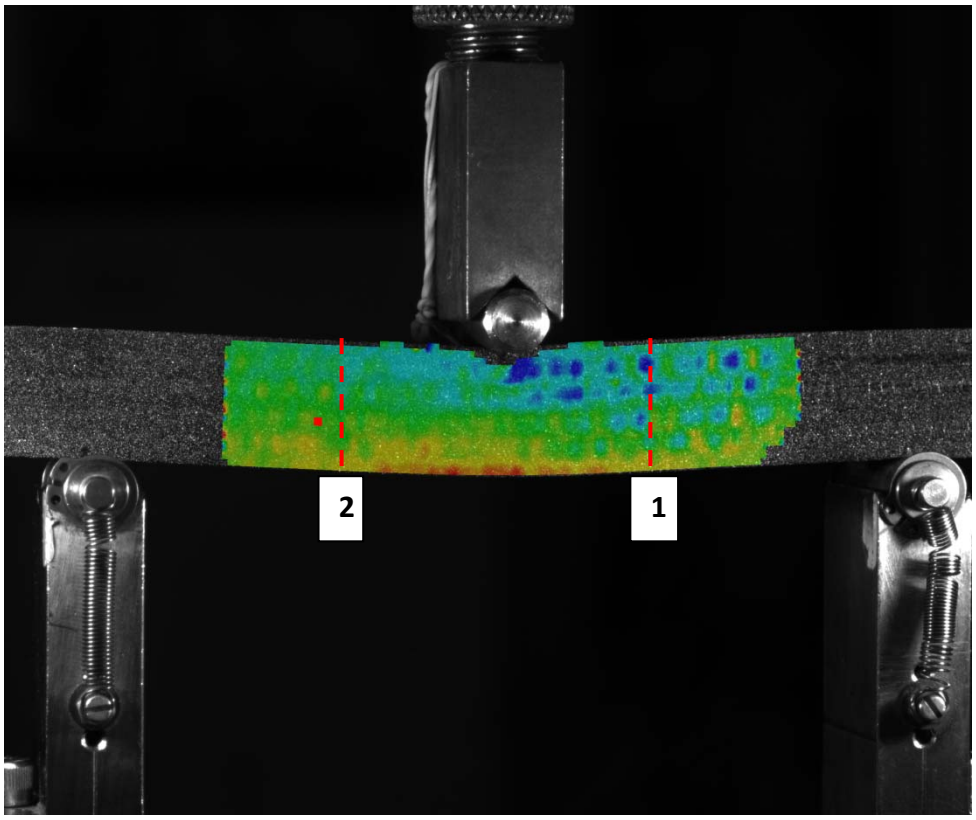

***FIGURE-6.44**: Bending Strain Map on Laminated Wood Reinforced with Glass Fibre Specimen*

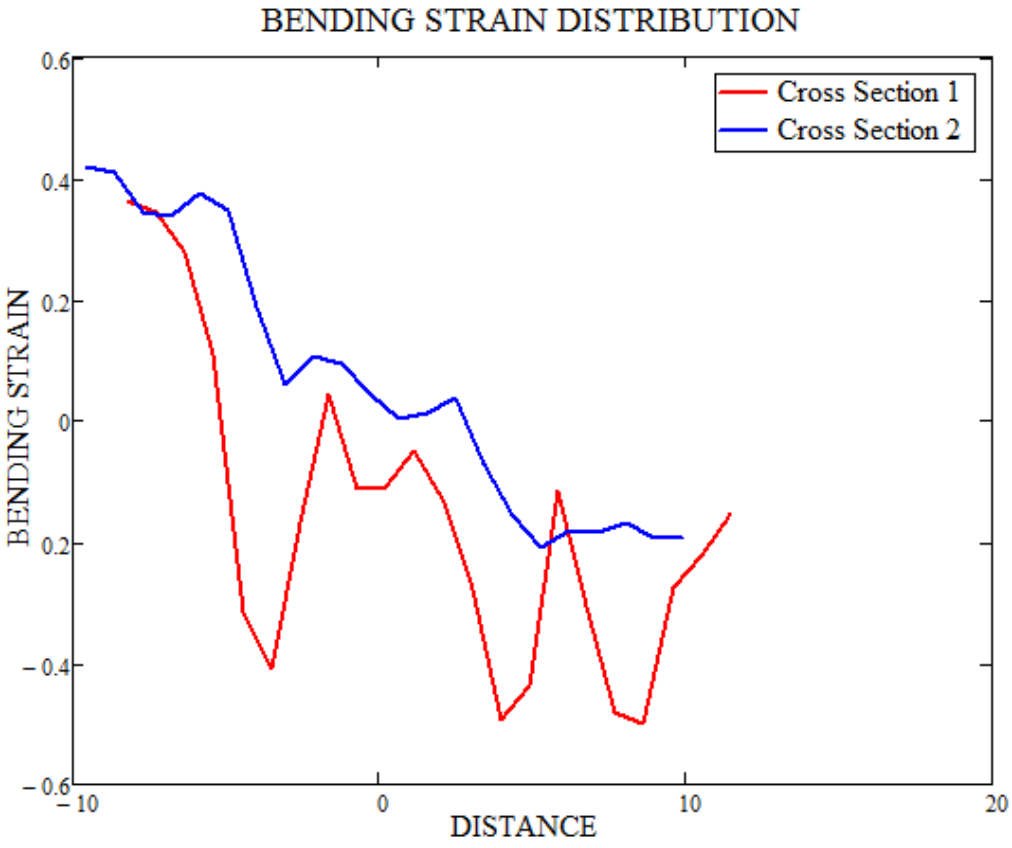

***FIGURE-6.45**: Bending Strain Comparison at Cross Sections 1 and 2*

6.12 Comparison of Transformerboard and Laminated Wood

Interlaminar shear strength of the transformerboard is lower than laminated wood due to the reasons explained earlier. In fact, transformerboard always fails due to interlaminar shear stresses under flexural loading. Shear strain distribution of the transformerboard is complicated by the addition of glue between the laminates changing the material properties and especially, the interlaminar shear strength. DIC data shows that the shear and bending strain map on the specimen resembles the one obtained by the full theoretical approach developed. This theory can be used to calculate the stresses acting at any point in the specimen. Moreover, strain data extracted from any cross-section from the DIC data can be processed to calculate the material properties. Laminated wood is stacked as a cross ply laminate to form desired thickness. Unlike transformerboard, the glue does not propagate through the thickness of a lamina. At low temperatures the dominant failure mode is tensile rupture of the outer fibers under tensional stresses. If the material is subjected to high temperatures for a certain period of time, the failure mode is changing to delamination of the laminas stacked at 90^0 suggesting that material properties in terms of load carrying capacity degrades. Laminated wood contains imperfections within the lamina resulting strain concentrations and due to this fact, bending strain distribution is much more complex than transformerboard. Under flexural loading conditions, laminated wood achieves higher load carrying capacity. This is due to the low interlaminar shear strength of the transformerboard.

Tests have also shown that transformerboard shows plastic deformation capability whereas laminated wood fractures in a brittle manner. Oil impregnation and removal of the moisture enhance the material properties and load carrying capacity of transformerboard both under tensional and flexural loading conditions.

7-VISCOELASTIC PROPERTIES OF TRANSFORMERBOARD

7.1 Introduction

Transformerboard is used at critical areas within the high voltage windings. Spacers, axial sticks and clamping rings are made of transformerboard due to its electrical properties. Power transformers are expected to work many years and during their service life the transformerboard is working in hot transformer oil. Transformer oil ages the transformerboard and both the mechanical and electrical properties degrade. These materials are also subjected to compressive and tensile loads due to applied pre-stress during manufacturing to provide resistance to short circuit forces. Combination of constant loading, temperature and chemical oil degrades the mechanical properties of the transformerboard and the load carrying capacity is decreased. Components made of transformerboard subjected to combination of these parameters should be designed so that the failure during the specified service life is avoided.

In [18] and [48], transformerboard is modelled as a viscoelastic structure possessing complex modulus during a dynamic short circuit event. A standard linear model is used to represent the transformerboard and the constants for the bulk modulus and the dashpot damper were found theoretically. The complex modulus of the transformerboard changes with frequency and temperature and in these studies the effect of temperature was neglected. The effect of the frequency was limited because of the assumed standard linear viscoelastic model.

In this chapter, the complex modulus of the transformerboard will be determined with the dynamic mechanical thermal analysis (DMTA) technique for oil-impregnated and dried specimens. A wide temperature and frequency range will be chosen to determine the response of the transformerboard to applied frequency and temperature.

Creep properties of the transformerboard will also be studied. A test rig is designed and developed to read creep data under constant load and varying temperature. Tests have been carried out in transformer oil and in air to distinguish the effect of the transformer oil on the transformerboard's service life and load carrying capacity. Notched samples are also manufactured with different notch dimensions to compare their effects within the specified temperature range.

7.2 Dynamic Mechanical Thermal Analysis (DMTA) Tests

In order to determine the viscoelastic response and hence the storage modulus and loss factor, DMTA test was performed on oil-impregnated and dried specimens. All specimens are placed in a vacuum resistant oven and heated up to 90^0C. In order to extract the moisture within the specimens, specimens are subjected to vacuum. Oil-impregnated specimens are taken out of the oven and placed in a vacuum resistant container. Treated transformer oil is pump into the container under vacuum and oil-impregnated specimens are prepared. The tests are planned to run up to 180^0C. Mineral transformer oil is flammable at this temperature and therefore, environmentally-friendly vegetable based transformer oil with a high flame point is used.

Storage modulus and loss factor were determined using the double cantilever configuration. Specimen dimensions are chosen as 7mm x 3.5mm x 2.3mm. Load is applied at the middle of the span length and the strain is chosen as 0.03% to ensure that no plastic deformation will take place.

Under short circuit conditions, exciting frequency of the short circuit current is the dominant frequency during the transient phase. During the steady-state phase, double exciting frequency is dominant. Exciting frequency of the transformer is either 50Hz or 60Hz and as a result, storage and loss modulus of the transformerboard is needed at these frequencies. Frequencies are set to 0.1Hz, 1Hz, 50Hz, 60Hz, 100Hz and 120Hz. Temperature range was selected between -10^0C to 180^0C. Before testing the specimens, the DMTA test machine was calibrated with a steel specimen with known dimensions and material properties. Temperature increment was set to 3^0C every minute. Liquid nitrogen was used to cool down the test chamber to initial test temperature, -10^0C. Specimens are cut in cross machine direction.

Figure-7.1 show the storage modulus measured within the specified temperature range. Curves are labelled from 1 to 6 representing frequencies between 0.1Hz to 120Hz. Storage modulus is higher as the applied frequency is increasing at all temperatures. However, the gap between the frequencies is decreasing with the increasing temperature. Storage modulus at 120Hz is only 1.5% higher than that of 50Hz. At around 115^0C, the storage

modulus is almost equal for the frequencies above 50Hz. The average ratio of storage modulus at 120Hz to 0.1Hz is 15%.

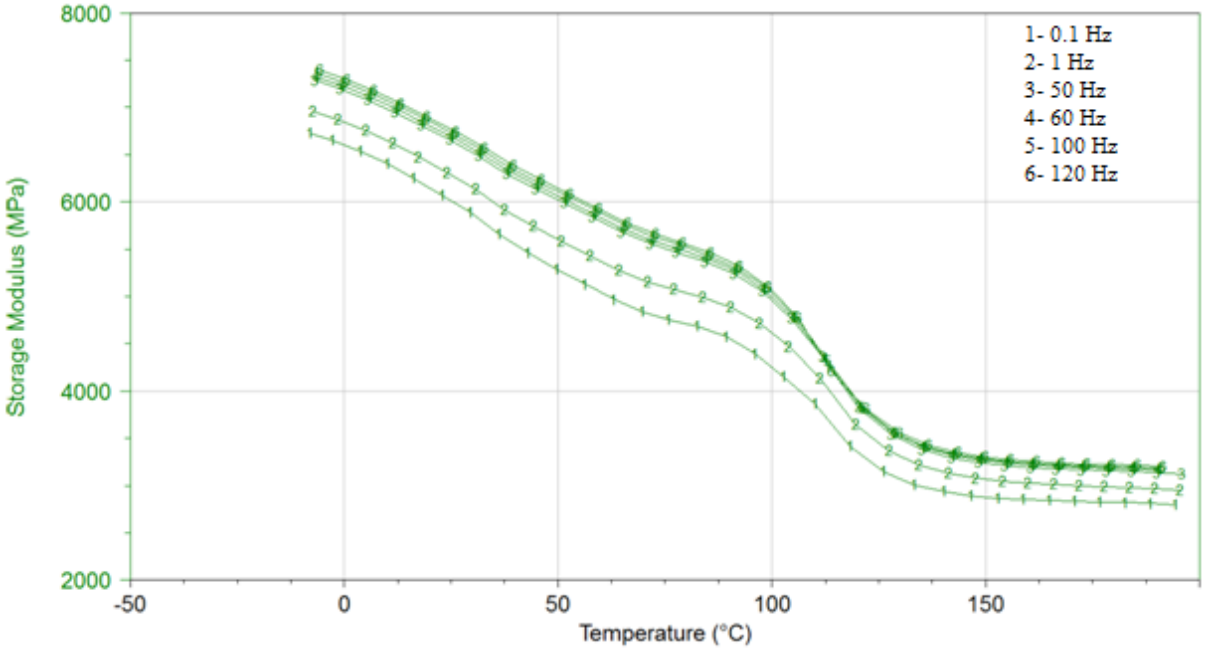

***FIGURE-7.1**: Storage Modulus of Transformerboard between -10^{0}C and 190^{0}C at Six Different Frequencies for Dried Specimen – CM Direction*

The effect of temperature on storage modulus is much more pronounced than frequency. The storage modulus at 180^{0}C is 41% of the value at -10^{0}C. Storage modulus is decreasing at almost constant ratio up to 100^{0}C. Over 130^{0}C, the change in storage modulus remains almost the same. Between 100^{0}C and 130^{0}C, the change in the magnitude of the storage modulus is increased. Transformerboard's storage modulus is decreasing at all temperatures up to 130^{0}C and there is no apparent transition temperature. However, transition temperature can be said to take place at 115^{0}C because between 100^{0}C and 130^{0}C, the change in storage modulus is accelerated.

Tan delta, which is the ratio of the loss modulus to storage modulus, is shown in Figure-7.2. Tan delta reaches its highest value at 0.1Hz at all temperatures. At 118^{0}C, tan delta reaches its peak value, 0.1045. Tan delta at 120Hz and 100Hz is slightly higher that the frequencies at 50Hz and 60Hz and hence, at the frequencies which occur during short circuit, tan delta remains almost the same. During actual short circuit tests, the temperature of the transformer oil is almost the same with ambient temperature and as a result, the temperature range between 20^{0}C to 40^{0}C can be selected to determine the loss modulus of the transformerboard. There is no significant peak value for tan delta at high frequencies.

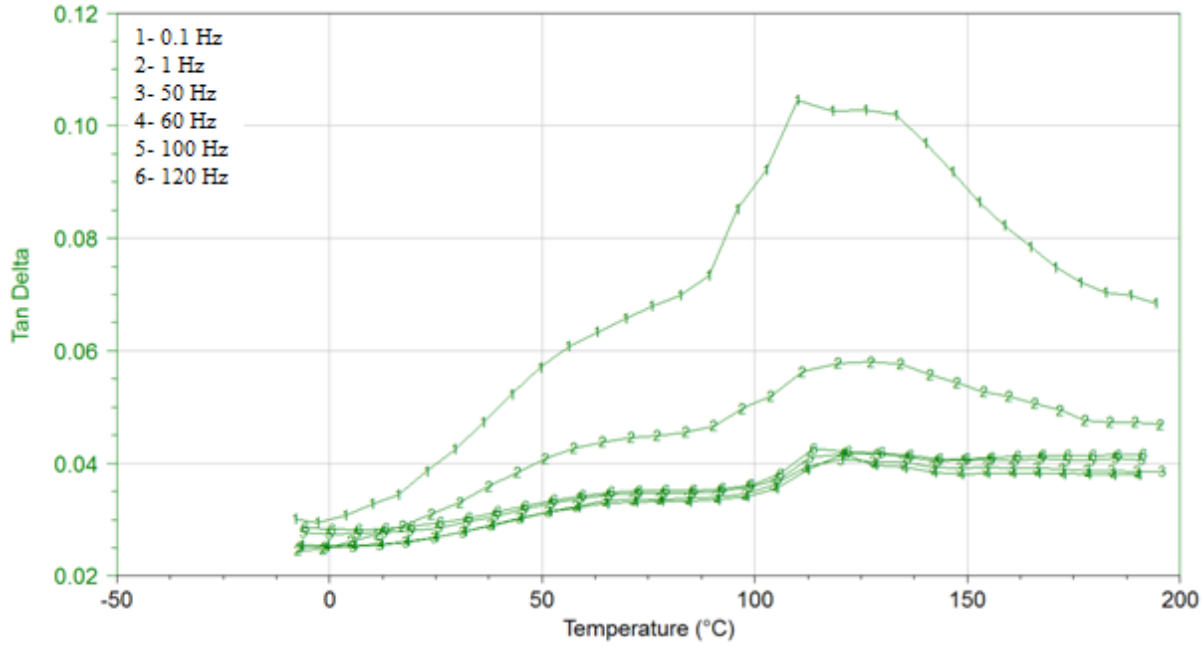

***FIGURE-7.2**: Tan Delta of Transformerboard between -10^{0}C and 190^{0}C at Six Different Frequencies for Dried Specimen – CM Direction*

Tan delta measured for dried transformerboard is small in magnitude and it is suspected that viscoelastic model introduced by previous researchers in [18] and [48] is valid. First of all, the formula developed in [18] involves Poisson's ratio of the transformerboard and Poisson's ratio was assumed constant. It was shown in Chapter-5 that the Poisson's ratio of the transformerboard through the thickness direction is not constant and increases with the applied load. Secondly, it can be seen from the Figure-7.2 that the loss modulus of the transformerboard is very small, especially between the temperature ranges of interest. Damping due to friction, for example, have more effect on dynamic response of transformer winding.

Figure-7.3 shows the storage modulus and tan delta of transformerboard for oil-impregnated specimen at 0.1Hz, 50Hz, 60Hz, 100Hz and 120Hz. The shape of the storage modulus and tan delta curves resembles the curves obtained for dried specimen. General behaviour of the transformerboard does not change when it is oil-impregnated but magnitudes change. Tan delta reaches its peak value at around 116^{0}C. The same conclusions can be drawn for oil-impregnated specimen.

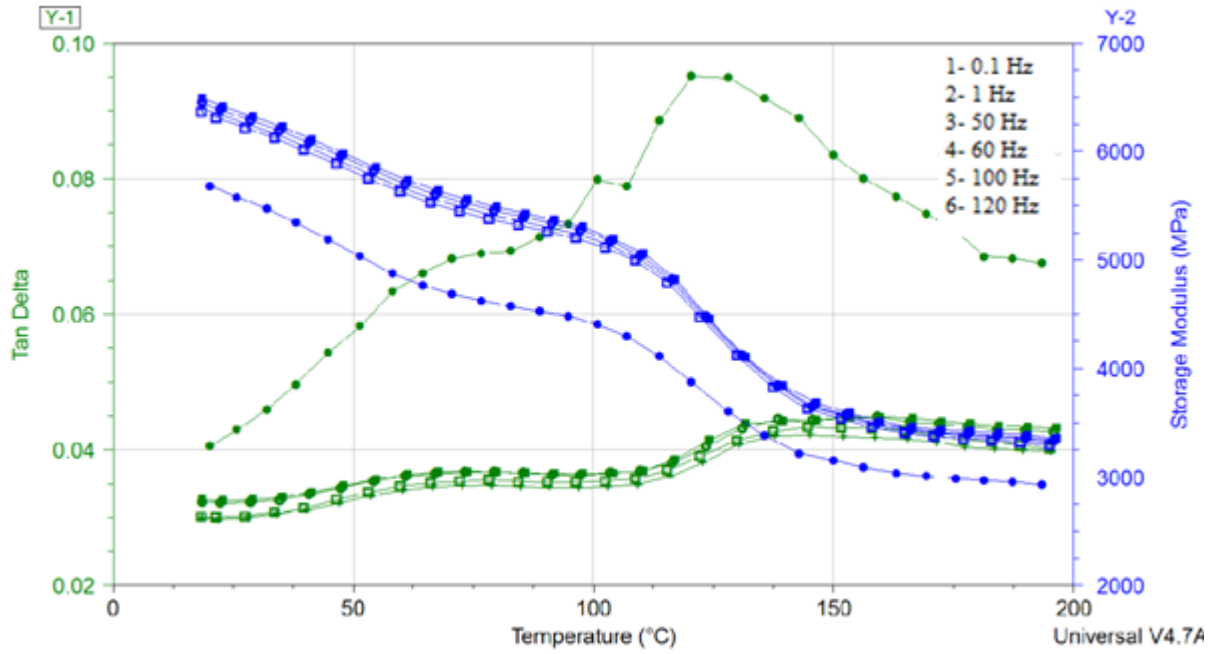

***FIGURE-7.3**: Tan Delta and Storage Modulus of Transformerboard between 20^{0}C and 190^{0}C at Five Different Frequencies for Oil Impregnated Specimen – CM Direction*

In transformer design, the hot-spot temperature is restricted to 118^{0}C because of the ageing characteristics of the cellulosic based materials. It was mentioned in [49] that thermal ageing reduces the mechanical strength of the cellulosic material. Cellulosic material becomes brittle and this process is irreversible. In order to determine the storage modulus and tan delta of transformerboard after 118^{0}C is exceeded, the test specimen is tested again using the same test setup. Figure-7.4 shows the storage modulus and tan delta. It can be seen from the graph that both the magnitudes and shapes of the curves are changed. Peak Tan delta is reduced to half of its original value. At 80^{0}C and for frequencies higher than 10Hz, tan delta reaches a minimum value and from this point, it increases with the temperature. At lower frequencies, the tendency of tan delta is to increase however the rate of increase is small. Storage modulus is decreasing at a constant rate up to 130^{0}C and at around this temperature, the tendency is still to decrease but with a higher rate.

The change in both the magnitude and the shape of these curves suggests that the material properties of the transformerboard changes and its response during short circuit event changes if the temperature limit is exceeded. These results show that the damping characteristic of the transformerboard can be neglected during dynamic short circuit forces.

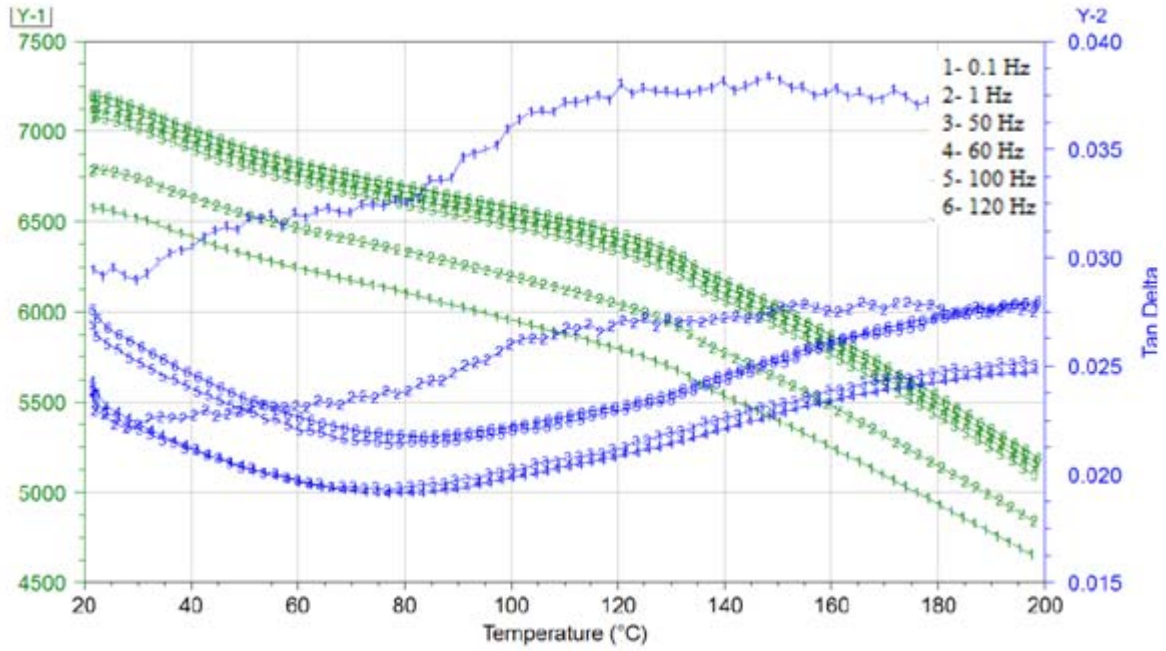

***FIGURE-7.4**: Tan Delta and Storage Modulus of Transformerboard between 20^{0}C and 190^{0}C at Six Different Frequencies for Dried Specimen after the Ageing Limit is Exceeded– CM Direction*

7.3 Test Setup to Determine Time Dependent Behaviour of the Transformerboard

A new test setup is required to determine the response of the transformerboard under constant load because conventional creep test setups do not have suitable grips and a container to heat and circulate the hot transformer oil. The test setup should include suitable grips, container to heat transformer oil, pump to circulate transformer oil, thermometer to control resistances and a second thermometer with contacts to cut the power supply if the temperature exceeds 140^{0}C to prevent fire as the transformer oil is flammable, hour-run-meter to measure to time to failure and equipment to measure displacement. Comparison of the creep data when the transformerboard is soaked in transformer oil and in air will also be determined. The test setup will be formed of six containers, three containers for tests in oil and the rest for tests in air.

Figure-7.5 shows the design of test setup and Figure-7.6 shows the design of grips. The loading arm ratio is designed to give 1:4 mechanical advantage. At one end, there are weights to provide constant load and at the other end, test specimen is attached with suitable grips. Bearings are used to minimise the effects of friction.

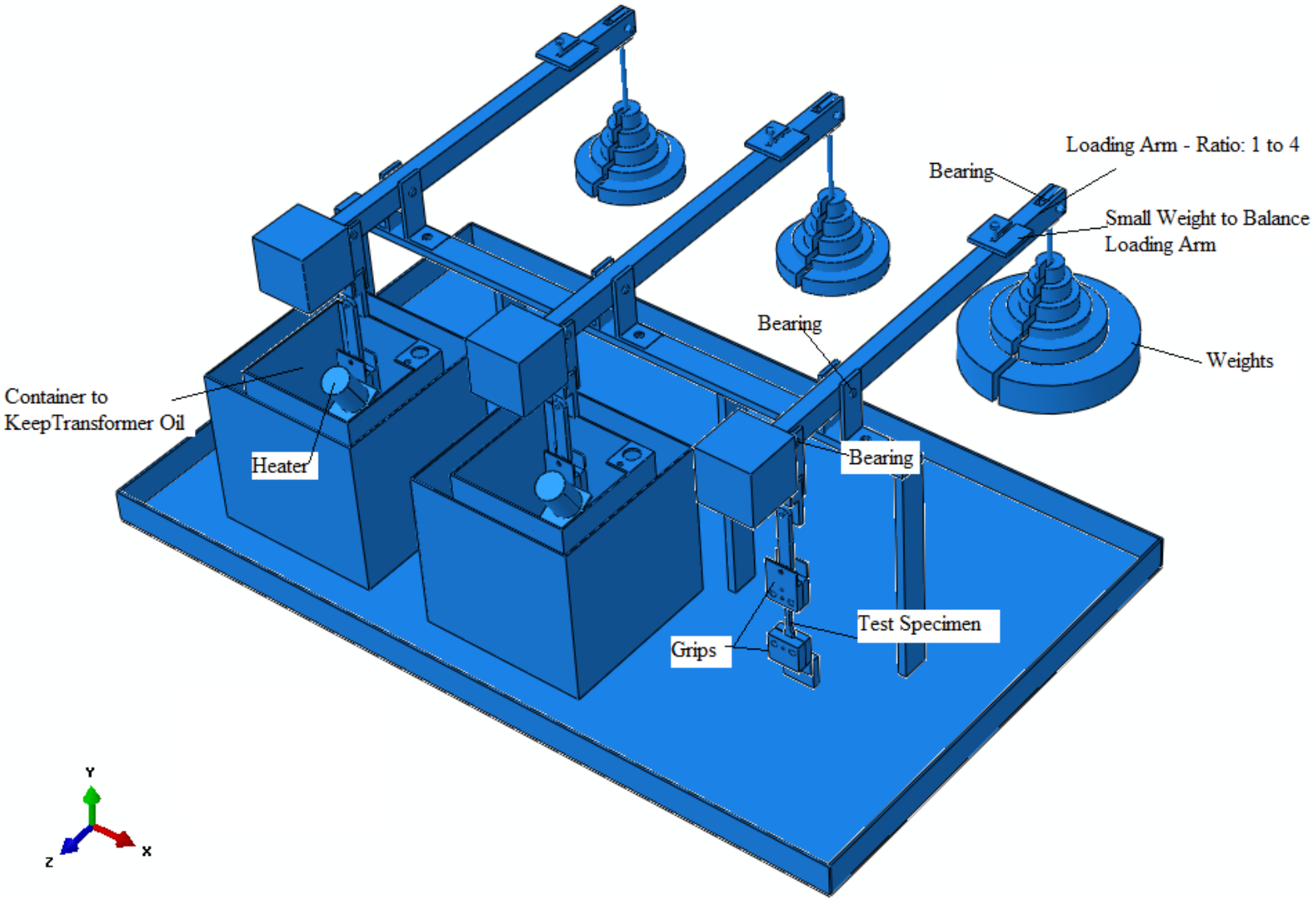

***FIGURE-7.5**: Creep Test Setup Design*

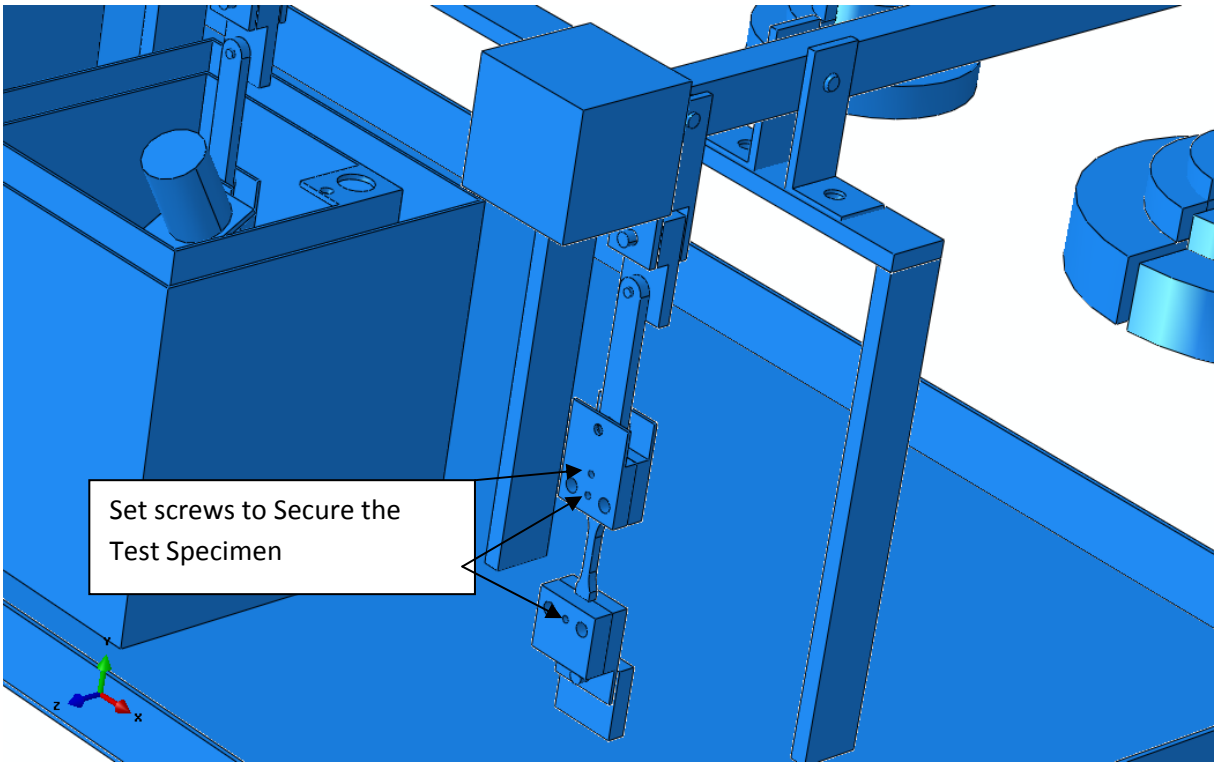

***FIGURE-7.6**: Grips and Test Specimen*

A small rectangular weight was also used at loading arm for balancing purposes at the beginning of the tests, if needed. The gap between the small and large container was filled with heat insulation material to minimise the heat transfer from the container. The grips are designed to rotate in X, Y and Z directions. Therefore, the weights provide tensional loading only and no bending and torsion stresses are generated on the test specimen. In this setup, three tests can be performed at the same time in oil. The same design will also be used for the tests in air and therefore, 6 specimens can be tested at the same time. Slots in the grips, where the test specimen is attached, are designed 4% smaller in dimensions to tighten the test specimen and prevent slippage of the specimen within the grips. Set screws are also used to secure the test specimen to the grips.

Digital dial indicators are used to measure the displacement. Accuracy of the dial indicators is 0.5 micro-meters and enables to save the recorded data into a PC and the displacement versus time graphs can be obtained automatically. This is achieved by the six channel digital interface. A special software, process analyzer and manager software, is used and every dial indicator can be operated separately. For instance if one specimen fails, only that channel is deactivated automatically and the rest of the channels continue to record and save data.

Data are saved at every recording time interval and in the event of power cut, the data are protected. Recording time interval can be set from 1 milisecond to 1 hour and six channels can be recorded simultaneously. For each channel, recording time interval can be set to a different value enabling to use smaller recording interval for tests at high temperature, where the time to failure is shorter.

For the tests in oil, hot transformer oil resistant gear pumps are used. The pumps' power is selected as 0.55kW which will provide a capacity of 4 litres per minute. Pumps are designed to work up to 150^0C and maximum test temperature is determined as 140^0C. Relief valves are used to protect the equipment from excessive internal pressure. Fans are used to circulate the hot air for the test setup instead of the pumps.

A control unit and visual indicators are designed to cut the power of the unit when the test is completed or in the event of faulty equipment. Visual indicators include pump running – pump failure, fans are running- fan failure, heaters on-off, end of test, power supply failure. Pumps work with 380VAC, heaters, lambs and PC equipment work with 220VAC and time indicators work with 120VDC. Suitable circuit breakers are used based on the voltage level of the equipment. The PC and dial indicator unit is connected to a UPS and all the rest of the equipment is connected to generator unit. Therefore, the units will continue to work in case of power cut.

Hour-run-meters are also used in order to increase the reliability of the system if the PC fails. Digital thermometers with $\pm1^0$C accuracy control the test temperature. Special thermometers with double contacts, used in power transformers to indicate oil temperature, are set to 150^0C to cut the power supply if the temperature of the oil exceeds the critical flash point. Second contact is set to 5^0C below the test temperature to indicate the faulty digital thermometer. Switches to cut power supply are installed under the loading arm. When the specimen breaks, the loading arm will drop due to weights and will cut the power of that unit as shown in Figure-7.8 All these precautions are necessary because the transformer oil is flammable over certain temperature. Figure-7.7, Figure-7.8 and Figure-7.9 show the test setup developed and shows the equipment used. The test setup is assembled in a dust and temperature controlled room.

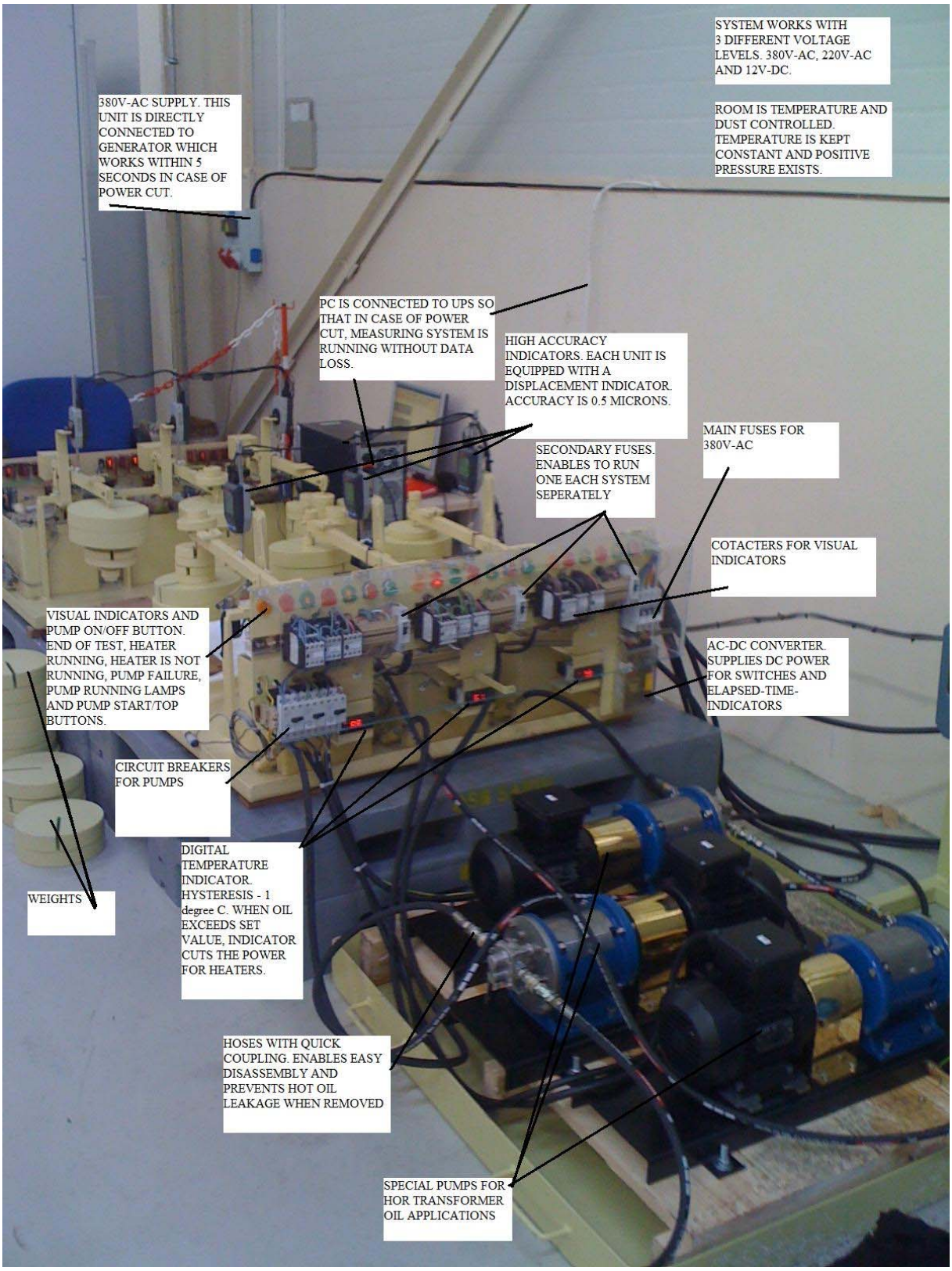

***FIGURE-7.7**: Creep Rig – View.1*

FIGURE-7.8 *Creep Rig – View.2*

***FIGURE-7.9**: Creep Rig – View.3*

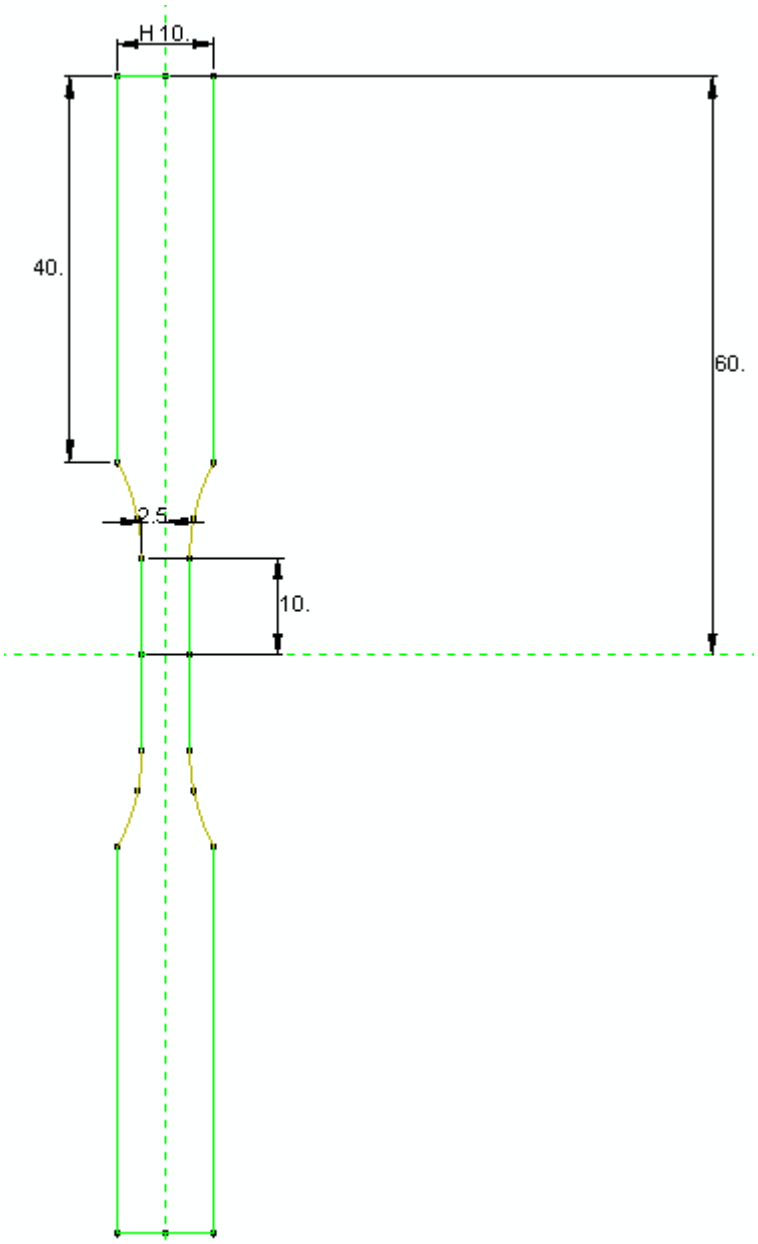

***FIGURE-7.10**: Creep Test Specimen Dimensions*

Figure-7.10 shows the dimensions of the test specimen. In order to prevent slippage of the test specimen under tension load, 40mm of grip length is provided to the both ends. Also, 40mm of grip length enabled to use more set screws to secure the test specimen to the test rig grips. Stress concentrations are expected at the areas where the test specimen is attached to the grips. In order to ensure that the failure will not occur at these areas and to provide more uniform stress distribution, the specimens are necked. Because the specimens will be soaked in oil bath, the length of the specimens is kept as small as possible and the quantity of the oil used during the tests is minimized. This is necessary because the

temperature distribution along the specimen within the container should be kept almost the same.

The test procedure was as follows. Test specimen was tightened between the upper and lower grips and secured using set screws. Specimen was placed in the container and using the small rectangular weight, the loading arm was balanced. This was to ensure that before assembling the weights, the loading arm was balanced with respect to fixed point. Digital thermometers were set to test temperature and protective thermometers were set. Heaters and pumps were turned on and when the test temperature was reached, specimen was left in the hot oil for 10 more additional minutes in order to ensure that the temperature distribution in the specimen was distributed uniformly. Hour-run-meters and dial indicators were reset and run and weights were assembled. Test setup automatically recorded the displacements within the selected time interval. Specimens were dried and oil impregnated in a special oven. The oven used was the same drying oven used to dry the complete power transformer active part. The drying procedure was the same for the specimens used in DMTA tests and the procedure will not be repeated here.

7.4 Creep Test Results

Tests in oil were performed at 25^0C, 60^0C, 80^0C, 100^0C, 120^0C and 140^0C. At the end of the tests, tests specimens were separated into two pieces as shown in Figure-7.11. The failure mechanism of the machine direction test specimens resembles the failure mechanism of the tensile test specimens at all test temperatures. Failure occurs through the thickness direction and propagates along the specimen. Conclusions drawn for failure mechanism of the tensile tests are valid. Failure mechanisms of the specimens tested in the air are failed similarly. Failure occurred through the thickness and propagated along the specimen.

***FIGURE-7.11**: Failed Specimen*

Figure-7.12 shows the displacement – time curve obtained from the test setup of a specimen tested in transformer oil at 140^0C. This curve is given to demonstrate the output of the designed test setup and will be replaced with processed data namely, strain – time curve as shown in Figure-7.13. Recording time interval was set to 10 seconds and the load value was chosen as 25kg. The applied stress was 4MPa and the ultimate strength of the transformerboard is 6.93MPa. The creep tests will be carried out at the different test loads to determine the material's response and the time to failure. Due to time constraints, the highest possible test load was chosen to obtain the initial test results.

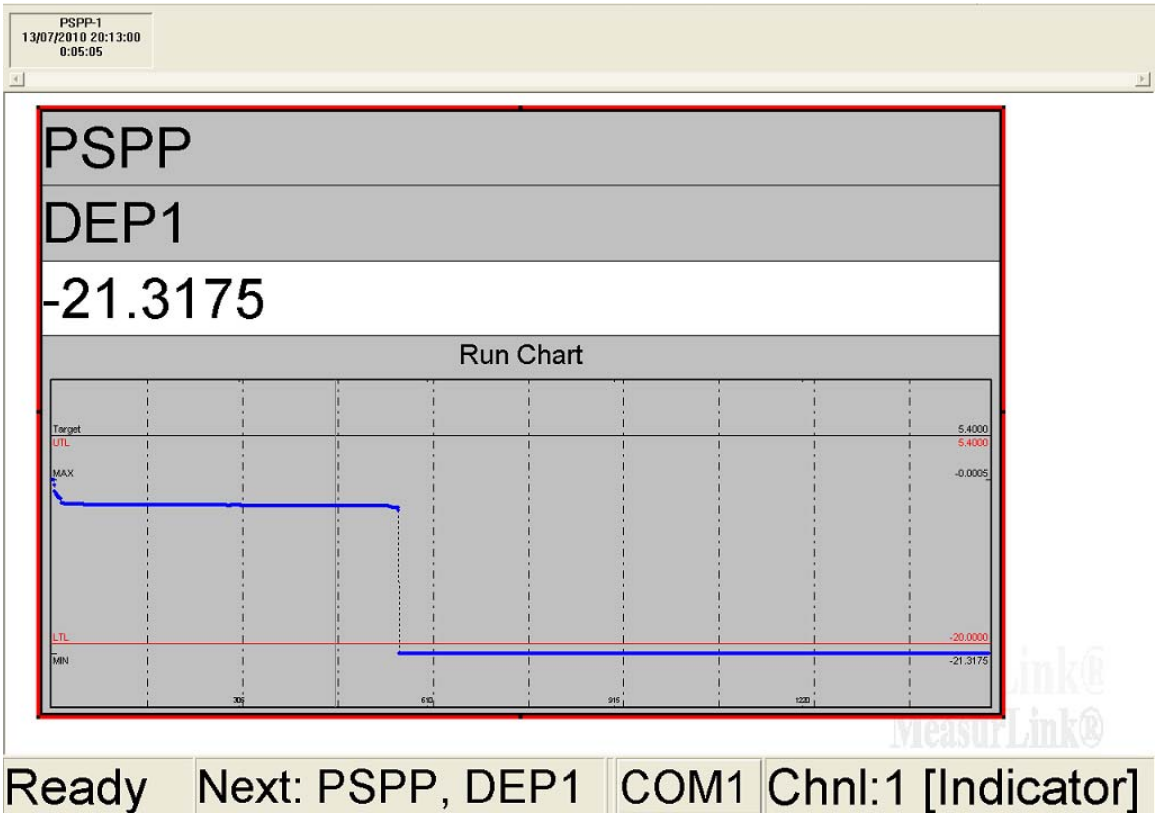

***FIGURE-7.12**: Displacement – Time Curve for Transformerboard Tested in Transformer Oil at 140^{0}C – Applied Stress 4MPa*

The specimen failed 93.7 minutes after being loaded with 25kg. After initial elongation, due to sudden response of the material to applied load, recorded strain increased within a short interval to % 15 strain rates. Material then elongated at almost constant rate with the time, 0.0075, up to the time of failure. Approximately 150 seconds before the final failure, the displacement measured by the dial indicators increased dramatically according to the curve. This indicates that the first failure occurred through the thickness direction and the crack propagated along the specimen up to the time of the final failure, separation of the test specimen into two pieces.

According to IEC standards, the hot-spot temperature of the transformer should be limited to 120^{0}C. This limitation is due to insulation materials used in the transformers and 140^{0}C test temperature was chosen to compare the time to failure of the transformerboard with respect to temperatures below 120^{0}C.

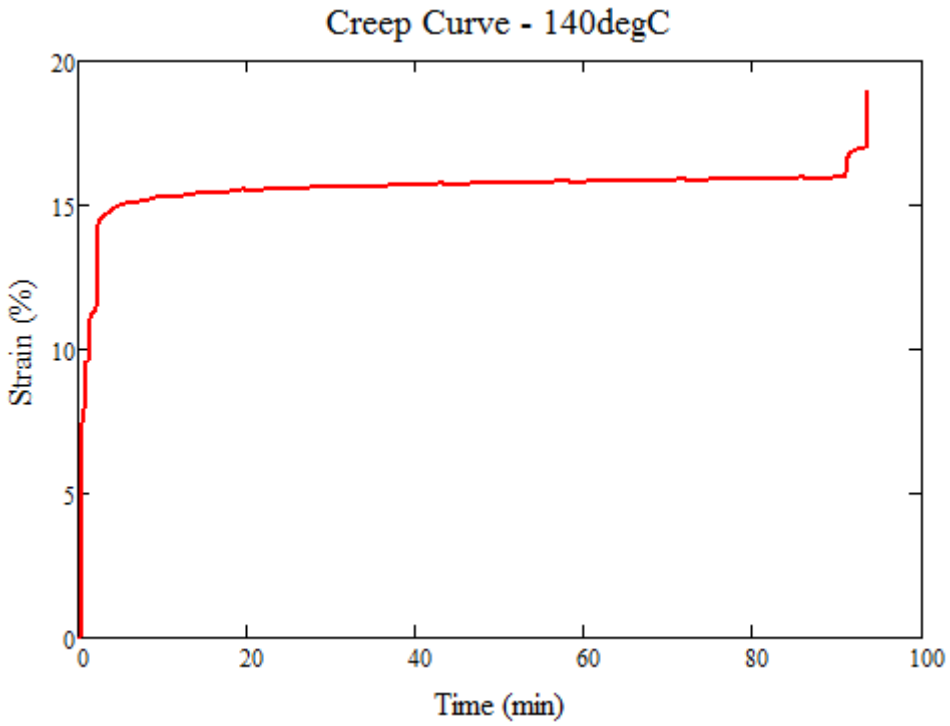

***FIGURE-7.13**: %Strain – Time Curve for Transformerboard Tested in Transformer Oil at 140^{0}C – Applied Stress 4MPa*

Figure-7.14 shows the %strain – time curve obtained from the test setup of a specimen tested in transformer oil at 120^{0}C. Recording interval was set to 3 minutes and 25kg of constant load was applied to the specimen. Material failed 1179 minutes after loading and time to rupture is 12.6 times higher than the specimen tested at 140^{0}C. The material's initial response to applied load is the same as before, recorded strain increased within short interval up to 12% strain rates. The constant rate of strain increment is about 0.0011. Measured %Strain for the specimen tested at 120^{0}C is lower than the specimen tested at 140^{0}C as expected. Although the failure mechanism is the same as the specimen tested at 140^{0}C, displacement just before failure was not recorded because the recording interval was set to 3 minutes.

Time to final failure will be given next for the specimens tested in oil and air. A single graph will be prepared to compare the creep curves of the specimens to be able to see the effects of temperature and chemical transformer oil more effectively.

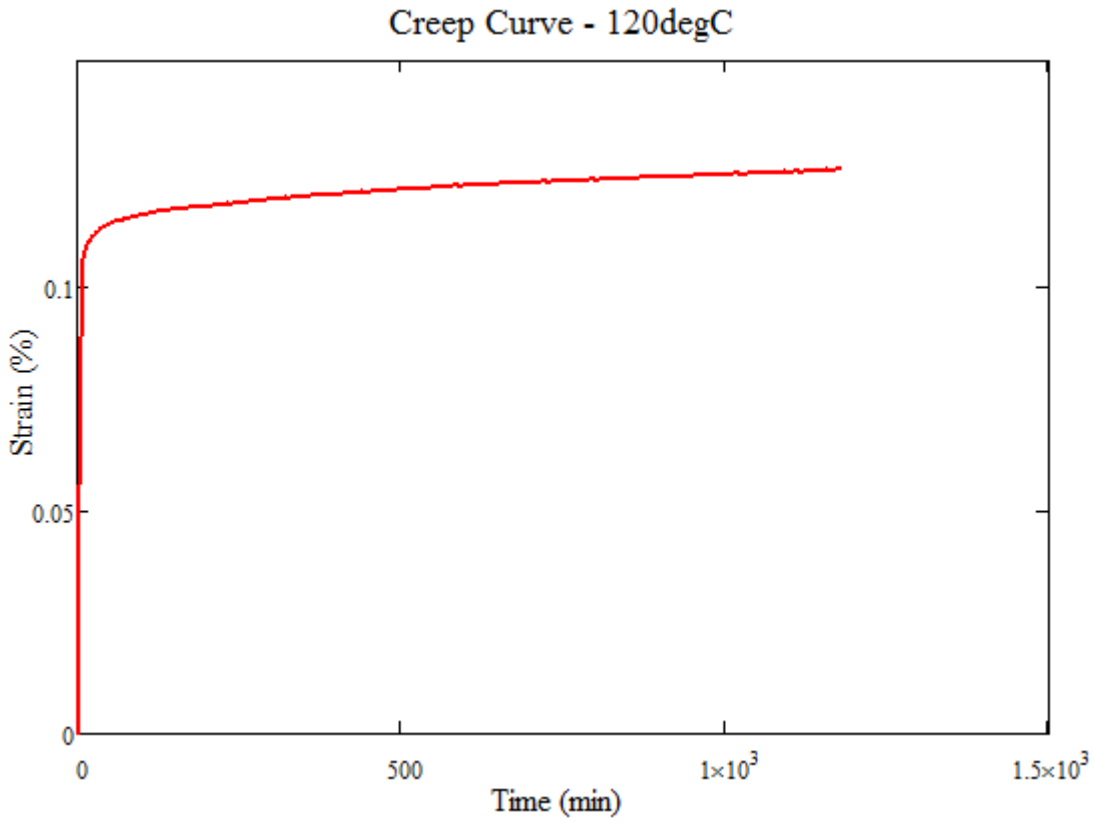

***FIGURE-7.14**: %Strain – Time Curve for Transformerboard Tested in Transformer Oil at 120^{0}C – Applied Stress 4MPa*

At 20^{0}C, the materials did not fail in both air and oil at the given load and the rate of increase in elongation is small. No failure is also observed for the materials tested in air at 40^{0}C. Chemical oil and temperature degrades the material properties and the time to final failure decreases dramatically with increasing temperature. Failure mode is the same for all materials. Failure in oil always occurs earlier at all test temperatures and the ratio of failure time in air to oil is decreasing with increasing temperature.

	140^{0}C	**120^{0}C**	**100^{0}C**	**80^{0}C**	**60^{0}C**	**40^{0}C**	**20^{0}C**
Oil	93.7	1179	1347	8751	15672	482736	------
Air	561	6926	12185	86213	218321	--------	------
Air/Oil Ratio	5.99	5.87	9.05	9.85	13.93		

***TABLE-7.1**: Time (Minutes) to Failure of Transformerboard Tested in Oil and Air at Different Test Temperatures*

Comparison of the creep curves is shown in Figure-7.15 up to 846 minutes in order to provide better comparison. As the temperature decreases, both the percentage strain and the elongation rate are decreasing.

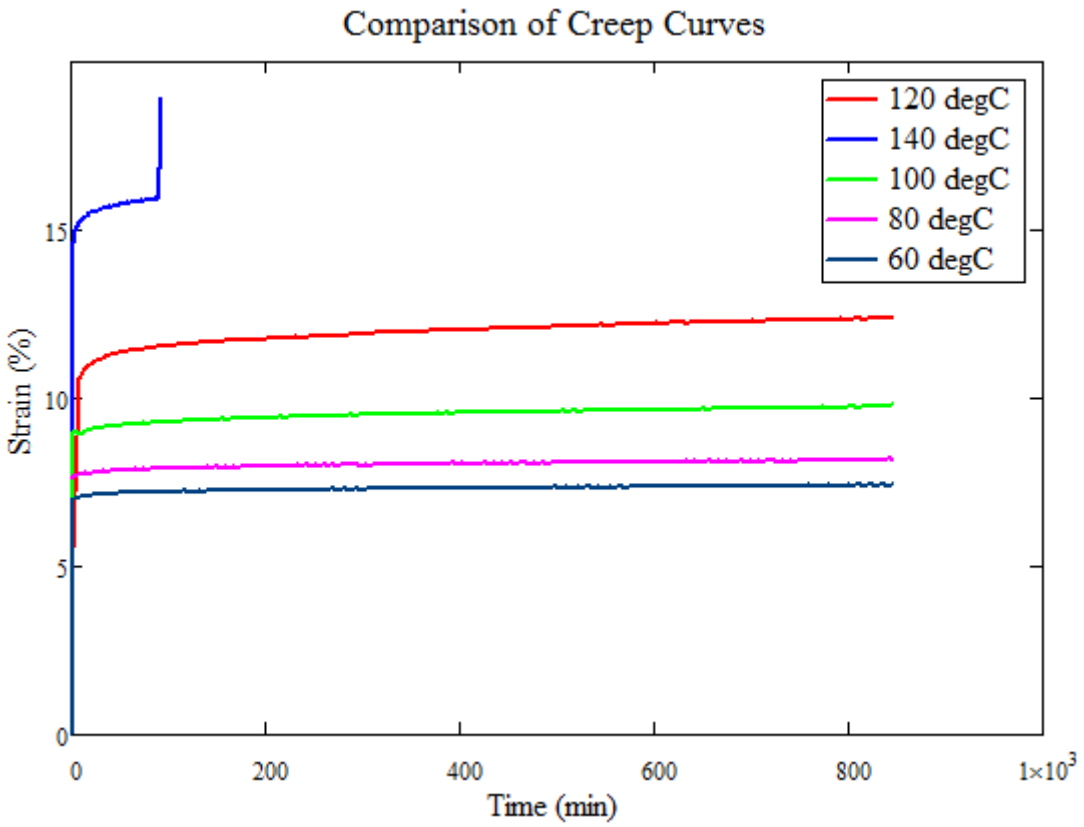

***FIGURE-7.15**: %Strain – Time Curve for Transformerboard Tested in Transformer Oil at Various Temperatures– Applied Stress 4MPa*

It was shown in previous chapters that the transformerboard always fails through the thickness direction and this is due to manufacturing technology as explained in Chapter-5. Geometric discontinuities can significantly reduce the life of the transformerboard during service because the failure always occurs through the thickness. Chemical oil and increased temperatures can reduce the life and the load carrying capacity and can cause unexpected failures. To study this effect, a notch was introduced and the material is tested in chemical oil at different temperatures. Figure-7.16 shows the dimensions of the notch. The other dimensions are kept the same. Table-7.2 shows the time to failure. At all temperatures, time to failure is reduced dramatically. Figure-7.16 compares the creep curves at 100^0C for the notched and normal specimens. The %strain is higher for notched specimen. This is due to higher stress introduced to test specimens because of the notches. At all temperatures, the %strain are higher between 1.6 to 2 times compared to the normal specimens.

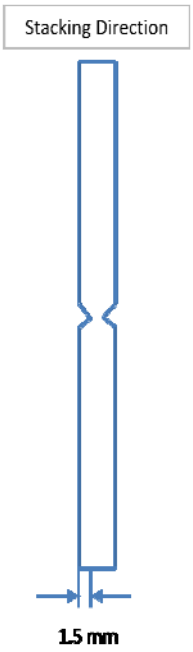

***FIGURE-7.16**: Test Specimen*

	140^{0}C	120^{0}C	100^{0}C	80^{0}C	60^{0}C	40^{0}C	20^{0}C
Notched	21	372	429	3587	6171	94623	------
Normal	93.7	1179	1347	8751	15672	482736	------
Normal/Notched Ratio	4.46	3.17	3.14	2.44	2.54	5.1	

***TABLE-7.2**: Time (Minutes) to Failure of Notched and Normal Transformerboard Specimens Tested in Oil at Different Test Temperatures*

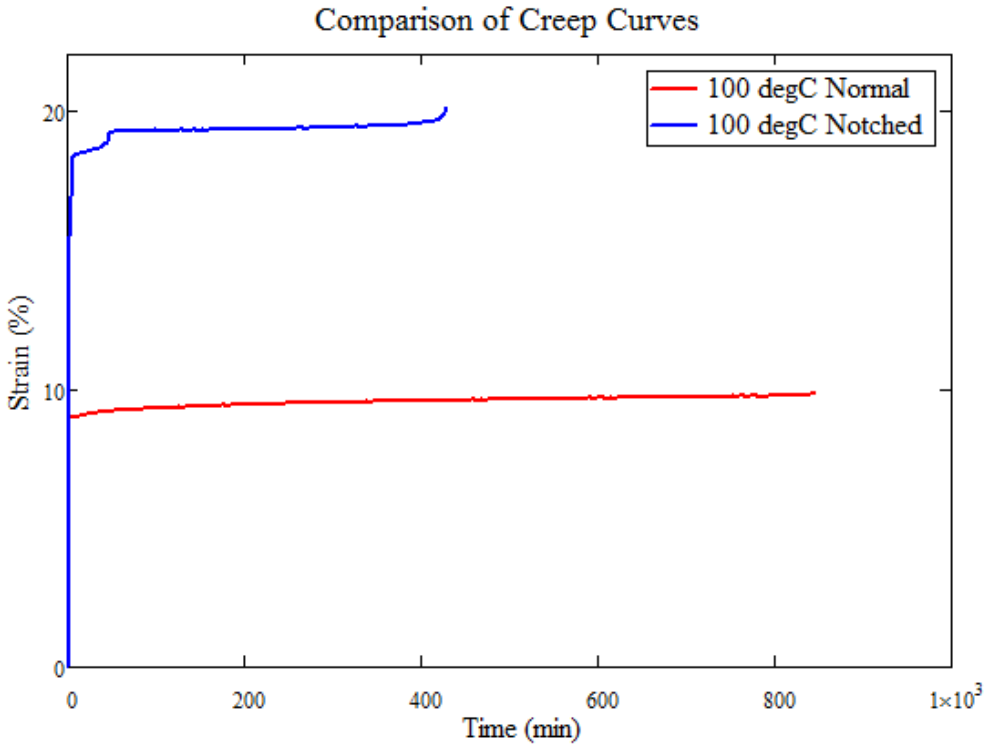

***FIGURE-7.17**: Comparison of %Strain – Time Curve for Transformerboard Tested in Transformer Oil at 100^{0}C for Notched and Normal Specimens - Applied Stress 4MPa*

7.5 Conclusions

Transformerboard is working in transformer oil up to 105^0C oil temperature and the hot-spot temperature is limited to 118^0C. The hot-spot temperature is generated by Joule losses and eddy losses. Eddy losses are higher at the winding ends because the magnetic flux fringes and radial component of the magnetic flux induces eddy currents because the axial dimension of the transformer winding is higher than radial dimension. The behaviour of transformerboard in transformer oil at elevated temperatures is required to determine the response of transformerboard to real working conditions.

Previous researchers, in [18] and [48], used a viscoelastic model to determine the winding's response under dynamic short circuit forces. They used a linear viscoelastic model to determine the complex modulus of the transformerboard. However, spring and dashpot constants required in the model were not given in detail. In section 7.1 of this Chapter, results of DMTA tests were presented. At the frequencies of interest, exciting frequency and double exciting frequency, tan delta and storage modulus were shown to not change much and remains almost constant. At the lower frequencies, peak tan delta was found to be 0.1, very small compared to polymers for example. Therefore, the viscoelastic damping does not have much effect on the dynamic response compared to damping due to friction, transformer oil etc. The change in tan delta and storage modulus with temperature has much more effect on transformerboard. Although an apparent transition temperature cannot be determined for transformerboard, between 100^0C and 130^0C, the decrease in storage modulus is accelerated.

A test setup was designed to determine time dependent elongation of transformerboard under constant loading in oil bath and in air at different temperatures. Test setup was designed to record displacements automatically in a PC at appropriate intervals. Time to failure and creep curves were plotted and compared for specimens tested in air and oil. It was shown that the transformerboard exhibits time dependent elongation and the rate of elongation is increasing with increasing test temperatures. Above 120^0C, ageing of transformerboard in transformer oil is increasing and both the load carrying capacity and time to failure was decreased dramatically.

A notch was introduced at stacking direction to study the effect of a notch on the test specimen. Time to failure was compared and %strain - time curves were plotted.

Tests were performed at 25kg of constant load for machine direction specimens. In order to provide full range of test data, tests have to be performed at different loads. Cross machine direction specimens need to be tested. When all tests are performed and the results are processed, simulations can be performed of clamping ring of transformerboard to simulate working conditions for overloading conditions, the worst case scenario that causes increase in temperature of transformerboard.

Electrical wiring diagrams of test setups are shown in Appendix-B. Figure-B.1 shows the wiring diagram for test setup to test specimens in air and Figure-B.2 shows the wiring diagram for test setup to test specimens in oil.

8-CONCLUSIONS & FUTURE WORK RECOMMENDATIONS

Transformers are one of the key components in power generation and transmission lines and their service life is expected to be a minimum of 25 years. Failures are caused by overvoltages, short circuit and ageing of the insulation materials due to excessive heating. To ensure that the transformer reaches the required service life, properties of the insulation material and conductors, forces and overvoltages of electromagnetic origin need to be calculated accurately. This thesis is aimed at providing new methods to calculate electromagnetic forces and mechanical stresses acting on transformer components and to provide insight into insulation materials using relatively new techniques such as DIC and fast speed photography.

In Chapter-3, an analytical method to calculate magnetic properties of power transformers is presented. This method relaxes the “infinitely permeable core” assumption and enables the calculation of open and short circuit properties of power transformers. Previous methods cannot calculate open circuit properties of power transformers and the solution technique also shows how to handle multiply connected permeable regions. Especially, self and mutual inductances can be calculated with great accuracy and the method can also be used as a model a lumped parameter model for transient voltage distribution. The method provides much more accurate results compared to previous techniques because the permeability of the core is taken into account. The extension of the widely used Roth’s method when transformer window is attached to a highly permeable region is also given. The proposed method was compared to finite element and near to perfect agreement was found. This solution technique can be extended to take into account harmonic loading conditions and AC losses induced on conductors can be calculated. Distribution of radial and axial short circuit forces along the winding is shown using the force density function.

Radial short circuit forces acting on the inner winding can cause collapse of the winding. In order to prevent the winding from collapse the number of axial sticks is increased or, if the conductor is CTC type, strands of CTC are bonded with epoxy. Shear stress acting on epoxy is critical because once the epoxy is broken, the radial strength of the winding will reduce significantly and failure will occur. Formulas given in [38] are updated in Chapter-4 to take

the effects of the shear stresses into account. With the developed formulas, bending and normal stresses are also corrected.

The dynamic representation of the transformer winding in axial direction is also shown. A solution technique is developed for non-proportional damping and a particular solution is developed where the forced part considers short circuit forces. A technique is shown to separate dynamic short circuit current from the magnetic flux density and as a result, the components of magnetic flux density are treated as a constant term.

3-D Digital Image Technique is used to determine material constants of transformerboard under tensional and bending type loading conditions. DIC results revealed that transformerboard's thickness increases with the applied load and Poisson's ratio is positive. It was also shown that the DIC technique provides better comparison and results compared to measurements with strain gauges because strain gauges need to be glued on the specimen surface and generate additional resistance. Transformerboard exhibits linearly plastic behaviour and plastic Poisson's ratios are determined. Shear modulus of the transformerboard is determined using the developed theoretical formulas and DIC data. Theoretical formulas for three point bending tests are developed considering orthotropic material properties. Shear strain distribution of transformerboard on the plane where short fibres are dominant is random and no apparent shear modulus can be found using the technique developed. Bending and shear strain distribution of transformerboard is shown and material properties calculated using DIC and the developed technique. Transformerboard is compared to resin laminated wood material with glass fibres. DIC results showed that although resin laminated wood material has higher bending strength, discontinuities develop as the load level increased and the load carrying capacity is affected. DIC results shows that the discontinuities occur on laminas stacked 90^0 to beam.

Viscoelastic properties of transformerboard are studied in Chapter-7. DMTA technique is used to determine tan delta and storage modulus of transformerboard material. These properties are especially important at the frequencies of interest and it is shown that transformerboard does not show significant viscoelastic damping. The value of maximum damping reached is very small compared to polymers. The effect of frequency on tan delta and storage modulus is small however these properties change significantly with

temperature. A test setup is designed to determine creep curves of the transformerboard material and creep curves are drawn for specimens tested in transformer oil and in air at different temperatures. The time to failure of the transformerboard at different temperatures is determined.

Creep tests are performed only for machine direction specimens at 25kg load. In order to provide full range of test data for simulation purposes, tests should be performed at different loads. The same tests should also be performed for cross machine direction specimens. Laminated wood material with different densities can also be tested with the developed test setup in order to provide data to compare transformerboard with laminated wood. Fatigue behaviour of transformerboard is not studied in this thesis. Not much data exist in the literature and an extensive test results are required for both transformerboard and resin laminated wood. Critical energy release rates of transformerboard also need to be studied and test methods developed in [30] to [33] can be used at different test speeds.

The analytical method introduced is developed in cartesian coordinates and as a result, curvature effect was neglected. The mean diameter is calculated for the short circuit case considering sum of ampere-turns. For the open circuit condition the mean diameter of the core is considered. The solution technique can be extended to cylindrical coordinates. This solution will involve Bessel and Struve functions of some orders and will be quite complicated. Roth's solution in cylindrical coordinates is quite cumbersome and a method similar to Rabins' can provide easier solution steps to solve the Poisson's region. The same solution technique explained in Chapter-3 can then be used to solve multiply connected permeable regions.

APPENDIX-A: FINAL MATRIX TO CALCULATE FOURIER COEFFICIENTS & ITS CONSTITUENTS

$$\begin{pmatrix} D \\ H \\ JJ \\ L \\ M \\ Y \\ Z \\ OO \\ OV \\ OZ \\ OQ \\ OP \end{pmatrix} = \begin{bmatrix} \alpha 1F_{k,s} & \alpha 2F_{k,s} & \alpha 3F_{k,s} & \alpha 4F_{k,s} & \alpha 5F_{k,s} & \alpha 6F_{k,s} & \alpha 7F_{k,s} & \alpha 8F_{k,s} & \alpha 9F_{k,s} & \alpha 10F_{k,s} & \alpha 11F_{k,s} & \alpha 12F_{k,s} \\ \beta 1F_{k,s} & \beta 2F_{k,s} & \beta 3F_{k,s} & \beta 4F_{k,s} & -\alpha 5F_{k,s} & -\alpha 6F_{k,s} & \beta 7F_{k,s} & -\alpha 8F_{k,s} & -\alpha 9F_{k,s} & -\alpha 10F_{k,s} & -\alpha 11F_{k,s} & -\alpha 12F_{k,s} \\ \gamma 1F_{s,k} & \gamma 2F_{s,k} & \gamma 3F_{s,k} & \gamma 4F_{s,k} & \gamma 5F_{s,k} & \gamma 6F_{s,k} & \gamma 7F_{s,k} & \gamma 8F_{s,k} & \gamma 9F_{s,k} & \gamma 10F_{s,k} & \gamma 11F_{s,k} & \gamma 12F_{s,k} \\ \delta 1F_{s,k} & \delta 2F_{s,k} & -\gamma 3F_{s,k} & -\gamma 4F_{s,k} & -\gamma 5F_{s,k} & \delta 6F_{s,k} & -\gamma 7F_{s,k} & -\gamma 8F_{s,k} & \delta 9F_{s,k} & -\gamma 10F_{s,k} & -\gamma 11F_{s,k} & \delta 12F_{s,k} \\ \varepsilon 1F_{s,k} & \varepsilon 2F_{s,k} & \varepsilon 3F_{s,k} & \varepsilon 4F_{s,k} & \varepsilon 5F_{s,k} & \varepsilon 6F_{s,k} & \varepsilon 7F_{s,k} & \varepsilon 8F_{s,k} & \varepsilon 9F_{s,k} & \varepsilon 10F_{s,k} & \varepsilon 11F_{s,k} & \varepsilon 12F_{s,k} \\ -\varepsilon 1F_{s,k} & -\varepsilon 2F_{s,k} & \theta 3F_{s,k} & \theta 4F_{s,k} & \theta 5F_{s,k} & -\varepsilon 6F_{s,k} & -\varepsilon 7F_{s,k} & -\varepsilon 8F_{s,k} & -\varepsilon 9F_{s,k} & \theta 10F_{s,k} & \theta 11F_{s,k} & -\varepsilon 12F_{s,k} \\ \eta 1F_{k,s} & \eta 2F_{k,s} & \eta 3F_{k,s} & \eta 4F_{k,s} & \eta 5F_{k,s} & \eta 6F_{k,s} & \eta 7F_{k,s} & \eta 8F_{k,s} & \eta 9F_{k,s} & \eta 10F_{k,s} & \eta 11F_{k,s} & \eta 12F_{k,s} \\ \eta 1F_{k,s} & \eta 2F_{k,s} & \eta 3F_{k,s} & \eta 4F_{k,s} & \eta 5F_{k,s} & \eta 6F_{k,s} & \eta 7F_{k,s} & \vartheta 8F_{k,s} & \vartheta 9F_{k,s} & \vartheta 10F_{k,s} & \vartheta 11F_{k,s} & \vartheta 12F_{k,s} \\ \chi 1F_{k,s} & \chi 2F_{k,s} & \chi 3F_{k,s} & \chi 4F_{k,s} & \chi 5F_{k,s} & \chi 6F_{k,s} & \chi 7F_{k,s} & \chi 8F_{k,s} & \chi 9F_{k,s} & \chi 10F_{k,s} & \chi 11F_{k,s} & \chi 12F_{k,s} \\ \chi 1F_{k,s} & \phi 2F_{k,s} & \chi 3F_{k,s} & \phi 4F_{k,s} & \phi 5F_{k,s} & \phi 6F_{k,s} & \phi 7F_{k,s} & \phi 8F_{k,s} & \phi 9F_{k,s} & \phi 10F_{k,s} & \chi 11F_{k,s} & \chi 12F_{k,s} \\ \lambda 1F_{s,k} & \lambda 2F_{s,k} & \lambda 3F_{s,k} & \lambda 4F_{s,k} & \lambda 5F_{s,k} & \lambda 6F_{s,k} & \lambda 7F_{s,k} & \lambda 8F_{s,k} & \lambda 9F_{s,k} & \lambda 10F_{s,k} & \lambda 11F_{s,k} & \lambda 12F_{s,k} \\ \xi 1F_{s,k} & \lambda 2F_{s,k} & \xi 3F_{s,k} & \lambda 4F_{s,k} & \xi 5F_{s,k} & \xi 6F_{s,k} & \xi 7F_{s,k} & \xi 8F_{s,k} & \lambda 9F_{s,k} & \lambda 10F_{s,k} & \xi 11F_{s,k} & \xi 12F_{s,k} \end{bmatrix}^{-1} \begin{pmatrix} \alpha 13F_{k,s} \\ -\alpha 13F_{k,s} \\ \gamma 13F_{s,k} \\ -\gamma 13F_{s,k} \\ \varepsilon 13F_{s,k} \\ -\varepsilon 13F_{s,k} \\ \eta 13F_{k,s} \\ \eta 13F_{k,s} \\ \chi 13F_{k,s} \\ \phi 13F_{k,s} \\ \lambda 13F_{s,k} \\ \xi 13F_{s,k} \end{pmatrix}$$

$$a2C_k = \frac{8y_1(-1)^{k+1}}{[\pi(2k-1)]^2}, \qquad Sup1a2 = \frac{\mu_1}{\mu_2}\left(\frac{-1}{(\kappa_1-\kappa_3)} - \left[\frac{(\kappa_2-\kappa_4)}{(\kappa_1-\kappa_3)} - 2y_1\right]SC_1\right), \qquad Sup2a2 = \frac{\mu_1}{\mu_2}\left(-\frac{(\kappa_2-\kappa_4)}{(\kappa_1-\kappa_3)} + 2y_1\right)SC_2$$

$$Sup3a2 = \frac{\mu_1}{\mu_2}\left(-\frac{(\kappa_2-\kappa_4)}{(\kappa_1-\kappa_3)} + 2y_1\right)SC_3, \qquad Sup4a2 = \frac{\mu_1}{\mu_2}\left(-\frac{(\kappa_2-\kappa_4)}{(\kappa_1-\kappa_3)} + 2y_1\right)\frac{1}{Constant2}$$

$$\alpha 1F_{k,s} = Diagonal(-\alpha 2_k) - a2C_k\frac{2y_1(-1)^{s+1}}{\pi(2s-1)a}(Sup1a2 + Sup3a2), \qquad \alpha 2F_{k,s} = -\alpha 5_{k,s} + a2C_k\frac{2x_1(-1)^{s+1}}{\pi(2s-1)b}Sup2a2$$

$$\alpha 3F_{k,s} = Diagonal(-\alpha 1_k) - a2C_k\frac{2y_1(-1)^{s+1}}{\pi(2s-1)a}Coth\left[\frac{\pi}{2y_1}(2s-1)x_2\right](Sup1a2 + Sup3a2), \qquad \alpha 4F_{k,s} = -a2C_k\frac{2x_2}{\pi(2s-1)b}Sup4a2$$

$$\alpha 5F_{k,s} = a2C_k\frac{b}{\pi sa}\frac{\mu_2}{\mu_1}Coth\left(\frac{\pi s}{b}x_2\right)\left[[1-(-1)^s]Sup1a2 + Sup3a2\right], \qquad \alpha 6F_{k,s} = a2C_k\frac{b}{\pi sa}\left[[1-(-1)^s]Sup1a2 + Sup3a2\right]$$

$$\alpha 7F_{k,s} = \alpha 4_{k,s} + a2C_k\frac{a}{\pi sb}[(-1)^s Sup4a2 - Sup2a2], \qquad \alpha 8F_{k,s} = a2C_k\frac{a}{\pi sb}\frac{\mu_2}{\mu_1}Coth\left(\frac{\pi s}{a}y_2\right)[(-1)^s Sup4a2 - Sup2a2]$$

$$\alpha 9F_{k,s} = a2C_k \frac{2x_1(-1)^{s+1}}{\pi(2s-1)b} Coth\left[\frac{\pi}{2x_1}(2s-1)y_2\right] Sup2a2\,, \qquad \alpha 10F_{k,s} = -a2C_k \frac{2x_2}{\pi(2s-1)b} Coth\left[\frac{\pi}{2x_2}(2s-1)y_2\right] Sup4a2$$

$$\alpha 11F_{k,s} = a2C_k \frac{2y_2}{\pi(2s-1)a} Coth\left[\frac{\pi}{2y_2}(2s-1)x_2\right] Sup1a2, \qquad \alpha 12F_{k,s} = a2C_k \frac{2y_2}{\pi(2s-1)a} Sup1a2$$

$$\alpha 13F_{k,s} = a2C_k \frac{\mu_1}{\mu_2}\left[a_{66}(y_2+b) - \left[\frac{Coef_1 - Coef_2}{(\kappa_1-\kappa_3)} + \left[\frac{(\kappa_2-\kappa_4)}{(\kappa_1-\kappa_3)} - 2y_1\right]\frac{Constant1}{Constant2}\right]\right]$$

$$\beta 1F_{k,s} = Diagonal(-\alpha 2_k) - \alpha 1F_{k,s} + Diagonal(\beta 2_k)\,, \qquad \beta 2F_{k,s} = -\alpha 5_{k,s} - \alpha 2F_{k,s}\,, \qquad \beta 3F_{k,s} = Diagonal(-\alpha 1_k) - \alpha 3F_{k,s} + Diagonal(\beta 1_k)$$

$$\beta 4F_{k,s} = -\beta 4_{k,s} - \alpha 4F_{k,s}\,, \qquad \beta 7F_{k,s} = -\beta 3_{k,s} - \alpha 5F_{k,s}$$

$$a3C_s = \frac{8x_1(-1)^{s+1}}{[\pi(2s-1)]^2}\,, \qquad Sup1a3 = -\frac{\mu_1}{\mu_2}\left[\frac{(\kappa_6-\kappa_8)}{(\kappa_5-\kappa_7)} + 2x_1\right] SC_1, \qquad Sup2a3 = \frac{\mu_1}{\mu_2}\left(\frac{1}{(\kappa_5-\kappa_7)} - \left[\frac{(\kappa_6-\kappa_8)}{(\kappa_5-\kappa_7)} + 2x_1\right] SC_2\right)$$

$$Sup3a3 = -\frac{\mu_1}{\mu_2}\left(\frac{(\kappa_6-\kappa_8)}{(\kappa_5-\kappa_7)} + 2x_1\right) SC_3, \qquad Sup4a3 = \frac{\mu_1}{\mu_2}\left[\frac{1}{(\kappa_5-\kappa_7)} - \left[\frac{(\kappa_6-\kappa_8)}{(\kappa_5-\kappa_7)} + 2x_1\right]\frac{1}{Constant2_2}\right]$$

$$\gamma 1F_{s,k} = -\gamma 4_{s,k} - a3C_s \frac{2y_1(-1)^{k+1}}{\pi(2k-1)a}(Sup1a3 + Sup3a3), \qquad \gamma 2F_{s,k} = Diagonal(-\gamma 2_s) + a3C_s \frac{2x_1(-1)^{k+1}}{\pi(2k-1)b} Sup2a3$$

$$\gamma 3F_{s,k} = -a3C_s \frac{2y_1(-1)^{k+1}}{\pi(2k-1)a} Coth\left[\frac{\pi}{2y_1}(2k-1)x_2\right](Sup1a3 + Sup3a3), \qquad \gamma 4F_{s,k} = -a3C_s \frac{2x_2}{\pi(2k-1)b} Sup4a3$$

$$\gamma 5F_{s,k} = a3C_s \frac{b}{\pi ka}\frac{\mu_2}{\mu_1} Coth\left(\frac{\pi k}{b}x_2\right)\left[[1-(-1)^k]Sup1a3 + Sup3a3\right], \gamma 6F_{s,k} = \gamma 5_{s,k} + a3C_s \frac{b}{\pi ka}\left[[1-(-1)^k]Sup1a3 + Sup3a3\right]$$

$$\gamma 7F_{s,k} = a3C_s \frac{a}{\pi kb}[(-1)^k Sup4a3 - Sup2a3]\,, \gamma 8F_{s,k} = a3C_s \frac{a}{\pi kb}\frac{\mu_2}{\mu_1} Coth\left(\frac{\pi k}{a}y_2\right)[(-1)^k Sup4a3 - Sup2a3]$$

$$\gamma 9F_{s,k} = Diagonal(-\gamma 1_s) + a3C_s \frac{2x_1(-1)^{k+1}}{\pi(2k-1)b} Coth\left[\frac{\pi}{2x_1}(2k-1)y_2\right] Sup2a3$$

$$\gamma 10F_{s,k} = -a3C_s \frac{2x_2}{\pi(2k-1)b} Coth\left[\frac{\pi}{2x_2}(2k-1)y_2\right] Sup4a3$$

$$\gamma 11F_{s,k} = a3C_s \frac{2y_2}{\pi(2k-1)a} Coth\left[\frac{\pi}{2y_2}(2k-1)x_2\right] Sup1a3, \gamma 12F_{s,k} = a3C_s \frac{2y_2}{\pi(2k-1)a} Sup1a3$$

$$\gamma 13F_{s,k} = a3C_s \frac{\mu_1}{\mu_2}\left[a_{66}(x_2+a) - \left[\frac{Coef_3 - Coef_4}{(\kappa_5-\kappa_7)} + \left[\frac{(\kappa_6-\kappa_8)}{(\kappa_5-\kappa_7)} + 2x_1\right]\frac{Constant1}{Constant2}\right]\right]$$

$$\delta 1F_{s,k} = -\gamma 4_{s,k} - \gamma 1F_{s,k}, \qquad \delta 2F_{s,k} = Diagonal(-\gamma 2_s) - \gamma 2F_{s,k} + Diagonal(\delta 2_s), \qquad \delta 6F_{s,k} = \gamma 5_{s,k} - \gamma 6F_{s,k} - \delta 3_{s,k}$$

$$\delta 9F_{s,k} = Diagonal(-\gamma 1_s) - \gamma 9F_{s,k} + Diagonal(\delta 1_s), \qquad \delta 12F_{s,k} = \delta 4_{s,k} - \gamma 12F_{s,k}$$

$$a5C_s = \frac{8x_2}{[\pi(2s-1)]^2}, \qquad Sup1a5 = -\frac{\mu_1}{\mu_2}\left[\frac{(\kappa_6-\kappa_8)}{(\kappa_5-\kappa_7)} + 2(x_1+a)\right] SC_1, \qquad Sup2a5 = \frac{\mu_1}{\mu_2}\left(\frac{1}{(\kappa_5-\kappa_7)} - \left[\frac{(\kappa_6-\kappa_8)}{(\kappa_5-\kappa_7)} + 2(x_1+a)\right] SC_2\right)$$

$$Sup3a5 = -\frac{\mu_1}{\mu_2}\left(\frac{(\kappa_6-\kappa_8)}{(\kappa_5-\kappa_7)} + 2(x_1+a)\right) SC_3, \qquad Sup4a5 = \frac{\mu_1}{\mu_2}\left[\frac{1}{(\kappa_5-\kappa_7)} - \left[\frac{(\kappa_6-\kappa_8)}{(\kappa_5-\kappa_7)} + 2(x_1+a)\right]\frac{1}{Constant2_2}\right]$$

$$\varepsilon 1F_{s,k} = a5C_s \frac{2y_1(-1)^{k+1}}{\pi(2k-1)a}(Sup1a5 + Sup3a5), \varepsilon 2F_{s,k} = -a5C_s \frac{2x_1(-1)^{k+1}}{\pi(2k-1)b} Sup2a5$$

$$\varepsilon 3F_{s,k} = \varepsilon 5_{s,k} + a5C_s \frac{2x_2}{\pi(2k-1)b} Coth\left[\frac{\pi}{2y_1}(2k-1)x_2\right](Sup1a5 + Sup3a5), \varepsilon 4F_{s,k} = Diagonal(-\varepsilon 1_s) + a5C_s \frac{2x_2}{\pi(2k-1)b} Sup4a5$$

$$\varepsilon 5F_{s,k} = \varepsilon 4_{s,k} - a5C_s \frac{b}{\pi k a}\frac{\mu_2}{\mu_1} Coth\left(\frac{\pi k}{b}x_2\right)\left([1-(-1)^k]Sup1a5 + Sup3a5\right), \varepsilon 6F_{s,k} = -a5C_s \frac{b}{\pi k a}\left([1-(-1)^k]Sup1a5 + Sup3a5\right)$$

$$\varepsilon 7F_{s,k} = -a5C_s \frac{a}{\pi k b}\left((-1)^k Sup4a5 - Sup2a5\right), \varepsilon 8F_{s,k} = -a5C_s \frac{a}{\pi k b}\frac{\mu_2}{\mu_1} Coth\left(\frac{\pi k}{a}y_2\right)\left((-1)^k Sup4a5 - Sup2a5\right)$$

$$\varepsilon 9F_{s,k} = -a5C_s \frac{2x_1(-1)^{k+1}}{\pi(2k-1)b} Coth\left[\frac{\pi}{2x_1}(2k-1)y_2\right] Sup2a5, \varepsilon 10F_{s,k} = Diagonal(-\varepsilon 2_s) + a5C_s \frac{2x_2}{\pi(2k-1)b} Coth\left[\frac{\pi}{2x_2}(2k-1)y_2\right] Sup4a5$$

$$\varepsilon 11F_{s,k} = -a5C_s \frac{2y_2}{\pi(2k-1)a} Coth\left[\frac{\pi}{2y_2}(2k-1)x_2\right] Sup1a5, \varepsilon 12F_{s,k} = -a5C_s \frac{2y_2}{\pi(2k-1)a} Sup1a5$$

$$\varepsilon 13F_{s,k} = a5C_s \frac{\mu_1}{\mu_2}\left[-a_{66}x_2 + \left[\frac{Coef_3 - Coef_4}{(\kappa_5 - \kappa_7)} + \left[\frac{(\kappa_6 - \kappa_8)}{(\kappa_5 - \kappa_7)} + 2(x_1 + a)\right]\frac{Constant1}{Constant2}\right]\right]$$

$$\theta 3F_{s,k} = \varepsilon 5_{s,k} - \varepsilon 3F_{s,k}, \quad \theta 4F_{s,k} = Diagonal(-\varepsilon 1_s) - \varepsilon 4F_{s,k} + Diagonal(\theta 2_s), \quad \theta 5F_{s,k} = -\theta 3_{s,k} + \varepsilon 4_{s,k} - \varepsilon 5F_{s,k}$$

$$\theta 10F_{s,k} = Diagonal(\theta 1_s) + Diagonal(-\varepsilon 2_s) - \varepsilon 10F_{s,k}, \quad \theta 11F_{s,k} = \theta 4_{s,k} - \varepsilon 11F_{s,k}$$

$$a8C_k = \frac{8y_2}{[\pi(2k-1)]^2}, \quad Sup1a8 = \frac{\mu_1}{\mu_2}\left(\frac{-1}{(\kappa_1 - \kappa_3)} - \left[\frac{(\kappa_2 - \kappa_4)}{(\kappa_1 - \kappa_3)} - 2(y_1 + b)\right]SC_1\right), \quad Sup2a8 = \frac{\mu_1}{\mu_2}\left(-\frac{(\kappa_2 - \kappa_4)}{(\kappa_1 - \kappa_3)} + 2(y_1 + b)\right)SC_2$$

$$Sup3a8 = \frac{\mu_1}{\mu_2}\left(-\frac{(\kappa_2 - \kappa_4)}{(\kappa_1 - \kappa_3)} + 2(y_1 + b)\right)SC_3, \quad Sup4a8 = \frac{\mu_1}{\mu_2}\left(-\frac{(\kappa_2 - \kappa_4)}{(\kappa_1 - \kappa_3)} + 2(y_1 + b)\right)\frac{1}{Constant2}$$

$$\eta 1F_{k,s} = -a8C_k \frac{2y_1(-1)^{s+1}}{\pi(2s-1)a}(Sup1a8 + Sup3a8), \quad \eta 2F_{k,s} = a8C_k \frac{2x_1(-1)^{s+1}}{\pi(2s-1)b} Sup2a8$$

$$\eta 3F_{k,s} = -a8C_k \frac{2y_1(-1)^{s+1}}{\pi(2s-1)a} Coth\left[\frac{\pi}{2y_1}(2s-1)x_2\right](Sup1a8 + Sup3a8), \quad \eta 4F_{k,s} = -a8C_k \frac{2x_2}{\pi(2s-1)b} Sup4a8$$

$$\eta 5F_{k,s} = a8C_k \frac{b}{\pi sa}\frac{\mu_2}{\mu_1} Coth\left(\frac{\pi s}{b}x_2\right)\left[[1-(-1)^s]Sup1a8 + Sup3a8\right], \quad \eta 6F_{k,s} = a8C_k \frac{b}{\pi sa}\left[[1-(-1)^s]Sup1a8 + Sup3a8\right]$$

$$\eta 7F_{k,s} = a8C_k \frac{a}{\pi sb}[(-1)^s Sup4a8 - Sup2a8], \quad \eta 8F_{k,s} = -\eta 4_{k,s} + a8C_k \frac{a}{\pi sb}\frac{\mu_2}{\mu_1} Coth\left(\frac{\pi s}{a}y_2\right)[(-1)^s Sup4a8 - Sup2a8]$$

$$\eta 9F_{k,s} = a8C_k \frac{2x_1(-1)^{s+1}}{\pi(2s-1)b} Coth\left[\frac{\pi}{2x_1}(2s-1)y_2\right] Sup2a8, \quad \eta 10F_{k,s} = \eta 5_{k,s} - a8C_k \frac{2x_2}{\pi(2s-1)b} Coth\left[\frac{\pi}{2x_2}(2s-1)y_2\right] Sup4a8$$

$$\eta 11F_{k,s} = Diagonal(\eta 1_k) + a8C_k \frac{2y_2}{\pi(2s-1)a} Coth\left[\frac{\pi}{2y_2}(2s-1)x_2\right] Sup1a8, \quad \eta 12F_{k,s} = Diagonal(\eta 2_k) + a8C_k \frac{2y_2}{\pi(2s-1)a} Sup1a8$$

$$\eta 13F_{k,s} = a8C_k \frac{\mu_1}{\mu_2}\left[a_{66}y_2 - \left[\frac{Coef_1 - Coef_2}{(\kappa_1 - \kappa_3)} + \left[\frac{(\kappa_2 - \kappa_4)}{(\kappa_1 - \kappa_3)} - 2(y_1 + b)\right]\frac{Constant1}{Constant2}\right]\right]$$

$$\vartheta 8F_{k,s} = -\vartheta 4_{k,s} + \eta 8F_{k,s} + \eta 4_{k,s}\,, \qquad \vartheta 9F_{k,s} = \vartheta 5_{k,s} + \eta 9F_{k,s}\,, \qquad \vartheta 10F_{k,s} = \eta 10F_{k,s} - \eta 5_{k,s}$$

$$\vartheta 12F_{k,s} = Diagonal(\vartheta 2_k) + \eta 12F_{k,s} - Diagonal(\eta 2_k), \qquad \vartheta 11F_{k,s} = Diagonal(\vartheta 1_k) + \eta 11F_{k,s} - Diagonal(\eta 1_k)$$

$$a5C1_k = \frac{4b}{(\pi k)^2}[y1[(-1)^k - 1] + b(-1)^k], \qquad a5C2_k = \frac{2b}{(\pi k)^2}[(-1)^k - 1]$$

$$\chi 1F_{k,s} = \frac{2y_1(-1)^{s+1}}{\pi(2s-1)a}\left[a5C1_k(SC_1 + SC_3) - \frac{a5C2_k}{\kappa_1 - \kappa_3}[1 + (\kappa_2 - \kappa_4)(SC_1 + SC_3)]\right], \chi 2F_{k,s} = \frac{2x_1(-1)^{s+1}}{\pi(2s-1)b}\left[-a5C1_k + \frac{a5C2_k}{\kappa_1 - \kappa_3}[(\kappa_2 - \kappa_4)]\right]SC_2$$

$$\chi 3F_{k,s} = \frac{2y_1(-1)^{s+1}}{\pi(2s-1)a}Coth\left[\frac{\pi}{2y_1}(2s-1)x_2\right]\left[a5C1_k(SC_1 + SC_3) - \frac{a5C2_k}{\kappa_1 - \kappa_3}[1 + (\kappa_2 - \kappa_4)(SC_1 + SC_3)]\right]$$

$$\chi 4F_{k,s} = -\chi 4_{k,s} + \frac{2x_2}{\pi(2s-1)b}\left[a5C1_k - \frac{a5C2_k}{\kappa_1 - \kappa_3}(\kappa_2 - \kappa_4)\right]\frac{1}{Constant2}$$

$$\chi 5F_{k,s} = Diagonal(\chi 2_k) + \frac{\mu_2}{\mu_1}\frac{b}{\pi s a}Coth(\frac{\pi s}{b}x_2)\left[-a5C1_k([1-(-1)^s]SC_1 + SC_3) + \frac{a5C2_k}{\kappa_1 - \kappa_3}\left[[1-(-1)^s] + [1-(-1)^s]SC_1 + SC_3\right](\kappa_2 - \kappa_4)\right]$$

$$\chi 6F_{k,s} = Diagonal(\chi 1_k) + \frac{b}{\pi s a}\left[-a5C1_k([1-(-1)^s]SC_1 + SC_3) + \frac{a5C2_k}{\kappa_1 - \kappa_3}\left[[1-(-1)^s] + [1-(-1)^s]SC_1 + SC_3\right](\kappa_2 - \kappa_4)\right]$$

$$\chi 7F_{k,s} = \chi 5_{k,s} + \frac{a}{\pi s b}\left[-a5C1_k + \frac{a5C2_k}{\kappa_1 - \kappa_3}(\kappa_2 - \kappa_4)\right]\left[\frac{(-1)^s}{Constant2} - SC_2\right]$$

$$\chi 8F_{k,s} = \chi 6_{k,s} + \frac{a}{\pi s b}\frac{\mu_2}{\mu_1}Coth(\frac{\pi s}{a}y_2)\left[-a5C1_k + \frac{a5C2_k}{\kappa_1 - \kappa_3}(\kappa_2 - \kappa_4)\right]\left[\frac{(-1)^s}{Constant2} - SC_2\right]$$

$$\chi 9F_{k,s} = \frac{2x_1(-1)^{s+1}}{\pi(2s-1)b} Coth\left[\frac{\pi}{2x_1}(2s-1)y_2\right]\left[-a5C1_k + \frac{a5C2_k}{\kappa_1-\kappa_3}(\kappa_2-\kappa_4)\right] SC_2$$

$$\chi 10F_{k,s} = -\chi 7_{k,s} + \frac{2x_2}{\pi(2s-1)b} Coth\left[\frac{\pi}{2x_2}(2s-1)y_2\right]\left[a5C1_k - \frac{a5C2_k}{\kappa_1-\kappa_3}(\kappa_2-\kappa_4)\right]\frac{1}{Constant2}$$

$$\chi 11F_{k,s} = \frac{2y_2}{\pi(2s-1)a} Coth\left[\frac{\pi}{2y_2}(2s-1)x_2\right]\left[-a5C1_k SC_1 + \frac{a5C2_k}{\kappa_1-\kappa_3}[1+(\kappa_2-\kappa_4)SC_1]\right]$$

$$\chi 12F_{k,s} = \frac{2y_2}{\pi(2s-1)a}\left[-a5C1_k SC_1 + \frac{a5C2_k}{\kappa_1-\kappa_3}[1+(\kappa_2-\kappa_4)SC_1]\right]$$

$$\chi 13F_{k,s} = \chi 3_k - a5C1_k \frac{Constant1}{Constant2} + \frac{a5C2_k}{\kappa_1-\kappa_3}\left[(Coef_1 - Coef_2) + \frac{Constant1}{Constant2}(\kappa_2-\kappa_4)\right]$$

$$\phi 13F_{k,s} = \phi 6_k - a5C1_k \frac{Constant1}{Constant2} + \frac{a5C2_k}{\kappa_1-\kappa_3}\left[(Coef_1 - Coef_2) + \frac{Constant1}{Constant2}(\kappa_2-\kappa_4)\right]$$

$$\phi 2F_{k,s} = -\phi 7_{k,s} + \chi 2F_{k,s}\,, \phi 4F_{k,s} = \chi 4_{k,s} + \chi 4F_{k,s}\,, \phi 5F_{k,s} = \chi 5F_{k,s} - Diagonal(\chi 2_k) + Diagonal(\phi 2_k)\,, \phi 7F_{k,s} = -\chi 5_{k,s} + \chi 7F_{k,s} + \phi 8_{k,s}$$

$$\phi 6F_{k,s} = \chi 6F_{k,s} - Diagonal(\chi 1_k) + Diagonal(\phi 1_k)\,, \qquad \phi 8F_{k,s} = -\chi 6_{k,s} + \chi 8F_{k,s} + \phi 9_{k,s}\,, \qquad \phi 9F_{k,s} = -\phi 10_{k,s} + \chi 9F_{k,s}$$

$$\phi 10F_{k,s} = \chi 10F_{k,s} + \chi 7F_{k,s}$$

$$a2C1_s = \frac{4a}{(\pi s)^2}[x1[(-1)^s - 1] + a(-1)^s], \qquad a2C2_s = \frac{2a}{(\pi s)^2}[(-1)^s - 1]$$

$$\lambda 1F_{s,k} = -\lambda 7_{s,k} + \frac{2y_1(-1)^{k+1}}{\pi(2k-1)a}\left[-a2C1_s - \frac{a2C2_s(\kappa_6-\kappa_8)}{\kappa_5-\kappa_7}\right](SC_1 + SC_3)\,, \qquad \lambda 2F_{s,k} = \frac{2x_1(-1)^{k+1}}{\pi(2k-1)b}\left[a2C1_s SC_2 + \frac{a2C2_s}{\kappa_5-\kappa_7}[(\kappa_6-\kappa_8)SC_2 - 1]\right]$$

$$\lambda 3F_{s,k} = -\lambda 9_{s,k} - \frac{2y_1(-1)^{k+1}}{\pi(2k-1)a} Coth\left[\frac{\pi}{2y_1}(2k-1)x_2\right]\left[a2C1_s + \frac{a2C2_s(\kappa_6-\kappa_8)}{\kappa_5-\kappa_7}\right](SC_1 + SC_3)$$

$$\lambda 4F_{s,k} = \frac{2x_2}{\pi(2k-1)b}\left[\frac{-a2C1_s}{Constant2} + \frac{a2C2_s}{\kappa_5-\kappa_7}\left[1 - \frac{(\kappa_6-\kappa_8)}{Constant2}\right]\right], \lambda 6F_{s,k} = \lambda 8_{s,k} + \frac{b}{\pi ka}\left[a2C1_s + \frac{a2C2_s(\kappa_6-\kappa_8)}{\kappa_5-\kappa_7}\right][SC_1[1-(-1)^k] + SC_3]$$

$$\lambda 5F_{s,k} = \lambda 10_{s,k} + \frac{b}{\pi ka}\frac{\mu_2}{\mu_1}Coth\left(\frac{\pi k}{b}x_2\right)\left[a2C1_s + \frac{a2C2_s(\kappa_6-\kappa_8)}{\kappa_5-\kappa_7}\right][SC_1[1-(-1)^k] + SC_3]$$

$$\lambda 7F_{s,k} = Diagonal(\lambda 1_s) + \frac{a}{\pi kb}\left[a2C1_s\left[\frac{(-1)^k}{Constant2} - SC_2\right] + \frac{a2C2_s}{\kappa_5-\kappa_7}\left[[1-(-1)^k] + \left[\frac{(-1)^k}{Constant2} - SC_2\right](\kappa_6-\kappa_8)\right]\right]$$

$$\lambda 8F_{s,k} = Diagonal(\lambda 2_s) + \frac{a}{\pi kb}\frac{\mu_2}{\mu_1}Coth\left(\frac{\pi k}{a}y_2\right)\left[a2C1_s\left[\frac{(-1)^k}{Constant2} - SC_2\right] + \frac{a2C2_s}{\kappa_5-\kappa_7}\left[[1-(-1)^k] + \left[\frac{(-1)^k}{Constant2} - SC_2\right](\kappa_6-\kappa_8)\right]\right]$$

$$\lambda 9F_{s,k} = \frac{2x_1(-1)^{k+1}}{\pi(2k-1)b}Coth\left[\frac{\pi}{2x_1}(2k-1)y_2\right]\left[a2C1_sSC_2 + \frac{a2C2_s}{\kappa_5-\kappa_7}[(\kappa_6-\kappa_8)SC_2 - 1]\right]$$

$$\lambda 10F_{s,k} = \frac{2x_2}{\pi(2k-1)b}Coth\left[\frac{\pi}{2x_2}(2k-1)y_2\right]\left[-\frac{a2C1_s}{Constant2} + \frac{a2C2_s}{\kappa_5-\kappa_7}\left[1 - \frac{(\kappa_6-\kappa_8)}{Constant2}\right]\right]$$

$$\lambda 11F_{s,k} = \frac{2y_2}{\pi(2k-1)a}Coth\left[\frac{\pi}{2y_2}(2k-1)x_2\right]\left[a2C1_s + \frac{a2C2_s}{\kappa_5-\kappa_7}(\kappa_6-\kappa_8)\right]SC_1, \lambda 12F_{s,k} = \frac{2y_2}{\pi(2k-1)a}\left[a2C1_s + \frac{a2C2_s}{\kappa_5-\kappa_7}(\kappa_6-\kappa_8)\right]SC_1$$

$$\lambda 13F_{k,s} = \lambda 6_s + a2C1_s\frac{Constant1}{Constant2} + \frac{a2C2_s}{\kappa_5-\kappa_7}\left[(Coef_3 - Coef_4) + \frac{Constant1}{Constant2}(\kappa_6-\kappa_8)\right]$$

$$\xi 13F_{k,s} = \xi 3_s + a2C1_s\frac{Constant1}{Constant2} + \frac{a2C2_s}{\kappa_5-\kappa_7}\left[(Coef_3 - Coef_4) + \frac{Constant1}{Constant2}(\kappa_6-\kappa_8)\right]$$

$$\xi 1F_{s,k} = \lambda 7_{s,k} + \lambda 1F_{s,k}, \quad \xi 3F_{s,k} = \lambda 9_{s,k} + \lambda 3F_{s,k}, \quad \xi 5F_{s,k} = -\lambda 10_{s,k} + \xi 7_{s,k} + \lambda 5F_{s,k}, \quad \xi 6F_{s,k} = -\lambda 8_{s,k} + \xi 5_{s,k} + \lambda 6F_{s,k}$$

$$\xi 7F_{s,k} = -Diagonal(\lambda 1_s) + Diagonal(\xi 2_s) + \lambda 7F_{s,k}, \quad \xi 8F_{s,k} = -Diagonal(\lambda 2_s) + Diagonal(\xi 1_s) + \lambda 8F_{s,k}, \quad \xi 11F_{s,k} = -\xi 6_{s,k} + \lambda 11F_{s,k}$$

$$\xi 12F_{s,k} = -\xi 4_{s,k} + \lambda 12F_{s,k}$$

APPENDIX-B: ELECTRICAL WIRING DIAGRAMS FOR THE TEST RIG

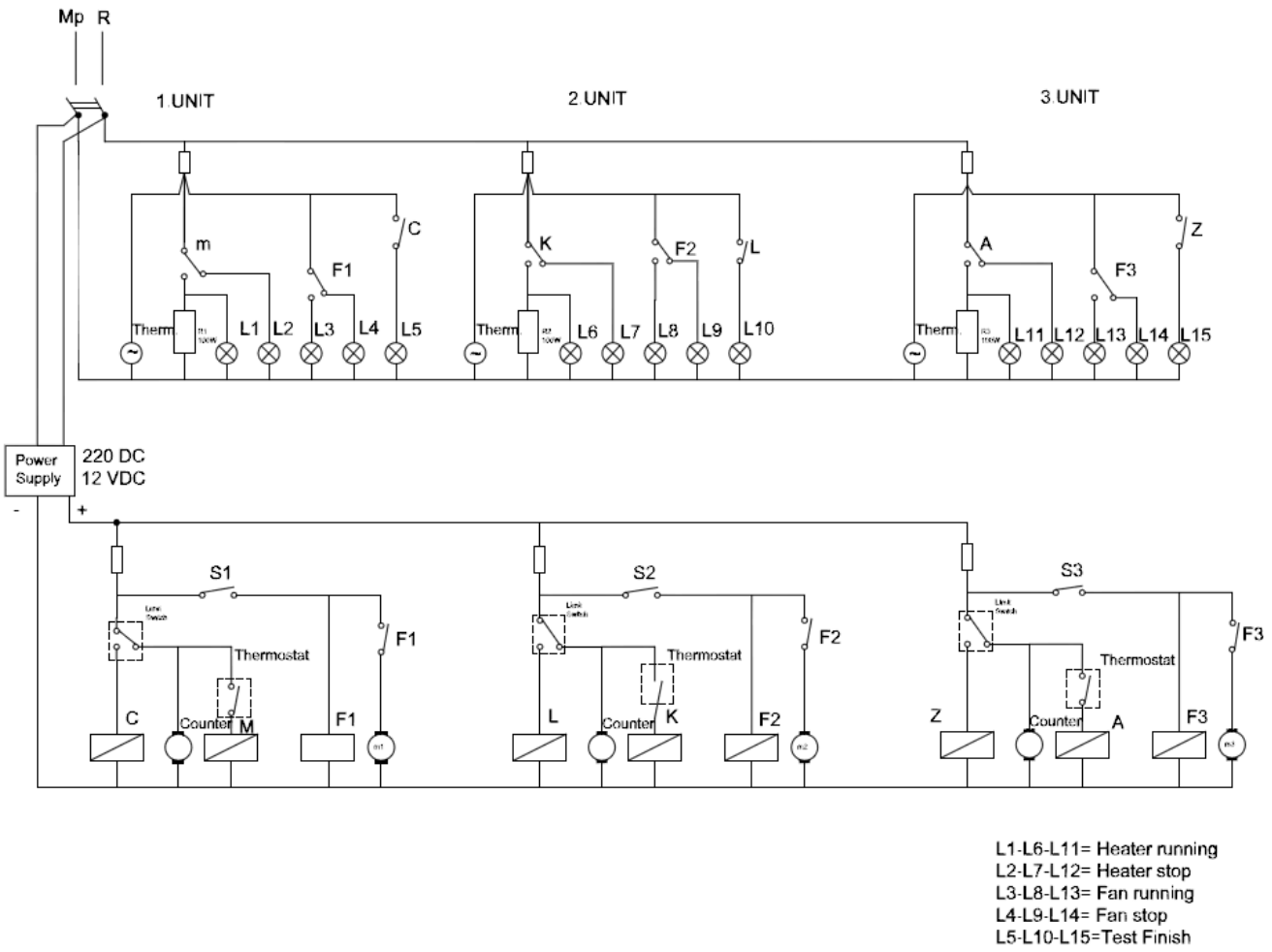

***FIGURE-B.1**: Wiring Diagram for Test Setup – For Tests in Air*

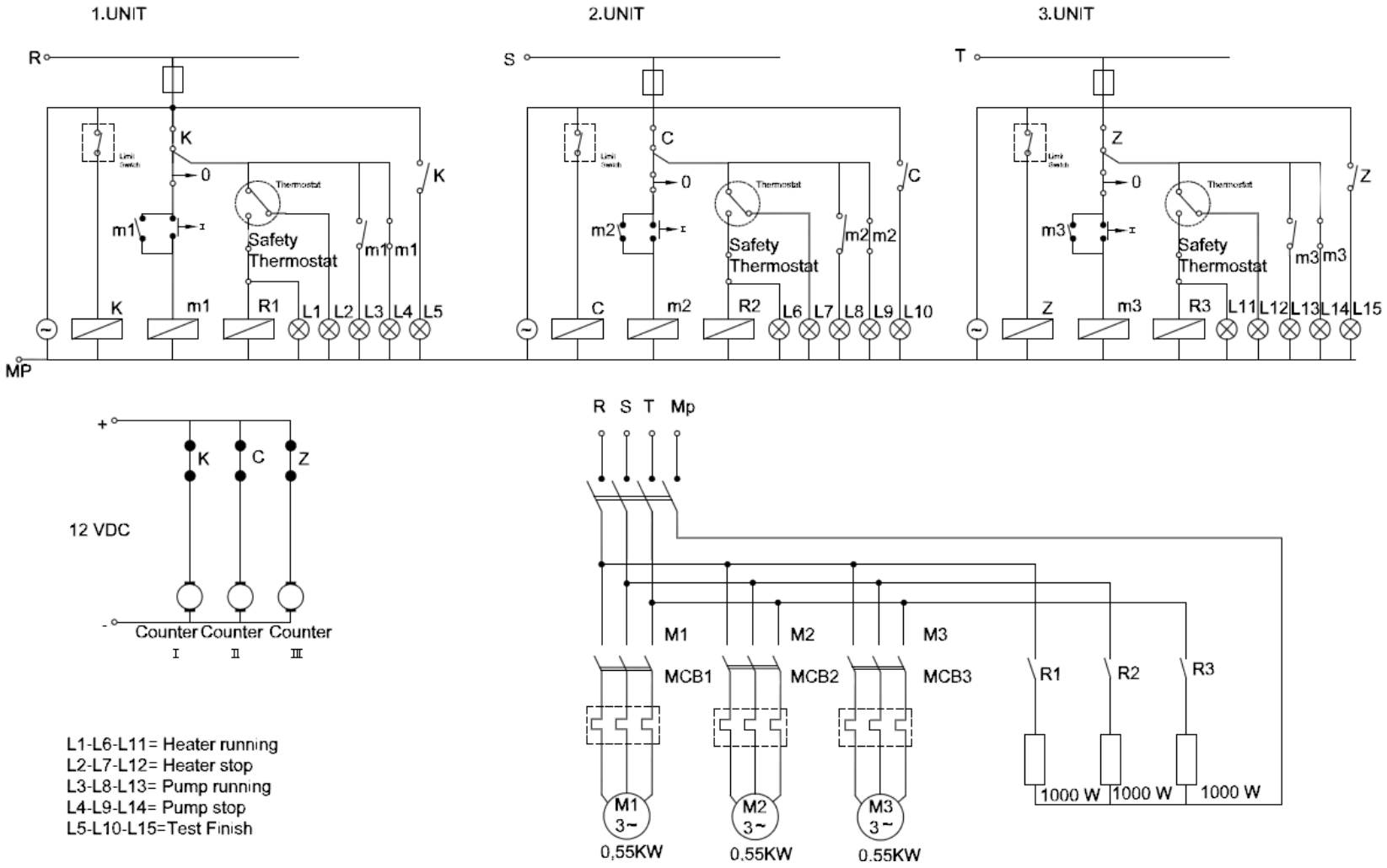

***FIGURE-B.2**: Wiring Diagram for Test Setup – For Tests in Oil*

REFERENCES

1. WATERS M, *The Short-Circuit Strength of Power Transformers*, McDonald&Co, 1966

2. MOSSER H P, *Transformerboard*, SCIENTIA ELECTRICA, 1979

3. STEPHENS H O, *Transformer Reactance and Losses with Non-uniform Windings*, AIEE Transactions Vol 53, 1934 pp. 346-349

4. ROGOWSKI W, *On the Leakage Field and the Leakage Induction Coefficient of a Transformer with Sandwich Windings and Divided End Coils*, Zeitschrift des Vereins Deutscher Ingeniure Vol 71, 1909 pp. 1-36

5. ROTH E, *Magnetic Leakage Inductance in Transformer with Cylindrical Windings and Forces Acting on the Windings*, Revue Generale de L'Electrite Vol 40, 1936 pp. 291-303, 326-336

6. HAMMOND P, *Roth's Method for the Solution of Boundary-Value Problems in Electrical Engineering*, PROC. IEEE Vol 114, 1967 pp. 1969 - 1976.

7. MULLINEUX, N.; REED, J.R.; De KUJIPER, C.; Hammond, P, *Roth's Method for the Solution of Boundary-Value Problems*, PROC. IEEE Vol 116 Issue: 2, 1969 pp. 291 - 293.

8. BILLIG E, *Calculation of the Magnetic Field of Rectangular Conductors in a Closed Slot and Its Applications to the Reactance of Transformer Windings*, Report Q/T106 British Electrical and Allied Industries Research Association, 1945

9. PRAMANIK, A., *Extension of Roth's method to 2-dimensional rectangular regions containing conductors of any cross-section,* Proceedings of the IEEE, Vol 116 No:7, 1969 pp. 1286 – 1288.

10. Rabins L, *Transformer Reactance Calculations with Digital Computers*, AIEE Transactions Vol 75, 1956 pp. 261-267

11. VEIN P R, *A Method Based on Maxwell's Equations for Calculating the Axial Short Circuit Stresses in the Concentric Windings of an Idealized Transformer*, Report Q/T151 British Electrical and Allied Industries Research Association Vol 168, 1960 pp. 817-820

12. SOLLERGREN M B et al, *Calculation of Short circuit Forces in Transformers***,** CIGRE ELECTRA Report Study Committee 12, Vol 69, pp.29-75

13. ANDERSEN, O.W., *Transformer Leakage Flux Program Based on the Finite Elements Method*, IEEE Transactions on Power Apparatus and Systems, Vol PAS-92 Issue: 2, 1973 pp. 682 – 689.

14. LURIE , A.I., ZENOVA, Z.P., PANIBRATETZ, A.N.,*Tangent Forces in Transformer Windings at Short Circuit,* The International Journal for Computation and Mathematics in Electrical and Electronic Engineering, 1991 Vol 11 No:1, pp. 133-136

15. PATEL M R, *Dynamic Stability of Helical and Barrel Coils in Transformers against Axial Short-Circuit Forces*, IEE Proceedings Vol 127 No5, 1980 pp. 281-284

16. TOURNIER et al, *A Study of the Dynamic Behaviour of Transformer Windings Under Short-Circuit Conditions*, CIGRE Reports No143, 1962 pp. 346-349

17. PATEL M R, *Dynamic Response of Power Transformers under Axial Short Circuit Forces. Part-1 Winding and Clamp as Individual Components*, IEEE Transactions on Power Apparatus and Systems Vol PAS-92 No5, 1973 pp. 1558-1566

18. PATEL M R, *Dynamic Response of Power Transformers under Axial Short Circuit Forces. Part-2 Winding and Clamp as Combined System*, IEEE Transactions on Power Apparatus and Systems Vol PAS-92 No5, 1973 pp. 1567-1575

19 KUMBHAR, G.B., KULKARNI, S.V., *Analysis of Short-Circuit Performance of Split-Winding Transformer Using Coupled Field-Circuit Approach*, IEEE Transactions on Power Delivery, Vol 22 Issue: 2, 2007 pp. 936 – 943

20. HIROYUKI et all, *Buckling Strength Analysis Of Large Power Transformer Windings Subjected To Electromagnetic Force Under Short Circuit*, , IEEE Transactions on Power Apparatus and Systems, Vol PAS-99 Issue: 3, 1980 pp. 1288 – 1297.

21. BAKSHI A, KULKARNI S.V., *Eigenvalue Analysis for Investigation of Tilting of Transformer Winding Conductors Under Axial Short-Circuit Forces*, , IEEE Transactions on Power Delivery, Vol 26 Issue: 4, 2011 pp. 2505 – 2512.

22. KNAACK W, *The Mechanical Stressing of Transformer Windings upon Short-Circuit*, CIGRE Reports No135, 1956

23. LUR'E S I, MIL'MAN L I, *Mechanical Characteristics of Insulating Materials for Transformer Windings*, Electrical Research Association Translation Ref. Trans. IB2265, 1964

24. LUR'E S I, MIL'MAN L I, *Mechanical Characteristics of Insulating Boards for Transformers*, Electrical Research Association Translation Ref. Trans. IB2270, 1963

25. SWIHART D O, WRIGHT D V, *Dynamic Stiffness and Damping of Transformer Pressboard During Axial Short Circuit Vibration*, IEE Transactions on Power Apparatus and Systems Vol PAS-95 No2, 1976 pp. 721-730

26. SJODAHL M., *Accuracy in electronic speckle photography,* Applied Optics, Vol 36, 1997 pp. 2875 – 2885.

27. GOM mbH., *ARAMIS User Manual,* GOM mbH, Rev.A, 2005

28. AMIT P et al., *Analysis of Wind Turbine Material using Digital Image Correlation,* Proceedings of the XIth International Congress and Exposition, 2008

29. SCHMIDT T et al., *Performance Verification of 3D Image Correlation using Digital High-Speed Cameras* , Proceedings of 2005 SEM Annual Conference and Exposition, 2005

30. WILLIAMS J G, *On the Calculation of Energy Release Rates for Cracked Laminates*, International Journal of Fracture 36, 1973 pp. 101-119

31. WILLIAMS J G, *Large Displacement and End Block Effects in the DCB Interlaminar Test in Modes I and II*, Journal of Composite Materials 21, 1987 pp. 330-347

32. WILLIAMS J G, *The Fracture Mechanics of Delamination Tests*, International Journal of Strain Analysis Vol 24, 1989 pp. 207-214

33. WILLIAMS J G, *End Corrections for Orthotropic DCB Specimens*, Composites Science and Technology 35, 1989 pp. 367-376

34. CHARLES, E. D., *Mechanical Forces on Current Carrying Conductors*, IEE Proceedings Vol 110 No:9, 1963 pp. 1671-1677.

35. LAWRANCE P H, *Basic Circuit Theory with Digital Computers*, Prentice-Hill, Inc. 1972

36. CORCORAN, R.J., PALMER, S., *Mechanical Properties of Copper in Relation to Power-Transformer Design*, Power Engineering Journal 1987 pp. 154-157.

37. TIMOSHENKO S, *Strength of Materials,* Part I and II 3rd Edition, 1956

38. BOERSMA R, WILDEBOER J, *The Short Circuit Strength of the Inner Windings of Transformers Against Radial Forces,* CIGRE Reports No147, 1962

39. TORSEKE L, *Short Circuit Problems in Large Transformers,* CIGRE Reports No142, 1962

40. Del-VECCHIO R M, POULIN B, FEGHALI P T, SHAH D M, AHUJA R, *Transformer Design Principles with Application to Core-type Power Transformers*, CRC Press, 2001

41. HUMAR J L, *Dynamics of Structures*, Taylor & Francis, 2005

42. STENKVIST E, *What is known about the Ability of Large Power Transformers to Withstand a Short Circuit? Comments on Existing Standards,* CIGRE Reports No106, 1956

43. IEC60076-5 Standard, Power Transformers – Ability to Withstand Short circuit

44. QUINNEY, D.A.,*Dynamic Response of Power Transformer Winding under Axial Short Circuit conditions,* Proceedings of the IEE, 1981 Vol 128 ,No:2, pp. 114-118.

45. OKUYAMA, K., HORI, Y., *Axial vibraiton Analysis of Transformer Windings under Short circuit Conditions ,* IEEE Transactions on Power Apparatus and Systems, Vol PAS-99 Issue: 2, 1980 pp. 443 – 451.

46. BIGGIE , K.M., PREVOST, T.A., *Calculation Method for Power Transformer Clamping Rings Made from Laminated Insulation Materials,* Electrical Insulation Conference and Electrical Manufacturing & Coil Winding Conference 2001 pp. 567-576.

47. WHITNEY, J., M., *Elasticity Analysis of Orthotropic Beams under Concentrated Loads ,* Composites Science and Technology, Vol 22, 1985 pp. 167 – 184.

48. McNUTT W J, JOHNSON W M, NELSON R A, AYERS R E, *Power Transformer Short Circuit Strength - Requirements, Design and Demonstration*, IEEE Transactions on Power Apparatus and Systems Vol PAS-89 No8, 1970 pp. 1955-1969

49. McNUTT W J, PATEL M R, *The combined Effects of Thermal Ageing and Short-Circuit Stresses on Transformer Life*, IEEE Transactions on Power Apparatus and Systems Vol PAS-95 No4, 1976 pp. 1275-1286

50. EL-MISSIRY, M. M., *Electromagnetic Forces in Sheet and Foil Wound Transformers*, IEE Proceedings Vol 129 No:2, 1982 pp. 86-92.

51. WATERS, M., *The Measurement and Calculation of Axial Electromagnetic Forces in concentric windings*, Report Q/T134 British Electrical and Allied Industries Research Association, 1963.

52. BILLIG, E., ,*Mechanical Stresses in Transformer Windings,* British Electrical and Allied Industries Research Association, 1973.

53. ARTURI, C.M., *Force Calculations in Transformer Windings Under Unbalanced MMFs by a non-Linear Finite Elements Code,* IEEE Transactions on Magnetics Vol 28 No:2, 1992 pp. 1363-1366.

54. NORRIS, E.T.,*Mechanical Strength of Power Transformers in Service,* Proceedings of the IEEE, 1957 Vol 104 ,Issue:16, pp. 289-300.

55. Bertula, T., Nordman, H., Saunamaki, Y., and Maaskola, J. *Short Circuit Stresses in Three-Limb Transformers with Delta Connected İnner Winding During Singlephase Faults,* CIGRE 1980, Paper No. 12–03.